VOL. 107 NO. ST11. NOV. 1981

JOURNAL OF THE STRUCTURAL DIVISION

PROCEEDINGS · OF
THE AMERICAN SOCIETY
OF CIVIL ENGINEERS

VOL.107 NO.ST11. NOV. 1981

JOURNAL OF THE STRUCTURAL DIVISION

PROCEEDINGS OF
THE AMERICAN SOCIETY
OF CIVIL ENGINEERS

Copyright© 1981 by
American Society
of Civil Engineers
All Rights Reserved
ISSN 0044-8001

John E. Bower, Editor
U.S. Steel Corporation

AMERICAN SOCIETY OF CIVIL ENGINEERS

BOARD OF DIRECTION

President
James R. Sims

Past President
Irvan F. Mendenhall

President Elect
John H. Wiedeman

Vice Presidents
Lyman R. Gillis
Albert A. Grant
Paul A. Kuhn
William H. Taylor

Directors
Martin G. Abegg
L. G. Byrd
Frederick W. DeWitt
Larry J. Feeser
John A. Focht, Jr.
Sergio Gonzalez-Karg
Kenneth D. Hansen
Ronald C. Hirschfield
Louis M. Laushey
Leon D. Luck
Arthur R. McDaniel
Robert L. Morris
Paul R. Munger
William R. Neuman
Leonard S. Oberman
John D. Parkhurst
Celestino R. Pennoni
Robert B. Rhode
Gerald E. Speitel
Lawrence E. Wilson, Jr.
Richard W. Woodruff

EXECUTIVE OFFICERS

Eugene Zwoyer, *Executive Director*
Julie E. Gibouleau, *Assistant to the Executive Director*
Louis L. Meier, *Washington Counsel/Assistant Secretary*
William H. Wisely, *Executive Director Emeritus*
Michael N. Salgo, *Treasurer*
Elmer B. Isaak, *Assistant Treasurer*

STAFF DIRECTORS

Donald A. Buzzell, *Managing Director for Education and Professional Affairs*
Robert A. Crist, Jr., *Managing Director for Publications and Technical Affairs*
Alexandra Bellow, *Director, Human Resources*
Joe DeFiglia, *Director, Management Information Services*
David Dresia, *Director, Publications Production and Marketing*
Barker D. Herr, *Director, Membership*
Richard A. Jeffers, *Controller*
Carl E. Nelson, *Director, Field Services*
Don P. Reynolds, *Director, Policy, Planning and Public Affairs*
Bruce Rickerson, *Director, Legislative Services*
Albert W. Turchick, *Director, Technical Services*
George K. Wadlin, *Director, Education Services*
R. Lawrence Whipple, *Director, Engineering Management Services*

COMMITTEE ON PUBLICATIONS

William R. Neumann, *Chairman*
Martin G. Abegg
John A. Focht, Jr.
Ronald C. Hirschfield
Paul R. Munger
Lawrence E. Wilson, Jr.

STRUCTURAL DIVISION

Executive Committee
Ronald G. Domer, *Chairman*
Roland L. Sharpe, *Vice Chairman*
John E. Bower
Joseph H. Appleton, *Management Group B Contact Member*
Donald McDonald
Sherman A. Nelson, *Management Group B Contact Member*

Publications Committee
John E. Bower, ***Chairman, Editor and Exec. Comm. Contact Member***
Mihran S. Agbabian
Marvin E. Criswell
John T. DeWolf
Douglas Foutch
Ovadia E. Lev
Le-Wu Lu
Bruce E. Lyons
Walter Podolny
Emil Simiu
John F. Stolz
C. K. Wang
James T. P. Yao

PUBLICATIONS SERVICES DEPARTMENT

David Dresia, *Director, Publications Production and Marketing*

Technical and Professional Publications
Richard R. Torrens, *Manager*
Chuck Wahrhaftig, *Chief Copy Editor*
Corinne Bernstein, *Copy Editor*
Linda Ellington, *Copy Editor*
Walter Friedman, *Copy Editor*
Shiela Menaker, *Production Co-ordinator*
Richard C. Scheblein, *Draftsman*

Information Services
Melanie G. Edwards, *Editor*

PERMISSION TO PHOTOCOPY JOURNAL PAPERS

Permission to photocopy for personal or internal reference beyond the limits in Sections 107 and 108 of the U.S. Copyright Law is granted by the American Society of Civil Engineers for libraries and other users registered with the Copyright Clearance Center, 21 Congress Street, Salem, Mass. 01970, provided the appropriate fee is paid to the CCC for all articles bearing the CCC code. Requests for special permission or bulk copying should be addressed to the Manager of Technical and Professional Publications, American Society of Civil Engineers.

CONTENTS

Curved Beam Element for Arch Buckling Analysis
by Robert K. Wen and Jose Lange 2053

Bolted Friction Connections with Weathering Steel
by Joseph A. Yura, Karl H. Frank, and Lloyd Cayes 2071

Procedure for Predicting Wind Damage to Buildings
by Kishor C. Mehta, James R. McDonald, and Douglas A. Smith . . . 2089

Uniform Loading for Steel-Deck-Reinforced Slabs
by F. Wayne Klaiber and Max L. Porter 2097

Abutment-Thermal Interaction of Composite Bridge
by Jack H. Emanuel and David B. Lewis 2111

Floating Bridge Drawspan Maintenance
by Colin B. Brown, Derald R. Christensen, John W. Heavner, Michael A. Landy, and Ramiah Vasu 2127

The Journal of the Structural Division (ISSN 0044-8001) is published monthly by the American Society of Civil Engineers. Publications office is at 345 East 47th Street, New York, N.Y. 10017. Address all ASCE correspondence to the Editorial and General Offices at 345 East 47th Street, New York, N.Y. 10017. Allow six weeks for change of address to become effective. Subscription price to members is $22.50. Nonmember subscriptions available; prices obtainable on request. Second-class postage paid at New York, N.Y. and at additional mailing offices. ST.

POSTMASTER: Send address changes to American Society of Civil Engineers, 345 East 47th Street, New York, NY 10017.

The Society is not responsible for any statement made or opinion expressed in its publications.

Field Measurements of Muskwa River Bridge
by Walter Dilger, J. C. Beauchamp, M. S. Cheung, and Amin Ghali 2147

Prediction of Temperatures in Concrete Bridges
by Allan Churchward and Yehuda J. Sokal 2163

Discrete Structural Optimization
by Judith S. Liebman, Narbey Khachaturian, and Visarn Chanaratna 2177

Response Measurements for Glass Cladding Panels
by James I. Craig and Barry J. Goodno 2199

Extensions to Curved Prestressed Concrete Beams
by Carlo Pace and Luigino Dezi 2215

Shear Strength of R/C Beam-Column Connections
by Donald F. Meinheit and James O. Jirsa 2227

Fundamental Analysis of Aggregate Interlock
by Joost C. Walraven 2245

Package for Optimization-Based Interactive CAD
by M. A. Bhatti, K. S. Pister, and E. Polak 2271

DISCUSSION

Proc. Paper 16616

Parametric Investigations of Vibrating Cable Networks, by Louis F. Geschwindner, Jr. and Harry H. West (Mar., 1979. Prior Discussion: Mar., 1981).
closure 2287

Suspension Bridge Vibrations: Computed and Measured,* by Peter G. Buckland, Roy Hooley, Brian D. Morgenstern, Johann H. Rainer, and Aegide M. van Selst (May, 1979).
by Robert H. Scanlan 2287

Aerodynamic Response of Long H-Sections, by Francis J. Maher and Larry E. Wittig (Jan., 1980).
errata 2289

*Discussion period closed for this paper. Any other discussion received during this discussion period will be published in subsequent Journals.

Dome Effect in RC Slabs: Elastic-Plastic Analysis, by Mikael W. Braestrup and C. T. Morley (June, 1980. Prior Discussion: Apr., 1981).
closure 2289

Concrete Reinforcing Net: Safe Design, by Zdenek P. Bazant, Tatsuya Tsubaki, and Ted B. Belytschko (Sept., 1980. Prior Discussion: July, 1981).
closure 2291

End Restraint and Column Stability,* by Wai F. Chen (Nov., 1980).
by Tibor Tarnai 2292

Nonlinear Creep Buckling of Reinforced Concrete Columns,* by Zdenek P. Bazant and Tatsuya Tsubaki (Nov., 1980).
by Jostein Hellesland and James G. MacGregor 2294
errata 2298
closure 2298

Research Needs in Stability of Metal Structures,* by Reidar Bjorhovde (Dec., 1980).
by S. Unnikrishna Pillai 2299
by Jacques Rondal 2301
by Donald R. Sherman 2301

Errors in Utilization of Cold-Formed Steel Members,* by Frank J. Zamecnik (Dec., 1980).
by Duane S. Ellifritt 2303
by Gilliam S. Harris 2304

Proposed Specifications for Steel Box Girder Bridges,* by Roman Wolchuk (Dec., 1980).
by F. Tupula Yamba and M. S. Troitsky 2305

Impact of Solid Missiles on Concrete Barriers,* by Wen S. Chang (Feb., 1981).
by Achintya Haldar 2307

Response of RC Shear Wall under Ground Motions,* by Awadh B. Agrawal, Leslie G. Jaeger, and Aftab A. Mufti (Feb., 1981).
by Catherine E. Wolfgram 2309

Experimental Evaluation of Composite Action,* by Rafik Y. Itani, Mossain M. Morshed, and Robert J. Hoyle (Mar., 1981).
by R. Hussein 2311

*Discussion period closed for this paper. Any other discussion received during this discussion period will be published in subsequent Journals.

STATEMENT OF OWNERSHIP

The *Journal of the Structural Division* is edited and published by the American Society of Civil Engineers, with general business offices at 345 East 47th Street, New York, N.Y. 10017. The Manager of Technical and Professional Publications is Richard R. Torrens.

This Journal is owned wholly by the American Society of Civil Engineers, a nonprofit educational and professional organization with about 78,000 members. There are no individual owners or stockholders.

	Average No. Copies Each Issue During Preceding 12 Months	Single Issue Nearest To Filing Date
Total no. copies printed (net press run)	11,054	11,056
Paid mail circulation	8,581	8,747
Sales through dealers and counter sales	None	None
Free distribution	None	None
Total distribution	8,581	8,747
Left Over (extra for new orders, office use, etc.)	2,473	2,309
Total	11,054	11,056

I certify that the above statements made by me are correct and complete.—Richard R. Torrens, Manager of Technical and Professional Publications.

16625 CURVED BEAM ELEMENT FOR ARCH BUCKLING ANALYSIS

KEY WORDS: **Analysis; Arches;** Bifurcations; **Bridges (arch); Buckling; Curved beams;** Finite elements; Models

ABSTRACT: A finite element model is presented for a beam initially curved in one plane but deformable in the three dimensional space. Geometric nonlinearities are included in the analysis and eigenproblems are formulated to calculate the bifurcation buckling loads of arches. Numerical results obtained for some problems indicated that [n2] had only negligible effect on the buckling load and that the rotation terms in [n1] should be deleted. Results thus obtained with the modified [n1] matrix and with only a few elements to represent the arch structure indicated very good agreement with known analytical solutions and available experimental data.

REFERENCE: Wen, Robert K. (Prof. of Civ. Engrg., Michigan State Univ., East Lansing, Mich.), and Lange, Jose, "Curved Beam Element for Arch Buckling Analysis," *Journal of the Structural Division,* ASCE, Vol. 107, No. ST11, **Proc. Paper 16625**, November, 1981, pp. 2053-2069

16644 BOLTED CONNECTIONS WITH WEATHERING STEEL

KEY WORDS: **Bolted joints; Bridges;** Connections (joints); Creep; Exposure; Friction; **Specifications; Steel; Weathering**

ABSTRACT: One hundred twenty-six slip tests were conducted on friction-type bolted connections fabricated from A588 weathering steel. The tests were conducted mainly on specimens with mill scale or blasted surfaces which were exposed to the atmosphere for periods up to one year. The test results indicate that A588 mill scale surface has a 33 percent lower slip resistance than those reported for other steels. Suggested revisions to the AASHTO Bridge Specifications based on this behavior are presented.

REFERENCE: Yura, Joseph A. (Prof., Dept. of Civ. Engrg., The Univ. of Texas, Austin, Tex.), Frank, Karl H., and Cayes, Lloyd, "Bolted Friction Connections with Weathering Steel," *Journal of the Structural Division,* ASCE, Vol. 107, No. ST11, **Proc. Paper 16644**, November, 1981, pp. 2071-2087

16645 PREDICTING WIND DAMAGE TO BUILDINGS

KEY WORDS: **Buildings; Damage patterns; Damage prevention;** Design; Inspection; Planning; Safety; **Storms;** Structural engineering; **Wind forces**

ABSTRACT: Experience gained from post-storm investigations of damaged buildings has made it possible to predict types of damage expected on existing buildings. Two procedures that involve different levels of engineering effort are outlined in the paper to predict wind damage to buildings. The level I procedure is a subjective one utilizing a questionnaire. Answers to the questionnaire for a particular building are used to ascertain the type and extent of potential damage to the building. The level II procedure is an analytical one. Structural analysis is performed using knowledge of wind-structure interaction, material properties, and a building's structural system to establish threshold failure wind speeds. Damage sequence and possible failure modes can be ascertained from the analysis. The two procedures have been used to predict damage to various types of ordinary buildings. The predictions are used for indentification of areas of safety for occupant protection for construction retrofitting of components to improve a building's wind resistance capabilities.

REFERENCE: Mehta, Kishor C. (Prof., Dept. of Civ. Engrg., Texas Tech Univ., P.O. Box 4089, Lubbock, Tex. 79409), McDonald, James R., and Smith, Douglas A., "Procedure for Predicting Wind Damage to Buildings," *Journal of the Structural Division,* ASCE, Vol. 107, No. ST11, **Proc. Paper 16645**, November, 1981, pp. 2089-2096

16642 UNIFORM LOADING FOR STEEL-DECK-REINFORCED SLABS

KEY WORDS: **Concrete (reinforced);** Deflection; Floors; **Load distribution;** Loads (forces); **Shear strength; Slabs; Structural engineering;** Ultimate strength

ABSTRACT: Previous research at Iowa State University has resulted in a shear-bond design equation which was based on data obtained from tests utilizing concentrated line loads on one-way elements. However, since most floor slabs are usually designed for uniformly distributed loads a shear-bond formulation for such loading is required. A modification of the shear-bound concentrated loading design equation is examined for use with uniformly loaded systems. The results of laboratory service and ultimate load tests which substantiated the equation conversion are presented. The full-scale slab element tests consist of three uniformly loaded specimens which are compared with three companion specimens subjected to concentrated line loads. A description of the loading system and test procedures utilized for each type of loading is given. In addition to the shear-bond strength comparison for the tests, significant behavioral characteristics involving failure, end slip, load-deflection, and cracking are presented.

REFERENCE: Klaiber, F. Wayne (Prof. of Civ. Engrg., Iowa State Univ., Ames, Iowa.), and Porter, Max L., "Uniform Loading for Steel-Deck-Reinforced Slabs," *Journal of the Structural Division,* ASCE, Vol. 107, No. ST11, **Proc. Paper 16642,** November, 1981, pp. 2097-2110

16631 ABUTMENT-THERMAL INTERACTION OF COMPOSITE BRIDGE

KEY WORDS: Bridge decks; Bridges; **Bridges (girder); Composite beams;** Composite structures; Concrete (reinforced); Movement; **Temperature distribution;** Thermal expansion; **Thermal stresses**

ABSTRACT: An experimental investigation is conducted to substantiate a prior study of environmental stresses induced in composite-girderbridge structures. The objectives of the study were to subject a two-span test structure, with tie-rods to simulate approach-slab forces, to thermal loading, and to correlate the resulatant strains and deflections with those obtained form the theoretical study. The experimental results and theoretical values are in reasonable agreement. It is concluded that the theoretical procedure provides a rational method for predicting the thermal behavior of composite-girder bridge structures and can be applied with reasonable confidence when used with realistic temperature profiles, material properties, and substructure stiffness characteristics.

REFERENCE: Emanuel, Jack H. (Prof. of Civ. Engrg., Univ. of Missouri-Rolla, Rolla, Mo. 65401), and Lewis, David B., "Abutment-Thermal Interaction of Composite Bridge," *Journal of the Structural Division,* ASCE, Vol. 107, No. ST11, **Proc. Paper 16631,** November, 1981, pp. 2111-2126

16627 FLOATING BRIDGE DRAWSPAN MAINTENANCE

KEY WORDS: Bascule bridges; **Bridge maintenance;** Bridges; Damage assessment; **Fatigue limit;** Life expectancy; **Methodology; Strain measurement;** Stress strain relations; **Wind forces**

ABSTRACT: A methodology for making maintenance decisions to avoid fatigue failure is proposed. The maintenance procedures developed for the drawspan mechanism of the Evergreen Point Bridge are used as an illustration of the methodology. The methodology includes, development of the stress/environment relationship for the critical member, collection of long-term environmental data and the computation of long-term stress distribution, determination of cycles at each stress level from the return period, and duration of various environmental conditions and the member frequency at the associated stress level, determination of the fatigue characteristics of the member (S-N) from a limited number of full-scale tests using the Prot procedure, and determination of yearly damage and, life expectancy using Miner's hypothesis.

REFERENCE: Brown, Colin B. (Prof. of Civ. Engrg., Univ. of Washington, Seattle, Wash., 98195), Christensen, Derald R., Heavner, John W., Landy, Michael A., and Vasu, Ramiah, "Floating Bridge Drawspan Maintenance," *Journal of the Structural Division,* ASCE, Vol. 107, No. ST11, **Proc. Paper 16627,** November, 1981, pp. 2127-2146

16656 FIELD MEASUREMENTS OF MUSKWA RIVER BRIDGE

KEY WORDS: **Bridges (box girder); Cold weather construction;** Composite structures; Computation; **Concrete (reinforced);** Field tests; Strain gages; **Strains;** Stresses; **Temperature effects**

ABSTRACT: The behaviour of a continuous, steel-concrete composite box girder bridge was monitored during construction of the concrete deck and during the first three years of operation. It was observed that cracking developed in the deck which was attributed to the temperature developed in the deck shortly after casting, the sequence of casting, the shrinkage of the deck concrete, and the rapid heating of the steel boxes exposed to direct sunlight. It was also found that the strain distributions across the depth and the width of the steel boxes are more or less linear. This beam theory can be applied with confidence for the design of this type of structure.

REFERENCE: Dilger, Walter (Prof. of Civ. Engrg., Univ. of Calgary, Calgary, Alberta, Canada), Beauchamp, J. C., Cheung, M. S., and Ghali, Amin, "Field Measurements of Muskwa River Bridge," *Journal of the Structural Division,* ASCE, Vol. 107, No. ST11, **Proc. Paper 16656,** November, 1981, pp. 2147-2161

16676 PREDICTION OF TEMPERATURES IN CONCRETE BRIDGES

KEY WORDS: Box girders; Bridges; **Bridges (box girder); Concrete; Monitoring;** Statistical analysis; Stress analysis; Temperature; **Temperature effects; Thermal analysis; Thermocouples**

ABSTRACT: A section of a poststressed twin box concrete bridge is instrumented for continuous recording of temperatures within the concrete and of environmental parameters outside. The recorded data are processed with the aim of presenting it in the form suitable for analysis of similar bridges for thermal effects. It is found that the necessary data can be represented through only two design variables, namely maximum differential temperature DTMAX and base temperature BT. Analytical expressions are derived which give vertical temperature profiles as function of DTMAX and environmental parameter insolation. The value of the average temperature is similarly obtained from empirical expressions which are functions of the two design variables and environmental parameter ambient air temperature. The derived expressions correlate satisfactorily with the measured data, however further research is required to test the effect on stresses and curvatures. A flow chart is given showing main steps in design.

REFERENCE: Churchward, Allan (Engr., Main Roads Dept., Brisbane, Queensland, Australia), and Sokal, Yehuda J., "Prediction of Temperatures in Concrete Bridges," *Journal of the Structural Division,* ASCE, Vol. 107, No. ST11, **Proc. Paper 16676,** November, 1981, pp. 2163-2176

16643 DISCRETE STRUCTURAL OPTIMIZATION

KEY WORDS: Concrete (reinforced); **Discrete distribution functions; Frames;** Gradients; **Optimization; Structural design;** Structural engineering

ABSTRACT: A new method for solving discrete structural optimization problems is presented. An interior penalty function is used to convert the original constrained problem into an unconstrained parametric problem. Then the search for the optimal solution to the parametric problem is based on a discrete direction gradient. Solving an appropriate sequence of these unconstrained parametric problems is equivalent to solving the original constrained optimization problem. This method is illustrated first on a small reinforced concrete problem, and then to the design of steel building frames which are made up of standard sections. Results for a one-story four-bay unsymmetrical frame and an eight-story three-bay symmetrical frame are described.

REFERENCE: Liebman, Judith S. (Assoc. Prof. of Operations Research, Dept. of Mechanical and Industrial Engrg., Univ. of Illinois at Urbana-Champaign, Urbana, Ill 61801), Khachaturian, Narbey, and Chanaratna, Visarn, "Discrete Structural Optimization," *Journal of the Structural Division,* ASCE, Vol. 107, No. ST11, **Proc. Paper 16643,** November, 1981, pp. 2177-2197

16673 RESPONSE MEASUREMENTS FOR GLASS CLADDING PANELS

KEY WORDS: Buildings; **Cladding; Dynamics; Finite elements;** Glass; **Models;** Plates; Stiffness; Structural engineering; Vibration; **Windows**

ABSTRACT: Response measurements in the laboratory of full scale glass cladding panels are presented and compared with the predictions of finite element models. The detailed static and dynamic behavior of a glass panel (window) mounted within a flexible frame and attached to a building frame by means of flexible connections was the focus of the studies. Both singles as well as double pane glass panels are handled. The present results are limited to dynamic response analyses and measurments only. The dynamic response measurements reveal the presence, as predicted, of double plate modes in which the plates move out of phase with respect to each other. One of these, involving no net interpane volume change, is found to occur at a low enough frequency to pose potential problems in large windows where significant pressure nonuniformity might provide excitation. For the range of parameters studied, the results are in good agreement with the predictions of the models and thus confirm their validity and appropriateness.

REFERENCE: Craig, James I. (Assoc. Prof., School of Aerospace Engrg., Georgia Inst. of Tech., Atlanta, Ga. 30332), and Goodno, Barry J., "Response Measurements For Glass Cladding Panels," *Journal of the Structural Division,* ASCE, Vol. 107, No. ST11, **Proc. Paper 16673,** November, 1981, pp. 2199-2214

16665 CURVED PRESTRESSED CONCRETE BEAMS

KEY WORDS: Beams; **Comparative studies; Concrete (prestressed);** Continuous beams; **Curved beams;** Linear transformations; Stress; **Theorems**

ABSTRACT: The theorem of Guyon is modified for a continuous curved beam and those forces that invalidate the theorem are determined in terms of equivalent loads. For these loads, influence coefficients for stress resultants and rotations at the ends of each single span are obtained. These coefficients are used to determine the effect of a linear transformation in the two most common schemes used in continous beams, and the results obtained are compared with those for straight beams.

REFERENCE: Pace, Carlo (Asst. Prof., Instituto di Tecnica delle Costruzioni, Ancona, Italy), and Dezi, Luigino, "Extensions to Curved Prestressed Concrete Beams," *Journal of the Structural Division,* ASCE, Vol. 107, No. ST11, **Proc. Paper 16665,** November, 1981, pp. 2215-2225

16668 SHEAR STRENGTH OF R/C BEAM-COLUMN CONNECTIONS

KEY WORDS: Axial compression; **Beam columns;** Building design; **Buildings (codes); Concrete (reinforced);** Connections; Inelastic action; **Joints;** Load shifting; **Reinforcement (structures); Shear strength**

ABSTRACT: Strength and load reversal tests were conducted on reinforced concrete beam-column connections. Fourteen tests investigated the influence of the column axial compressive stress, the amount of hoop reinforcement in the connection, the size and location of transverse beams, and the geometry of the connection region. The test results indicate that the current state-of-the-art design procedure underestimates the capabilities of concrete in the beam-column connection and overestimates the contribution of hoop reinforcement in the connection. It appears that satisfactory load reversal behavior can be achieved if the shear stress in the connection is about half of the monotonic shear strength.

REFERENCE: Meinheit, Donald F. (Sr. Structural Engr., Wiss, Janney, Elstner, and Assoc., Inc. Northbrook, Ill.), and Jirsa, James O., "Shear Strength of R/C Beam-Column Connections," *Journal of the Structural Division,* ASCE, Vol. 107, No. ST11, **Proc. Paper 16668,** November, 1981, pp. 2227-2244

16664 FUNDAMENTAL ANALYSIS OF AGGREGATE INTERLOCK

KEY WORDS: **Analysis; Concrete; Concrete aggregates; Cracks;** Particle distribution; Shear distribution; Shear forces

ABSTRACT: A model for aggregate interlock has been developed based on the behavior of micro scale. The relation between displacements and stresses across the crack faces are defined to be a function of deformation and sliding at particle level. This relation is derived for one particle projecting from one of the crack faces with an arbitrary diameter and an arbitrary embedment depth. The most probable distribution of aggregate particles, crossed by the plane of cracking and their positions with regard to this plane are assessed by a statistical analysis. The general relations between stresses and displacements for a unit crack area are obtained by integrating all particle contributions. The model proves to give adequate results, compared with experiments, carried out on several types of (cracked) concrete. Using this model, further analysis of the mechanism of aggregate interlock has been carried out, explaining tendencies observed in tests of other investigators.

REFERENCE: Walraven, Joost C. (Sr. Research Engr., Univ. of Technology, Delft, The Netherlands), "Fundamental Analysis of Aggregate Interlock," *Journal of the Structural Division,* ASCE, Vol. 107, No. ST11, **Proc. Paper 16664,** November, 1981, pp. 2245-2270

16675 PACKAGE FOR OPTIMIZATION-BASED INTERACTIVE CAD

KEY WORDS: **Computer applications; Computerized design;** Computers; **Constraints;** Design; Dynamics; **Optimum design;** Problem solving; **Time dependence**

ABSTRACT: An interactive program, based on a method of feasible directions, for solving a constrained minimization problem with time-dependent constraints is described. The interaction, involving both alphanumeric and color-graphic display, permits the designer a number of options, including, changing parameters in the problem or design algorithm, Single steping through any loop in the algorithm, and displaying relevant data, writing small "macro" programs to perform an unforeseen test or computation, and performing side calculations. An example to demonstrate the advantages of user interaction in reducing computational effort is included.

REFERENCE: Bhatti, M. A. (Asst. Prof., Division of Materials Engrg., Univ., of Iowa, Iowa City, Iowa 52240), Pister, K. S., and Polak, E., "Package for Optimization-Based Interactive CAD," *Journal of the Structural Division,* ASCE, Vol. 107, No. ST11, **Proc. Paper 16675,** November, 1981, pp. 2271-2284

U.S. Customary-SI Conversion Factors

In accordance with the October, 1970 action of the ASCE Board of Direction, which stated that all publications of the Society should list all measurements in both U.S. Customary and SI (International System) units, the following list contains conversion factors to enable readers to compute the SI unit values of measurements. A complete guide to the SI system and its use has been published by the American Society for Testing and Materials. Copies of this publication (ASTM E-380) can be purchased from ASCE at a price of $3.00 each; orders must be prepaid.

All authors of *Journal* papers are being asked to prepare their papers in this dual-unit format. To provide preliminary assistance to authors, the following list of conversion factors and guides are recommended by the ASCE Committee on Metrication.

To convert	To	Multiply by
inches (in.)	millimeters (mm)	25.4
feet (ft)	meters (m)	0.305
yards (yd)	meters (m)	0.914
miles (miles)	kilometers (km)	1.61
square inches (sq in.)	square millimeters (mm^2)	645
square feet (sq ft)	square meters (m^2)	0.093
square yards (sq yd)	square meters (m^2)	0.836
square miles (sq miles)	square kilometers (km^2)	2.59
acres (acre)	hectares (ha)	0.405
cubic inches (cu in.)	cubic millimeters (mm^3)	16,400
cubic feet (cu ft)	cubic meters (m^3)	0.028
cubic yards (cu yd)	cubic meters (m^3)	0.765
pounds (lb) mass	kilograms (kg)	0.453
tons (ton) mass	kilograms (kg)	907
pound force (lbf)	newtons (N)	4.45
kilogram force (kgf)	newtons (N)	9.81
pounds per square foot (psf)	pascals (Pa)	47.9
pounds per square inch (psi)	kilopascals (kPa)	6.89
U.S. gallons (gal)	liters (L)	3.79
acre-feet (acre-ft)	cubic meters (m^3)	1,233

CURVED BEAM ELEMENT FOR ARCH BUCKLING ANALYSIS

By Robert K. Wen,[1] M. ASCE and Jose Lange[2]

INTRODUCTION

In this paper a finite element model is presented for a beam initially curved in one plane but deformable in three-dimensional space. Geometric nonlinearities have been included in the analysis and eigenproblems formulated to calculate the bifurcation buckling loads of arches. Although a considerable amount of work has been done on arch buckling, most past works have dealt with the stability in the plane of the curved structure. Previous studies that dealt with out-of-plane buckling have been limited to circular or parabolic arches. The curved beam element presented herein can be used to calculate the in-plane or out-of-plane buckling loads of arches of different shapes, as well as other structures involving curved beam components.

The curved axis of the element considered is represented by a fourth order polynomial that can enforce continuity of the slopes and curvatures of contiguous elements. The displacement functions are approximated by cubic polynomials. Geometric nonlinearities are considered by including the effect of rotations on the longitudinal strains. The element is assumed to have a constant cross-section with two axes of symmetry. Effects of possible warping restraint are neglected.

An expression was derived for the strain energy based on the nonlinear longitudinal strains and a linear relationship between twist and torsional moment. The linear stiffness matrix k and the first and second order incremental stiffness matrices, $[n1]$ and $[n2]$ were derived by differentiating the strain energy. These matrices can be used for linear equilibrium and nonlinear equalibrium analysis (on the Lagrangian basis, if the rotations are not large). They can also be used for incremental equilibrium analysis. Herein, following a presentation by Mallet and Marcal (13), they were used to formulate eigenproblems for buckling loads by setting the structural incremental stiffness to zero and assuming that the displacement increases linearly with the applied loads.

[1]Prof. of Civ. Engrg., Michigan State Univ., East Lansing, Mich.
[2]Formerly, Grad. Student, Dept. of Civ. Engrg., Michigan State Univ., East Lansing, Mich.

Note.—Discussion open until April 1, 1982. To extend the closing date one month, a written request must be filed with the Manager of Technical and Professional Publications, ASCE. Manuscript was submitted for review for possible publication on July 21, 1981. This paper is part of the Journal of the Structural Division, Proceedings of the American Society of Civil Engineers, ©ASCE, Vol. 107, No. ST11, November, 1981. ISSN 0044-8001/81/0011-2053/$01.00.

For certain numerical problems solved in this study, the influence of the second order incremental stiffness matrix, $[n2]$, on the buckling load seemed negligible. For some other problems, it appeared that the terms that correspond to rotations in the first order incremental stiffness matrix, $[n1]$, should be deleted. The performance of the method thus resembled that of the classical linear theory of stability. Numerical results obtained using the modified incremental stiffness matrix for certain test problems indicated very good agreement with known solutions. Small differences may be mainly attributed to the assumption concerning the extensibility of the axis of the arch, and the support conditions.

For linear equilibrium problems, Ashwell and Sabir (1) have discussed the use and limitations of several types of shape functions for finite elements for circular arches deformed in a plane. Dawe (7) has studied the use of higher order polynomials for shape functions. Gellert and Laursen (10) have presented a mixed formulation of finite elements for arches of arbitrary shape. Mebane and Stricklin (16) have pointed out that rigid body motion could be considered implicitly included in the polynomial form of shape functions as the number of elements used to represent the structure increases.

The area of classical buckling analysis of curved structures has been investigated by many researchers. Austin (2) has summarized the state of the knowledge of the in-plane bending and buckling of arches. His presentation was concerned with the available experimental and analytical data and their relations to design applications. Austin and Ross (3) have compared the solutions of the in-plane buckling of symmetrically loaded arches between the classical buckling theory and the exact, nonlinear buckling load analysis. They found that, except for buckling in the symmetric mode (snap-through), the buckling load obtained with the classical theory is very close to the bifurcation load obtained with the exact theory.

Ojalvo and Newman (17) have reported a basic theoretical work on the linear elastic stability of a curved beam in space. Ojalvo, Demuts, and Tokarz (18) followed the preceding work to study the out-of-plane buckling of a member curved in one plane. The theory was also applied by Shukla and M. Ojalvo (20) to calculate the buckling loads which may be tilted, as would be the case for an arch bridge with a horizontally rigid deck. As a particular case of the equations presented in (17), Tokarz and Sandhu (22) developed the linear differential equations and obtained solutions for the lateral-torsional buckling of a parabolic arch subjected to a uniformly distributed load.

Nonlinear finite element analyses of arches including bifurcation loads and limit loads have been reported by Walker (23), Dawe (6), Sabir and Lock (19), and Mak and Kao (14). Ebner and Ucciferro (8) have reported comparison of several versions of incremental stiffness matrices for beam elements. These works, however, are all limited to behavior in a plane.

Method of Analysis

Potential Energy and Strain Energy: Consider a structure-load system with a finite number of degrees of freedom, subjected to conservative loading. The potential energy, Φ, may be written as

$$\Phi = U - \{Q\}\{P\} \quad \ldots\ldots\ldots\ldots\ldots\ldots\ldots\ldots\ldots\ldots\ldots\ldots\ldots\ldots (1)$$

in which U = strain energy; $[Q]$ = row vector of the degrees of freedom of the structure; and $\{P\}$ = the load vector corresponding to $[Q]$. The strain energy, U, = the sum of the strain energy of the constituent elements of the structure. The strain energy of a curved beam element is derived subsequently.

Displacement-Strain Relation.—Consider a beam element curved in one plane, as shown in Fig. 1. The centroidal axis curves in the x-z plane with radius of curvature R (which may vary). The x, y, and z axes form a right-handed coordinate system with corresponding displacements u, v, and w. Assuming that plane sections remain plane after bending deformation and neglecting effects of possible warping restraint, the expression for the longitudinal strain at a point (ξ, η) in a section s, measured along the curved centroidal axis, may be written as

$$\epsilon)_{s,\xi,\eta} = \epsilon_z)_o + \eta\,\kappa_x - \xi\,\kappa_y \quad \ldots\ldots\ldots\

$$\beta_x = -u\,\bar{k}_z - \frac{dv}{ds} + w\,\bar{k}_x = -\frac{dv}{ds} \quad \ldots\ldots (4a)$$

$$\beta_y = \frac{du}{ds} - v\,\bar{k}_z + \bar{k}_y\,w = \frac{du}{ds} + \frac{w}{R} \quad \ldots\ldots (4b)$$

$$\beta_z = \beta \quad \ldots\ldots (4c)$$

in which β = the twist of the cross-section about the z-axis. Substituting Eqs. 4*a*–4*c* into Eqs. 3*a*–3*c*

$$\kappa_x = \frac{\beta}{R} - \frac{d^2 v}{ds^2} \quad \ldots\ldots (5a)$$

$$\kappa_y = \frac{d^2 u}{ds^2} + \frac{dw}{ds}\frac{1}{R} + w\frac{d}{ds}\left(\frac{1}{R}\right) \quad \ldots\ldots (5b)$$

$$\kappa_z = \frac{1}{R}\frac{dv}{ds} + \frac{d\beta}{ds} \quad \ldots\ldots (5c)$$

It may be noted that for the case of a circular member and inextensional deformation, the above expressions reduce to those of Eqs. 7–32 of Ref. 21.

The longitudinal strain at the centroidal axis may be written as

$$\epsilon_z)_o = \left(\frac{dw}{ds} - \frac{u}{R}\right) + \frac{1}{2}\left(\frac{du}{ds} + \frac{w}{R}\right)^2 + \frac{1}{2}\left(\frac{dv}{ds}\right)^2 \quad \ldots\ldots (6)$$

in which the quantity in the first parenthesis = the usual linear hoop strain in a curved element, and the next two terms (which are nonlinear), represent the contributions to the strain by the rotations of the centroidal axis about the y and x-axis, respectively. Substituting Eqs. 5*a*–5*c* and 6, into Eq. 2, the expression for the longitudinal strain is obtained:

$$\epsilon = \epsilon_z)_{x,\xi,\eta} = \left(\frac{dw}{ds} - \frac{u}{R}\right) + \frac{1}{2}\left(\frac{du}{ds} + \frac{w}{R}\right)^2 + \frac{1}{2}\left(\frac{dv}{ds}\right)^2$$
$$+ \eta\left(\frac{\beta}{R} - \frac{d^2 v}{ds^2}\right) - \xi\left[\frac{d^2 u}{ds^2} + \frac{1}{R}\frac{dw}{ds} + w\frac{d}{ds}\left(\frac{1}{R}\right)\right] \quad \ldots\ldots (7)$$

Element Strain Energy.—The expression for the strain energy of the element may be written as

$$U_E = U_\epsilon + U_t \quad \ldots\ldots (8)$$

in which U_ϵ = the strain energy due to the longitudinal strain; and U_t = that due to St. Venant torsion. They are given by the expressions

$$U_\epsilon = \int_{\text{vol}} \frac{E\epsilon^2}{2}\,dV = \int_s \int_A \frac{E\epsilon^2}{2}\,dA\,ds$$

$$U_t = \int_s \frac{G K_t}{2}\left(\beta_s + \frac{1}{R}v_s\right)^2 ds \quad \ldots\ldots (9)$$

in which ϵ = the longitudinal strain, as expressed by Eq. 7; A = the cross-sectional area; E and G = Young's modulus and shear modulus; and K_t = the torsion constant of the cross-section. In the preceding equation, the notation of using a subscript to represent a differentiation has been used, e.g., $\beta_{,s} \equiv d\beta/ds$.

Finite Element Formulation.—Element Geometry: Referring to the curved element shown in Fig. 2, the coordinates of the nodes A and B, with respect to the global coordinate system are, (X_A, Y_A) and (X_B, Y_B) respectively. Their relative position is defined by $X_L = X_B - X_A$ and $Y_L = Y_B - Y_A$. The origin of the element local coordinate system is located at node A, with the x-axis in the radial direction, the y-axis normal to the plane of curvature, and the z-axis tangent to the curved centroidal axis forming an angle ϕ_A with the global X-axis. The coordinates (x_B, z_B) of node B in the element coordinate system are given by

$$x_B = -X_L \sin \phi_A + Y_L \cos \phi_A \quad \ldots \quad (10a)$$

$$z_B = X_L \cos \phi_A + Y_L \sin \phi_A \quad \ldots \quad (10b)$$

The angle ϕ in Fig. 2 varies from zero at node A to θ at node B; s varies

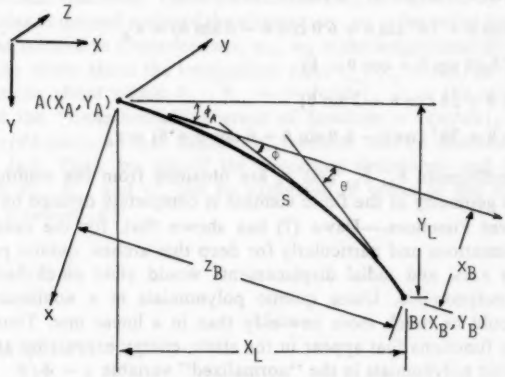

FIG. 2.—Typical Element

along the longitudinal axis; and the radii of curvature R at nodes A and B are $R1$ and $R2$, respectively.

At any point along the curve the following relations hold:

$$dz = ds \cos \phi$$

$$dx = ds \sin \phi \quad \ldots \quad (11)$$

The curve is approximated by a fourth-order polynomial:

$$s = b_1 \phi + b_2 \phi^2 + b_3 \phi^3 + b_4 \phi^4 \quad \ldots \quad (12)$$

The boundary conditions used to solve for the coefficients b_i are the following:

1. at $\phi = 0, R = R1$ . . . . . (13*a*)

2. at $\phi = \theta$, $R = R2$ . . . . . (13*b*)

3. $$\int_0^{x_B} dx = \int_0^{\theta} \sin\phi \, R \, d\phi = x_B \quad \ldots\ldots\ldots\ldots\ldots\ldots \quad (13c)$$

4. $$\int_0^{z_B} dz = \int_0^{\theta} \cos\phi \, R \, d\phi = z_B \quad \ldots\ldots\ldots\ldots\ldots\ldots \quad (13d)$$

The radius of curvature is obtained by differentiating Eq. 12:

$$R = \frac{ds}{d\phi} = b_1 + 2\,b_2\phi + 3\,b_3\phi^2 + 4\,b_4\phi^3 \quad \ldots\ldots\ldots\ldots\ldots\ldots \quad (14)$$

From the first condition, $b_1 = R1$. Conditions 2, 3, and 4 yield three linear equations for b_2, b_3 and b_4:

$$R1 + 2b_2\theta + 3b_3\theta^2 + 4b_4\theta^3 = R2 \quad \ldots\ldots\ldots\ldots\ldots\ldots \quad (15a)$$

$$R1(1 - \cos\theta) + 2b_2(\sin\theta - \theta\cos\theta)$$
$$+ 3b_3(-\theta^2\cos\theta + 2\theta\sin\theta + 2\cos\theta - 2)$$
$$+ 4b_4(-\theta^3\cos\theta + 3\theta^2\sin\theta + 6\,\theta\cos\theta - 6\sin\theta) = x_B \quad \ldots\ldots\ldots \quad (15b)$$

$$R1\sin\theta + 2b_2(\theta\sin\theta + \cos\theta - 1)$$
$$+ 3b_3(\theta^2\sin\theta + 2\theta\cos\theta - 2\sin\theta)$$
$$+ 4b_4(\theta^3\sin\theta + 3\theta^2\cos\theta - 6\,\theta\sin\theta - 6\cos\theta + 6) = z_B \quad \ldots\ldots\ldots \quad (15c)$$

Once the coefficients b_2, b_3, and b_4 are obtained from the solution of Eqs. 15*a*–15*c*, the geometry of the finite element is completely defined by Eq. 12.

Displacement Functions.—Dawe (7) has shown that, for the case of linear inplane deformations and particularly for deep thin arches, quintic polynomials for both the axial and radial displacements would yield much better results than cubic polynomials. Using quintic polynomials in a nonlinear analysis, however, would be much more unwieldy than in a linear one. Thus, the four displacement functions that appear in the strain energy expression are approximated by cubic polynomials in the "normalized" variable $\gamma = \phi/\theta$:

$$u = \lambda_1 + \lambda_2\gamma + \lambda_3\gamma^2 + \lambda_4\gamma^3 \quad \ldots\ldots\ldots\ldots\ldots\ldots \quad (16a)$$

$$v = \lambda_5 + \lambda_6\gamma + \lambda_7\gamma^2 + \lambda_8\gamma^3 \quad \ldots\ldots\ldots\ldots\ldots\ldots \quad (16b)$$

$$w = \lambda_9 + \lambda_{10}\gamma + \lambda_{11}\gamma^2 + \lambda_{12}\gamma^3 \quad \ldots\ldots\ldots\ldots\ldots\ldots \quad (16c)$$

$$\beta = \lambda_{13} + \lambda_{14}\gamma + \lambda_{15}\gamma^2 + \lambda_{16}\gamma^3 \quad \ldots\ldots\ldots\ldots\ldots\ldots \quad (16d)$$

in which the λ's are coefficients.

Element Strain Energy.—By use of Eqs. 7, 8, and 9, the strain energy of the element may be written as

$$U_E = U_2 + U_3 + U_4 \quad \ldots\ldots\ldots\ldots\ldots\ldots \quad (17)$$

in which U_2, U_3, and U_4 contain respectively the quadratic, cubic, and quartic terms of the displacement field variables:

$$U_2 = \frac{E}{2}\int_0^1 \left[\frac{A}{R\theta}(w_\gamma - \theta u)^2 + I_\xi \frac{\theta}{R^3}\left(R\beta - \frac{v_{\gamma\gamma}}{\theta^2} - v_\gamma \gamma_{zz} R^2\right)^2 + \frac{I_\eta}{R^3\theta^3}(u_{\gamma\gamma} + u_\gamma \gamma_{zz} R^2\theta^2 + w_\gamma \theta + w\gamma_{z\gamma} R\theta^2)^2\right] d\gamma + \frac{GK_t}{2}\int_0^1 \frac{1}{R^3\theta}(R\beta_\gamma + v_\gamma)^2\, d\gamma \quad (18)$$

$$U_3 = \frac{EA}{2}\int_0^1 \frac{1}{R^2\theta^2}(w_\gamma - \theta u)[(u_\gamma + \theta w)^2 + v_\gamma^2]\, d\gamma \quad (19)$$

$$U_4 = \frac{EA}{8}\int_0^1 \frac{1}{R^3\theta^3}[(u_\gamma + \theta w)^2 + v_\gamma^2]^2\, d\gamma \quad (20)$$

Upon substituting the displacement functions given by Eqs. 16*a*–16*d* into Eqs. 18, 19, and 20, U_2, U_3, and U_4 become functions of the coefficients λ_i in the displacement functions. These coefficients may be replaced by the displacement variables at the end nodes of the element: u_A, u_B = the radial displacements; v_A, v_B = the transverse displacements; w_A, w_B = the longitudinal displacements; β_A, β_B = the twists about the longitudinal axis; θ_{y_A}, $\theta_{y_B} = (du/ds + w/R)_{A,\text{or}\,B}$ = the rotations about y-axis; θ_{x_A}, $\theta_{x_B} = (-dv/ds)_{A,\text{or}\,B}$ = the rotations about x-axis; and the "nonessential" degrees of freedom = $(dw/ds)_A$, $(dw/ds)_B$, $(d\beta/ds)_A$, $(d\beta/ds)_B$. These degrees of freedom will be denoted collectively by vector $\{q\}$. Thus, by use of the preceding definitions and Eqs. 16, 18, 19, and 20, U_2, U_3, and U_4 can be expressed in terms of the element nodal degrees of freedom $\{q\}$:

$$U_2 = \int_0^1 f_2(\{q\})\, d\gamma \quad (21a)$$

$$U_3 = \int_0^1 f_3(\{q\})\, d\gamma \quad (21b)$$

$$U_4 = \int_0^1 f_4(\{q\})\, d\gamma \quad (21c)$$

in which f_2, f_3, and f_4 are, respectively, quadratic, cubic, and quartic functions of the q's.

The linear element stiffness matrix $[k]$ may be obtained as

$$[k] = [k_{ij}] = \left[\frac{\partial^2 U_2}{\partial q_i \partial q_j}\right] = \left[\int_0^1 \frac{\partial^2 f_2}{\partial q_i \partial q_j}\, d\gamma\right] \quad (22)$$

The "incremental stiffness matrices," $[n1]$ and $[n2]$, may be calculated from

$$[n1] = [(n1)_{ij}] = \left[\frac{\partial^2 U_3}{\partial q_i \partial q_j}\right] = \left[\int_0^1 \frac{\partial^2 f_3}{\partial q_i \partial q_j}\, d\gamma\right] \quad (23)$$

$$[n2] = [(n2)_{ij}] = \left[\frac{\partial^2 U_4}{\partial q_i \partial q_j}\right] = \left[\int_0^1 \frac{\partial^2 f_4}{\partial q_i \partial q_j}\, d\gamma\right] \quad \ldots\ldots\ldots\ldots (24)$$

The expressions for the integrands in terms of the q's in Eqs. 22, 23, and 24 are too lengthy to be presented here. They are explicitly given in a subroutine of a computer program contained in (11). The integrals themselves, in general, need be evaluated numerically.

System Equilibrium Equations.—The structural linear stiffness $[K]$ and incremental stiffness matrices $[N1]$ and $[N2]$ can be assembled from the corresponding element matrices in the usual fashion of finite element analysis. The potential energy may be written as (13)

$$\Phi = \tfrac{1}{2}[Q]\left[[K] + \tfrac{1}{3}[N1] + \tfrac{1}{12}[N2]\right]\{Q\} - [Q]\{P\} \quad \ldots\ldots\ldots (25)$$

The first variation of the potential energy produces the equilibrium equation

$$\left[[K] + \frac{1}{2}[N1] + \frac{1}{3}[N2]\right]\{Q\} = \{P\} \quad \ldots\ldots\ldots\ldots\ldots\ldots (26)$$

The equations governing the linear incremental behavior follow from the second variation of the potential energy and are given by

$$([K] + [N1] + [N2])_{\{\bar{Q}\}}\{\Delta Q\} = \{\Delta P\} \quad \ldots\ldots\ldots\ldots\ldots\ldots (27)$$

in which $\{\bar{Q}\}$ = the reference equilibrium position.

Formulation of Eigenvalue Problems.—A basis for obtaining a critical load of a structural system is the vanishing of $\{\Delta P\}$ in Eq. 27. This leads to

$$([K] + [N1] + [N2])_{\{\bar{Q}\}}\{\Delta Q\} = \{0\} \quad \ldots\ldots\ldots\ldots\ldots\ldots (28)$$

Eq. 28 may be written for each point on the fundamental path. That path, of course, can be determined only by a solution of the nonlinear equilibrium equation, i.e., Eq. 26. For a given load vector $\{\bar{P}\}$ and displacement vector $\{\bar{Q}\}$ on the fundamental path, if a nontrivial solution of $\{\Delta Q\}$ is obtained from Eq. 28, the load $\{\bar{P}\}$ would be an "exact" buckling load (the bifurcation or snap-through load).

In order to avoid dealing with the nonlinear equations, however, an approximate solution of the buckling load may be obtained from Eq. 28 by assuming that the displacement of the structure increases linearly with the applied load until buckling occurs (13). Thus, assuming that the load vector $\{P\}$ is representable by a scalar parameter p in $\{P\} = p\{P_o\}$, in which $\{P_o\}$ = a reference load vector, Eq. (28) may be written as

$$([K] + p_{cr}[N1] + p_{cr}^2[N2])_{\{Q_o\}}\{\Delta Q\} = \{0\} \quad \ldots\ldots\ldots\ldots\ldots\ldots (29)$$

in which p_{cr} = the value of p at which buckling occurs. Note that in Eq. 29 the incremental stiffness matrices are evaluated at $\{Q\} = \{Q_o\} = [K]^{-1}\{P_o\}$. This equation represents a quadratic eigenvalue problem for estimating the buckling loads and their associated buckling modes.

If it can be assumed that at buckling the displacements are sufficiently small, then the matrix $[N2]$ may be neglected. Thus, Eq. 29 reduces to a linear eigenvalue problem, i.e.,

$$([K] + p_{cr}[N1])_{(Q_o)}\{\Delta Q\} = \{0\} \quad \ldots \quad (30)$$

Based on the analysis previously presented, a computer program has been prepared for the calculation of the buckling loads of arches by use of Eqs. 29 and 30.

Numerical Results

For the numerical results presented herein, the stiffness and incremental stiffness matrices have been evaluated by three-point Gauss quadrature. Only the smallest buckling load was calculated. For simplicity, no units of the data have been given. The dimensions of the various quantities are self-consistent; i.e., if the basic units of length and force are taken to be inches and pounds, then the values of area, moment of inertia, and distributed load given would have units of in.^{2}, in.^{4}, and lb/in., respectively. In each case, the reference load was set equal to unity. Distributed loads on the arches were converted to "work equivalent loads" (9), for application to the finite element model.

TABLE 1.—Linear Versus Quadratic Eigenproblem Solutions

Type of arch[a] (1)	Type of load (2)	A (3)	Ixx (4)	Iyy (5)	Buckling Load		
					Linear (6)	Quadratic (7)	Ratio (8)
Circular in-plane	Radial	0.1875	0.9765×10^{-3}	0.8789×10^{-2}	51.41	51.64	0.99
Circular out-of-plane	Radial	1.00	0.5208×10^{-2}	1.333	27.44	27.44	1.00
Parabolic out-of-plane	Vertical	1.50	1.7578×10^{-2}	2.00	189.61	189.67	0.99

[a]Circular Arches: $R = 30$, $2\alpha = \pi/2$, $E = 10^7$. Parabolic Arch: $H = 9.6$, $L = 48$, $E = 29 \times 10^6$.

Linear Versus Quadratic Eigenproblem Solutions.—To consider the importance of matrix $[N2]$ in the calculation of the buckling loads, three types of problems were solved: (1) The in-plane buckling of a circular arch with an opening angle $2\alpha = 90°$ under a uniformly distributed radial load; (2) the out-of-plane buckling of the same type of arch under the same loading; and (3) the out-of-plane buckling of a parabolic arch subjected to a uniformly distributed vertical load. All three arches were hinged at the ends. At the supports, the "nonessential" degrees of freedom, dw/ds and $d\beta/ds$, were not restrained. For the out-of-plane cases, the rotation degrees of freedom about the x-axis and z-axis at the supports were restrained.

Table 1 shows the values and the ratios of the buckling load as computed from the linear eigenproblem to that from the quadratic eigenproblem. The linear problems were solved by the method of inverse vector iteration (4) with a tolerance of 0.0001, and the quadratic problems by the method of determinant search (4). The number of elements was kept constant at 12. It is seen that

in each case the ratio is very close to unity. This would seem to indicate that for these types of problems considered the inclusion of matrix $[N2]$ in the eigenvalue problem would not give significantly different results from the case in which it is neglected. Since much computer time can be saved by ignoring $[N2]$, this has been done in obtaining the following results.

Effects of Rotations.—It may be seen from the expression for U_3, Eq. 19

Problem	Structure-Load Systems Considered
1	Circular arch subjected to uniform pressure R = 30; 2α = 90° E = 10^7; A = 0.1875 I = 0.8789×10^{-2}
2	Circular arch subjected to concentrated load R = 10; 2α = 180° E = 1.04×10^7; A = 0.0775 I = 6.21×10^{-6}
3	Circular arch subjected to uniform load on horizontal projection 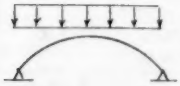 R = 318.2; 2α = 90° E = 4.176×10^6 A = 2.7 I = 2.03125
4	Parabolic arch subjected to uniform load on horizontal projection 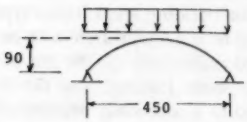 E = 4.176×10^6; G = 1.606×10^6 A = 2.7; Ixx = 4.45 Iyy = 32.5 K_T = 5.785

FIG. 3.—Convergence Studies

and Eq. 23 that the first order incremental stiffness, $[n1]$, contains terms involving three types of deformations: (1) $(dw/ds - u$, axial strain); (2) $(du/ds + w/R$, rotation about y-axis); and (3) $(dv/ds$, rotation about x-axis). In the classical linear stability formulation, the effects of prebuckling rotations are neglected. Correspondingly, for the present finite element formulation, the matrix obtained from $[n1]$ with the rotation terms neglected will be denoted by $[n1^*]$.

Solutions using both $[n1]$ and $[n1^*]$ had been obtained. In general, it was found that the differences between the buckling loads obtained by using matrices $[n1]$ and $[n1^*]$ increased with the amount of bending (or prebuckling rotational deformation) in the structure. Thus, typically, for problems involving uniform distributed loading that entails little or no bending, results obtained using $[n1]$ and $[n1^*]$ showed only small differences, say, of the order of one or two percent. However, for the case of a concentrated load at the crown of a semicircular arch the buckling load corresponding to $[n1]$ would be as small as only one third of that using $[n1^*]$.

Since $[n1]$ has included the effects of rotations, it may seem that the eigenvalue corresponding to $[n1]$ would be a more accurate representation of the buckling load than that corresponding to $[n1^*]$. But for the concentrated load problem, the buckling load obtained by use of $[n1^*]$ agrees very closely with experimental data (12) and the bifurcation load as computed from nonlinear equilibrium analysis (5). It seems that for the problems considered, the assumption that led to the eigenproblem of Eq. 29 has exaggerated the weakening effects of the rotations

TABLE 2.—Convergence Studies: Buckling Load

Number of Elements (1)	Problem 1 (2)	2 (3)	3 (4)	4 (5)
2	64.24	5.08	5.19	9.40
4	52.34	4.52	5.47	7.51
6	51.81	4.40	4.38	7.39
8	51.71	4.37	4.06	7.37
12	51.68	4.37	3.94	7.36
16	51.67	4.37	3.93	7.36
24	51.67	4.37	3.94	7.36
Reference value	48.83	4.17	4.11	7.89
From reference	(21)	(12)	(3)	(22)
Ratio	1.06	1.05	0.96	0.93

on the structural stiffness. More discussions on these points will be presented after the numerical results. The results presented in the following have been obtained using $[n1^*]$.

Convergence of Solutions.—To consider the convergence of the finite element model, four problems were studied. They are defined in Fig. 3. The buckling mode observed is in-plane and antisymmetrical for Problems 1, 2 and 3. For Problem 4 it is out-of-plane and symmetrical. Table 2 lists the buckling loads. It is seen that the buckling loads "converge" rather rapidly. Results obtained using only two elements to represent the structure differ by approximately 25% from the "converged" value.

For purposes of comparison, certain reference values of the buckling loads are also listed in Table 2. While the differences between the finite element answers and the reference values are not large, some explanation may be given. The buckling loads reported in the references noted in Table 2 have all been based on the assumption that the axis of the arch is inextensible. This assumption

has not been used in the present finite element method. Thus, while no pre-buckling axial deformations exist in the reference cases, the present method has accounted for such deformations. It also follows that, for the reference cases, the buckling loads are independent of the cross-sectional area. The effect of cross-sectional area is considered in the next section.

Effect of Cross-Sectional Area.—For a consideration of the effects of the cross-sectional Area A on the buckling load p_{cr}, the data shown in Table 3 have been collected. The parameter A/A_o has been varied over a range of four orders of magnitude for Problems 1 and 4 of Table 2, A_o being the value of A given therein. For all cases, 12 elements were used for the arch. It is seen that in general the effect is negligible except for very small values of A/A_o, or very small values of the "slenderness ratio," $\bar{L}/r$, as defined in Table 3.

It would be expected that, everything being equal, larger A should increase the stiffness and hence the buckling load, however slightly. It is interesting to note that at very small values of A, the values of p_{cr} actually decreased

TABLE 3.—Effect of Cross-Sectional Area

	Problem 1			Problem 4		
A/A_o[a] (1)	p_{cr} (2)	H (3)	$\bar{L}/r$[b] (4)	p_{cr} (5)	H (6)	$\bar{L}/r$[c] (7)
10^{-2}	56.3	19.7	10.9	9.15	187	19.3
10^{-1}	52.1	22.3	34.4	7.52	249	60.9
10^{0}	51.8	22.6	108.8	7.36	256	192.5
10^{1}	51.6	22.6	344.1	7.33	257	608.6
10^{2}	51.8	22.6	1,088.2	7.21	255	1,924.6

[a] A_o = cross-sectional area used in Table 2.
[b] $\bar{L}$ = half of curved length of arch.
[c] r = radius of gyration.

with an increase in A. The reason for this appears to lie in the support or boundary conditions and is qualitatively explained as follows.

The full curved line in Fig. 4 represents a uniformly compressed arch in equilibrium with the end thrust that has a horizontal component H_0. The boundary conditions of hinged ends require both ends to move horizontally by a distance, d. To bring this about, additional horizontal force H_1 is applied. The total horizontal force is $H = H_0 - H_1$. Denote by h_A and h_I the horizontal stiffness due to area A and moment of inertia I, respectively. Noting that h_A varies with A for the present parametric study, h_I is constant, and d is inversely proportional to A, it follows that $H_1 = h_A d + h_I d \cong c_1 A(c_2/A) + h_I(c_2/A) = c_3 + c_4/A$, in which the c's are constants. Therefore, when A is large, H_1 is essentially independent of A. When A is small, H_1 increases with a decrease in A. An increase in H_1 decreases the total horizontal reaction, H, and would lessen the tendency of buckling and increase the buckling load. To corroborate this observation, the values of the horizontal reaction, H, due to a unit distributed loading on the hinged arches are listed in Table 3. It is

seen that at very small values of A/A_o, the values of H are smaller and the buckling loads are larger.

Discussion

It is well known that to compute the smallest bifurcation buckling load of a structure load system, the classical theory of elastic stability can be used to formulate an eigenproblem based on the initial, undeformed geometry of the structure. Since the pre-buckling deformation is neglected, the accuracy of the buckling load computed depends on the extent of that deformation. When it is not negligible, it usually would be of the flexural or rotation nature. Thus, the domain of validity of the classical theory of elastic stability generally covers only those problems involving little prebuckling bending deformation.

In the formulation of the eigenproblem for buckling analysis by finite elements presented by Mallet and Marcal (13) and used herein, the prebuckling deformation is not ignored. Instead, it is taken to be linearly proportional to the load. Numerical

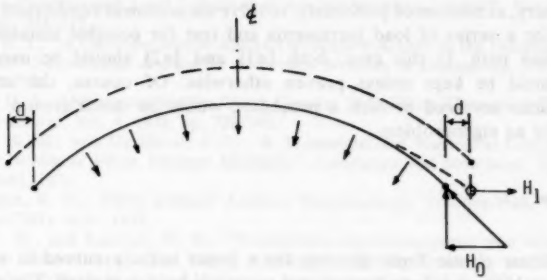

FIG. 4.—Effect of Axial Flexibility

results obtained in this study seem to indicate that, for systems that involved little prebuckling bending, the buckling loads calculated were quite accurate. But if the system involved substantial prebuckling bending, the procedure would produce inaccurate results.

The method was modified by dropping the rotation terms in $[n1]$. Of course, neglecting such terms does not mean neglecting rotations in the analysis. It merely means neglecting the weakening effect of bending deformations on the axial stiffness, while the weakening effect of axial deformations on the bending stiffness remains. The modified matrix, $[n1^*]$, appears to be analogous to the well-known "geometric stiffness matrix" for straight beam elements (9). The performance of the resulting method resembled that of the classical theory of elastic stability. The resemblance included the seemingly exceptional fact that an eigenproblem solution would provide a good estimate of the buckling load for the case of a concentrated load on the crown of a nonshallow circular arch.

The preceding was observed from the numerical results obtained. Until a more thorough study is made, a tentative explanation is offered in the following:

For problems within the domain of the classical theory of elastic stability, it matters little whether or not the rotation terms are included in [$n1$] as the rotations are negligible anyway. When the rotations are not small, the assumption of a linear relation between displacements and load may simply render the method invalid as the actual behavior is nonlinear.

The system of a concentrated load at the crown of a nonshallow arch has a bifurcation load lower than the limit load. Thus, the prebuckling deformation is smaller at the former load than at the latter. At the former load, the buckling mode is antisymmetric; at the latter, the mode is symmetric. For the antisymmetric bifurcation buckling load, the effect of the rotation terms in [$n1$] apparently was enough to invalidate the result. However, the prebuckling deformation may not be large enough to invalidate the classical theory of elastic stability. It is interesting to note that in this case the classical theory does yield accurate results (3), as does the present procedure of using [$n1^*$]. For the symmetric buckling mode, the limit load obtained by the classical theory erred greatly (3), apparently on account of significant prebuckling deformations. For such problems there seems to be no short-cut to obtaining the buckling load. It would be necessary, as mentioned previously, to solve the nonlinear equilibrium problem, Eq. 26, for a series of load increments and test for possible instability along the solution path. In this case, both [$n1$] and [$n2$] should be used and all terms should be kept unless proven otherwise. Of course, the amount of computations involved in such a procedure would be much greater than that needed for an eigenproblem.

Conclusion

A nonlinear elastic finite element for a beam initially curved in one plane but deformable in the three-dimensional space has been presented. The geometric representation of the element allows continuity of the slopes and curvatures of contiguous elements. Quadratic and linear eigenproblems were formulated and programmed to calculate the in-plane and out-of-plane buckling loads of arches.

The following observations are made from the limited numerical results obtained for this study and should not be regarded as general conclusions:

1. The buckling loads, as computed from the quadratic eigenproblem, differed insignificantly from those computed from the linear eigenproblem.
2. The terms in the [$n1$] matrix containing the rotational displacements would excessively weaken the stiffness, yielding values of the buckling loads that are generally too low; they should be deleted. The resulting buckling load would essentially correspond to those of the classical linear theory of stability, i.e., the bifurcation buckling loads.
3. For most engineering purposes, sufficiently accurate buckling loads may be obtained by using a few, perhaps six, elements to represent the arch.
4. The buckling load was not entirely independent of the cross-sectional area. However, the dependence is significant only for arches with $\bar{L}/r$ values so small that they are probably outside the ranges of practical proportions.

Acknowledgment

The work reported herein is supported in part by the National Science Foundation under Grant No. ENG-7822478.

Appendix I.—References

1. Ashwell, D. G., and Sabir, A. B., "Limitations of Certain Curved Finite Elements when Applied to Arches," *International Journal of Mechanical Science*, Vol. 13, No. 2, Feb., 1971, pp. 133–139.
2. Austin, W. J., "In-Plane Bending and Buckling of Arches," *Journal of the Structural Division*, ASCE, Vol. 97, ST5, May, 1971, pp. 1575–1592.
3. Austin, W. J., and Ross, T. J., "Elastic Buckling of Arches Under Symmetrical Loading," *Journal of the Structural Division*, ASCE, Vol. 102, No. ST5, May, 1976, pp. 1085–1095.
4. Bathe, K. J., and Wilson, E. L., *Numerical Methods in Finite Element Analysis*, Prentice-Hall, Inc., Englewood Cliffs, N.J., 1976.
5. DaDeppo, D. A., and Schmidt, R., "Sidesway Buckling of Deep Circular Arches Under a Concentrated Load," *Journal of Applied Mechanics*, ASME, Vol. 36, June, 1969, pp. 325–327.
6. Dawe, D. J., "A Finite-Deflection Analysis of Shallow Arches by the Discrete Element Method," *International Journal for Numerical Methods in Engineering*, Vol. 3, 1971, pp. 529–552.
7. Dawe, D. J., "Numerical Studies Using Circular Arch Finite Elements," *Computers and Structures*, Vol. 4, 1974, pp. 729–740.
8. Ebner, A. M., and Ucciferro, J. J., "A Theoretical and Numerical Comparison of Elastic Nonlinear Finite Element Methods," *Computers and Structures*, Vol. 2, pp. 1043–1061, 1972.
9. Gallagher, R. H., *Finite Element Analysis Fundamentals*, Prentice-Hall, Inc., Englewood Cliffs, N.J., 1975.
10. Gellert, M., and Laursen, M. E., "Formulation and Convergence of a Mixed Finite Element Method Applied to Elastic Arches of Arbitrary Geometry and Loading," *Computer Methods in Applied Mechanics and Engineering*, Vol. 7, 1976, pp. 285–302.
11. Lange, J., "Elastic Buckling of Arches by Finite Element Method," thesis presented to Michigan State University, at East Lansing, Mich., in 1980, in partial fulfillment of the requirements for the degree of Doctor of Philosophy.
12. Langhaar, H. L., Boresi, A. P., and Carver, D. R., "Energy Theory of Buckling of Circular Elastic Rings and Arches," *Proceedings of the Second U.S. National Congress of Applied Mech.*, 1954, pp. 437–443.
13. Mallett, R. H., and Marcal, P. V., "Finite Element Analyses of Nonlinear Structures," *Journal of the Structural Division*, ASCE, Vol. 94, No. ST9, Sept., 1968, pp. 2081–2105.
14. Mak, C. K., and Kao, D., "Finite Element Analysis of Buckling and Post-Buckling Behaviors of Arches with Geometric Imperfections," *Computers and Structures*, Vol. 3, 1973, pp. 149–161.
15. Martin, H. C., and Carey, G. F., "Introduction to Finite Element Analysis," McGraw-Hill, Inc., New York, N.Y., 1973.
16. Mebane, P. M., and Stricklin, J. A., "Implicit Rigid Body Motion in Curved Finite Elements," *American Institute of Aeronautics and Astronautics*, Vol. 9, No. 2, 1971, pp. 344–345.
17. Ojalvo, I. U., and Newman, M., "Buckling of Naturally Curved and Twisted Beams," *Journal of the Engineering Mechanics Division*, ASCE, Vol. 94, No. EM5, Oct., 1968, pp. 1067–1087.
18. Ojalvo, M., Demuts, E., and Tokarz, F., "Out-of-Plane Buckling of Curved Elements," *Journal of the Structural Division*, ASCE, Vol. 95, No. ST10, Oct., 1969, pp. 2305–2316.
19. Sabir, A. B., and Lock, A. C., "Large Deflection, Geometrically Nonlinear Finite Element Analysis of Circular Arches," *International Journal of Mechanical Sciences*, Vol. 15, 1973, pp. 37–47.

20. Shukla, S., and Ojalvo, M., "Lateral Buckling of Parabolic Arches with Tilting Loads," *Journal of the Structural Division*, ASCE, Vol. 97, No. ST6, June, 1971, pp. 1763–1773.
21. Timoshenko, S. P., and Gere, J. M., *Theory of Elastic Stability*, second edition, McGraw-Hill Book Company, New York, N.Y., 1961.
22. Tokarz, F. J., and Sandhu, R. S., "Lateral-Torsional Buckling of Parabolic Arches," *Journal of the Structural Division*, ASCE, Vol. 98, No. ST5, May, 1972, pp. 1161–1179.
23. Walker, A. C., "A Nonlinear Finite Element Analysis of Shallow Arches," *International Journal of Solids and Structures*, Vol. 5, 1969, pp. 97–107.
24. Wempner, G. A., and Kesti, N. E., "On the Buckling of Circular Arches and Rings," *Proceedings of the 4th U.S. National Congress of Applied Mech.*, Vol. 2, June, 1962, pp. 843–849.

Appendix II.—Notation

The following symbols are used in this paper:

A = area of cross-sections;
A, B = end nodes of an element;
b_2, b_3, b_4 = element geometry coefficients;
d = horizontal displacement of arch ends due to compression;
E = Young's modulus of elasticity;
G = shear modulus;
H = rise of the arch;
H = horizontal reaction at support;
H_0 = horizontal component of end thrust of bending free arch;
H_1 = corrective horizontal force for hinged ends;
h_A, h_I = horizontal stiffness due to A and I, respectively;
I = moment of inertia;
I_ξ, I_η = moment of inertia of cross-section;
$[K]$ = structural linear stiffness matrix;
$[k]$ = element linear stiffness matrix;
K_t = torsion constant of cross-section;
k_x, k_y, k_z = current curvatures about x, y, z axes;
$\bar{k}_x, \bar{k}_y, \bar{k}_z$ = initial curvatures about x, y, z axes;
L = span or arch;
$\bar{L}$ = half of curved length of arch;
$[N1]$ = first order structural incremental stiffness matrix;
$[N2]$ = second order structural incremental stiffness matrix;
$[n1]$ = first order element incremental stiffness matrix;
$[n1^*]$ = $[n1]$ with rotation terms deleted;
$[n2]$ = second order element incremental stiffness matrix;
$\{P\}$ = vector of applied loads;
p_{cr} = critical value of applied loads;
$\{P_o\}$ = reference load;
$\{Q\}$ = displacement vector;
$\{\bar{Q}\}$ = reference displacement vector;
$\{Q_o\}$ = $[K]^{-1}\{P_o\}$;
R = radius of curvature;
$R1, R2$ = radii of curvature at ends of an element;
s = longitudinal axis of curved beam member;

u, v, w = displacements along x, y, z axes, respectively;
U = strain energy of structure;
U_E = strain energy of element;
U_ϵ = strain energy due to longitudinal strain;
U_t = strain energy due to torsion;
U_2, U_3, U_4 = quadratic, cubic, and quartic parts of strain energy;
X, Y, Z = structure global coordinate system;
X_L, Y_L = relative position of end nodes of an element;
x, y, z = element coordinate system;
(x_B, z_B) = coordinates of node B in element coordinate system;
α = one half of angle of opening of circular arch;
β = twist of cross-section about z-axis;
$\beta_x, \beta_y, \beta_z$ = rotations about x, y, z axes, respectively;
γ = ϕ/θ = normalized position variable;
ϵ = longitudinal strain;
θ = angle of tangent at node B (Fig. 2);
θ_x = rotation about x-axis;
θ_y = rotation about y-axis;
$\kappa_x, \kappa_y, \kappa_z$ = changes in curvature about x, y, z axes;
Δ = incremental operator;
$\{\ \}$ = column vector;
$\lfloor\ \rfloor$ = row vector; and
$[\ ]$ = rectangular matrix.

BOLTED FRICTION CONNECTIONS WITH WEATHERING STEEL

By Joseph A. Yura,[1] M. ASCE, Karl H. Frank,[2] A. M. ASCE, and Lloyd Cayes[3]

INTRODUCTION

The principal variable that affects the slip resistance of a high-strength bolted shear connection is the slip coefficient, k_s, which is an indicator of surface friction. There are currently no reliable theoretical models for predicting slip resistance, so experiments on small connections are conducted to determine the slip load. The slip coefficient, k_s, is calculated as

$$k_s = \frac{\text{slip load}}{\text{clamping force} \times \text{number of slip planes}} \quad \ldots \ldots \ldots \ldots \ldots \ldots \ldots \ldots \quad (1)$$

A summary of slip coefficients for various steel types, surface treatments and surface coatings is presented in Ref. 2. These data have been used to develop the allowable bolt shear stresses in friction joints which appeared in the *Specification for Structural Joints Using ASTM A325 or A490 Bolts*, hereinafter referred to as the Bolt Spec, in 1976 (9). The American Association of State Highway and Transportation Officials (AASHTO) reduced the Bolt Spec values by about 10% and incorporated them into the 1978 Interim Bridge Specifications (5). The AASHTO design recommendations for unprotected steel surfaces are reproduced in Table 1. Values given for surface classes A, B, and C were based on over 700 slip tests for steels with specified yield points between 33 ksi (228 MPa) and 100 ksi (690 MPa). Some specimens were exposed to the atmosphere to permit surface corrosion prior to assembling and testing.

None of the documented slip tests were conducted on ASTM A588 steel (weathering steel), which is very common on bridge structures with mill scale, and blasted and painted surface conditions. Tests have indicated that the type of steel has little effect when the surfaces are painted (3). However, the bare

[1]Prof., Dept. of Civ. Engrg., The Univ. of Texas, Austin, Tex.
[2]Assoc. Prof., Dept. of Civ. Engrg., The Univ. of Texas, Austin, Tex.
[3]Struct. Research Engr., Federal Highway Administration, Washington, D.C.

Note.—Discussion open until April 1, 1982. To extend the closing date one month, a written request must be filed with the Manager of Technical and Professional Publications, ASCE. Manuscript was submitted for review for possible publication on February 11, 1981. This paper is part of the Journal of the Structural Division, Proceedings of the American Society of Civil Engineers, ©ASCE, Vol. 107, No. ST11, November, 1981. ISSN 0044-8001/81/0011-2071/$01.00.

steel condition may show some differences for A588 steel, since the surface which provides the improved corrosion resistance is different from other structural steels. In addition, no data are available on A588 steel to address the issues of the effect of exposure on slip resistance and the effect of faying surface corrosion on the bolt clamping force.

An experimental program was undertaken to determine the slip characteristics of connections using A588 steel. Static slip tests and creep tests were conducted on connections with blasted and mil scale surfaces. Some joints were weathered over time intervals up to 1 yr. Bolt forces were monitored on the exposed creep tests. Different grades of A588 steel (10) as well as different heats of steel within a certain grade were studied so that design recommendations would represent the variations to be expected. A total of 126 slip tests were conducted.

In the subsequent sections, the test program and results are presented. The results are compared to those obtained for other structural steels, and design recommendations for friction connections in structures using A588 steel are developed.

Experimental Program

Program Variables.—A test program was designed to provide statistically valid slip data for friction connections with A588 steel. The program was devoted principally to connections with unprotected surfaces, both mill scale and blasted, and the effect of surface corrosion on the slip characteristics. A few pilot tests were designed to investigate the significance of what were presumed to be minor effects related to creep, paints on A588 steel, and changes in bolt clamping forces. Both tension-type and compression-type slip tests were considered. A schematic diagram summarizing the slip test program is shown in Fig. 1. The number of tests conducted is shown in parentheses. In general, five replicate specimens were tested for each principal variable. The experimental work was conducted at two separate agencies, The University of Texas at Austin (UT) and the Federal Highway Administration (FHWA).

Steel.—There are nine different grades (A–H, J) of A588 steel, based on variations in their chemical composition, with the same mechanical properties. Three different heats from Grade A and two heats from Grade B were used in the study. One heat of A588 Grade A was used for all tests conducted at the University of Texas and is identified as Steel A1. The remaining two heats of Grade A (Steels A2 and A3) and the two heats of Grade B (Steels B1 and B2) were used in the FHWA tests. All steel was purchased on the open market. Chemical analyses and tensile coupon tests confirmed that the steels satisfied the chemical and physical requirements for A588 steel. The connection test results from the five heats of A588 steel should provide a reasonable indication of the mean slip coefficient and its variation for this type of steel.

Surface Conditions.—In bridge structures A588 steel is used with mill scale, blasted, and painted surface conditions. Because other research had shown that steel type had no effect when the surfaces were painted, all but two of the 126 slip tests were conducted on mill scale or blasted surfaces. All blasted plates for the UT tests were dry sandblasted with a No. 3 blasting sand (fine) to a white metal condition. Plates for the FHWA tests were grit-blasted to

white metal using a 100-mesh aluminum oxide. All sandblasting was done at one time; a similar situation was arranged for the grit-blasting. Prior to assembling the connection, the faying surfaces were cleaned with acetone.

Two connections with zinc-rich primer, one organic and the other inorganic, were tested. The paints were the same as those used in another study (3), a modified single package organic zinc-rich phenoxy and a two-component silicate base inorganic primer. On both connections the zinc primer was sprayed in

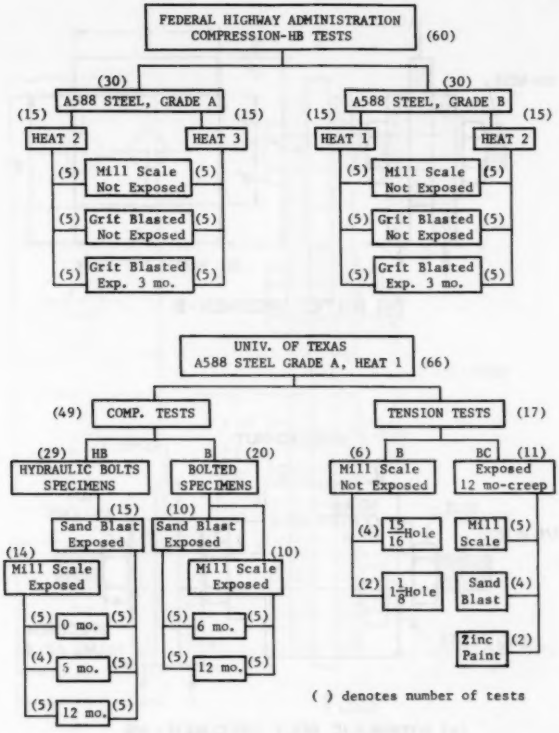

FIG. 1.—Slip Test Program

multiple coats to a dry thickness of 5 mil on a surface sandblasted to a white condition which satisfied the paint manufacturer's surface treatment recommendations.

Exposure.—A variety of questions were considered in the design of the experimental program as follows: (1) How is the slip resistance affected if the connection components are exposed in open air prior to assembly? (2) Is the slip load affected by exposure after the connection is assembled? (3) Will faying

surface corrosion after assembly affect the tensile load in the bolt? (4) Is there any effect on slip resistance if there is a significant applied shear load on the assembled condition during exposure? (5) Is the rate of surface corrosion affected by the applied load?

The test program at UT was principally devoted to the exposure effects. Three categories of specimens considered in detail in the next section were developed to resolve these questions. The specimens were left continuously in the open air suspended vertically on racks until testing. Nineteen slip tests

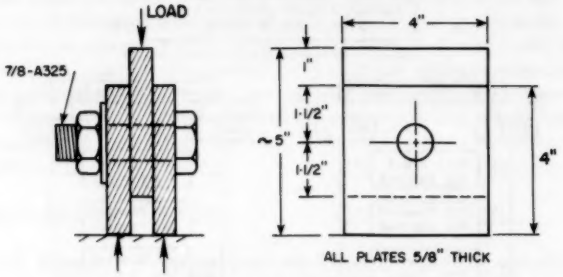

(a) BOLTED SPECIMEN - B

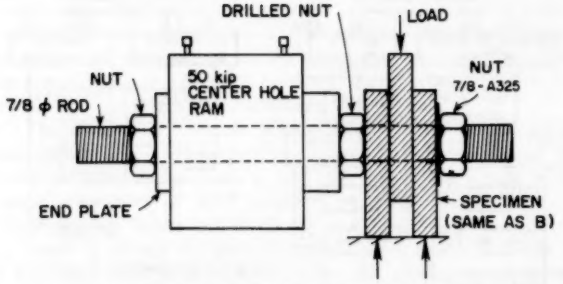

(b) HYDRAULIC BOLT SPECIMEN - HB

FIG. 2.—Compression Specimens (1 in. = 25.4 mm)

were conducted after 6 months exposure, 31 tests after 12 months exposure. The specimens were exposed to 23 in. (580 mm) of rainfall and periodic wetting with Austin city water (alkaline) during dry spells. The humidity was usually less than 60%. In the FHWA program five grit-blasted specimens from each heat of steel were exposed to the Washington, D.C., atmosphere for a period of 3 months prior to assembly and testing. During this period, 4.5 in. (114 mm) of rainfall were recorded, and the relative humidity was typically 64%.

Test Specimens and Arrangement.—Four different test specimens using two different test arrangements (compression test or tension test) were developed to meet the program objectives. Both compression-type and tension-type specimens were used because of convenience and also to determine if the type of test affects the slip load. Some limited previous data indicated that the type of test did not significantly influence the slip load (4). The details of the specimens are given in Figs. 2, 3, and 4.

All specimens were constructed from A588 steel bar stock and the contact

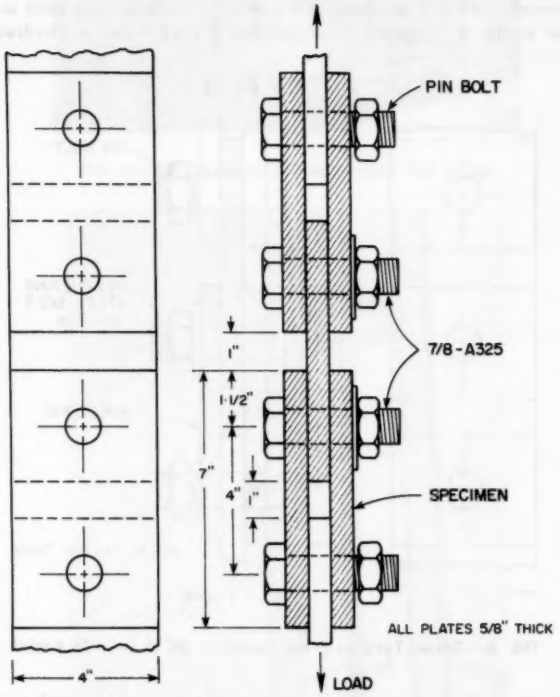

FIG. 3.—Bolted Tension Specimen-B (1 in. = 25.4 mm)

surface area was 4 in. (102 mm) × 3 in. (76 mm). A hardened washer was used under the nut. Two specimens had 1-1/8-in. (29-mm)-diam oversize holes with 7/8-in. (22-mm) fasteners; all other specimens had standard 15/16-in. (24-mm) holes. All bolts were 7/8-in. (22-mm) A325 (Type 3—weathering for the exposure tests) and were tightened by a modified turn-of-nut method (9) examined later. All connections were assembled in a jig for alinement with the fasteners in bearing in a direction opposite to the planned loading to ensure

obvious slip deformation. A description of each test specimen and test setup follows.

Compression-B.—These bolted specimens were assembled prior to exposure. The purpose of this type of specimen was to provide slip data for conditions simulating a shop-bolted connection (no significant exposure prior to assembly) with maximum shear load applied at a later time in service. After assembly, the connection was placed outside and exposed continuously for 6 months or 12 months. The slip load was measured after this exposure, as shown schematically in Fig. 2(*a*).

Compression-HB.—The connection which is shown crosshatched in Fig. 2(*b*) is similar to the B specimen described above except that a "hydraulic bolt"

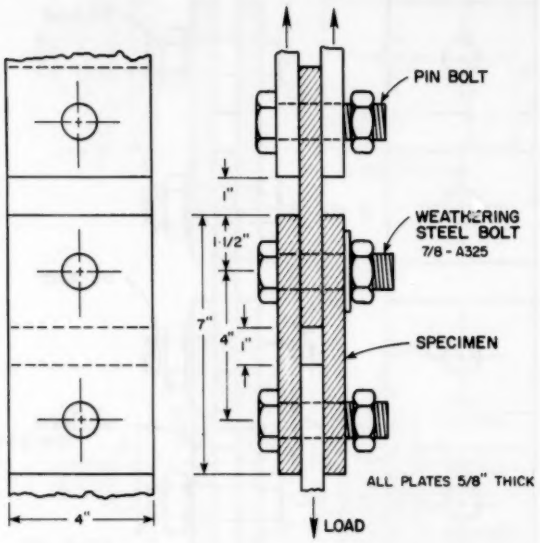

FIG. 4.—Bolted Tension Creep Specimen-BC (1 in. = 25.4 mm)

is used to clamp the plates together. A threaded rod passes through a centerhole ram and is locked in position by nuts at both ends. Oil pressure is applied to the ram, which forces the drilled nut, a 7/8-in. (22-mm) 2H nut with threads drilled out so it can slip along the threaded rod, against the connection plate. The drilled nut provides the same plate contact area as a bolt. Oil pressure is increased until the desired clamping force is reached. The clamping force is easily maintained at the desired level while the test machine applied shear load to the connection. A clamping force of 39 kips (174 kN) was used, which is the minimum specified for a 7/8-in. (22-mm) A325 bolt (9). The details and development of this test arrangement are described more fully in Ref. 3, where more than 600 slip tests using the HB compression test setup are reported.

FIG. 5.—HB Connection Compression Test Setup

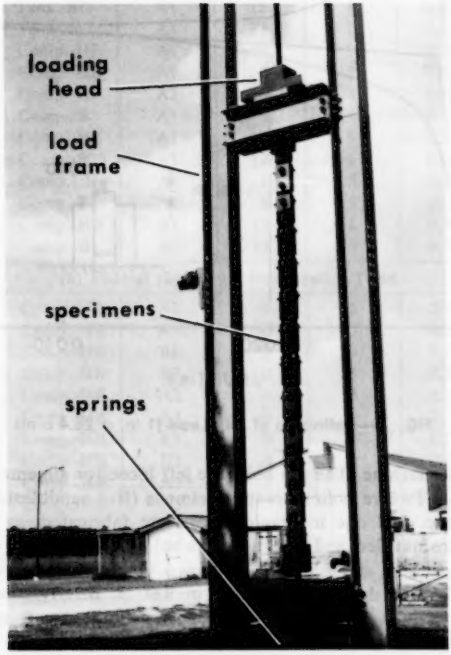

FIG. 6.—Creep Chain Test Setup

A photo of the HB specimen in the compression test machine is shown in Fig. 5.

This test specimen was the principal one used in both the UT and FHWA programs because of its reliability and ease of testing. It was also used to simulate conditions found in field-bolted connections in which the component plates are exposed to the atmosphere for some time before assembly and the connection subjected to load reasonably soon after field bolting.

Tension-B.—Three tension specimens were designed to provide a direct comparison with the slip load from the HB compression specimens with unexposed mil scale surface. The symmetrical design of the test specimen shown cross-hatched in Fig. 3 permits two independent slip load tests. The end fixture plate, shown solid, fits between the plates of the test specimen and is gripped by

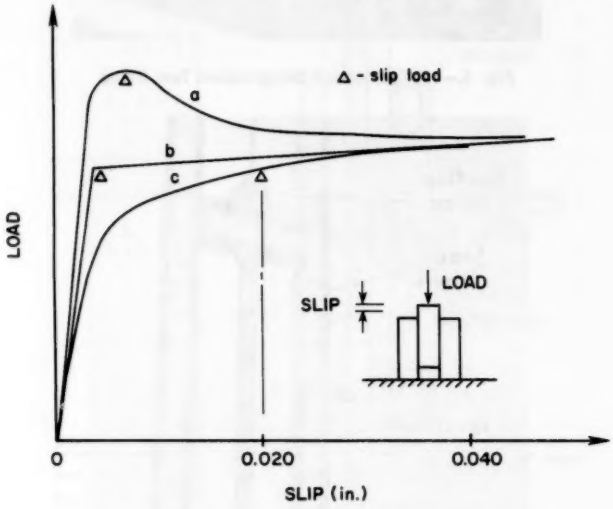

FIG. 7.—Definition of Slip Load (1 in. = 25.4 mm)

the tension test machine. The pin bolts are left loose for alinement.

Tension-BC.—Twelve bolted creep specimens (five sandblasted, 5 mil scale, one organic zinc, and one inorganic zinc) were fabricated, as shown in Fig. 4. The bolts were installed, and then, using pin bolts, the specimens were connected in series outside in a single chain, as shown in Fig. 6. The creep test setup is similar to the one described in detail in Ref. 7. Briefly, the lower end of the specimen chain was attached to a set of calibrated soft springs and the upper end to a loading fixture. The upper fixture was used to load the chain to the desired force level, and the springs reasonably maintained the load at this level as creep or slip occurred. Small adjustments were made periodically to keep the load constant. When the creep experiment was terminated after 1 yr, the chain was unloaded and static slip tests conducted.

Bolt Calibration.—In the test specimens assembled with A325 bolts, it is necessary to establish the bolt clamping force in order to derive the slip coefficient from Eq. 1. Three bolts from each of the two lots used in the program were tested to establish the average relationship between bolt tension and elongation. This bolt calibration procedure is described in detail elsewhere (7) and was

TABLE 2.—Summary of Slip Test Results

Surface condition (1)	Type of test (2)	Steel identity (3)	Months exposed (4)	Number of tests (5)	Average slip coefficient (6)	Standard deviation (7)
(*a*) University of Texas Tests						
M. scale	Tens.-B	A1	0	4	0.20	0.015
M. scale	Tens.-B	A1	0	2[a]	0.20	—
M. scale	Tens.-BC	A1	12	5	0.29[b]	0.019
Sand Bl	Tens.-BC	A1	12	4	0.65	0.047
Inorg. zinc	Tens.-BC	A1	12	1	0.67	—
Org. zinc	Tens.-BC	A1	12	1	0.52[b]	—
M. scale	Comp.-HB	A1	0	5	0.20	0.009
Sand Bl	Comp.-HB	A1	0	5	0.86	0.038
M. scale	Comp.-HB	A1	6	4	0.27	0.009
M. scale	Comp.-B	A1	6	5	0.18	0.004
M. scale	Comp.-HB	A1	12	5	0.37	0.068
M. scale	Comp.-B	A1	12	5	0.19	0.011
Sand Bl	Comp.-HB	A1	6	5	0.74	0.043
Sand Bl	Comp.-B	A1	6	5	0.77	0.035
Sand Bl	Comp.-HB	A1	12	5	0.59	0.080
Sand Bl	Comp.-B	A1	12	5	0.75	0.020
(*b*) Federal Highway Administration Tests						
M. scale	Comp.-HB	A2	0	5	0.26	0.016
M. scale	Comp.-HB	A3	0	5	0.28	0.008
M. scale	Comp.-HB	B1	0	5	0.23	0.019
M. scale	Comp.-HB	B2	0	5	0.23	0.016
Grit Bl	Comp.-HB	A2	0	5	0.59	0.083
Grit Bl	Comp.-HB	A3	0	5	0.38	0.018
Grit Bl	Comp.-HB	B1	0	5	0.50	0.078
Grit Bl	Comp.-HB	B2	0	5	0.60	0.047
Grit Bl	Comp.-HB	A2	3	5	0.78	0.078
Grit Bl	Comp.-HB	A3	3	5	0.87	0.063
Grit Bl	Comp.-HB	B1	3	5	0.86	0.073
Grit Bl	Comp.-HB	B2	3	5	0.83	0.042

[a] 1-1/8 in. (29-mm) diam holes. All other specimens had 15/16-in. (24-mm) diam holes.
[b] Previously slipped into bearing during creep experiment.

similar to that used by others (8). The average calibration curve for the particular lot under consideration and the measured bolt elongation in each connection were used to establish the clamping force.

To minimize variations in the clamping forces, bolts were installed by a modified

turn-of-nut method (9) to produce bolt elongations within the flat yield plateau of the average calibration curves. A 5/8 turn from the snug position was applied initially and then sometimes a slight additional rotation to bring the bolt within the desired elongation range. Normal turn-of-nut installation practice for this bolt length would require a one-third turn ±30° (between 1/4 and 5/12 turns). The typical clamping forces for the two lots were 48 kips (214 kN) and 54.5 kips (243 kN) using the modified procedure.

Test Procedure and Instrumentation

Slip Tests.—The test procedures for compression-type slip tests and tension-type were the same. The specimens were alined in the test machine to minimize eccentricities. In the case of compression-type specimens, a spherical head was used to ensure uniform compression along the edge of the plate. Pin bolts (see Fig. 3) were used to connect the tension specimens to the end fixtures which eliminated bending in the specimen. Linear potentiometers or DCDT's were located on each side of the specimen and connected in a manner to give the average relative displacement (slip) between the interior connection plate and the two side plates, as shown in Fig. 5. The slip and the load applied to the specimen were plotted automatically using an X-Y recorder. The applied loading rate was approx 25 kips (111 kN)/min or 0.003 in. (0.076 mm) of slip/min. The test was terminated when a total slip reached approx 1/16 in. (2 mm), the nominal hole clearance.

The slip load was determined from the connection load-deflection plot, some typical types of which are shown in Fig. 7. The slip load was recorded as one of the following: (1) The maximum load if this maximum occurred before a total slip of 0.02 in. (0.51 mm) occurred; (2) the load at which the slip rate suddenly increases, typically as shown by curve b; and (3) the load measured when the slip is 0.02 in. (0.51 mm). This definition controls when the load-slip curve shows a gradual change in response, as shown by curve c.

Creep Tests.—The magnitude of the load in the creep chain was chosen to produce a theoretical bolt shear stress of 16.5 ksi (114 MPa). This stress level is just 3% greater than the maximum allowable of 16.0 ksi (110 MPa) for mill scale surfaces given in Table 1. The allowable stresses for the other surfaces in the chain (blasted and zinc-rich paint) based on the AASHTO Specification are greater than 19 ksi (131 MPa). Initially, a load equal to 75% of the maximum desired level was applied and maintained for 1 month. Then, the bolt shear stresses were increased to 16.5 ksi (114 MPa) and maintained at this level until the chain was dismantled about 1 yr later.

During the creep experiment, adjustments were made to the applied load to maintain the bolt shear stress with ±0.25 ksi (1.7 MPa) of the desired level. The detailed procedure for applying and maintaining the loads is given elsewhere (7,11). A micrometer was used to measure the relative shear movement between the inside plate and the two outer plates of the creep specimen shown in Fig. 4. Creep measurements provided deformation data reliable to ±0.0004 in. (0.0102 mm) (7).

Bolt Forces.—The change in bolt elongation was monitored in the exposed specimens. The bolt length was recorded after assembly using a mechanical extensometer. The length of an unassembled bolt was also recorded as the standard gage to account for changes in the extensometer and temperature.

The elongations of the standard gage bolt and the connection bolts were recorded again when the connections were prepared for the slip tests, either 6 months or 1 yr later. The bolt elongations were converted to bolt forces using the bolt calibration curves described earlier.

Test Results and Analysis

Static Slip Tests.—A summary of the 126 slip tests is presented in Table 2. Two of the tests were on painted surfaces; 69 had blasted contact surfaces. In all B and BC type tests, the plates were assembled in the final connection with 7/8-in. (22-mm) A325 bolts prior to exposure; in the HB tests, the plates were exposed in the unassembled state. The number of tests listed in each category are on different replicate connections. The slip coefficients were calculated using Eq. 1, based on the slip loads as defined in Fig. 7.

Mil Scale Surfaces.—Five different heats from two grades of A588 steel were tested in the unweathered state. The k_s for the five heats taken from Table 2 are: A1—0.20; A2—0.26; A3—0.28; B1—0.23; and B2—0.23. Treating these five averages as individual samples, the average k_s for all heats is 0.24. If the 31 slip tests are treated as individual samples, the average k_s is 0.23 (standard deviation, s.d. = 0.034), a slight reduction from the average of the heats because 11 tests were conducted on steel A1 and five tests on each of the other heats. The average values for k_s are 0.25 and 0.23 for Grades A and B, respectively. The six tension tests and five HB compression tests on the A1 steel gave the same average k_s, indicating the type of test has no effect. There was no difference in the k_s for standard and oversize holes. This was due to the fact that the modified turn-of-nut method resulted in the same clamping force for both conditions. Using standard tightening techniques, a lower clamping force, and consequently a lower slip load, would be expected (2).

The average $k_s = 0.23$ for A588 steel is significantly lower than the average for mil scale surfaces, $k_s = 0.34$, reported by Fisher and Struik (2) for steels with yield strengths of 50 ksi (345 MPa) or less. Their summary of 312 slip coefficients is shown in Fig. 8 along with the 31 test results for A588 steel, shown in black. The data suggest that the current allowable stress in the Bolt Spec is not applicable to A588 steel. The average k_s for A588 steel is only 68% of the value for other steels. Further analysis will be presented in a subsequent section dealing with design recommendations.

Blasted Surfaces.—The 25 unweathered blasted specimens gave a mean $k_s = 0.58$ (s.d. = 0.17). This standard deviation is quite large and is caused by combining the results of the five sandblasted specimens, mean $k_s = 0.86$, s.d. = 0.04, and the 20 grit-blasted specimens, mean $k_s = 0.52$, s.d. = 0.10. The type of blasting had a significant effect on the surface roughness. Considering the scatter within the replicates for the four heats of grit-blasted specimens, there is no significant effect of steel grade on k_s.

Since only one heat of steel was sandblasted, there is insufficient data to suggest that all sandblasted A588 steels have a typical k_s in excess of 0.8, which is the highest k_s reported in the literature. Fouad's (3) tests on 103 sandblasted specimens with three different steels—A36, $F_y = 36$ ksi (248 MPa); A572, $F_y = 50$ ksi (345 MPa); A514, $F_y = 100$ ksi (690 MPa), gave an average $k_s = 0.52$, which is similar to the average value reported by Fisher and Struik

(2), $k_s = 0.49$, for 168 tests on mild carbon steel which were grit- or sandblasted. Their data show that the type of blasting does not significantly affect the average slip characteristics of nonweathering steels. Until additional test data are available on sandblasted A588 steel, it is recommended that no distinction be made between

TABLE 1.—Allowable Bolt Shear Stresses, in kips per square inch (megapascals); AASHTO Interim Bridge Specification (Abridged)

Class of surface (1)	Surface condition of bolted parts (2)	Standard Holes		Oversize and Short Slotted Holes	
		A325 (3)	A490 (4)	A325 (5)	A490 (6)
A	Clean mill scale	16.0 (110)	20.0 (138)	13.5 (93)	17.0 (117)
B	Blast-cleaned carbon and low alloy steel	25.0 (172)	31.0 (214)	21.0 (145)	26.5 (183)
C	Blast-cleaned quenched and tempered steel	17.0 (117)	21.0 (145)	14.5 (100)	18.0 (124)

Note: 1 ksi = 6.9 MPa.

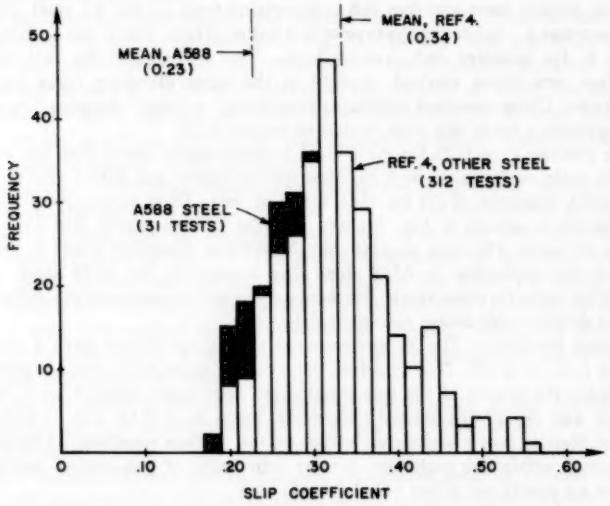

FIG. 8.—Distribution of Slip Coefficient for Clean Mill Scale

sandblasted and grit-blasted A588 steel and that a k_s of 0.5 be considered appropriate for all blasted steel surfaces.

Exposure.—With 3 months exposure, the four heats of grit-blasted A588 tested

by the FHWA showed a 60% increase in the average k_s, from 0.52–0.83. The sandblasted HB specimens exposed in Austin showed a decrease in k_s with increased exposure; 0.86, 0.74, and 0.59 for 0 months, 6 months, and 12 months exposure, respectively, as shown by a solid line in Fig. 9, where each data point represents the average of five tests. It could be reasoned that surface corrosion deteriorated the rough unweathered surface profile of the sandblasted plates which had developed very high k_s, whereas the smoother grit-blasted plates were further roughened by the weathering. Specimens bolted up prior to exposure (B) showed little change over 12 months. Examination of the B specimens after testing indicated very little surface corrosion on the faying surfaces.

Tests underway in England (6) on the effect of exposure indicate that 1 yr

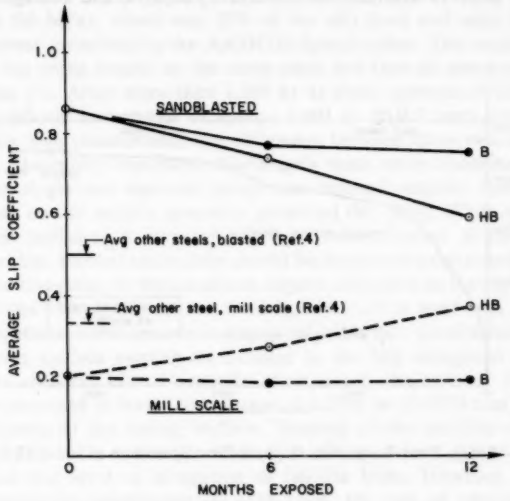

FIG. 9.—Effect of Exposure on Slip Resistance

of weathering improved the slip coefficient of grit-blasted plates for both Grade 50 steel and weathering steel. The initial slip coefficients for the two steels, 0.42 and 0.37, respectively, were improved to 0.52 and 0.49 by exposure.

The sandblasted BC tension slip specimens gave an average k_s of 0.65 after 12 months of exposure under load in the creep chain. This k_s is 15% lower than the results from the compression B specimens which were exposed a similar amount but not under shear load. Examination of the faying surfaces after testing indicated the stressed connections (BC) weathered at a faster rate than the unloaded connections (B). The bolted sandblasted specimens gave higher k_s than the HB plates which were unassembled and showed significant weathering after 12 months exposure.

The unbolted exposed mill scale plates (HB) visually showed the results of 12 months exposure, and they also "felt rough" compared to the unexposed plates. After 12 months, the average k_s for the HB mil scale plates increased from 0.20–0.37. The slip coefficient for the mil scale BC tension specimens exposed for 12 months gave a slip coefficient of 0.29, assuming two shear planes as in all other tests. However, this value cannot be compared to the compression B specimen results for 12 months exposure because these creep specimens had already slipped into bearing during the creep experiment, as described later.

These test data indicate that exposure of sand and grit-blasted A588 steel up to 1 yr prior to connection assembly does not produce k_s less than the average value for clean blasted surfaces of other steels. Exposure improved the slip resistance of A588 mil scale surfaces. However, it took 10 months of exposure prior to assembly to increase k_s to 0.34, the average value for

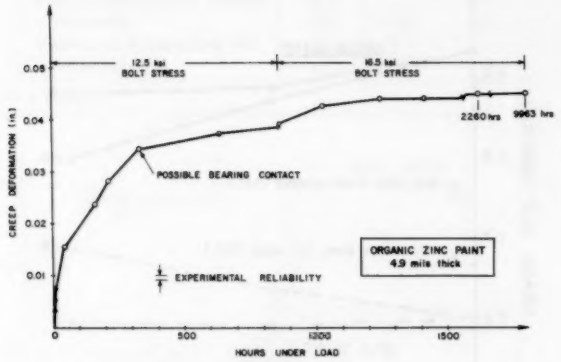

FIG. 10.—Creep-Time Response, Organic Zinc Specimen (1 in. = 25.4 mm)

mil scale surfaces of other steels. It would normally be expected that the steel be exposed only a few months before assembly. Since the exposure effect is almost linear, as shown in Fig. 9, a few months exposure will not significantly improve the slip load.

Creep Tests.—All 12 specimens in the creep chain were subjected to the same load history, a 12.5 ksi (86 MPa) bolt shear stress for 36 days (865 hr) and then 16.5 ksi (114 MPa) for an additional year (9,098 hr). The maximum connection load applied was 91% of the average expected slip load based on the measured k_s = 0.20 for the mil scale surfaces and a 54.5-kip (243-kN) bolt clamping force. When the load reached the first stage of 12.5-ksi (86-MPa) bolt stress, significant slip was recorded for two specimens, 0.009 in. (0.228 mm) for a mil scale connection and 0.003 in. (0.076 mm) for the organic zinc specimen. No significant additional movement occurred during the 36 days this level was maintained except in the organic zinc specimen. The deformation-time

response for this specimen, shown in Fig. 10, indicates continuous creep until approx 300 hr elapsed. Then the creep rate significantly reduced because bearing contact occurred (11).

When the load was increased, corresponding to a 16.5-ksi (114-MPa) bolt shear stress, all five mil scale specimens suddenly slipped into bearing with loud reports after the load was held for 2 hr. An examination of the individual slip tests on unexposed mill scale surfaces, which were summarized in Table 2, showed that some connections slipped at loads slightly lower than those applied to the creep chain. Because of the small range of k_s, 0.18–0.22, for the 11 A1 steel specimens, the dynamic effect caused by slip in one specimen could trigger slip in the remaining connections. During the 1 yr creep experiment, the sandblasted and inorganic zinc specimens which were subjected to shear loads equal to 55% of their slip loads showed no significant creep or slip.

Creep did occur in the organic zinc specimen at a bolt shear stress level of 12.5 ksi (86 MPa), which was 25% of the slip level and only 66% of the allowable stress permitted by the AASHTO Specification. This single test does not follow the creep results on the same paint and type of specimen reported by Nanninga (7). After more than 1,000 hr at shear stresses of 21.4 ksi (148 MPa), insignificant movements of approx 0.001 in. (0.025 mm) were recorded in 12 organic zinc connections. The difference between these two sets of data cannot be adequately explained. Nanninga's tests were conducted indoors, whereas the single test reported herein was exposed outside. Perhaps higher temperatures on the outside specimen promoted the creep. While a single test result is not sufficient to develop broad recommendations, it should not be dismissed either. Further creep tests should be conducted on exposed specimens with organic zinc paint. In the meantime, organic zinc paint on the faying surfaces of connections with significant sustained loads should be used with caution.

Bolt Elongations.—One concern in unpainted joints is the possibility of corrosion on the faying surface causing an increase in the bolt elongation so that the bolt fails in tension. After 12 months of exposure, the bolts in 20 unpainted specimens increased in length an average of 0.0008 in. (0.0203 mm), consistent with weathering of the faying surface. Because of the ductility of the A325 bolt established in the calibration tests, it would take about 100 yr of constant increases of this level of elongation to fail the bolts. However, due to the claimed weathering mechanism of A588 steel, the rate of weathering would not remain constant over this period of time. It can, therefore, be concluded that faying surface weathering will not adversely affect the bolt performance in A588 steel connections in which the bolts are placed in compact patterns. If bolts are widely spaced such that some plate material is not in good contact, it may be possible that expansion at the faying surface due to corrosion would cause some prying forces on the bolt. This possibility was not considered in the research project and would not be of concern in typical friction-type shear connections.

The bolts in the painted specimens showed decreases in length due to creep in the paint in the direction of the clamping force. The loss in clamping force corresponding to a reduction in length of 0.0009 in. (0.0229 mm), assuming elastic unloading and using the bolt calibration data, is 5 kips (22.2 kN) or 9% of the initial clamping force of 54.5 kips (243 kN). The k_s for the two painted specimens given in Table 2 is based on the reduced clamping force

of 49.5 kips (220 kN). Relaxation of the bolt clamping force due to paint creep has been reported by others (1,7).

Design Recommendations

In the 1966 Bolt Specification (19a), the allowable bolt shear stress of 15 ksi (103 MPa) for mil scale surfaces was based on a $k_s = 0.35$, the minimum specified clamping force, and a factor of safety of 1.51. In building structures, there has been almost 20 yr of satisfactory connection performance using this stress level. Data collected since then reduced the average k_s for mill scale to 0.336 (2), so that the factor of safety using the 1966 stress level would be 1.45. In 1976 the Bolt Spec increased the allowable stress to 17.5 ksi (121 MPa) mainly on the basis of laboratory data which indicated that the clamping force for calibrated wrench tightening would be typically 13% higher than the minimum specified.

In the writers' opinion, the possible increase above the minimum specified clamping force should not be considered in the development of design recommendations for the following reasons:

1. The statistics which indicate higher than minimum specified clamping have typically been developed from laboratory data, with the bolts tightened carefully by researchers. This may not be representative of actual field installation by fabricators and erectors.
2. Much of the turn-of-nut tightening data was based on one-half turn from snug, but current specifications would permit many of these bolts to be tightened to one-third turn, resulting in a lower clamping force.
3. Tension control techniques such as load indicator washers produce results closer to the minimum specified clamping force which should be acceptable.
4. Losses in bolt clamping force due to paint creep.

A factor of safety of 1.45 with the minimum specified clamping and the mean k_s from the tests reported herein is used to develop the design recommendations for A588 steel. For mil scale surfaces with $k_s = 0.23$, the allowable stress is 10 ksi (69 MPa) with A325 bolts. For blasted surfaces, using $k_s = 0.52$, typical of the grit blasting, the allowable stress is 23 ksi (159 MPa), indicating considerable structural advantage to blast clean the faying surfaces of A588 steel. The allowable stresses would be valid for plates exposed for up to 1 yr prior to assembly. There should be no difference between the k_s of painted A588 steel and other steels with the same paint. The use of organic zinc paint with sustained loads on the faying surface should be limited until additional data are generated.

Summary and Conclusions

An extensive experimental program was undertaken to establish the slip resistance of shear connections constructed from A588 (weathering) steel. The test program included connections exposed to the atmosphere for periods up to 1 yr. The data indicated that A588 mill scale surfaces have less slip resistance than the mil surfaces of other steels. It was recommended that the allowable

bolt shear stress be reduced for A588 steel. Because of this low slip strength it is recommended that the faying surfaces be sand- or grit-blasted whenever possible. Exposed creep tests indicated that corrosion on the base steel surfaces will not be detrimental to the strength of compact bolted connections. An organic zinc-rich paint on the faying surface of one connection did exhibit significant creep and further studies are recommended to investigate this problem.

Acknowledgments

The research reported herein documents the results of a joint cooperative project between the Federal Highway Administration and The University of Texas at Austin, sponsored by the Federal Highway Administration under Grant No. DOT-FH-11-8900. The writers wish to acknowledge the many staff members of both organizations who contributed to this research effort. The contents of this paper reflect the views of the writers. The contents do not necessarily reflect the views or policies of the Federal Highway Administration. This report does not constitute a standard, specification, or regulation.

Appendix.—References

1. Baldwin, J. W., Jr., and Murphy, D. D., "Loss of Bolt Tension in Steel Bridges," *Missouri Cooperative Highway Research Program 77-2*, Final Report, Dept. of Civ. Engrg., Univ. of Missouri, Columbia, Mo., Jan., 1978.
2. Fisher, W., and Struik, J. H. A., *Guide to Design Criteria for Bolted and Riveted Joints*, John Wiley and Sons, Inc., New York, N.Y., 1974.
3. Fouad, F. H., "Slip Behavior of Bolted Friction-type Joints with Coated Faying Surfaces," thesis presented to The University of Texas at Austin, Tex., in Jan., 1978, in partial fulfillment of the requirements for the degree of Master of Science.
4. Hechtman, R. A., Young, R. D., and Savikko, E. R., "Slip of Joints under Static Loads," *Proceedings*, ASCE, Vol. 80, Separate No. 484, Sept., 1954, pp. 1–18.
5. *Interim Bridge Specifications*, 1978, American Association of State Highway and Transportation Officials, Washington, D.C., 1978.
6. Moss, D. S., "High Strength Friction Grip Bolted Joints—Effects After One Year of Weathering under Load," *Supplementary Report 499*, Transport and Road Research Laboratory, Crowthorne, Berkshire, England, 1979.
7. Nanninga, M. G., "Creep Behavior of Friction-type Joints with Coated Faying Surfaces," thesis presented to The University of Texas, at Austin, Tex., in Jan., 1978, in partial fulfillment of the requirements for the degree of Master of Science.
8. Rumpf, J. L., and Fisher, J. W., "Calibration of A325 Bolts," *Journal of the Structural Division*, ASCE, Vol. 89, No. ST6, Proc. Paper 3731, Dec., 1963, pp. 215–234.
9. *Specification for Structural Joints Using ASTM A325 and A490 Bolts*, Research Council on Structural Connections (formerly Research Council on Riveted and Bolted Structural Joints), Feb., 1976; (a) 6th ed., Sept., 1966.
10. "Standard Specification for High-Strength Low-Alloy Structural Steel with 50,000 psi Minimum Yield Point to 4 in. Thick," *ASTM A588-71*, American Society for Testing Materials, Philadelphia, Pa., 1971.
11. Yura, J. A., Frank, K. H., and Cayes, L., "Friction-Type Bolted Shear Connections with A588 Weathering Steel," *Report No. FHWA-RD-80*, (Final Report), Federal Highway Administration, Washington, D.C., Aug., 1980.

PROCEDURE FOR PREDICTING WIND DAMAGE TO BUILDINGS[a]

By Kishor C. Mehta,[1] James R. McDonald,[2] Members ASCE, and Douglas A. Smith,[3] A. M. ASCE

INTRODUCTION

Hurricane Allen, the tornadoes that struck Grand Island, Neb., and the thunderstorm winds that hit Lubbock, Tex., are typical storms that occur on a regular basis in the United States each year. While it is not practical to design ordinary buildings to resist storms which produce wind loads significantly in excess of current design practices, it is desirable for a building owner to know what type of damage might take place and what the consequences of that damage might be on the operations carried out in the building. With such knowledge, emergency plans can be formulated and alternative plans of operation can be developed.

In more than 40 post-storm investigations conducted by the Institute for Disaster Research at Texas Tech University (6), personnel have systematically categorized the types of damage to buildings produced by windstorms. The studies include assessment of the performance of structural components as well as the architectural features of the building. The knowledge gained from these post-storm investigations has been utilized in the development of procedures for predicting potential wind damage to existing buildings.

Two procedures are described in this paper that involve different levels of engineering effort. Level I is a subjective approach, whereas Level II is an analytical approach. The Level I procedure is accomplished by conducting an on-site survey of the building and completing a questionnaire that establishes details of the building construction. The type of damage to the existing building can be deduced from knowledge of the behavior of similar buildings in windstorms. The Level II procedure involves structural analysis based on knowledge of wind-structure interaction and the strengths of materials used in the construction.

[a]Presented at the October 27–31, 1980 ASCE Convention and Exposition, held at Hollywood-By-The-Sea, Fla. (Preprint 80-644).

[1]Prof., Dept. of Civ. Engrg., Texas Tech Univ., P.O. Box 4089, Lubbock, Tex. 79409.
[2]Prof., Dept. of Civ. Engrg., Texas Tech Univ., Lubbock, Tex. 79409.
[3]Design Engr., Southwestern Public Service Co., Amarillo, Tex.

Note.—Discussion open until April 1, 1982. To extend the closing date one month, a written request must be filed with the Manager of Technical and Professional Publications, ASCE. Manuscript was submitted for review for possible publication on January 15, 1981. This paper is part of the Journal of the Structural Division, Proceedings of the American Society of Civil Engineers, ©ASCE, Vol. 107, No. ST11, November, 1981. ISSN 0044-8001/81/0011-2089/$01.00.

Results of the analysis give wind speeds associated with a specific sequence of damage. The probability of the damage sequence can be determined if a tornado hazard probability model has been developed for the region containing the site (2). This paper presents a brief description of the two procedures. Refs. 4 and 7 provide specific details.

Level I—Subjective Procedure

The subjective procedure is relatively simple and can be performed by architects or engineers who are familiar with wind-caused building damage. The damage potential is determined by subjective judgment based on a survey of the building and answers to the questionnaire. The procedure and questionnaire initially were developed by McDonald and Lea in an effort to predict potential wind damage to Veterans Administration facilities (4). A copy of the questionnaire and explanation for its interpretation are contained in Ref. 2.

Exterior Survey.—This part of the survey determines information about the exterior walls and cladding. The location and extent of window glass in the exterior walls is documented. A survey of the immediate area surrounding the site provides information on potential windborne debris. Identification of the location of utilities tie-ins, mechanical equipment, and emergency equipment it used to assess potential damage and possible disruption of services to the building.

Survey from Roof.—This survey identifies the type and conditions of roofing material, the height of parapet walls, the type of coping, drainage conditions (potential for ponding), and the location of radio or TV antennas. The anchorage of mechanical equipment to the roof is inspected to determine the size of openings in the roof that would be exposed if the mechanical equipment is blown away. A view of the surrounding terrain and adjacent buildings indicates possible shielding or channeling effects. The presence of roof gravel on adjacent buildings is a threat to window glass located downwind from the roof gravel source.

Survey of Mechanical and Electrical Equipment Rooms.—The location of vital mechanical and electrical equipment such as emergency generators, natural gas regulators, and electrical transformers are noted. The susceptibility of equipment to flooding also is included in the survey.

Study of Construction Drawings and Specifications.—Construction drawings and specifications are viewed with the purpose of identifying the type of structural system, the reinforcement, or lack thereof, in load-bearing masonry walls, and the type of anchorages and connections used. The wind loads should be traced from the walls and roof through the structural system and into the foundation. A sharp eye should be on the lookout for weak links in the lateral load resisting system.

Once the survey and the questionnaire are complete, the inspector is in a position to make subjective judgments on potential damage to the building. Features observed in the survey are compared with the performance of similar features in buildings that have been affected by windstorms in the past.

There are three principal types of potential damage: (1) Overall structural collapse; (2) failure of individual structural or architectural components; and (3) breach of the building containment. Overall structural collapse is not likely in ordinary buildings that have received some degree of engineering attention

in the design process. Failure of an individual structural component such as a load-bearing wall can lead to progressive failure of other components or overall collapse. Likewise, the failure of a roof-to-wall anchorage can lead to removal of all or part of the roof. Breach of the building containment may be the result of a structural or architectural component failure. A nonload-bearing wall could collapse, a window glass could break, or loss of mechanical equipment could expose an opening on the roof. Breach of the containment allows wind or water, or both, to get inside a building, causing problems with personnel comfort and damage to equipment and furnishings.

Level II—Analytical Procedure

This analytical procedure not only predicts the type of damage to low-rise buildings, but also predicts the wind speeds at which a sequence of failures will take place. The analytical procedure utilizes state-of-the-art knowledge of

TABLE 1.—Increments of the Three-Task Analytical Procedure for Predicting Windstorm Damage (7)

Task (1)	Data (2)	Function (3)	Result (4)
1. Data collection	Collection of: Structural drawings Architectural drawings Specifications	Action of: Site visit Determination of material strengths	Knowledge of: Structural systems Material strengths Site characteristics
2. Analysis	Knowledge of: Structural systems Material strengths Site characteristics	Analysis using: Structural mechanics Wind loads Engineering judgment	Establishment of: Threshold-failure wind speeds for each building component
3. Interpretation	Knowledge of: Threshold-failure wind speeds for each building component	Analysis using: Structural response Engineering judgment	Establishment of: Damage sequence Wind speed ranges Probability of damage

wind loads, the physical properties of construction materials, and the response of building systems to wind loads in order to predict the wind speed associated with a sequence of failures.

The analytical procedure is divided into three tasks: (1) Data collection; (2) analysis; and (3) interpretation. Each task consists of three increments: (1) data; (2) function; and (3) result. Assembly of information, action of the analyst, and formulation of results constitute the data, function, and result increments, respectively. The three-task procedure, with three increments per task, is shown in Table 1. The results of Tasks 1 and 2 are the input data for Tasks 2 and 3, respectively. The result of Task 3 is the interpretation in terms of damage sequence and probability of damage.

The procedure assumes that the building may experience wind from any direction and that each building component experiences wind from the most critical direction. The procedure is restricted to low-rise buildings.

The structural response of a building component is made up of a static and a dynamic part. For low-rise buildings and relatively stiff components, the contribution of the dynamic part of the response can be neglected. The fundamental frequencies of low-rise buildings or their components are much higher than wind gust frequencies. For example, components such as masonry walls or metal roof decks have fundamental frequencies greater than 3 Hz, while most of the free field wind gust spectrum energy is in the frequency range that is less than 0.5 Hz (1). The disparity between fundamental frequencies of building components and gust frequencies of the wind suggests that the dynamic part of the response is negligible for ordinary structures.

Data Collection.—The collection of data is the first task of the procedure, as indicated in Table 1. The information desired includes the structural drawings, architectural drawings, and construction specifications. These items should be reviewed prior to a site visit. This review will allow the evaluator to determine if the facility has been built according to the plans. He will be aware of any modifications or additions that may have been poorly documented. In addition, a review of the drawings will indicate those construction materials for which strength properties will be needed. Once the documents have been reviewed, a site visit should be planned and arrangement for tests, if needed, should be made. The site visit and the establishment of strength properties are the functions to be performed as increments of Task 1 (cf. Table 1).

The site visit provides the analyst with personal contacts with individuals who have access to information about the building. These individuals may be able to quickly provide information not contained in the drawings and specifications. In addition, the site visit provides an opportunity for the analyst to obtain a personal knowledge of the building which may facilitate interpretation of the drawings.

Use of the questionnaire in the Level I approach is a good starting point on the site visit. A subjective formulation of probable damage can be made by using the questionnaire. Specific building components can be identified which are particularly susceptible to windstorm damage. In addition, the subjective judgments can be used as a basis for a decision as to whether or not a detailed analysis (Level II) is warranted.

Since the strengths of most engineering materials are higher than assumed in specifications, median strengths should be used in the analyses. The median strength represents the middle, or average, value of a statistical distribution which describes the variation of material strength. Representative median strength properties are essential for the analysis. Median strengths which are either too high or too low will result in either underpredicting or overpredicting the potential damage to a building. Therefore, establishing representative median material strengths is critical to producing accurate results.

The result of Task 1 is a knowledge of the structural systems employed in the building, the strength of the construction materials, and the site characteristic. The results of Task 1 are utilized as the data increment for Task 2.

Analysis of Building.—Analysis of the building is accomplished using the results of Task 1 as the data increment for Task 2. This data includes knowledge

of the structural systems employed in the building, the strengths of the construction materials, and the site characteristics. This information, along with the use of structural mechanics, wind loading conditions, and engineering judgment is used to perform a structural analysis for each component of the building. The structural analyses establish a failure pressure for each component of the building. The failure pressure is used to calculate threshold wind speeds associated with the postulated failure.

Possible failure modes for various building components are listed in Table 2. The failure modes are produced by pressure and impact. A failure mode

TABLE 2.—Building-Component Failure Modes (7)

Building components (1)	Failure Mode	
	Pressure loading (2)	Impact loading (3)
Doors, windows, louvers	Anchorage, support	Perforation
Roof:		
Deck or slab	Excessive shear or bending stresses, anchorage, support	Perforation
Beams, joists, purlins	Excessive shear or bending stresses, anchorage, support	Excessive deformation, collapse
Walls	Excessive shear or bending stresses, anchorage, support	Perforation, excessive deformation, collapse
Structural frames	Excessive plastic deformation, formation of a mechanism, connections, bolts, welds, anchorage, support	Excessive deformation, collapse
Footings	Rotation, uplift	—

TABLE 3.—Loading Conditions (7)

Loading (1)	Part of building affected (2)
Wind pressure alone	Exterior walls, roof, structural frame
Wind plus APC	Exterior walls, roof, sealed rooms with exterior walls
APC alone	Sealed rooms protected from winds
Windborne debris[a]	Exterior walls, roof, structural components

[a]Combinations of impact with any one of the other three conditions are possible, but are neglected.

associated with pressure is caused by aerodynamic wind loads or atmospheric pressure change (APC). A failure mode associated with impact is caused by wind-borne debris. The failure modes associated with a roof joist, e.g., include excessive stress due to shear or bending, anchorage failure, and support failure (cf. Table 2). An anchorage failure might be the pullout of an anchor bolt which attaches the joist to the wall. A support failure occurs when a load-bearing wall collapses, leaving no support for the joist end reaction.

The analysis of a building to determine the threshold wind speeds for failure of each building component may include four possible loading combinations, as shown in Table 3. The analysis may not involve all four loading combinations. For example, if a building is vented or if the winds are not tornadic, the effects of APC need not be considered.

The result of Task 2 is the threshold wind speeds for failure of each component of the building. This information is used in Task 3 to establish a damage sequence for the building.

TABLE 4.—Typical Damage Sequence (5)

Threshold wind speed, in miles per hour (kilometers per hour) (1)	Damage sequence (2)
88 (142)	Exterior door at southeast corner of building could fail
140 (225)	Other exterior doors could collapse inward, resulting in some wind circulation through building; west interior wall of Rod Fabrication Area could collapse
(167) (269)	Joist anchorage failure occurs along west eave of the lab area; 10-ft (3-m)-wide strip of roof along west wall will tend to uplift, but will be restrained by inplane roof truss; joists and roof decking will subsequently collapse downward to floor
184 (296)	A 20-ft (6.1-m)-wide section of exterior wall could collapse at wall corners (except at vault) due to failure of first column from corner or due to formation of mechanism in parapet beam; if this failure occurs in south wall at southeast corner, joists bearing on this wall (through brackets attached to column) and the 20-ft (6.1-m)-wide section of roof will collapse downward
204 (328)	Exterior walls collapse inward due to windward pressures; if this occurs in south wall, joists bearing on wall will collapse downward; all walls not likely to collapse, but rather portions of walls would be affected
231 (372)	Additional joist anchorage failure could occur, resulting in portions of roof collapsing to floor
250 (402)	At these wind speeds, integrity of laboratory building expected to be lost; most of the walls will collapse along with inplane roof truss; vault not likely to sustain damage at this wind speed

Damage Sequence.—The result from Task 2 is the postulated component failures and their associated threshold wind speeds. This information is the data increment in Task 3. These threshold wind speeds are used to formulate a damage sequence which defines the predicted damage to a building for increasing values of wind speeds. The damage sequence is initially formulated by arranging the threshold wind speeds for all components in ascending order. Engineering judgment, based on knowledge of building performance in windstorms, is applied to define the

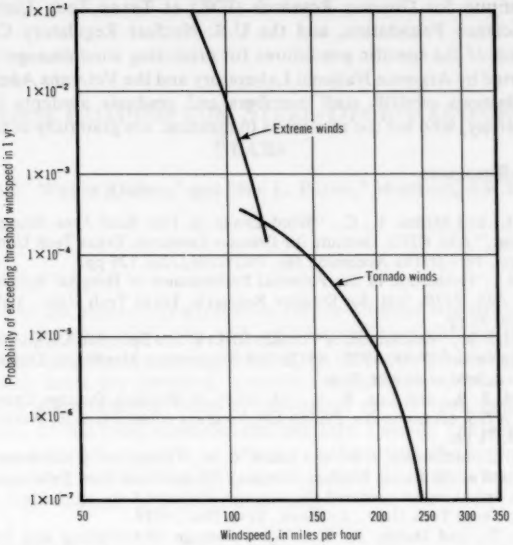

FIG. 1.—Wind Speed Hazard Probability Model for Lubbock Tex. (7)

progressive failure of the building. The relationship between various component failures is ascertained based on the analyses performed in Task 2 of the procedure. A typical damage sequence is shown in Table 4 to show the type of information included.

If it is necessary to establish the probability associated with a postulated damage sequence, a wind speed hazard probability model is required. The probability of occurrence of the damage sequence is the probability of exceeding the threshold wind speed in one year. A typical wind speed hazard probability model developed using the procedure outlined in Ref. 3 for Lubbock, Tex., is shown in Fig. 1.

Conclusions

Two procedures, one subjective and one analytical, can be used to evaluate potential windstorm damage to existing buildings. Results of these evaluations are useful in determining the responses of the architectural and structural systems of the building. From the evaluation, areas of safety can be identified for occupant protection and alternate plans for building function in the event of a windstorm can be formulated. If warranted, the architectural and structural systems could be retrofitted to improve their windstorm resistance characteristics.

Acknowledgments

Support of the Research work used as a background for this paper was provided

by the Institute for Disaster Research (IDR) at Texas Tech University, the National Science Foundation, and the U.S. Nuclear Regulatory Commission. Development of the specific procedures for predicting wind damage to buildings was supported by Argonne National Laboratory and the Veterans Administration. The contributions of IDR staff members and graduate students from Texas Tech University, who are too numerous to mention, are gratefully acknowledged.

APPENDIX.—REFERENCES

1. Kim, S. I., and Mehta, K. C., "Wind Loads on Flat Roof Area through Full Scale Experiment," *IDR #28D*, Institute for Disaster Research, Texas Tech Univ., Lubbock, Tex., Sept., 1977 (NTIS Accession No. PB292156/AS), 129 pp.
2. Lea, P. A., "Evaluation of the Potential Performance of Hospital Buildings in Windstorms," *IDR #19D*, Inst. for Disaster Research, Texas Tech Univ., Lubbock, Tex., Aug., 1978, 97 pp.
3. McDonald, J. R., "Assessment of Tornado Risks at Site Specified Locations," presented at the September 17–19, 1979, ASCE 3rd Engineering Mechanics Division Specialty Conference, held at Austin, Tex.
4. McDonald, J. R., and Lea, P. A., "A Study of Building Damage Caused by Wind Forces," *NTIS Accession No. PB 286 604*, Veterans Administration, Washington, D.C., Jan., 1978, 71 pp.
5. Mehta, K. C., McDonald, J. R., and Smith, D. A., "Response of Structures to Extreme Wind Hazard at the Exxon Nuclear Company Mixed Oxide Fuel Fabrication Facility," Vol. I, technical report prepared for Argonne National Lab. by the Inst. for Disaster Research, Texas Tech Univ., Lubbock, Tex., Dec., 1979.
6. Minor, J. E., and Mehta, K. C., "Wind Damage Observations and Implications," *Journal of the Structural Division*, ASCE, Vol. 105, No. ST11, Proc. Paper 14980, Nov., 1979, pp. 2279–2291.
7. Smith, D. A., Mehta, K. C., and McDonald, J. R., "Procedure for Predicting Wind Damage to Buildings," *IDR #45D*, Inst. for Disaster Research, Texas Tech Univ., Lubbock, Tex., Sept., 1979, 122 pp.

Uniform Loading for Steel-Deck-Reinforced Slabs

By F. Wayne Klaiber,[1] and Max L. Porter,[2] Members, ASCE

Introduction

Derivation of the shear-bond expression for the ultimate strength of one-way concrete slab elements reinforced with cold-formed steel decking is based on the assumption that the system is subjected to concentrated loading. In cases where uniform loads are involved, however, modification of the shear-bond expression by substituting a value of one-fourth of the span length, L, for the shear span, L', has been recommended (see Refs. 3 and 6). The tests described in this paper were developed in an effort to substantiate the assumption that a slab element with concentrated loads at the quarter points behaves in a similar manner to a slab element with uniform loading.

Description of Test Slabs

Six slab elements were constructed with nominal depths and widths of 4 3/8 in. and 24 1/4 in. (111.1 mm and 616.0 mm), respectively. Two of the slab elements were 8 ft (2.44 m) long, two were 12 ft (3.66 m), and two were 16 ft (4.88 m). Each slab element was constructed with a single standard panel width of steel deck having a depth of 1.55 in. (39.4 mm). The average measured thickness of the steel was 0.030 in. (0.76 mm), and the modulus of elasticity was assumed to be 29,500 ksi (2.03×10^8 kN/m^2). The deck had an average yield strength of 38.7 ksi (2.66×10^5 kN/m^2), as determined by the manufacturer.

All six specimens were constructed in the laboratory utilizing concrete obtained from a local ready-mix plant. Two batches of concrete were required for casting the specimens. The 12 ft and 16 ft (3.66 m and 4.88 m) specimens were cast from the first batch and the 8 ft (2.44 m) specimens were cast from the second batch. Control cylinders of 6 in. × 12 in. (152.4 mm × 304.8 mm) size, slump tests, and modulus of rupture beams of 6 in. × 6 in. × 36 in. (152.4 mm × 152.4 mm × 914.4 mm) size were made at intervals while the concrete was being placed. The resulting concrete compressive strengths are shown in Table

[1]Prof. of Civ. Engrg., Iowa State University, Ames, Iowa.
[2]Assoc. Prof. of Civ. Engrg., Iowa State University, Ames, Iowa.

Note.—Discussion open until April 1, 1982. To extend the closing date one month, a written request must be filed with the Manager of Technical and Professional Publications, ASCE. Manuscript was submitted for review for possible publication on April 11, 1980. This paper is part of the Journal of the Structural Division, Proceedings of the American Society of Civil Engineers, ©ASCE, Vol. 107, No. ST11, November, 1981. ISSN 0044-8001/81/0011-2097/$01.00.

1. All slab elements, cylinders, and modulus of rupture beams were cured under wet burlap and polyethlene for seven days, followed by air drying until the time of testing.

The 8-ft (2.44-m) long specimens were cast with supports only at the ends. The 12 ft and 16 ft (3.66 m and 4.88 m) specimens were cast with supports at both ends and at midspan to simulate shoring.

Description of Test Setup

The method for applying the concentrated loads to the slab elements at the quarter-points is shown in Fig. 2. The loading was applied by two hydraulic cylinders mounted on structural tubes, beneath the structural tie-down floor.

TABLE 1.—Concrete Properties

Length of slab element, in feet (1)	Age at time of test, in days (2)	Average compressive strength, in pounds per square inch (3)
8	24	4,297
12	26	3,715
16	32	3,784

Note: 1 ft = 0.305 m; 1 psi = 6.894 kN/m^2.

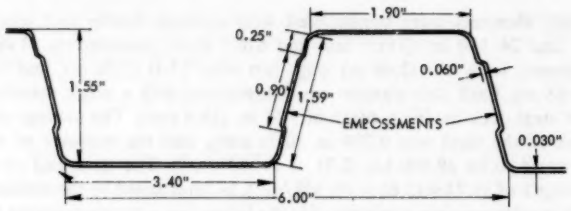

FIG. 1.—Typical Cross Section of Steel Deck Reinforcement

Force was applied to the test specimens by the cylinders acting against the tie-down floor and the structural tubes to which the load rods were attached (see Fig. 2).

The typical test arrangement for the slab elements that were uniformly loaded is shown in Fig. 3. The uniform loading was applied by inflating a plastic bag which was confined by the top surface of the test specimen and an inverted rigid box. The confinement box was held in place by essentially the same system of structural tubing and rods that was used for applying the concentrated loading. Air was forced inside the plastic bag and monitored by both a water manometer and a mercury manometer. The total force on the slab element was determined by observations of hydraulic cylinder pressure and checked by means of strain gages attached to the vertical tie-down rods.

Primary measurements taken on the specimens throughout each of the tests

were: (1) Vertical deflections at midspan and at quarter-span points; (2) horizontal differential slip between steel deck and concrete at the ends of the specimen (termed as end-slip); and (3) strains (via electrical resistance gages) taken across the specimen section at midspan and at quarter-span.

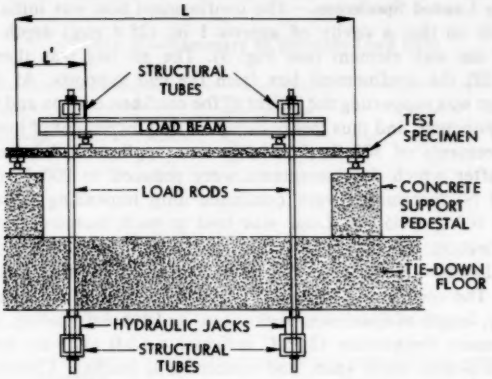

FIG. 2.—Cut-Away View of Concentrated Load Tests

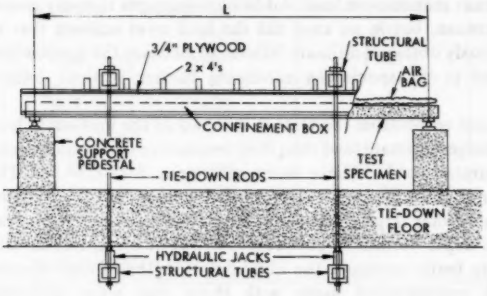

FIG. 3.—Cut-Away View of Box and Air Bag for Uniformly Loaded Specimens

The strain measurements were utilized in determining the existence of composite action between the concrete and steel decking.

Test Procedure and Behavioral Results

Concentrated Loaded Specimens.—Due to the nature of the test setup as shown in Fig. 2, the weight of the loading system was applied first. By means of the hydraulic cylinders, load was next applied in increments of 500 lb (2,224 N) for the first portion of the test. When large increases in deflection occurred,

the loading increment was reduced to 200 lb (889 N), and as the beam approached failure the increment was reduced to 100 lb (445 N). The load was held at each level until vertical deflection, end-slip, and strain gage readings could be taken. In most cases, the time interval for each increment of load was about one minute.

Uniformly Loaded Specimens.—The confinement box was initially supported at both ends so that a cavity of approx 1 in. (25.4 mm) depth existed over the top of the slab element (see Fig. 3). The air bag was then sufficiently inflated to lift the confinement box from the end supports. At this point the test specimen was supporting the weight of the confinement box and the remaining tie-down equipment, and thus this became the first increment of loading. Further loading increments of 500 lb (2,224 N) were applied until larger deflections occurred, after which the increments were reduced to 200 lb (889 N). The 200 lb (889 N) increments were continued until impending failure, and then reduced to 100 lb (445 N). Load was held at each increment until end slip, vertical deflection, strain gage, and manometer readings could be taken.

Ultimate Loads.—A summary of specimen data and ultimate loads is given in Table 2. The specimen designation in the first column of Table 2 indicates, respectively, length of specimen, shear span, and type of loading. For example, the slab element designation 12-35-C indicates a 12-ft (3.66-m) long specimen, a 35-in. (889.0-mm) shear span, and concentrated loading. Uniform loading is indicated by the letters UN.

For both the concentrated and the uniformly loaded specimens, ultimate load was accompanied by a large end slip between steel deck and concrete, followed by a significant reduction in load. Additional attempts to apply more load resulted in some increase, but in no case did the load ever achieve that corresponding to the previously obtained ultimate failure. In all cases the application of additional load resulted in the specimens exhibiting further vertical deflection and end slip.

A significant result from the tests is that two of the uniformly loaded members exhibited a larger ultimate load than their respective companion members carrying two concentrated loads. These were specimens 8-23-UN and 12-35-UN. This result was not the case with 16-47-UN, however, as its companion, 16-47-C, carried a somewhat larger load. This latter inconsistency, however, is believed to be due to depth variations between the 16-ft (4.88-m) test members.

In order to better compare the ultimate strengths of slab elements that were loaded with concentrated loads with those that were uniformly loaded, a compensation for variations in slab depth was necessary. Data obtained from previous work (2,4,5) showed that for each 1 in. (25.4 mm) increase in depth, the experimental shear, V_{ue}, increased by approx 300 lb/ft (406.7 N/m) width. Table 3 shows the experimental and adjusted shear values based on an adjusted total depth of 4 1/2 in. (110,430 mm) [or an adjusted effective depth of 3.88 in. (98.6 mm)]. Based on the adjusted values, the uniformly loaded specimens carried from 3%–19% more load than did the corresponding concentrated load specimens.

Load-Deflection Behavior.—The load-deflection behavior for the six slab elements is shown in Fig. 4. The figure shows that the deflections for all three pairs of test specimens corresponded closely. This result is to be expected since, according to the elastic theory, a beam with a given load, W, which

is uniformly distributed would deflect at midspan an amount given by

$$\Delta = \frac{5WL^3}{384\,EI} \quad \ldots\ldots\ldots\

partially explained as being due to the variation in depth of the specimens. The reloading of specimen 12-35-C indicated in Fig. 4 was necessitated due to a stability problem with the loading apparatus.

Table 4 shows measured deflections and computed deflections, based on several different methods, for each slab element when loaded to 50% of ultimate load. The first theoretical deflection is computed using the effective moment of inertia, I_e, as given in Ref. 1, by the following relationship:

$$I_e = \left(\frac{M_{cr}}{M_a}\right)^3 I_g + \left[1 - \left(\frac{M_{cr}}{M_a}\right)^3\right] I_{cr} \quad \ldots\ldots\ldots\ldots\ldots\ldots\ldots\ldots (3)$$

in which I_{cr} = moment of inertia of cracked section transformed to concrete,

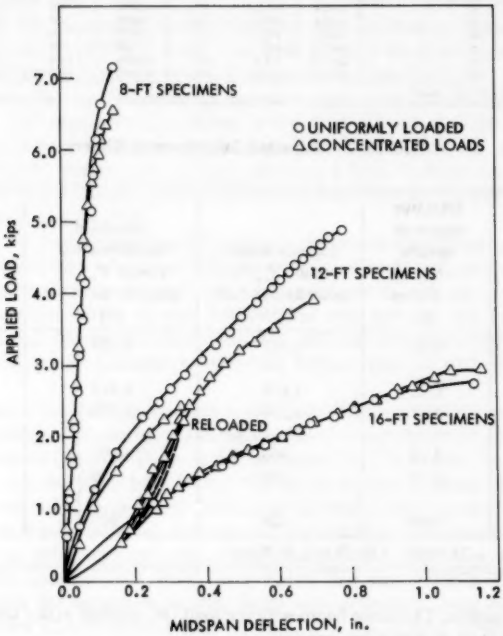

FIG. 4.—Load-Deflection Curves for all Slab Elements

in inches^4; I_g = moment of inertia of gross concrete section about the centroidal axis, in inches^4; M_a = maximum moment in member at stage for which the deflection is being computed, in inch-pounds; and M_{cr} = cracking moment, in inch-pounds. The second theoretical deflection is computed using an uncracked section while the third is computed using a cracked section. The fourth theoretical deflection is the average of the deflections from the second and third methods. The value immediately following the deflection for each method is the ratio

of that computed deflection to the measured deflection.

An examination of the computed deflections shows that those based on a simple average of the uncracked and the cracked sections is the best predictor

TABLE 4.—Measured and Computed Deflection at 1/2 P_u

Slab element (1)	Measured values, Δ, in inches (2)	Calculated Values, in inches, based on			
		I_e (3)	I_{unc} (4)	I_{cr} (5)	$\Delta_{cr} + \Delta_{unc}/2$ (6)
8-23-UN	0.058	0.051/0.88	0.040/0.69	0.105/1.81	0.072/1.24
8-23-C	0.053	0.039/0.74	0.039/0.74	0.101/1.91	0.070/1.32
12-35-UN	0.26	0.386/1.40	0.169/0.65	0.386/1.48	0.278/1.07
12-35-C	0.23	0.367/1.59	0.170/0.74	0.382/1.66	0.267/1.16
16-47-UN	0.35	0.535/1.53	0.234/0.67	0.535/1.53	0.384/1.10
16-47-C	0.36	0.631/1.75	0.276/0.77	0.631/1.75	0.454/1.26

Note: 1 in. = 25.4 mm.

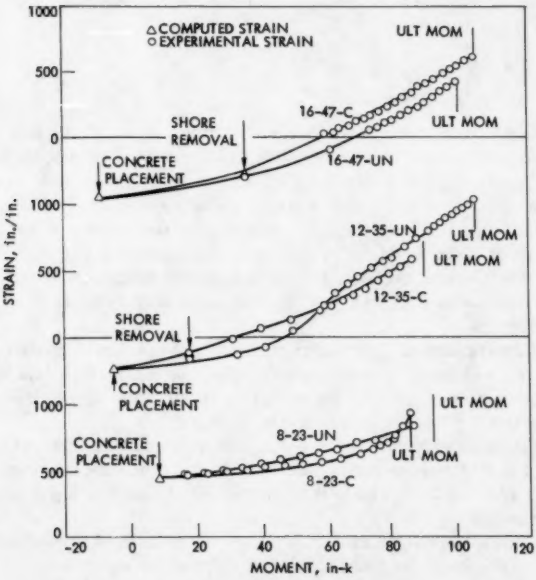

FIG. 5.—Relationship between Strain and Bending Moment for all Slab Elements

of deflection at 1/2 P_u which is approximately equal to the allowable service load.

Bending Strain Behavior.—The relationship between bending strain in the

bottom fiber of steel deck and applied moment at midspan is shown in Fig. 5. Strain gage readings taken at shore removal provided an incremental strain, which, when added to the computed strain at concrete placement resulted in the experimental values shown for the 12 ft and 16 ft members. In the case of the 8 ft member, which did not have shoring, the first strain gage reading was taken at the time of the first test-load increment. The corresponding strain increment was added to the computed strain at concrete placement to give the strain at first load increment. The linear character of all of the strain-load relationships indicates a significant degree of composite action up to ultimate load.

Cracking Characteristics.—Fig. 6 shows the major cracks and their location on each of the six specimens and the end at which end slip occurred. The figure shows that the major cracks on each concentrated loaded specimen occurred at or near the load point (one-fourth point), while major cracks on the uniformly loaded members occurred near the one-third-point of the span.

Shear-Bond Analysis of Results

Porter, et al. (4) have determined that the best relationship for predicting shear-bond capacity is

$$V_u = \frac{\phi bd}{s}\left(\frac{m\rho d}{L'} + k\sqrt{f'_c}\right) \quad \ldots\ldots\ldots\ldots\ldots\ldots\ldots\ldots\ldots\ldots\ldots\ldots\ldots\ldots (4)$$

The terms and units of Eq. 4 are defined as follows: V_u = ultimate computed shear based on shear-bond failure in pounds per foot of width; ϕ = capacity reduction factor, usually taken as 0.85. (3); b = width of slab, taken as 12 in. (304.8 mm); d = effective slab depth, in inches; s = spacing of shear transfer devices other than embossments, in inches; ρ = reinforcement ratio, A_s/bd; L' = length of shear span, in inches; m = slope of a linear regression line; f'_c = concrete compressive strength, in pounds per square inch; k = intercept of a linear regression line; and A_s = area of steel deck cross section, in inches per foot of width.

For all deck sections of a particular profile where the shear transferring device is a fixed pattern such as embossments, the spacing in Eq. 4 is ignored or simply taken as unity as was done in this study. For further discussion of the spacing term, s, one may consult Ref. 4.

Eq. 4 is for slab elements subjected to concentrated line loads at a distance of L' (see Fig. 2) from the center line of supports. Since the majority of design conditions utilize uniform rather than concentrated loads, a slight modification of Eq. 4 is needed.

For uniformly loaded systems, L' may be taken as $L/4$, one-quarter of the span length. The basis for this assumption is the equating of areas of the shear diagram for concentrated versus uniform load cases as is now demonstrated.

Fig. 7 shows shear diagrams for concentrated and uniform load cases. The area of the left-hand portion of the shear diagram in Fig. 7(a) is $(1/2)(V_u L/2)$, and the area under the shear diagram in Fig. 7(b) is $V_u L'$. Equating Figs. 7a and 7b yields $L' = L/4$.

The preceding comparison of Fig. 7(a) and Fig. 7(b) for the same total applied

loads provides for equal end shears and equal center-span moments. The previously shown corresponding deflections are only 10% greater at midspan

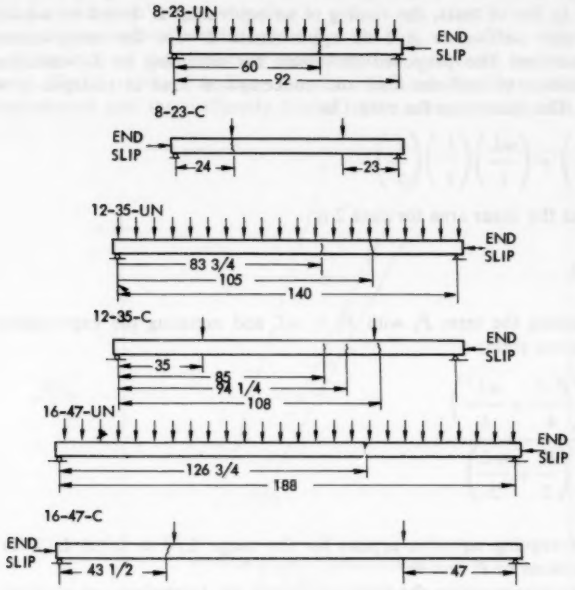

Note: All dimensions are given in inches.

FIG. 6.—Crack Locations for all Slab Elements (1 in. = 25.4 mm)

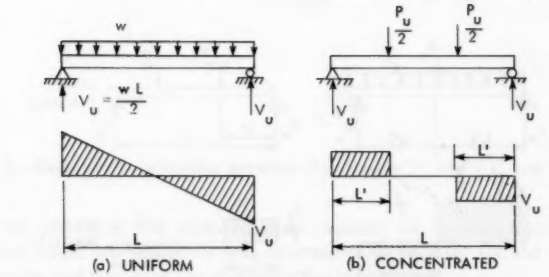

FIG. 7.—Uniform and Concentrated Load Application

for the concentrated load case than for the uniform load case (see Eq. 1 versus Eq. 2). If several concentrated loads exist, the designer may elect to treat the system as an equivalent uniformly loaded beam.

Combinations of uniform and concentrated load systems may require special attention for the proper selection of the L' distance. In certain instances, the loading combination may require tests to determine the proper L' for use in Eq. 4. In lieu of tests, the finding of an equivalent L' based on equating shear areas may suffice to give an approximate L' for the most common load combinations. The proposed procedure for obtaining an L' distance for the combination of uniform load and concentrated load at midspan is shown in Fig. 8. The shear area for case 1 is

$$\frac{P_1}{2}\left(\frac{L}{2}\right)+\left(\frac{wL}{2}\right)\left(\frac{L}{2}\right)\left(\frac{1}{2}\right)$$

whereas the shear area for case 2 is

$$\frac{P_2}{2}(L')$$

Replacing the term P_2 with $P_1 + wL$ and equating the expressions for the shear areas yields

$$L'=\frac{\left(\frac{P_1 L}{4}+\frac{wL^2}{8}\right)}{\left(\frac{P_1}{2}+\frac{wL}{2}\right)} \quad \ldots\ldots\ldots\ldots\ldots\ldots\ldots\ldots\ldots\ldots\ldots\ldots\ldots\ldots (5)$$

The foregoing equation applies for the range $L/4 \leq L' \leq L/2$ for various combinations of P_1 and w.

Before incorporating the given procedure for determining an equivalent shear span, L', into design recommendations, further experimental verification is required utilizing various combinations of uniform and concentrated loads.

Substituting for $L' = L/4$ in Eq. 4 results in the following form of the recommended design equation

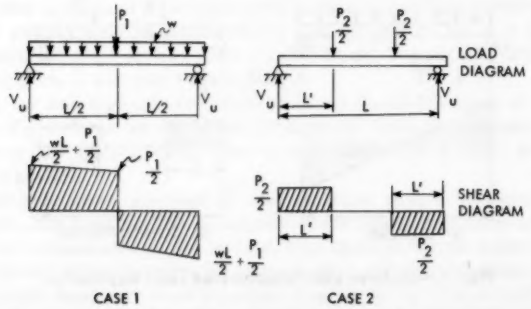

FIG. 8.—Uniform Load in Combination with Single Concentrated Load Placed at Midspan Compared with Two Concentrated Loads

$$V_u = \frac{\phi bd}{s}\left(\frac{4m\rho d}{L} + k\sqrt{f'_c}\right) \quad \ldots\ldots\ldots\

and uniformly loaded series when L' is set equal to $L/4$ and not as good agreement when L' is set equal to $L/3$. Thus, based on the six specimens tested, the shear-bond regression formulation utilizing $L' = L/4$ appears valid for uniformly loaded specimens.

Conclusions

The test results from three uniformly loaded slab specimens and three nearly identical slab specimens with quarter-point concentrated loading yielded the following conclusions:

1. The shear-bond regression analysis is reasonably valid for uniformly loaded as well as concentrated loaded specimens.
2. The replacement of L' in the ultimate strength shear-bond relationship for conversion to uniformly loaded cases with a value of $L/4$ was verified and found to give a better prediction of the specimen strength than a value of $L/3$.
3. Conservative prediction of deflection at 50% of ultimate (which is approximately equal to expected service load) can be obtained by averaging the calculated deflections based on cracked and uncracked moments of inertia.

Acknowledgments

This work was supported through the Engineering Research Institute at Iowa State University, with funds provided by the American Iron and Steel Institute (AISI). Valuable guidance in the conduct of the research was provided by the AISI Task Committee on Composite Construction of the Joint Engineering Subcommittee of the Committees of Hot-Rolled and Cold-Rolled Sheet and Strip Producers and Galvanized Sheet Producers under the chairmanship of T. J. McCabe and past chairman A. J. Oudheusden. The assistance of the many people who participated in this research is gratefully acknowledged. The writers particularly wish to extend their thanks to C. E. Ekberg for his guidance and encouragement during the course of this investigation.

Appendix I.—References

1. *Building Code Requirements for Reinforced Concrete*, ACI 318-77, American Concrete Institute, Detroit, Mich., 1977.
2. Ekberg, C. E., Jr., "Special Review of Test Data for the Ad Hoc Task Group on the Tentative Recommendations for the Design of Cold-Formed Steel Decking as Reinforcement for Concrete Floor Slabs," presented to the American Iron and Steel Institutes Ad Hoc Task Group on the Tentative Recommendations, Washington, D.C., Aug. 2, 1973.
3. Porter, M. L., and Ekberg, C. E., Jr., "Design Recommendations for Steel Deck Floor Slabs," *Journal of the Structural Division*, ASCE, Vol. 102, No. ST11, Proc. Paper 12528, Nov., 1976, pp. 2121–2136.
4. Porter, M. L., Ekberg, C. E., Jr., Greimann, L. F., and Elleby, H. A., "Shear-Bond Analysis of Steel-Deck-Reinforced Slabs," *Journal of the Structural Division*, ASCE, Vol. 102, No. ST12, Proc. Paper 12611, Dec., 1976, pp. 2255–2268.
5. Porter, M. L., Timm, L. W., and Ekberg, C. E., Jr., "Compilation of Test Data Pertaining to One-Way Concrete Slab Elements Reinforced with Cold-Formed Steel

Decking," Iowa State University Engineering Research Institute Report ERI-74086, Ames, Iowa, May, 1974, pp. 19.
6. Schuster, R. M., "Strength and Behavior of Cold-Rolled Steel-Deck Reinforced Concrete Floor Slabs," thesis presented to the Iowa State University, at Ames, Iowa, in 1970, in partial fulfillment of the requirements for the degree of Doctor of Philosophy.

APPENDIX II.—NOTATION

The following symbols are used in this paper:

A_s = cross-sectioned area of steel deck, in square inches per foot of width;
b = width of slab element, taken as 12 in.;
C = indicates a specimen subjected to concentrated line loads;
c.g.s. = center of gravity of steel deck;
D_{avg} = out-to-out measured average depth of slab element specimen, in inches;
D_{cr} = out-to-out measured depth of slab element specimen taken at the failure crack, in inches;
d = effective slab element depth measured from extreme compression fiber to c.g.s. of steel deck, in inches;
d_{cr} = effective slab element depth measured from extreme compression fiber to c.g.s. of steel deck taken at the failure crack, in inches;
E = modulus of elasticity of concrete, in pounds per square inch;
f'_c = compressive strength of concrete, in pounds per square inch;
I = moment of inertia of transformed composite concrete section, in inches^4 per foot of width;
I_{cr} = cracked moment of inertia of transformed composite concrete section, in inches^4 per foot of width;
I_e = effective moment of inertia of transformed composite concrete section from Ref. 1, in inches^4 per foot of width;
I_g = gross moment of inertia of composite cross section, in inches^4 per foot of width;
I_{unc} = uncracked moment of inertia of transformed composite concrete section, in inches^4 per foot of width;
k = intercept of linear regression line for shear-bond strength determination;
L = span length, in inches;
L' = length of shear span, in inches;
M_a = applied moment, in inch-pounds per foot of width;
M_{cr} = moment to cause cracking of concrete in composite section, in inch-pounds per foot of width;
m = slope of linear regression line for shear-bond strength determination;
P_u = ultimate total computed applied load, in pounds;
P_{ue} = ultimate total applied experimental load, in pounds;
s = spacing of shear transfer devices, in inches;
UN = indicates a specimen subjected to uniform loading;
V_u = computed shear capacity, in pounds;
V_{ue} = ultimate experimental shear, in pounds;
W = total supplied load, in pounds;

w = uniformly supplied load, in pounds per foot;
Δ = deflection, in inches;
Δ_{cr} = calculated deflection based upon cracked transformed section properties;
Δ_{unc} = calculated deflection based upon uncracked transformed section properties;
ρ = reinforcement ratio, A_s/bd; and
ϕ = capacity reduction factor.

ABUTMENT-THERMAL INTERACTION OF COMPOSITE BRIDGE

By Jack H. Emanuel,[1] F. ASCE and David B. Lewis,[2] A. M., ASCE

INTRODUCTION

A major factor in the movement of bridges is temperature change. Temperature change induces thermal stresses unless the structure is homogeneous, free of restraints, and of constant temperature, nonexistent conditions for a composite design structure. Thus, designers try to anticipate structural behavior, and attempt to provide for structural movements by using a variety of supporting and expansion devices (5).

Field observations show that these attempts are very often unsuccessful (27,28,30). Abutment movements caused by compaction, settling, or shifting of approach fill, growth or expansion of approach slabs, and "frozen" supporting and expansion devices are common observations. The significance of the combined effect of the resultant stresses and thermally-induced stresses is often manifested in a variety of types of bridge distress. Some investigators have reported that thermally-induced stresses in a composite design structure can reach 30–40% of the design strength (3,16,30).

One design which has become popular in recent years eliminates expansion devices by connecting the superstructure to a flexible substructure with either pinned or integral connections at the abutments. Thus, the entire bridge moves as a single unit. As with structures with expansion type supporting devices, if the approach slabs bind the abutments, a large external force on the ends of the structure may result when the approach slab and the structure both expand as a result of increasing temperatures.

Thermally-induced stresses have been the subject of a number of investigations in the past several years (2,3,4,11,12,13,14,15,16,18,19,22,23,24,25,26,28,29,30, 31). Those conducted in Australia, New Zealand, Europe, and Canada have principally been concerned with concrete box-girder bridges rather than with concrete-steel composite bridges. Although the heat transfer analysis is similar for the two types of construction, the determination of strains and stresses is much more complex for a composite design structure.

[1]Prof. of Civ. Engrg., Univ. of Missouri-Rolla, Rolla, Mo. 65401.
[2]Asst. Sr. Engr., Mobil Research and Development Corp. Dallas, Texas.

Note.—Discussion open until April 1, 1982. To extend the closing date one month, a written request must be filed with the Manager of Technical and Professional Publications, ASCE. Manuscript was submitted for review for possible publication on October 8, 1980. This paper is part of the Journal of the Structural Division, Proceedings of the American Society of Civil Engineers, ©ASCE, Vol. 107, No. ST11, November, 1981. ISSN 0044-8001/81/0011-2111/$01.00.

Because of the increased usage of bridge structures supported by flexible substructures, and the concern of design engineers regarding bridge behavior and induced stresses associated with bridges of this type, a study was conducted at the University of Missouri-Rolla to explore the feasibility of developing rational design criteria for bridges with semi-integral end bents. It was concluded that development of rational design criteria for bridges with semi-integral end bents is feasible, but the anticipated cost precluded continuation of subsequent phases to fruition as desired (6). However, subsequent rigorous studies (7,8,16,17) investigated thermally-induced stresses from a theoretical standpoint. A later investigation correlated experimental results obtained from a model test structure subjected to thermal loading with calculated values obtained from the theoretical approach, and provided substantiative data toward acceptance of the theoretical procedure in the development of rational design criteria (9,30).

This study and a current on-going study were initiated to extend the areas of experimental-theoretical correlation, utilizing the test structure of the prior investigation. The objective of this study was to develop correlative experimental-theoretical data on the combined effect of approach slab thrust and thermal loading by: (1) Restraining the abutments of the two-span laboratory test structure with tie rods, simulating approach slab thrust; (2) subjecting the structure to thermal loading; and (3) correlating the experimental results with calculated values obtained by utilizing the theoretical study.

Test Structure

The test structure utilized was a 45 in. (114 cm) wide by 15 ft–15 ft (4.6 m–4.6 m) two-span continuous composite-design bridge constructed for a prior investigation conducted in the Civil Engineering Structural Laboratory of the Engineering Research Laboratory, University of Missouri-Rolla (9,30). A curved steel plate and pintle bearing was used at the pier, and integral abutments were used at the ends. The structure was designed and constructed as an adequate rather than true model.

The abutment assembly consisted of a 6 in. × 1/2 in. (152 mm × 13 mm) steel-plate pile cap welded to three 5 in. × 1/2 in. × 72 in. (130 mm × 13 mm × 1,830 mm) steel-bar piles buried 66 in. (1,680 mm) in a 7 ft × 3 ft × 6 ft (2.1 m × 0.9 m × 1.8 m) sandbox of uniform density. As the steel pile cap was bolted to the substructure stringers, the abutment assembly simulated an integral stub abutment with flexible piling.

The pier group was composed of three 2 in. (51 mm) diameter by 76 1/2 in. (1,930 mm) long standard pipe sections spaced 20 in. (510 mm) on center and welded to a 12 in. × 1/2 in. (305 mm × 13 mm) base plate anchored to the floor. A 6 in. × 1/2 in. (152 mm × 13 mm) plate was used as a pier cap. The pier simulated a cantilever beam fixed to the existing floor. The cantilever simulation for the pier agrees with the fact that in the field most piers have a relative point of fixity and the portion above this point acts as a cantilever.

The superstructure was composed of three M6 × 4.4 steel stringers spaced 20 in. (510 mm) on center, with a 1.5 in. (38 mm) thick reinforced concrete deck. Ten sets of C4 × 5.4 channels were used for the diaphragms, as shown in Fig. 1. Shear connectors consisted of 3/8 in. (10 mm) diameter by 7/8 in. (22 mm) studs spaced at 4 in. (102 mm) on center, except for high tensile zones.

The reinforced concrete deck was limited to a depth of 1.5 in. (38 mm) to prevent the deck from becoming too stiff in relation to the stringers. Two layers of 16-gauge 2 5/8 in. (68 mm) longitudinal by 2 in. (51 mm) transverse galvanized welded wire mesh were selected for the reinforcement. The top layer of mesh was positioned 1/4 in. (6 mm) from the top of the finished deck, and the lower layer was set 1 1/4 in. (32 mm) from the top of the deck.

The concrete mix was composed of 20.6 lbf (91.7 N) water, 34.6 lbf (154 N) cement, 68.0 lbf (303 N) sand, 68.0 lbf (303 N) (3/8 in. (10 mm) nominal maximum size) crushed limestone, and 4 cc of air entraining agent. The concrete had a 28 day compressive strength of 4,400 psi (30,316 kPa) and an air content of 5 1/2 ± 1 1/2%.

Four 1 1/4 in. (32 mm) diameter by 30 ft (9.1 m) long steel rods were used to simulate approach slab thrust on the abutments. These rods were anchored by four 1 1/2 in. (38 mm) diameter by 6 in. (152 mm) long tubes welded to the abutment caps at 15 in. (381 mm) centers. The dead load of the rods was

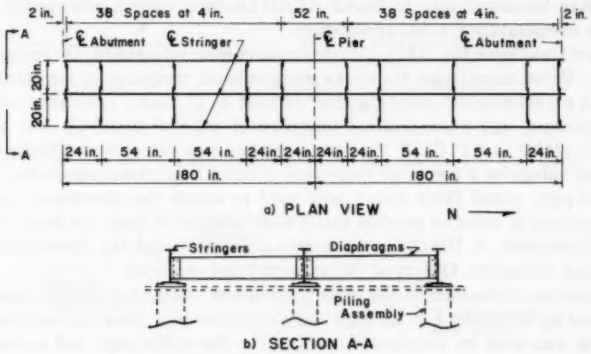

FIG. 1.—Steel Layout (1 in. = 25.4 mm)

supported by two wooden supports at the third points of the rods. To assure uniform seating and symmetrical loading from the rods, the rods were uniformly pretensioned to a specified force. The rods were threaded at the ends and thus pretensioned by sequential nut tightening immediately prior to each load sequence.

Instrumentation

Instrumentation was installed to record temperatures, strains, and displacements at selected points on the structure. To achieve this, thermistors, electrical resistance strain gages, and dial indicators were used. Data recording equipment consisted of four 10-channel Automation Industries Model SB-1 switch and balance units connected to an Automation Industries Model P-350 strain indicator, a 10-channel Baldwin-Lima-Hamilton Model 225 switch and balance unit connected to a Baldwin-Lima-Hamilton Model 120C strain indicator, an 8-channel Strain

Sert switch, balance, and strain indicator, and a 100-channel thermistor stepping unit connected to a digital voltmeter (Dana Model 5400).

Two types of carbon-steel temperature-compensated SR-4 strain gages were used. The first type was Micro-Strain Model 6C-2 × 2-120 w/1 with a gage factor of 2.05, resistance of 120 ohms, grid size of 1/4 in. × 1/4 in. (6.4 mm × 6.4 mm) and an overall size of 3/8 in. by 5/16 in. (9.5 mm × 7.9 mm). The second type of strain gages was Baldwin-Lima-Hamilton Model FAE-25-12-56EWL with a gage factor of 2.06, resistance of 120 ohms, grid size of 1/8 in. × 9/32 in. (3.2 mm × 7.1 mm), and an overall size of 9/16 in. × 1/4 in. (14.3 mm × 6.4 mm). The Micro-Strain gages were used on the bridge structure, while the BLH gages were used on the rods connecting the abutments.

The adhesive used for the Micro-Strain gages was Micro-Measurements M-Brand AE-15 two-part epoxy. This epoxy exhibits essentially creep-free performance up to 200° F (93° C) when cured at temperatures 25° F (4° C) greater than maximum operating temperatures. The adhesive used for the BLH gages was Micro-Measurements M-Brand AE-10 two-part epoxy, adequately cured at room temperature for this application.

Fenwal Uni-Curve No. UUA 33J1 thermistors were selected for the temperature sensors. These thermistors are epoxy encapsulated, temperature sensitive resistors with a maximum spherical diameter of 0.095 in. (2.4 mm), resistance tolerance of ±1 percent, and a temperature tolerance of ±0.4° F (0.22° C) over a range of 30° F–175° F (−1.1° C–79° C). Actual temperature values were obtained from observed values by a computer reduction utilizing logarithmic equations.

A two-part, metal filled epoxy was used to attach the thermistors to their base locations in order to provide better heat conduction from the base material to the thermistor. A 100-channel stepping unit interfaced the thermistor leads to a digital voltmeter. Observed values were hand-recorded.

Transducers embedded in the deck to measure strain and temperature were fabricated by mounting a strain gage and thermistor to a glass microscope slide. Beeswax was used to waterproof and protect the strain gage and a two-part, steel-filled epoxy was used to attach the thermistor to the slide. The 1 in. × 3 in. × 1/10 in. (25 mm × 76 mm × 2.5 mm) glass slides, with a coefficient of linear thermal expansion of 5×10^{-6}/°F (9×10^{-6}/°C), a thermal conductivity of 0.53 BTU/hr-ft-°F (0.92 W-m-°C), and a Young's Modulus of 10,300,000 psi (71,000,000 kPa), were selected because of the similarity of their thermal conductivity and coefficient of thermal expansion to that of the concrete. Slots were cut in the sides of the slides to provide a better mechanical bond to the deck concrete.

For confirmation of uniaxial stress and a uniform temperature gradient, four strain gages, equally spaced around the perimeter, and two thermistors, at the top and bottom surfaces, were mounted to each abutment tie-rod.

The total longitudinal deck deflection and the vertical deflection at the midspans were recorded by using dial indicators with a least count of 0.001 in. (0.025 mm). The indicators for vertical deflection were mounted on wooden standards, whereas the indicators at the abutments were attached to metal channels that were rigidly attached to the sandbox frame.

Instrumentation Orientation.—Five locations were chosen for the placement of the transducer groups, as shown in Fig. 2. Two groups were distributed

through the deck midway between the stringers, and the other three groups were placed on and immediately over the center stringer. Both thermistors and strain gages were used in each group. Slab transducers consisted of a glass microscope slide, strain gage, and thermistor as shown in Fig. 3.

Induced strains were read at the top, bottom, and four intermediate points of the slab and at the top and bottom of the stringer at Locations 2, 3, and 4. At Locations 1 and 5, midway between the center and outside stringers, slab transducers were placed in 4 in. (101 mm) wide by 9 in. (229 mm) long cantilever temperature-reference bars enclosed on the two sides and the end by 1/2 in. (13 mm) thick flexible styrofoam. Wire mesh was omitted in these bars so that the concrete could expand freely under unrestrained thermal

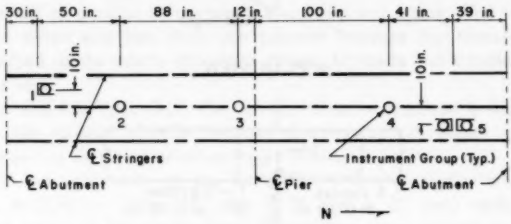

FIG. 2.—Plan View of Deck Instrumentation Groups (1 in. = 25.4 mm)

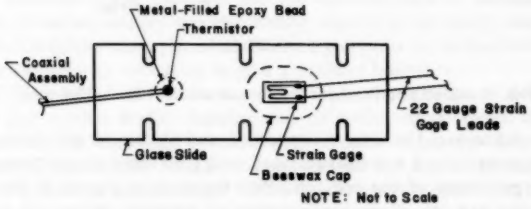

FIG. 3.—Slab Transducer

expansion. The styrofoam produced essentially no resistance to small expansive movements and provided insulation between the boundaries.

Instrumentation Locations 2, 3, and 4 were at sections along the center stringer. As noted previously, strain gages and thermistors were placed at six points vertically through the deck slab. The sixth, or lowest point, was the interface between the slab and the stringer, and at this point two gages and one thermistor were attached to the top of the stringer flange. Seven thermistors were evenly spaced down the stringer web, and two were attached to the bottom flange, one at the outer edge of the flange and the other directly beneath the web. Strain gages mounted on the top and bottom flanges were spaced 1/4 in. (6 mm) on each side of the centerline of the flange. A typical plan view and an elevation of this instrumentation are shown in Fig. 4. The slab transducers

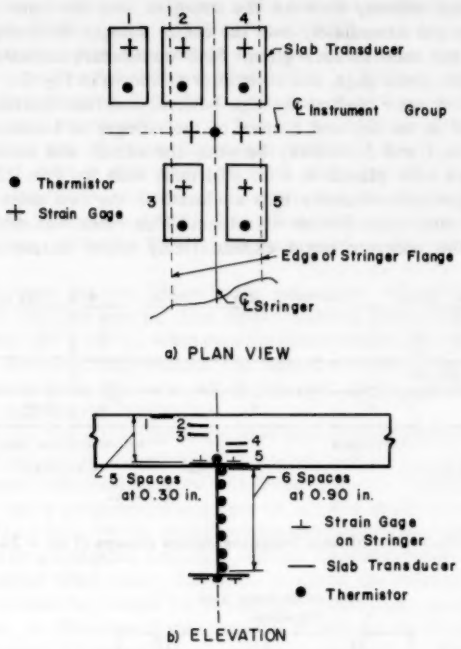

FIG. 4.—Slab and Stringer Instrumentation (1 in. = 25.4 mm)

were staggered to avoid excessive congestion and placement problems.

Each abutment tie-rod was instrumented with four strain gages placed equally around the perimeter of the rod, and two thermistors placed at the top and bottom of the rod, to allow confirmation of uniaxial stress and a uniform temperature gradient. This entire instrumentation group was placed 14 ft (4.3 m) from the north abutment of the bridge.

Dial indicators with a least count of 0.001 in. (0.025 mm) were used to measure the vertical deflection of the center stringer at midspans (Locations 2 and 4) and the longitudinal deck displacements at each abutment. The total deck movement at the bearing elevation was obtained by summing the abutment displacements.

Two thermistors were also positioned at 2 in. and 12 in. (51 mm and 305 mm) above the top of the deck and two at 12 in. and 30 in. (305 mm and 762 mm) below the deck to give an indication of the still air temperature and thermal gradients around the bridge.

TESTING

Heat Source.—Radiation heating from 120 General Electric model 250R40 (250 watt) infared reflector heat lamps was used to thermally load the test structure.

The lamps were placed in four rows along the length of the bridge and were spaced 12 in. (305 mm) center-to-center both longitudinally and transversely for uniformity of approximately 150° F (65.6° C). Alternate rows were staggered 6 in. (152 mm) to provide a more uniform radiation level. The bulb faces were placed 20 in. (508 mm) above the deck in accordance with the manufacturer's recommendation that the distance of the lamp from the heated subject be at least 1.6 times the lamp spacing for uniform radiation distribution. Radiation heating was chosen rather than a constant temperature source, because it was simpler and approximated actual field conditions imposed by the sun.

The lamps were divided into five circuits, each with a 240-volt Variac transformer to vary the thermal loading. The 115-volt lamps were connected in series by pairs to split the 240-volt transformer output. These pairs were then connected in parallel to complete a transformer string. The voltage drop through the wires was less than one percent because the transformer leads were connected to the center of a bulb string. All leads and couplers consisted of 12-gauge wire.

to obtain uniform heat flux, the outside circuits required a higher voltage input than the interior circuits because the overlap of radiant energy along the edges was not as pronounced as in the center.

To check the uniformity of the heat flux, a heat receptor was fabricated of a 5 in. × 3 in. × 1 in. (127 mm × 76 mm × 25 mm) carbon steel bar painted flat black on the upper face. Thermistors were placed on both faces, and the bar was encased in styrofoam to prevent the loss of heat from the sides and to limit the convection to the top and bottom surfaces. The painted side was exposed to the radiation and the opposite face to ambient air. The uniformity of radiant energy was checked by observing the steady state temperatures of the receptors when placed at different points on the bridge deck. Voltages were then adjusted as necessary to give a uniform heat flux.

Testing Procedure.—Before each testing cycle, the laboratory was sealed to eliminate any outside drafts—heating and air return ducts sealed, door cracks taped, and outside openings covered with plastic. Thus, the only source of forced convection would be air currents caused by either thermal gradients above and below the test structure which develop into a cyclic draft as a result of the laboratory's high ceiling, or by cross currents which develop between the warm and cool ends of the large laboratory.

A test cycle then consisted of the following sequential steps:

1. All strain gages and dial indicators were "zeroed," and the bridge and ambient air thermistor readings recorded for use as the reference temperatures at zero strain.

2. Each of the four rods was tensioned to a uniform tensile strain equal to the thermal elongation which would result solely from the temperature change of the rods during the test, and strain gage readings recorded for possible future reference. The force in the rods initially varied during the test, decreasing as the shaded rods elongated when their temperature increased, increasing as a result of the larger differential movement of the superstructure (subjected to a greater heat flux), and eventually reaching a constant force under steady-state gradients. The computer program for calculation of the theoretical values could accommodate the elastic spring modulus of the tie rods, but not the simultaneous

action of the thermal-variable prestress force. By equating the initial strain with the thermal strain, a uniform initial seating rod-force could be applied, and the resultant structural response of the restrained test structure to thermal loading could be obtained from the original (Step 1) and the final steady state conditions.

3. The transformers were turned on and each circuit adjusted until a uniform heat flux was produced on the deck. Uniformity was checked by observing the temperature gradients of the receptors when placed at different locations on the bridge deck.

4. When steady state temperatures were achieved after approximately ten hours of heating, strain gage, thermistor, and dial indicator readings were hand-recorded. Recorded values included longitudinal strains and temperatures at previously described points on the stringer and in the slab, strains at the base of the pier to determine any lateral movement at the top of the pier, lateral displacements at the abutments, vertical displacements at the midspans, and ambient temperatures above and below the deck.

5. After all data were recorded, the heat lamps were turned off, the rods were loosened, the structure was allowed to cool to room temperature, and strain, thermistor, and dial indicator readings were recorded for comparison of cyclic action and instrumentation drift.

Data Reduction

Temperature.—Conversion of thermistor readings to temperature would be generally accomplished by the use of a manufacturer supplied ohm–°C conversion graph or table. In this instance, the internal resistance of the 100-channel stepping unit, needed to interface the large number of thermistors, precluded the reading of thermistor output in ohms. Thus, the output was read in millivolts, equations were developed for ohm-°C conversion at 20° F (11° C) temperature increment ranges, and a computer program was written and used for conversion of millivolts to ohms, ohms to °C, and °C to °F.

Strain.—Reduction of observed data obtained from the carbon-steel, temperature-compensated SR-4 strain gages required correction for apparent strain, self-temperature-compensation (STC) mismatch, and compensated (nonindicated) thermal strain.

Theoretically, a steel-temperature-compensated gage attached to an unrestrained steel specimen should indicate no strain when subjected to a temperature change (20,21). However, changes in the electrical resistance properties of the gage, caused by external temperature change, internal heating, and small differences in material between the gage and specimen, will produce an indicated apparent strain. The electrical resistance-apparent strain relationship is shown on graphs furnished by the gage manufacturer for data reduction.

STC mismatch is the indicated thermal strain produced by the difference in thermal coefficients of expansion when a self-temperature-compensated gage is mounted on an unrestrained specimen having a thermal coefficient of expansion other than that for which the gage is compensated.

Compensated, or nonindicated, thermal strain is the unit thermal strain which would be induced in an unrestrained specimen subjected to a temperature change, i.e., $\alpha \cdot \Delta Y$, the product of the thermal coefficient of expansion and the change in temperature.

Also included in the observed (indicated) strain is the effect of any restraint to free movement of the specimen. The combination of apparent strain, STC mismatch, and compensated strain, coupled with varying degrees of restraint, combine to provide solutions to such problems as: (1) The experimental determination of the coefficient of thermal expansion (1,20,21); (2) The determination of strain without stress (unrestrained movement, but very little observed (indicated) strain); (3) stress without strain (totally restrained movement, but a large amount of observed (indicated) strain); and (4) stress induced by partial restraint. It should be noted that one may find the term "apparent strain" used to express any or all of the terms discussed above.

A computer program was developed and used for conversion of observed, as recorded, strain to actual, thermally induced, strain. Initial and final dial indicator readings were reduced and combined to provide point deflections and overall structural movement.

Results of Experimental Investigation

Temperature Distribution.—Consistent, repeated-test results were obtained. Temperature profiles fell with a 6° F (3.3° C) band as shown in the typical

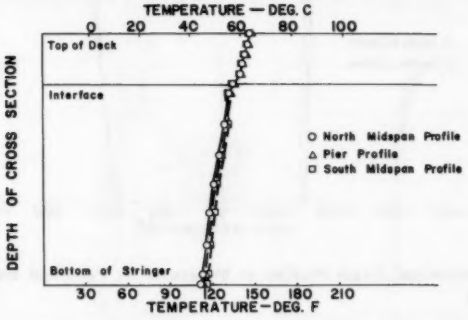

FIG. 5.—Experimental Temperature Profiles

experimental profiles of Fig. 5. The difference between the north and south midspan profiles was less than 1° F (0.6° C). These profiles were used as input for computer calculation of theoretical strains. As shown in Fig. 5, the temperature varied from 147° F (64° C) at the top surface of the deck, to 125° F (52° C) at the bottom of the deck, and 111° F (44° C) at the bottom flange of the stringer.

Ambient temperatures were 114° F (46° C) and 111° F (44° C) at 2 in. (51 mm), and 12 in. (305 mm), respectively, above the deck surface. Below the deck, ambient temperatures were 85° F (29° C) at 12 in. (305 mm) and 84° F (29° C) at 30 in. (762 mm). Ambient temperatures greatly affect temperature profiles. On a still day, the ambient air temperature lies somewhere between the surface temperature of the deck and the temperature at some distance away

from the structure. In the laboratory, with the deck surface 60° F–80° F (33° C–44° C) warmer than the air at some distance away from the structure, the ambient air temperature above the deck was approximately the average of the surface temperature and that of the surrounding air, and the ambient temperature beneath the deck was 15° F–20° F (8° C–11° C) above that of the surrounding air.

Strain Distribution.—As previously discussed, the observed strains included apparent strain, STC mismatch, and the effect of tie-rod, abutment, and pier restraints. The apparent strain correction is a function of temperature, and is usually assumed to be a linear function within certain temperature ranges. For the tie-rod gages, the correction ranged from zero at 75° F (24° C) to −65 micro strain at 150° F (66° C). The apparent strain correction for all the other gages ranged from zero at 100° F (38° C) to −100 micro strain at 200° F (93° C). A computer program was developed for reduction of the observed strain to actual thermally-induced strain, taking into account the apparent strain, STC mismatch, nonindicated compensated strain, and resistance effect.

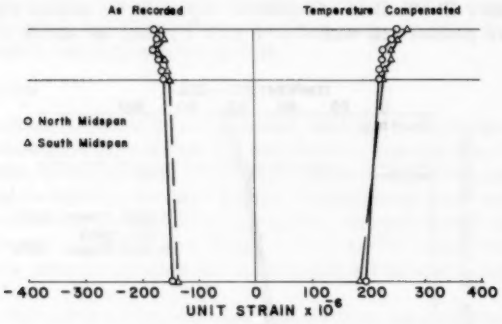

FIG. 6.—Experimental Strain Profiles at Midspans, as Recorded and Temperature Compensated

Strains for repeated tests fell within a narrow band width, similar to that for the temperature profiles. The slight difference between the north and south midspan strains is shown in Fig. 6.

As in the prior study (9,30), some consistent erratic strains were apparent in the slab. Data obtained from instrument Group 3, located 12 in. (305 mm) south of the pier, were not plotted because several gages were unstable or inoperative.

The strain profiles show negative curvature (lengthening of top deck fibers greater than of bottom flange fibers) at the midspan locations, and valid data from instrument Group 3 indicate positive curvature at the pier. These relationships are compatible with the temperature profiles (the top of the section warmer than the bottom) and the superposition of abutment-slab thrust.

There was no differential strain at the base of the pier, which indicates that no longitudinal displacement occured at the bearing elevation of the pier, thus resulting in symmetrical longitudinal displacements about the center of the

structure. This symmetrical action was substantiated by the dial indicator readings of 0.04 in. (1.02 mm) at each abutment that were virtually identical for each test.

From the data obtained from the cantilever sections of instrument groups 1 and 5, the coefficient of thermal expansion of the concrete was determined to be 4.1×10^{-6}/°F (7.4×10^{-6}/°C). The change in value from 3.5×10^{-6}/°F (6.3×10^{-6}/°C), as determined in the prior investigation, reflects the age effect (approximately 4 yr) and other factors influencing the thermal coefficient of expansion (1,20).

TABLE 1.—Material Properties

Property (1)	Value	
	Steel (2)	Concrete (3)
Young's modulus	29.0×10^6 psi (20.0×10^7 kPa)	4.5×10^6 psi (3.1×10^7 kPa)
Poisson's ratio	0.3	0.18
Coefficient of thermal expansion	6.5×10^{-6}/°F (11.7×10^{-6}/°C)	4.1×10^{-6}/°F (7.4×10^{-6}/°C)

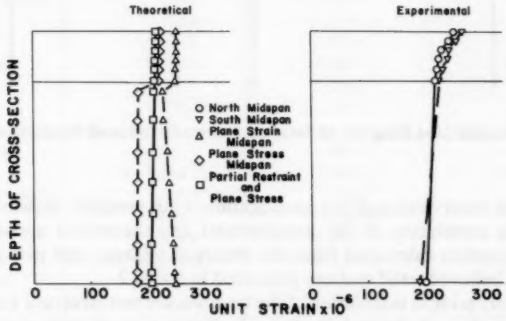

FIG. 7.—Theoretical and Experimental Strain Profiles at Midspans

The experimental temperature profiles were used with the previously described procedure of Emanuel and Hulsey (7), and the computer program developed by Hulsey (16), to obtain the theoretical strains and stresses. The material properties shown in Table 1 were used to calculate the theoretical values of Fig. 7.

The theoretical and corrected experimental midspan strains are compared in Fig. 7. As in the prior theoretical (16) and experimental (9,10,30) studies, three theoretical cases were analyzed: (1) Both the slab and the beam in plane stress; (2) the slab in plane strain and the beam in plane stress; and (3) the slab in some state between plane stress and plane strain (partially restrained), and the beam in plane stress.

For the slab, the closest agreement between experimental and theoretical strains is for Case b, the slab in plane strain and the beam in plane stress; whereas for the beam, the closest agreement is for Case c, the slab in some state between plane stress and plane strain (partially restrained) and the beam in plane stress.

The observed theoretical vertical deflection at midspans, and the horizontal deflections at the abutments were in reasonable agreement, i.e., within 15%. The observed values were slightly larger than the theoretical values for the vertical deflections, and slightly lower for the horizontal deflections. Part of this difference may be explained by the fact that in the theoretical modeling of the bridge, the pier was assumed to resist uplift of the superstructure. Although there was no measurable vertical deflection at the pier, the curved steel rocker and pintle provided no upward restraint. Also, the negative moment induced at the abutments by the tie-rods increased the negative chamber at the midspans, and may have offset some dead load deflection at the pier. A distorted line diagram of superstructure deformation is shown in Fig. 8.

The theoretical procedure uses the interaction of longitudinal, transverse, and vertical strains, and Poisson's ratio in determination of stress, of which longitudinal strain is the major parameter. Thus, a prediction of stress based on the

FIG. 8.—Distorted Line Diagram of Relative Thermally Induced Superstructure Deflections

experimental observations of the investigation is not possible. However, because of the close correlation of the experimental and theoretical midspan strains, theoretical stresses calculated from the observed midspan and pier temperature profiles are believed valid and are presented in Table 2.

Immediately prior to installation of the tie-rods, the test structure was subjected to several cycles of thermal loading, duplicating as closely as possible the maximum power level of the prior study (30), and the experimental data recorded. This provided a data bank for comparison of the effect of the tie-rods in this study, and the effect of the change in modulus of elasticity and coefficient of thermal expansion from those of the prior study. Again, because of the close correlation of the theoretical and experimental (corrected) strains, comparison of theoretical stresses is believed valid.

With the tie-rods in place, the compressive stress at the top of the deck for Cases *a*, *b*, and *c* ranged from 1.7–3.5 times the no-tie-rod condition at both the pier and midspans. The compressive stress at the top of the stringer increased by a factor of approximately 1.4, and the tensile stress at the bottom of the stringer decreased by a factor of approximately 2.3.

As compared with the prior study, having a smaller modulus of elasticity and thermal coefficient of expansion, the compressive stress in the concrete

at the top of the deck (no-tie-rod condition) increased by a factor of approximately 2.5 and the concrete stress at the bottom of the deck doubled. The compressive stress at the top of the stringer and the tensile stress at the bottom of the stringer each decreased, by a factor of approximately 1.7 and 1.1 to 1.4, respectively.

As discussed in the prior study, integral abutments, as contrasted with roller supports, introduce the following effects: As the substructure stiffness increases, changes in the longitudinal stress patterns result from the interaction of axial (P/A) and flexural (My/I) stresses produced by the resistance to movement at the abutments. At midspans, the primary influence is an My/I superposition

TABLE 2.—Theoretical Stresses

Location (1)	Case *a*, in pounds per square inch (kilopascals) (2)	Case *b*, in pounds per square inch (kilopascals) (3)	Case *c*, in pounds per square inch (kilopascals) (4)
Midspans			
Top of slab	−177.7	−275.6[a]	−257.9
	(−1,224.4)	(−1,898.9)	(−1,776.9)
Bottom of slab	26.5[b]	−28.9[b]	89.5[a]
	(182.6)	(−199.1)	(616.7)
Top of stringer	−3,525.0	−2,772.0	−4,192.0[a]
	(−24,287.3)	(−19,099.1)	(−28,882.9)
Bottom of stringer	−155.9	1,821.0[a]	597.0
	(−1,074.2)	(12,546.7)	(4,113.3)
Pier			
Top of slab	−195.1	−297.0[a]	−281.1
	(−1,344.2)	(−2,046.3)	(−1,936.8)
Bottom of slab	25.9[b]	−29.7[b]	88.7[a]
	(178.5)	(−204.6)	(611.1)
Top of stringer	−3,529.0	−2,777.0	−4,198.0[a]
	(−24,314.8)	(−19,133.5)	(−28,924.2)
Bottom of stringer	270.6	2,374.0[a]	1,167.0
	(1,864.4)	(16,356.9)	(8,040.0)

[a]Maximum of the three cases.
[b]Magnitude too small to be significant.

from a moment that induces positive curvature, caused by the resistance of the abutment (piling) to rotation of the superstructure.

In this study, the approach slab (tie-rod) thrust, being below the neutral axis of the composite section, induced an My/I negative curvature superposition. However, because of the proximity of the neutral surface to the deck slab, the compressive P/A stress, being greater than the negative My/I curvature effect on the slab, produced a resultant compressive increase at the top of the deck at the midspans. At the bottom of the stringers, the P/A and My/I stresses, both being compressive stresses, were additive, producing a decrease of tensile stresses at the midspans and pier.

Conclusions

Based on the correlation of consistent experimental readings and calculated theoretical values, the following conclusions were reached:

1. The theoretical procedure is adequate for a reasonable prediction of abutment-thermal interaction of composite-girder bridge structures subjected to thermal loading.
2. The theoretical longitudinal curvature is somewhat smaller than that observed. This is believed to be a result of the assumption that there is no vertical deflection of the abutments or pier.
3. The observed and theoretical longitudinal strain are in reasonable agreement. Resultant stresses in the test structure, which are functions of longitudinal, transverse, and vertical strains, can be expected to parallel the theoretical values.
4. For the slab, the closest agreement between experimental and theoretical strains is for Case b, the slab in plane strain and the beam in plane stress; whereas for the beam, the closest agreement is for Case c, the slab in some state between plane stress and plane strain (partially restrained) and the beam in plane stress.
5. The interaction of externally applied abutment forces may increase thermally-induced stresses in the slab and stringer by a significant amount, in this instance up to 9% of the allowable compressive stress in the concrete and up to 19% of the allowable compressive stress in the steel at the midspans.

Further substantiation and modification from field testing of prototype structure to develop rational design criteria for thermal behavior are desirable and feasible.

Recommendations for Further Study

During the course of any investigation, questions arise as the result of the research. Some of these questions are resolved, but many are beyond the scope of the study and remain unanswered. The following topics could be of immediate practical value to the development of rational design procedure that would account for thermal behavior of bridge structures and should be explored:

1. Development of a theoretical program capable of taking into account the interaction of bridge weight and upward movement of the piers.
2. Cyclic cooling of the bridge deck to well below freezing temperatures.
3. A study of the effect of diaphragm and beam-slab action on differential stringer deflection and torsional stringer rotation.
4. A study of the effect of shear connector continuity, or discontinuity on beam-slab interaction, or both.
5. Correlation of experimental laboratory and field prototype temperature profiles.
6. A determination of the thermal coefficient of expansion of reinforced concrete bridge decks, based on the percentage of reinforcing steel.
7. A study of the probabilistic combinations of loading, including environmental loadings, and their relative effect on structural behavior.

Other studies of value to bridge engineers and those in related fields were suggested in the prior studies (9,10,16,30).

Appendix I.—References

1. Berwanger, C., and Sarkar, A. F., "Effect of Temperature and Age on Thermal Expansion and Modulus of Elasticity of Concrete," *Behavior of Concrete Under Temperature Extremes*, American Concrete Inst. Special Publication SP-39, 1973, pp. 1–22.
2. Berwanger, C., and Symko, Y., "Thermal Stresses in Steel-Concrete Composite Bridges," *Canadian Journal of Civil Engineering*, Vol. 2, No. 1, 1975, pp. 66–84.
3. Berwanger, C., and Symko, Y., "Finite-Element Solutions for Thermal Stresses in Steel-Concrete Composite Bridges," *Experimental Mechanics*, Vol. 16, No. 5, May, 1976, pp. 168–175.
4. Black, W., Moss, D. S., and Emerson, M., "Bridge Temperatures Derived from Measurement of Movement," *TRRL Report LR 748*, Transport and Road Research Lab., Crowthorne, Berkshire, England, 1976.
5. Ekberg, C. E., and Emanuel, J. H., "Problems of Bridge Supporting and Expansion Devices and an Experimental Comparison of the Dynamic Behavior of Rigid and Elastomeric Bearings," *Final Report, Project 574-S*, Engineering Research Inst., Iowa State Univ., Ames, Iowa, Aug., 1967.
6. Emanuel, J. H., et al., "An Investigation of Design Criteria for Stresses Induced by Semi-Integral End Bents: Phase I—Feasibility Study," *Missouri Cooperative Highway Research Program Final Report 72-9*, University of Missouri-Rolla, Rolla, Mo., 1973.
7. Emanuel, J. H., and Hulsey, J. L., "Thermal Stresses and Deformations in Nonprismatic Indeterminate Composite Bridges," *Transportation Research Record 607*, Transportation Research Board, National Academy of Sciences, Washington, D.C., 1976, pp. 4–6.
8. Emanuel, J. H., and Hulsey, J. L., "Temperature Distribution in Composite Bridges," *Journal of the Structural Division*, ASCE, Vol. 104, No. ST1, Proc. Paper 13474, Jan., 1978, pp. 65–78.
9. Emanuel, J. H., and Wisch, D. J., "Thermal Stresses Induced in a Composite Model Bridge Structure," *Missouri Cooperative Highway Research Program Final Report 75-2*, Univ. of Missouri-Rolla, Rolla, Mo., 1977.
10. Emanuel, J. H., and Wisch, D. J., "Thermal Response of a Continuous Two-Span Composite Bridge Structure," *Transportation Research Record 711*, Transportation Research Board, National Academy of Sciences, Washington, D.C., 1979, pp. 40–46.
11. Emerson, M., "The Calculation of the Distribution of Temperature in Bridges," *TRRL Report LR 561*, Transport and Road Research Lab., Crowthorne, Berkshire, England, 1973.
12. Emerson, M., "Extreme Values of Bridge Temperatures for Design Purposes," *TRRL Report LR 744*, Transport and Road Research Lab., Crowthorne, Berkshire, England, 1976.
13. Emerson, M., "Temperature Differences in Bridges: Basis of Design Requirements," *TRRL Report LR 765*, Transport and Road Research Lab., Crowthorne, Berkshire, England, 1977.
14. Emerson, M., "Temperature in Bridges During the Hot Summer of 1976," *TRRL Report LR 783*, Transport and Road Research Lab., Crowthorne, Berkshire, England, 1977.
15. Hambly, E. C., "Temperature Distributions and Stresses in Concrete Bridges," *Structural Engineering*, Vol. 56A, No. 5, May, 1978, pp. 143–148.
16. Hulsey, J. L., "Environmental Effects on Composite-Girder Bridge Structures," thesis presented to the University of Missouri-Rolla, at Rolla, Mo., in 1976, in partial fulfillment of the requirements for the degree of Doctor of Philosophy.
17. Hulsey, J. L., and Emanuel, J. H., "Finite Element Modeling of Climatically Induced Heat Flow," Numerical Methods for Differential Equations and Simulation, Bennett, A. W., and Vichnevetsky, R., eds., North-Holland, Amsterdam, 1978, pp. 111–114.

18. Hunt, B., and Cooke, N., "Thermal Calculations for Bridge Design," *Journal of the Structural Division*, ASCE, Vol. 101, No. 9, Sept., 1975, pp. 1763–1781.
19. Lanigan, A. G., "The Temperature Response of Concrete Box Girder Bridges," *Report No. 94*, School of Engineering, thesis presented to the University of Auckland, at Auckland, New Zealand, in 1973, in partial fulfillment of the requirements for the degree of Doctor of Philosophy.
20. Lewis, D. B., "Abutment-Thermal Interaction of a Composite Bridge," thesis presented to the University of Missouri-Rolla at Rolla, Mo., in 1980, in partial fulfillment of the requirements for the degree of Master of Science.
21. Micro-Measurements Division, Measurements Group, "Temperature-Induced Apparent Strain and Gage Factor Variation in Strain Gages," *Tech Note TN-128-3*, Raleigh, N.C., 1976.
22. Priestly, M. J. N., "Design Thermal Gradients for Concrete Bridges," *New Zealand Engineering*, Vol. 31, No. 9, Sept., 1976, pp. 213–219.
23. Priestly, M. J. N., "Design of Concrete Bridges for Temperature Gradients," *Journal of the American Concrete Institute*, Vol. 75, No. 5, May, 1978, pp. 209–217.
24. Radolli, M., and Green, R., "Thermal Stresses in Concrete Bridge Superstructures under Summer Conditions," *Transportation Research Record 547*, Transportation Research Board, National Academy of Sciences, Washington, D.C., 1975, pp. 23–26.
25. Rahman, F., and George, K. P., "Thermal Stress Analysis of Continuous Skew Bridge," *Journal of the Structural Division*, ASCE, Vol. 105, No. ST7, July, 1979, pp. 1525–1541.
26. Rambhai, P., "Thermal Effects in Concrete Box Girder Bridges," *School of Engineering Report No. 139*, Univ. of Auckland, Auckland, New Zealand, 1976.
27. Reynolds, J. D., and Emanuel, J. H., "Thermal Stresses and Movements in Bridges," *Journal of the Structural Division*, ASCE, Vol. 100, No. ST1, Proc. Paper 10275, Jan., 1974, pp. 63–78.
28. Thurston, S. J., "Thermal Stresses in Concrete Structures," *Research Report No. 78-21*, Civil Engineering, thesis presented to the University of Canterbury, at Christchurch, New Zealand, in 1978, in partial fulfillment of the requirements for the degree of Doctor of Philosophy.
29. Wah, T., and Kirksey, R., "Thermal Characteristics of Highway Bridges," *Highway Research Board Final Report, SWRI Project No. 03-1835*, Highway Research Board, National Academy of Sciences, Washington, D.C., 1969.
30. Wisch, D. J., "Thermal Stresses Induced in a Model Composite Bridge Structure," thesis presented to the University of Missouri-Rolla, at Rolla, Mo., in 1977, in partial fulfillment of the requirements for the degree of Master of Science.
31. Zuk, W., "Thermal and Shrinkage Stresses in Composite Beams," *Journal of the American Concrete Institute*, Vol. 58, No. 3, Sept., 1961, pp. 327–340.

FLOATING BRIDGE DRAWSPAN MAINTENANCE

By Colin B. Brown,[1] M. ASCE, Derald R. Christensen,[2]
John W. Heavner,[3] Michael A. Landy,[4]
and Ramiah Vasu[5]

Floating bridges prove to be attractive structures for long, deep-water crossings. A drawspan device is often necessary to allow the transit of large ships. The mechanical features of such drawspans suffer cumulative damage in storms which may lead to failure. An example of this situation is the four-lane Evergreen Point Bridge across Lake Washington. Much of its 7,518 ft (2,293 m) length is a floating structure pierced by a 200 ft (61 m) drawspan, as shown in Figs. 1 and 2. In order to maintain a straight road alignment, the drawspan is opened by the vertical lift of the side span (7 in Fig. 3), and the longitudinal motion of the drawspan (8 and 9 in Fig. 3) into the vacated space. Fig. 4 is a view of this process. These motions are controlled by trunnions, and a closed pontoon is ensured by locks. It is these trunnions and locks, together with their holding devices, that suffer damage in storms such as the one shown in Fig. 5.

This paper reports the 6 yr study of the mechanical features of the Evergreen Point Bridge drawspan. In particular, the complete results for the vertical trunnion anchor rods provide examples for the establishment of a maintenance program and orderly changes in designed details. The report begins by identifying the structural parts involved and the design of the study, and then the field and laboratory experiments with their relevant analyses. These results lead to a prediction of structural life and a proposed maintenance program. The results also suggest detail changes in the trunnion rods. In the light of their experience with these original details, the Washington State Department of Transportation has made such changes. The redesigned members were also tested and the anticipated improvement in fatigue life is reported.

[1]Prof. of Civ. Engrg., Univ. of Washington, Seattle, Wash. 98195.
[2]Research Assoc., Dept. of Civ. Engrg., Univ. of Washington, Seattle, Wash.
[3]Research Asst., Dept. of Civ. Engrg., Univ. of Washington, Seattle, Wash.
[4]Aerospace Engr., Structures Div., ASD/ENF, Wright Paterson Air Force Base, Ohio.
[5]Research Asst., Orthopaedic Research Laboratories, Mass. General Hospital, Boston, Mass.

Note.—Discussion open until April 1, 1982. To extend the closing date one month, a written request must be filed with the Manager of Technical and Professional Publications, ASCE. Manuscript was submitted for review for possible publication on November 7, 1980. This paper is part of the Journal of the Structural Division, Proceedings of the American Society of Civil Engineers, ©ASCE, Vol. 107, No. ST11, November, 1981. ISSN 0044-8001/81/0011-2127/$01.00.

STRUCTURAL PARTS

Fig. 3 shows the moving parts of the drawspan. The operation requires the raising of two 105 ft (32 m) steel grid decks by 7.2 ft (2.2 m) to allow the longitudinal movement of drawspan pontoons into the vacated spaces. The lift

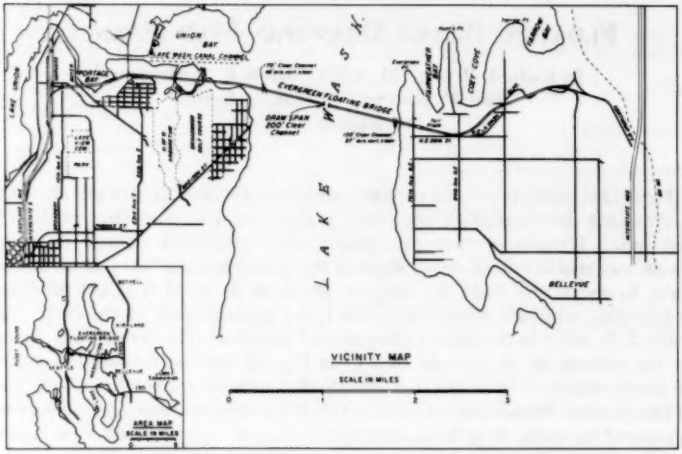

FIG. 1.—Location of Structure (Note: 1 mile = 1.61 km)

FIG. 2.—View along Bridge to West

mechanism is unaffected by wave battering on the bridge; the control mechanisms for the longitudinal movement do, however, suffer damage. The horizontal motion is induced by drive motors and controlled by guiding trunnions. These trunnions

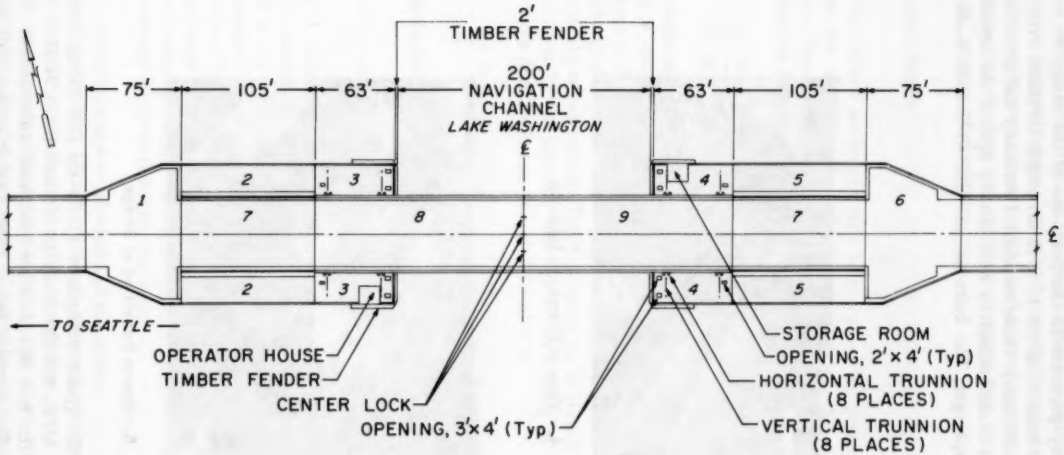

FIG. 3.—Plan View of Drawspan (Note: 1 ft = 0.305 m)

maintain longitudinal motions and restrain lateral and vertical ones. They consist of pairs of 18.125 in. (479 mm) radius cast steel rollers held in an equalizer frame which is secured by prestress to the pontoons of the bridge by 3 in. (76 mm) diameter anchor bolts of about 16 ft (5 m) length threaded over the end, 5 in.–12 in. (127 mm–305 mm). These are aligned vertically and prestressed in position. The prestress is maintained by nuts bearing against the equalizer frame and a pontoon diaphragm. The bolts are of AISI 4140 steel made to

FIG. 4.—View of Drawspan Opening

FIG. 5.—Storm Buffetting of Bridge

ASTM specification 193; B7 [yield strength = 111.74 ksi (770 MPa), tensile strength = 137.4 ksi (947 MPa), and the modulus of elasticity = 31.25×10^3 ksi (215 GPa)]. Initially, the bolt threads were machined; subsequently they were replaced with cold rolled threaded bolts. These twelve anchor rods were instrumented with gages to record the strains associated with relative vertical motions between the drawspan and the pontoon. At first, two diametrically

opposite gages were employed. Subsequently, as no significant bending was recorded, only one gage was employed.

As well as these vertical trunnion anchorage rods, the end and center locks, trunnion support beams, horizontal trunnion supports, and the floating section anchor cables were also examined, and extensive strain measurements completed. The locking devices and trunnion supports had previously been damaged by wave battering of the bridge.

Program Design

The broken anchorage rods were caused by progressive failure propagating from the valley of the thread and indicated that a fatigue study should be made. The resulting planning and design has revolved around Miner's hypothesis where the fatigue damage, D, is measured by the ratio

$$D = \sum_i \frac{n_i}{N_i} \quad \ldots \ldots \ldots

The N_i term in Eq. 3 requires laboratory measurements of actual structural elements. Only six such elements of each type were available and it was decided to use Basavaraju's and Lim's (1) modification of Prôt's (4) accelerated fatigue test procedure.

The availability of all the features of Eq. 3 allowed the fatigue life to be predicted and thus a maintenance program could be implemented. The use of Miner's hypothesis is essential in establishing Eq. 3, and in the use of Prôt's procedure for accelerated fatigue testing. Bright (2) has compared the hypothesis and criterion with other postulates for cumulative fatigue damage. He has concluded that, in the light of limited data, Miner's work is as valid as any other. Certainly, in the work presented here, the important data are limited and use of Miner's hypothesis and criterion appears justified.

Wind-Stress Relationship

The experimental arrangement for determining wind speed and direction and local stresses, involved extensive instrumentation. This centered around the recorder system, which was designed for this project. The recorder has 44 8-bit input channels and a 12-bit clock channel. The 8-bit shift registers have a maximum count of 256 (including the zero bit), which give a resolution of 1/256 of the maximum output allowed for in-calibration adjustment of each transducer. Each data sample (word) is made up of a 5-step gap, 2-step preamble, 91-step data block (2 steps per 8-bit register times 44 inputs, plus 3 steps for the clock), and a 1-step longitudinal character check. This provides a total of 99 4-bit steps for each sample (the recorder has 4 tracks and 4 bits are recorded for each 3.3 ms step), and is the maximum allowable word length. In this study, a discrete mode was used. For such a mode two channels were sampled twice a second, and for each start up of the recorder, 2,047 samples were taken. The individual records were 17 min long, giving 12 records for each cassette. The mode of operation required that the recorder was initiated when the wind speed reached a definite level of 20 mph (32.2 kmph). Sampling then continued for 1 min, and if the wind speed persisted at over 20 mph, the system was turned on and 2,047 samples taken. After one hour the wind speed was checked and if over 20 mph the process was repeated. This continued until the wind speed dropped below 20 mph.

The 44 channels were utilized as follows: two wind speed and direction (W1, W2); two wave pressure transducers (P1, P2); four anchor cambe displacements (A1–A4); 18 horizontal trunnion strains (1HL1–4HL1, 1HT1–4HT1, 3HL2, 4HL2, 3HT2, 4HT2, 3HRL1–3HRL3, 3HRT1–3HRT3); 12 vertical trunnion anchor rod strains (1V1–4V1, 1V2–4V2, 3V3, 3V4, 4V3, 4V4); three center lock strains (C1–C3); one end lock (L1); and two support beams of vertical trunnions strains (S1, S2). These are marked on Fig. 6.

Of critical importance in the study are the eight measurements at W1, W2 and 1V1–4V1, 3V3, and 4V3. These gave duplicated results to their partners on the trunnions 1V2–4V2, 3V4, and 4V4.

The field results consisted of 429 68 min records collected over the 1974–1978 period of study. Such a collection was comprised of the following: (1) Wind speed, direction and duration; and (2) strains on the horizontal trunnions, vertical trunnions, locks and support beams shown in Fig. 6.

The readings were only taken for wind speeds over 20 mph (32.2 kmph) and were treated in the following manner:

1. The mean of the wind speed and direction in each hourly interval was computed.
2. The maximum, minimum, mean, and standard deviations of the strains were computed in each hourly interval.

In order to determine a relationship between wind and strain, the aforementioned results were included in a regression analysis for the vertical trunnion anchorage

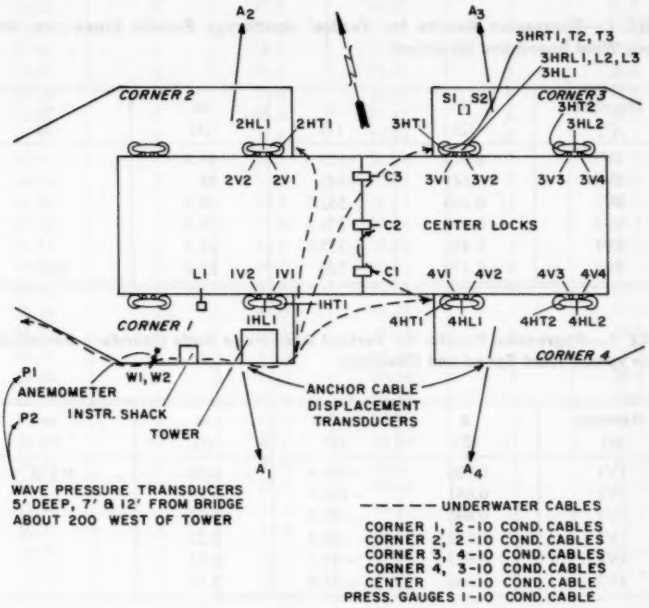

FIG. 6.—Instrumentation on Drawspan (Note: 1 ft = 0.305 m)

rods. The form of the first regression was

$$y = c + mx + nz \quad \ldots\ldots\ldots\

in which ϵ_m and ϵ_c = the measured and computed |max-min| strains.

Similar regression analysis was performed in which y = standard deviation of strain. The results of Table 2 were then obtained in which ϵ_m and ϵ_c = the standard deviation of strain in the calculation of R.

The correlations provided can be compared with the correlation between the strains of adjacent rods A1 and A4 of 0.99. Similar analyses were carried out using $z = Ln$ (mean wind speed) and $y = Ln$ (wind direction). The results did not improve the correlations.

Only 196 of the 429 records were employed in the regression analyses. The excluded records were those which were nonstationary in the wind and the strain. Such nonstationary conditions occur at the beginning of the storms where

TABLE 1.—Regression Results for Vertical Anchorage Results (|max-min| Strain versus Wind Speed and Direction)

Member (1)	R (2)	c (3)	m (4)	n (5)
1V1	0.672	−923	49.9	
2V1	0.641	−847	45	
3V1	0.600	−552.7	29.6	
3V3	0.487	−375.6	19.4	
4V1	0.486	−335.8	24.3	
4V3	0.470	−526	25.8	0.43

TABLE 2.—Regression Results for Vertical Anchorage Rods (Standard Deviation of Strain versus Wind Speed and Direction)

Member (1)	R (2)	c (3)	m (4)	n (5)
1V1	0.705	−151.4	6.95	0.112
2V1	0.681	−120.1	6.09	
3V1	0.696	−79.4	4.03	
3V3	0.529	−45.2	2.22	
4V1	0.633	−87.7	5.03	
4V3	0.646	−58.9	3.16	

transient behavior was involved. To remove these records the first two hours of each storm record were deleted. This amounted to 168 deletions from the records of 84 storms included in the 429 68 min records. Also, another 65 record deletions were made where the differences with previous hourly records of wind and strain were of different sign, e.g., where the strains increased while the wind decreased.

The duration of the storms is given in Table 3. This provided for 84 storms and gives the mean wind speed, duration in hours, and maximum gust speed. The average storm duration was 4.714 hr.

Long-Term Stress Distribution

Measurements every 8 hr were made on the Evergreen Point Bridge between

TABLE 3.—Storm Duration and Wind Speeds

Mean wind speed, in miles per hour (1)	Duration, in hours (2)	Maximum gust, in miles per hour (3)	Mean wind speed, in miles per hour (4)	Duration, in hours (5)	Maximum gust, in miles per hour (6)
20.42	1	31.9	19.32	14	43.7
24.88	1	31.3	17.16	14	27.1
27.82	5	37.6	15.63	2	29.7
21.82	5	32.9	14.67	1	17.5
18.18	1	29.0	15.63	1	21.1
27.43	3	38.3	15.79	2	21.7
23.92	6	31.6	12.44	1	20.6
23.29	1	35.4	16.38	6	22.3
23.92	5	35.4	15.35	8	36.4
19.57	3	31.6	17.74	10	27.7
25.31	3	32.5	22.01	7	34.8
24.99	3	39.6	20.62	8	29.0
21.90	3	40.8	36.11	12	81.3
25.52	1	37.0	24.74	11	47.5
28.71	1	38.0	15.50	1	20.4
29.54	5	44.0	20.81	8	37.3
26.48	7	37.6	21.05	9	38.6
26.16	2	45.0	18.18	1	37.3
26.39	7	45.3	18.08	6	25.8
26.16	6	44.0	18.18	1	23.9
28.66	13	50.4	20.58	2	29.0
16.27	6	38.6	25.17	11	69.5
19.46	7	41.2	24.47	7	41.8
29.72	11	40.8	23.98	11	80.7
31.42	2	45.0	26.8	1	80.1
15.63	6	24.2	18.61	9	37.0
13.72	1	17.5	16.51	4	25.5
16.75	2	19.8	28.82	3	49.1
19.30	2	26.2	20.87	12	38.0
17.39	2	24.5	20.42	8	35.4
23.29	1	37.0	26.16	2	35.4
17.39	2	25.2	19.08	10	30.6
17.23	2	—	19.46	3	27.8
14.99	1	19.5	16.91	3	23.9
29.41	11	66.5	22.33	1	28.7
26.16	2	33.5	21.88	5	32.2
19.14	5	30.3	17.86	2	23.9
17.74	5	32.5	15.9	2	22.3
16.27	1	21.7	16.9	1	26.5
26.43	7	45.9	21.5	2	40.5
17.04	12	27.1	17.1	2	46.6
16.67	4	29.1	25.73	9	35.4

Note: 1 mph = 1.61 kmph.

March 1964 and June 1975. These 12,150 long-term results are listed in Table 4. Eq. 4 and Tables 1 and 2 provide a relationship between hourly mean wind and both the absolute value and the standard deviation of stresses. Using these regression results and Table 4, the long-term stresses in terms of the standard deviation (σ_D) are given in Table 5, and |max-min| in Table 6 as functions of the wind speed. As an example, two records of wind speeds, between 50 mph and 60 mph (80 kmph and 97 kmph) from the southeast, exist as the in one year, 1,095 eight hourly intervals occur and the number of occurrences in Table 4 is multiplied by 1,095/12,150.

S-N Characteristics

Two sets of trunnion rods were available, one with machined threads, and the other with rolled threads. Six rods were in each set. This was not an adequate data base for the conventional generation of S-N curves at single amplitude stress repetitions. However, the accelerated procedures of Prôt (4), with modi-

TABLE 4.—Long Term Wind Speeds at Evergreen Point Bridge (8 Readings at 8 Hour Intervals from March 1964 to June 1975)

Speed, in miles per hour (1)	Under 20 (2)	20–30 (3)	30–40 (4)	40–50 (5)	50–60 (6)	60–70 (7)	Over 70 (8)
S	2,274	848	484	129	26	5	3
SE	1,245	179	59	15	2		
SW	774	264	124	36	6	3	
E	238	6	1				
W	220	5	1				

Note: 1 mph = 1.61 kmph.

fications by Basavaraju and Lim (1), did allow the construction of S-N curves.

In the Prôt test the amplitude of stress, S, is increased from zero at a rate $\dot{S}$ until failure occurs at stress S_d at N_d cycles after crossing the endurance limit S_f. For various $\dot{S}$ and S_d a relationship

$$S_d = S_f + K\dot{S}^k \quad \ldots \ldots \ldots

TABLE 5.—Standard Deviation Stresses (ksi) for Various Wind Speeds for Anchor Rods

Wind speed, in miles per hour (1)	20–30 (2)	30–40 (3)	40–50 (4)	50–60 (5)	60–70 (6)	75 (7)
1V1	0.67	2.75	4.84	6.92	9.01	11.09
2V1	0.96	2.79	4.61	6.45	8.28	10.1
3V1	0.63	1.84	3.05	4.25	5.46	6.66
3V3	0.31	0.98	1.64	2.31	2.97	3.64
4V1	1.14	2.65	4.16	5.67	7.18	8.69
4V3	0.6	1.55	2.50	3.45	4.40	5.34

Note: 1 mph = 1.61 kmph; 1 ksi = 6.89 MPa.

TABLE 6.—|max-min| Stresses (ksi) for Various Wind Speeds for Anchor Rods

Wind speed, in miles per hour (1)	20–30 (2)	30–40 (3)	40–50 (4)	50–60 (5)	60–70 (6)	75 (7)
1V1	9.73	24.7	39.67	54.65	69.6	84.6
2V1	8.34	21.8	35.34	48.84	62.34	75.84
3V1	5.62	14.5	23.38	32.26	41.14	50.02
3V3	3.28	9.10	14.92	20.74	26.56	32.38
4V1	8.15	15.44	22.72	30.02	37.31	44.60
4V3	3.57	11.31	19.05	26.79	23.53	42.27

Note: 1 mph = 1.61 kmph, 1 ksi = 6.89 MPa.

TABLE 7.—Number of Annual Occurrences and Stresses ($3\sigma_D$, ksi) for Various Wind Ranges and Anchor Rods

Wind speed, in miles per hour (1)	20–30 (2)	30–40 (3)	40–50 (4)	50–60 (5)	60–70 (6)	75 (7)
Occurrences per year ($\bar{\alpha}_i$)	116.44	60.29	33.17	3.97	.72	.27
			(*a*) $3\sigma_D$ (ksi)			
1V1	2.01	8.25	14.52	20.76	27.03	33.27
2V1	2.88	8.37	13.83	19.35	24.84	30.3
3V1	1.89	5.52	9.15	12.75	16.83	19.98
3V3	0.93	2.94	4.92	6.93	8.91	10.92
4V1	3.42	7.95	12.48	17.01	21.54	26.07
4V3	1.8	4.64	7.50	10.35	13.20	16.02

Note: 1 mph = 1.61 kmph, 1 ksi = 6.89 MPa.

The results in Table 5 for |max-min| stresses enclose $6\sigma_D$ obtained from Table 6. This information provides some confirmation of the measurements and the analyses in as much as $\pm 3\sigma_D$ should include over 99% of the occurrences; but the extremes should include 100% of the occurrences.

Table 7 shows the number of occurrences of each year in each wind speed range and also a stress measure ($3\sigma_D$) in each rod. The stress measure is obtained from Table 5 and the number of occurrences by assuming that the effect of the winds blowing from the south arc is independent of attack angle. Then

The conventional S-N relationship is

$$(S - S_f)^m N = C \quad \ldots \quad (8)$$

and Basavaraju and Lim (1) developed relationships for m and C in terms of K and k. These are

$$m = \frac{1 - k}{k} \quad \ldots \quad (9)$$

and $$C = k K^{1/k} \quad \ldots \quad (10)$$

TABLE 8.—Fatigue Test Results

Specimen (1)	$\dot{S}$ (psi per cycle) (2)	S_d, in ksi (3)
Machined	4.567	31.719
Machined	2.634	30.281
Machined	1.365	25.531
Machined	0.771	22.656
Machined	0.467	19.438
Machined	0.237	16.719
Rolled	0.1262	40.522
Rolled	0.0884	37.938
Rolled	0.0624	36.225
Rolled	0.0375	34.375

Note: 1 ksi = 6.89 MPa; 1 psi = 6.89 kPa.

The assumptions of this method for obtaining S-N curves are the following:

1. The S-N curve and the $S_d - N_d$ curve are higher order hyperbola, asymptotic to S_f, and the increasing stress axis at $N = 0$ and $N = N_d$, respectively.
2. $D = 0$ for $S < S_f$.
3. Miner's hypothesis is valid.

Tests were at 1 Hz and the loading replicated the bridge state of oscillating axial tension. The various rates $\dot{S}$ were obtained by maintaining the lowest value of S at each cycle as zero. The rods tested were 3 in. (76 mm) diameter and between 15.3 ft (4.67 m) and (16.6 ft) (5.06 m) long. The material was AISI steel with a yield of 111.7 ksi (770 MPa), and an ultimate tension strength of 137.4 ksi (947 MPa). Six rods had machined 3–4 UNC-2A threads over

the end 6 in. (152 mm). Six rods had cold rolled 3–8 UN-2A threads over 6 in. (152 mm) at one end, and 15 in. (381 mm) at the other.

Table 8 shows the experimental results for machined and rolled threads. Thus, for Eq. 4, with stresses in psi

$$S_d = 16{,}484 + 6{,}380\,\bar{S}^{0.6342} \quad \ldots \quad (11)$$

for machined threads, and

$$S_d = 29{,}000 + 42{,}500\,\bar{S}^{0.6342} \quad \ldots \quad (12)$$

for the rolled threads. Using Eq. 9 and 10, $m = 0.5768$ and $C = 617{,}746$ for the machined, and $m = 0.5768$ and $c = 12{,}600{,}000$ for the rolled threads. Thus, for machined threads

$$(S_i - 16{,}484)^{0.5768}\,N_i = 617{,}746 \quad \ldots \quad (13)$$

and for the rolled threads

$$(S_i = 29{,}000)^{0.5768}\,N_i = 12{,}600{,}000 \quad \ldots \quad (14)$$

Fig. 7 shows the S-N curves for the two rod types.

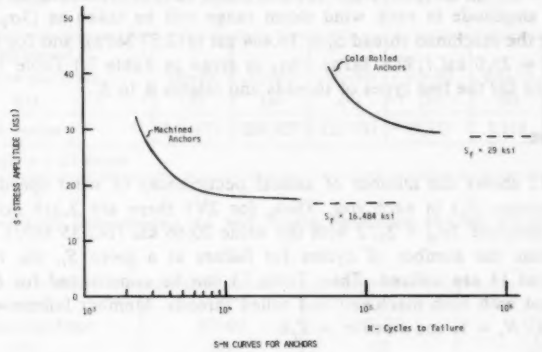

FIG. 7.—S-N Curves for Anchors (Note: 1 ksi = 6.89 MPa)

Applied Stress Cycles

The previous section provided the N_i term in Eq. 3. In the light of the measurements on the site and the long-term wind data, the results in Table 7 have been obtained and give, for each wind speed increment, the occurrences in each year ($\bar{\alpha}_i$) and the stress measure $3\sigma_D$. It is necessary to find the expected number of cycles in each year, namely

$$\bar{n}_i = \omega_i T_i = \omega_i \bar{\alpha}_i \bar{t}_i \quad \ldots \quad (15)$$

in which ω_i = the frequency (Hertz); and $\bar{t}_i$ the duration for the ith wind increment.

The duration $\bar{t}_i$ can be considered from the 84 storm occurrences listed in Table 3. Assigning the maximum wind in each occurrence into 10 mph (16.1 kmph) intervals, and ignoring the single hourly input which produced 80.1 mph (129 kmph) maximum, then the average duration of each range maxima is given in Table 9. This is a representation of $\bar{t}_i$.

The process of Eq. 3 is narrow banded and ω_i can be obtained by counting the frequency from the measurements. Table 10 gives these results. These agree with the modified Barnet formula

$$\omega = 27.23 F^{-0.31} u^{-0.38} \quad \ldots \quad (16)$$

in which F = fetch in ft; and u = wind speed in ft/sec.

$\bar{n}_i$ is now determined from Eq. 15 in which the ω_i, $\bar{\alpha}_i$, and $\bar{t}_i$ terms are in Tables 7, 9 and 10 respectively, and is as Table 11.

In order to complete the picture of the damage incidence on the members, it is necessary to determine the stress amplitude, S_i, associated with each wind speed range of Table 12 and each anchorage rod. Storms producing the wind speeds of Table 12 will incur member stresses varying from zero to over $3\sigma_D$ in amplitude. However, over 99% of these stresses will be included in $\pm 3\sigma_D$. Stresses below the endurance limit, S_f, will incur no damage. Interest must be focused on the values of $S_f < \sigma < 3\sigma_D$ as damaging the member. Stresses greater than $3\sigma_D$ are infrequent and are ignored. As an estimate, the value of stress amplitude in each wind storm range will be taken as $(3\sigma_D + S_f)/2 = S_i$. For the machined thread S_f = 16.484 ksi (113.57 MPa), and for the rolled thread S_f = 29.0 ksi (199.8 MPa). ($3\sigma_D$ is given in Table 7.) Table 12 is then constructed for the two types of threads and relates $\bar{n}_i$ to S_i.

Fatigue Life

Table 12 shows the number of annual occurrences of wind speed ($\bar{n}_i$) and stress measure (S_i) in each rod. Thus, for 2V1 there are 2,218 occurrences of stress measure $3\sigma_D + S_f/2$ with the value 20.66 ksi (142.35 MPa). In order to determine the number of cycles for failure at a given S_i, the results of Eqs. 13 and 14 are utilized. Then Table 13 can be constructed for $\bar{n}_i$ and N_i of each rod with both machined and rolled threads. Member failure will occur when $\Sigma_i\, n_i/N_i = 1$, and since $n_i = T_f \bar{n}_i$

$$T_f = \left(\sum_i \frac{\bar{n}_i}{N_i} \right)^{-1} \quad \ldots \quad (17)$$

The N_i is obtained from Eqs. 13 and 14, or from Fig. 6. For example, member 1V1 machined threads have

$$\sum_i \frac{\bar{n}_i}{N_i} = \frac{19{,}323}{7{,}419} + \frac{3{,}318}{4{,}393} + \frac{1{,}190}{3{,}368} = 3.71 \quad \ldots \quad (18)$$

$$\text{Thus} \quad T_f = \frac{1}{3.41} = 0.27 \text{ years} \quad \ldots \quad (19)$$

Completing such calculations for all other members with both types of thread

TABLE 9.—Storm Duration

Maximum gusts, in miles per hour (1)	20–30 (2)	30–40 (3)	40–50 (4)	50–60 (5)	60–70 (6)	75 (7)
Average duration, in hours ($\bar{t}_i$)	2.89	4.76	5.71	8[a]	8[a]	8[a]

[a]The 8 hourly readings of the long-term data limit these results.
Note: 1 mph = 1.61 kmph.

TABLE 10.—Member Frequency for Various Wind Speeds

Wind speed, in miles per hour (1)	20–30 (2)	30–40 (3)	40–50 (4)	50–60 (5)	60–70 (6)	75 (7)
Frequency (ω_i), in hertz	0.216	0.194	0.180	0.169	0.160	0.153

Note: 1 mph = 1.61 kmph.

TABLE 11.—Number of Cycles in a Year for Each Wind Range

Wind speed, in miles per hour (1)	20–30 (2)	30–40 (3)	40–50 (4)	50–60 (5)	60–70 (6)	75 (7)
$\bar{n}_i$ cycles	261,671	200,427	122,731	19,323	3,318	1,190

Note: 1 mph = 1.61 kmph.

TABLE 12.—Yearly Occurrences ($\bar{n}_i$) and Stress Amplitude (S_i) for Various Wind Speeds

Wind speed, in miles per hour (1)	50–60 (2)	60–70 (3)	75 (4)
Occurrences/year ($\bar{n}_i$)	19,323	3,318	1,190
(*a*) Rod machined $S_i = (3_D + S_f)/2$ ksi			
1V1	18.62	21.78	24.88
2V1	17.92	20.66	28.39
3V1			18.23
4V1	16.75	19.01	21.28
(*b*) Rolled			
1V1			31.14
2V1			29.64

Note: 1 mph = 1.61 kmph; 1 ksi = 6.89 MPa.

allows Table 14, which gives the estimated member life, to be constructed.

Comments

The field measurements were more abundant than those obtained in the laboratory. The function of the field measurements was to obtain a relationship between wind and stress. This relationship, together with the laboratory results, is of critical importance in any subsequent maintenance procedure. The following

TABLE 13.—N_i and $\bar{n}_i$ for Various Wind Speeds and Anchorage Rods

Wind speed, in miles per hour (1)	50–60 (2)	60–70 (3)	75 (4)
$\bar{n}_i$	19,323	3,318	1,190
(*a*) Machined threads N_i			
1V1	7,419	4,393	3,368
2V1	9,327	5,039	3,770
3V1	24,668	6,734	4,652
(*b*) Rolled threads			
1V1			151,143
2V1			300,526

Note: 1 mph = 1.61 kmph.

TABLE 14.—Estimated Life of Anchor Bolts

Member (1)	Life, in years	
	Machined (2)	Rolled (3)
1V1	0.27	127
2V1	0.33	252
3V1	7	Indefinite
3V3	Indefinite	Indefinite
4V1	0.65	Indefinite
4V3	Indefinite	Indefinite

comments will focus on these two matters.

The removal of nonstationary measurements of wind and strain left only 196 hourly records, out of 429 completed, for use in the regression analysis. It was found that without such deletions the correlation coefficient R of Eq. 5 dropped to about 0.2–0.3. Obviously, leaving out offending data is attractive in establishing reliable regression formulas. It is claimed here that not only is it attractive, but it is also reasonable to omit measurements that are nonstationary. It was found that the application of the tests for stationarity of the process produced acceptable regression correlations. The final results responded to the question: "What is the relationship between strain and wind when conditions

are steady?" No attempt was made to determine transient relations. Nearly all of the deletions (168) were at low strain levels at the beginning of a storm. The remaining 65 deletions must be associated with changes in the air environment to which the water and structure had insufficient time to respond. These were not necessarily at low strains. The 168 deletions at low strains may be considered as having little effect on the prediction of fatigue damage. No such claim can be made about the other 65 deletions, and if this type of work should be carried further, methods for including such transient behavior into regression analyses would have to be employed.

The application of the wind-stress relationships to extensive long-term wind measurements taken at 8 hr intervals causes some concern. Clearly, these measurements sampled, without discretion, include stationary and nonstationary processes. The collection was for different purposes than for this study; however, it was made at the bridge site. The alternative was a collection made at the lake level at 1 hr intervals at a location 3 miles north of the bridge. There appeared no sensible relationship between the statistics of the two collections. The on-site collection was therefore preferred even though the more frequent measurements at the distant site would have allowed some tests for stationarity. In a future collection of long-term data on wind, hourly readings would be preferred.

The S-N results were obtained from few samples. Two approaches were considered. One involved subjecting the rods to a loading sequence with the same statistics as the on-site members. The other was to use the Prôt method and thus derive an S-N result. The second approach was used. It was thought that if there were any sins in the obtaining of the on-site statistics, then these would be replicated in the use in laboratory experiments. On the other hand, concern must be shown about the actual meaning of the Prôt results.

The Prôt tests give some measure of fatigue damage and capacity. There appears to be little information to confirm the relation of these measures to conventional S-N results. Whatever that relationship is, the Prôt procedure is attractive when limited samples are obtainable and where comparisons of details are needed. The six results here for machined threads led to endurance limits well below those obtained from results on cold rolled threads. (One test had to be abandoned when heat was applied to the threaded region; another test was completed on a modified rod.) These differences in fatigue limits are in line with common experience in the aircraft industry where rolled threads are consistently preferred. The results contradict those of Frank (3) who observed no such difference. It may be that the difference is not evident in the low strength steel bolts that Frank used in his comparison.

The S-N curve obtained by analyzing the Prôt results on six machine threaded specimens (Eq. 13 and Fig. 7) had lower misfit of data for $k = 0.6342$ than for other values of the exponent. In the case of results for four rolled threaded specimens (Eq. 14 and Fig. 7), much the same fit was obtained for a variety of exponents, k. These resulted in endurance limits, S_f, between 27 ksi and 30.5 ksi (186 and 210 MPa), for k lying between 0.5 and 0.8. All these showed a marked increase of S_f over the machine threaded rods. For comparison purposes, the same $k = 0.6342$ was maintained with consequent $S_f = 29$ ksi (200 MPa). It would appear that the more test results available, the more evident is the appropriate S-N curve. As mentioned previously, there is little evidence

to indicate whether this convergence is to the correct S-N curve. The Prôt method appears very attractive; it measures some characteristics and further work to identify the actual relationship to conventional S-N curves would appear useful.

The Prôt test was carried out with an increasing mean and zero minimum stress. This meant that in high stress amplitude the mean was in the range of prestress of the rods in the bridge. Failure occurred at the threaded ends at both the loading and reacting ends of the apparatus. Bending strains were below 5% of the axial strains.

Maintenance Programs

The results available can be used in maintenance programs. One method is to use the results in Table 14 and replace bolts before the predicted failure date. This approach makes evident that some members (3V1, 3V3, and 4V3) are very safe and that 1V1, 2V1, and 4V1 are progressively more susceptible to fatigue failure. An alternative approach is to monitor the damage to individual bolts by an automatic computer procedure which

1. Records the hourly wind speed.
2. From this and Eq. 4, with Table 2, obtains $3\sigma_D$ for each rod.
3. Determines S_i and the number of occurrences, $\tilde{N}_i$, in that hour from ω_i (Table 10).
4. Determines the damage $D_i = \tilde{N}_i / N_i$ for S_i from Eq. 13 or 14.
5. Adds to previous D_i and compares with unity.
6. Has visual signal when $\Sigma_i D_i = 0.8$.

The above operation can be completely automatic and reflects the experimental and analytical work of this paper, together with the actual experience of the member.

Conclusions

A methodology for making maintenance decisions to avoid fatigue failure has been proposed. The maintenance procedures developed for the drawspan mechanism of the Evergreen Point Bridge have been used as an illustration of the methodology. The methodology has the following steps:

1. Development of the stress-environment relationship for the critical member.
2. Collection of long-term environmental data and, thus, from (1) the computation of long-term stress distribution.
3. Determination of cycles at each stress level from the return period, and duration of various environmental conditions and the member frequency at the associated stress level.
4. Determination of the fatigue characteristics of the member (S-N) from a limited number of full-scale tests using the Prôt procedure.
5. Determination of yearly damage and, thus, life using Miner's hypothesis.

Acknowledgment

This work was performed at the Department of Civil Engineering of the

University of Washington under the support of the Washington State Department of Transportation and the Federal Highway Administration. However, the contents do not necessarily reflect the official views or policies of those bodies. The contents reflect the views of the writers, who are responsible for the facts and accuracy of the data presented. It does not constitute a standard, specification, or regulation.

Appendix I.—References

1. Basavaraju, C., and Lim, C., "An Analytical Approach to Determine Conventional S-N Curves from Accelerated-Fatigue Data," *Experimental Mechanics*, Vol. 17, No. 10, pp. 375–380.
2. Bright, A., "A Comparison of Fatigue Theories and Design Recommendations for Fatigue," thesis presented to the University of Washington, in 1980, in partial fulfillment of the requirements for the degree of Master of Science.
3. Frank, K. H., "Fatigue Strength of Anchor Bolts," *Journal of the Structural Division*, ASCE, Vol. 106, No. ST6, Proc. Paper 15465, June, 1980, pp. 1279–1293.
4. Prôt, E., "Fatigue Testing Under Progressive Loading, a New Technique for Testing Materials," *Revue de Metallugie*, Vol. 45, 1948, pp. 481–489 (Translation, WADG TR-52-148, 1952).

Appendix II.—Notation

The following symbols are used in this paper:

C = Prôt parameter;
c = regression constant;
D = fatigue damage;
D_1 = fatigue damage in one year;
E = modulus of elasticity;
F = fetch;
K, k = Prôt parameters;
m = Prôt parameter, regression constant;
N_d = cycles at $\hat{S}$ to failure, beyond S_f;
N_i = cycles at S_i to failure;
n = regression constant;
n_i = cycles at S_i applied to member;
$\bar{n}_i$ = n_i in one year;
R = multiple correlation coefficient;
S_d = stress amplitude at N_d;
S_f = endurance limit;
S_i = stress amplitude at N_i;
$\hat{S}$ = stress change per cycle in Prôt test;
T_f = fatigue life ($D = 1$);
T_i = time at S_i in year = $\bar{\alpha}_i \bar{t}_i$;
$\bar{t}_i$ = duration of ith wind increment;
u = wind speed;
x, y, z = regression variables;
$\bar{\alpha}_i$ = number of ith increments in year;
ϵ_m, ϵ_c = measured, computed |max-min| strains;

ϵ_d = standard deviation of strains;
σ_d = standard deviation of stresses; and
ω_i = applied frequency at S_i.

Field Measurements of Muskwa River Bridge

By Walter Dilger,[1] M. ASCE, J. C. Beauchamp,[2] M. S. Cheung,[3] M. ASCE and Amin Ghali,[1] M. ASCE

Introduction

The Muskwa River Bridge is located near Fort Nelson, British Columbia, Canada, at mile 297 on the Alaska Highway. Because of the extreme climatic conditions (the geographic location is 58° 57′N) and relatively large span length, it was decided to monitor the bridge and collect the performance data, during the construction of the deck slab and during the first few years in operation.

The bridge is a two-lane steel-concrete composite bridge, continuous over five spans (Fig. 1). The total length is about 1,080 ft (330 m). The testing was done on the two 300-ft (91.44-m) spans. The objective of the study was to provide information about:

1. Strains and deflections developed during the different stages of construction of the concrete deck.
2. Strains and deformations caused by the time-dependent properties of the concrete shrinkage and creep.
3. Temperature distribution in the bridge during construction and in service when it is subject to the conditions encountered in northern British Columbia and the Yukon.
4. Cracks developing in the concrete deck.
5. Slip occurring in one of the field splices on the steel box.

Approx 15,000 strain and temperature measurements were recorded. Detailed information about this research project is provided in Ref. 7.

General Description of Bridge and Sequence of Construction

The elevation and cross section of the bridge are shown in Fig. 1. It is composed of two steel boxes 8 ft, 6 in. (2.59 m) wide and their height varies between

[1]Prof. of Civ. Engrg., Univ. of Calgary, Calgary, Alberta, Canada.
[2]Chief Bridge Engr., Public Works Canada, Ottawa, Ontario, Canada.
[3]Mgr., Civ. Engrg., Development, Public Works Canada, Ottawa, Ontario, Canada.

Note.—Discussion open until April 1, 1982. To extend the closing date one month, a written request must be filed with the Manager of Technical and Professional Publications, ASCE. Manuscript was submitted for review for possible publication on January 22, 1981. This paper is part of the Journal of the Structural Division, Proceedings of the American Society of Civil Engineers, ©ASCE, Vol. 107, No. ST11, November, 1981. ISSN 0044-8001/81/0011-2147/$01.00.

12 ft, 6.75 in. (3.83 m) at support C and 5 ft, 0.75 in. (1.54 m) in span EF. In spans BC and CD, investigated in this study, the minimum depth at midspan was 8 ft, 0.75 in. (2.46 m). In the negative moment, zone near support C the stiffened bottom plates have a thickness of 1 in. (25.4 mm) and the webs are 0.56 in. (14.3 mm) thick. The top flanges consist of plates 2 in. × 30 in. (50.8 mm × 762 mm). No shear connectors are provided in a zone extending 30 ft (9.14 m) on either side of the piers B, C, and D.

The stiffeners of the web and the bottom plates near support C are shown in Fig. 1, together with the stiffened diaphragm. The reinforced concrete deck has a minimum thickness of 8 in. (203 mm) and is reinforced as in Fig. 2.

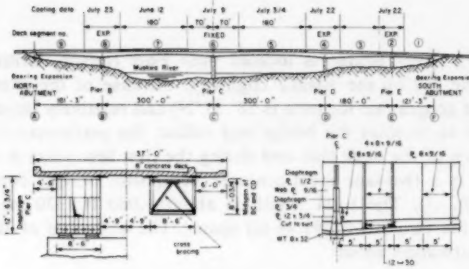

FIG. 1.—Elevation and Cross Sections of Bridge

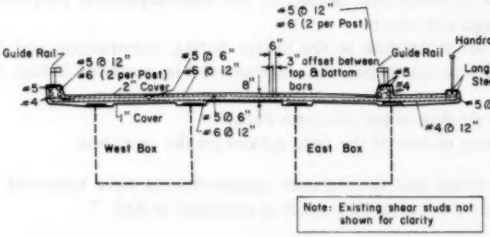

FIG. 2.—Reinforcement of Deck

The steel boxes, fabricated by Dominion Bridge of Vancouver, Canada, were erected in winter 1974–1975 using the ice of the frozen river as a construction base. Construction of the concrete deck started in spring of 1975. The casting dates of the deck segments are shown in Fig. 1. Deck segments 1, 3, and 9 were poured before measurements were taken. The bridge was opened to traffic in October, 1975.

MATERIALS

Steel.—Atmospheric corrosion resisting steel was used for the steel boxes. The steel is of type CSA G40.21–50A, high-strength, low-alloy steel, with a

minimum yield point of 50 ksi (345 MPa) and a minimum tensile strength of 70 ksi (483 MPa). For the evaluation of the strain measurements, a modulus of elasticity of $E = 29 \times 10^6$ psi (200 GPa) and a coefficient of thermal expansion $\alpha t = 6.5 \times 10^{-6}/°\,F$ ($11.7 \times 10^{-6}/°\,C$) are assumed according to the above standard.

Concrete

Fresh Concrete Properties and Strengths.—The 28-day design strength of the deck concrete was 4,000 psi (27.6 MPa), which was intended to be achieved with the concrete mix of Table 1. Statistical evaluation of the 28-day strength (measured on 6 in. (153 mm) standard cylinders) yielded a mean concrete strength

TABLE 1.—Concrete Mix Design

Component (1)	Measurement (2)
Water	281 lb/cu yd (167 kg/m^3)
Gravel	1,926 lb/cu yd (1,143 kg/m^3)
Sand	1,123 lb/cu yd (666 kg/m^3)
Cement (Lafarge type I)	625 lb/cu yd (371 kg/m^3)
Total from above	3,955 lb/cu yd (2,347 kg/m^3)
Water/cement ratio	0.45
Admixtures	Pozzolith 300 N
Design strength	4,000 psi (27.6 MPa)
Slump (in lab mix)	2.25 in. (57 mm)
Air content (in lab mix)	5.9%

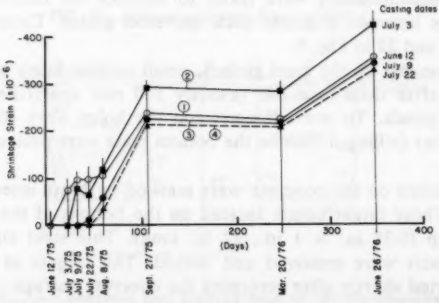

FIG. 3.—Shrinkage Development with Time

of 4,900 psi (33.8 MPa) with a standard deviation of 345 psi (2.4 MPa) indicating good control of the concrete production.

Shrinkage.—Shrinkage was measured on eight standard cylinders cast simultaneously with the control cylinders for strength testing. Each cylinder had a thermocouple embedded in its center so that temperature measurements, essential for separating the shrinkage strains from the total strains measured, could be determined. Readings began one day after casting and continued over approx a one-year period. The temperature effects were deducted from the total strain readings by assuming a coefficient of thermal expansion of 5×10^{-6}/°F (9×10^{-6}/°C) according to a recent investigation by Berwanger and Sarkar (3). The development of shrinkage with time is depicted in Fig. 3. It is evident that shrinkage developed rapidly during the first few months (until the end of September) and stopped during the winter months.

After the winter, shrinkage resumed, reaching a midsummer average of 360×10^{-6}, approx one year after casting. Given the temperature conditions and the specimen dimensions, a final shrinkage of about 520×10^{-6} is expected. This is arrived at according to (Comité Euro-International du Béton-Federation Internationale de la Précontrainte), CEB, recommendations (6), assuming an effective thickness of 3 in. (76 mm) and that moisture movement occurred during a six-month period (excluding the six winter months) from casting. For the 8 in. (203 mm) concrete deck, a final free shrinkage strain of about 410×10^{-6} was established on the basis of measurements and CEB Recommendations.

Instrumentation

Deflection Measurements.—A precision level was used to measure the deflection of the main girders inside the west box at stations 1–9 (Fig. 4).

Strain Measurements.—Strain measurements were taken at nine stations, approx 75 ft (22.86 m) apart in the two long spans BC and CD (Fig. 4) using a mechanical strain indicator. One division on the dial corresponds to 2×10^{-3} mm. When related to the strain indicator's 500 mm base length, this shows a strain of 4×10^{-6}. At each station, 17 measurements were taken on each of the two steel boxes, 16 on the concrete deck, and 9 on the top surface. The position of the targets and their numbering are shown in Fig. 5. At stations 2, 3, and 6, additional measurements were taken to monitor the relative displacement at the interface between concrete deck and steel girder. These measurements are number 18 and 22 in Fig. 5.

For measurements on the steel girders, small conical holes were drilled with a center drill after their locations (exactly 500 mm apart) had been marked with a center punch. To prevent corrosion the holes were filled with grease immediately after drilling. Holes on the bottom plate were protected by adhesive tape.

The target points on the concrete were marked by brass inserts cast in place on the deck. Those target points located on the bottom of the slab were held by a steel strip (0.38 in. × 1 in., 22 in. long). This steel strip and the nut holding the insert were removed and reused. The targets at the top of the slab were inserted shortly after screening the concrete surface.

Mechanical measurements were also taken across one splice, located at a distance 45 ft (13.72 m) from support C, between stations 5 and 6 in the west

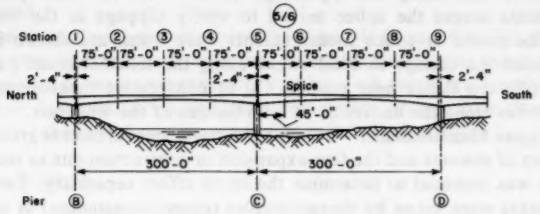

FIG. 4.—Stations of Measurements

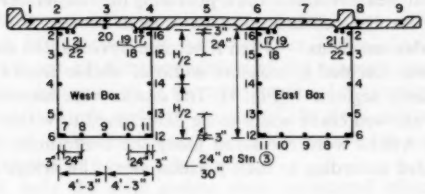

FIG. 5.—Position and Numbering of Mechanical Strain Measurements

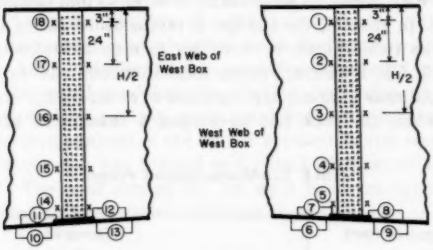

FIG. 6.—Measurements Across Splice

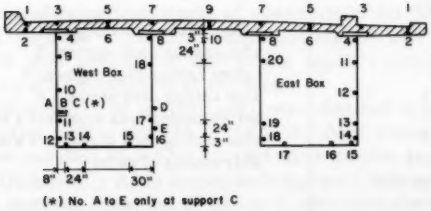

FIG. 7.—Locations and Numberings of Thermocouples

box, (Fig. 4), and along the top flange of the west box near pier C. The measurements across the splice served to verify slippage in the bolted field splices. The points at which measurements were taken are shown in Fig. 6. To determine the change in steel stress along the most stressed part of the structure (the top flange near support C), 11 consecutive measurements were taken in series along the underside of both flanges of the west box.

Temperature Measurements.—Because the strain measurements give the combined effect of stresses and the free expansion or contraction due to temperature change, it was essential to determine the latter effect separately. Temperature measurements were taken by thermocouples (copper-constantan) at stations 1, 3, 5, 7, and 9 at the points indicated in Fig. 7. The thermocouples were attached to the steel box or cast in the concrete between the two target points used for the mechanical measurements, thus, providing the temperatures at the desired points. The temperature measurements were reliable to ±0.2° F (±0.1° C).

Crack-Width Measurements.—When it became obvious that the concrete deck had cracked, it was decided to measure width of visible cracks on the finished deck surface in deck segment 7 (Fig. 1). The cracks were measured by a special microscope that allowed crack width to be determined to within 0.0004 in. (0.01 mm). The crack widths were measured along the centerlines of the two steel boxes and recorded according to their position along the bridge axis.

Schedule of Measurements

Most sets of measurements were taken at night so that temperature variations were minimum. In general, the change in temperature during one complete set of measurements (which took between six to nine hours) was not more than about 4° F (2.2° C). However, some measurements had to be taken under considerable nonlinear temperature variation over the bridge cross section, e.g., after casting when the deck had developed a substantial heat of hydration.

TABLE 2.—Measurement Program

Date of measurement (1)	Remarks (2)
June 10 and 11, 1975	zero readings
June 13, 1975	deck segment 7 cast on June 12, 1975
June 26, 1975	
July 3, 1975	before casting deck segment 5
July 4, 1975	after casting deck segment 5
July 9, 1975	before casting deck segment 6
July 10, 1975	after casting deck segment 6
July 21, 1975	before casting deck segments 4 and 8
July 23, 1975	after casting deck segments 4 and 8
August 6, 1975	after casting of curbs
September 26, 1975	
March 3, 1976	
June 26, 1976	
August 3, 1976	after application of asphaltic wearing surface
April, 1979	final measurement (selected stations only)

In this case, the strains resulting from temperature-induced stresses could not be eliminated.

The casting of deck segments near the piers (4, 6, and 8 in Fig. 1) did not change the stresses significantly and, thus, is not discussed in this paper. Emphasis was placed on the measurements after casting deck segments 7 and 5 (loading cases 1 and 2, respectively) and after completion of the deck (loading case 3). The time schedule of the measurements is indicated in Table 2.

Theoretical Stresses

Two different types of analysis were done to compare experimental and theoretical results: a beam analysis for the whole length of the east box, and a finite element analysis for half of the east box between stations 4 and 6 (Fig. 4). The beam analysis was carried out for three different stages of construction: (1) After casting of deck segment 7 (Fig. 1); (2) after casting of deck segment 5; and (3) after completion of the concrete deck.

For this analysis the variation of the cross-sectional properties was considered at 15 ft (4.57 m) intervals and the weight of the deck concrete of the East box was calculated to be 208 kips/ft (30.3 kN/m), which corresponds to an average slab thickness of 8.5 in. (216 mm).

For loading 1, only the steel girders were considered effective in resisting the moments due to the weight of the deck concrete. In loading case 2, the concrete of segment 7 was assumed to act elastically. The assumed modular ratio, $n = 8$, corresponded approximately to the concrete strength at time of casting segment 5. In the analysis of loading case 3, the modular ratio for the concrete of segment 5 was assumed to be higher, $n = 10$, because the concrete was only 5 days old when deck segment 6 was poured. These assumptions represented well the actual conditions shortly after producing the concrete deck. However, for longer time periods, such simplified analyses are not adequate. A detailed step-by-step analysis of the time-dependent effects was not warranted because of the cracks that had formed in the deck of segment 7 when segment 5 was produced. The load carried by the west box was lighter than on the east box. A detailed study revealed a difference of 11%.

Results

Deflections.—The deflections of spans BC and CD (west girder) are shown in Fig. 8 for the following four stages of construction: (1) After pouring the slab in span BC on June 12, 1975; (2) after pouring the slab in span CD on July 4, 1975; (3) after pouring the slab in the negative moment area at the support C; and (4) after completion of the deck.

The largest deflection, 9.09 in. (231 mm), was observed at the middle span BC (station 3) after casting the 180 ft (54.86 m) deck segment 7. The same loading condition resulted in a 3.98 in. (101 mm) camber at midspan of the adjacent span CD (station 7). After casting deck segment 5, a downward deflection of 4.65 in. (118 mm) was observed at station 7. After completion of the bridge deck, the deflection of both spans was almost equal. The difference between theoretical and recorded deflection is due to the heat developed in the concrete deck the day after pouring the deck. The larger than theoretical deflections

for stage (4) can be explained by the extensive cracking of the concrete deck.

Temperature Measurement.—The objective of the temperature measurement was twofold: first, to eliminate the effect of the temperature on the strain readings; second, to provide information about temperature variations over the cross section under the extreme conditions that occur shortly after casting the concrete deck or during the periods of rapidly changing temperature.

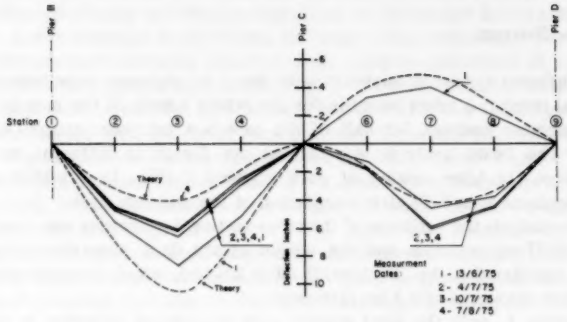

FIG. 8.—Deflections of Spans BC and CD of West Box (1 in. = 25.4 mm)

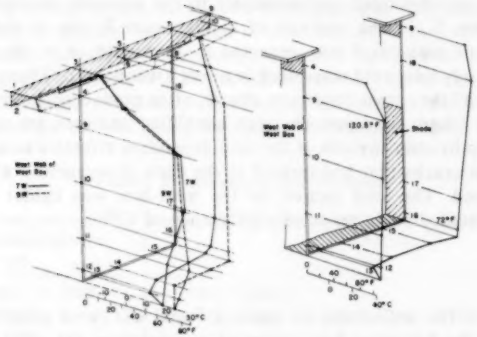

FIG. 9.—Temperature Profiles: (*a*) March 20, 1976, at 14:30 PM at Stations 7W and 9W; (*b*) Before Casting the Deck at Station 5W

The most extreme temperature difference was recorded on the afternoon of March 20, 1976. The minimum and maximum air temperatures recorded on that day at the Fort Nelson Airport were 0° F (−18° C) and 24° F (−4.4° C).

After a cold night, the concrete deck had reached a temperature of about 16° F (−9° C) shortly before noon. The direct sun heated the west web in less than 2 hr. At 12:50, the temperature of the steel was about 30° F (−1° C), and it rose to 89° F (32° C) by 14:30, a temperature difference of 73° F (41° C).

The recorded temperature profiles for sections 7W and 9W are shown in Fig. 9(*a*). This increase in steel temperature caused the air temperature inside the box to rise from 25° F (−4° C) to over 70° F (21° C), which in turn increased the temperature of the steel plates not exposed to the direct sunlight (Fig. 9). However, the temperature of the concrete deck changed only by about 7° F (4° C) during the same time period. The temperature of the east box (not exposed to the direct sunlight) was about the same as that of the concrete deck. The rapid heating of the air inside the box was possible only because it was completely enclosed. Although the month of March was selected in the hope that extreme temperature differences might be recorded, the measured temperature difference did not represent the most extreme variation occurring in that bridge.

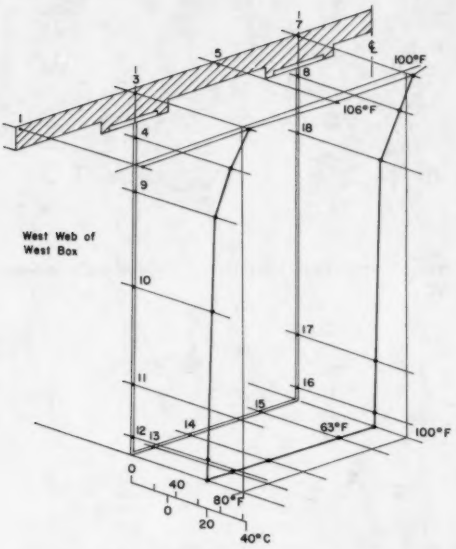

FIG. 10.—Temperature Profile Recorded Shortly after Casting Deck at Station 5W

Two other sets of measurements are shown in Figs. 9(*b*) and 10 for station 5, one for the steel box before casting the deck (Fig. 9(*b*)), and the other taken shortly after pouring the concrete (Fig. 10). In the first case, the temperature difference between steel plates exposed to the sun and those in the shade is about 50° F (28° C). The temperature difference between the concrete deck and the steel box shortly after pouring the deck concrete was about 43° F (24° C), with a gradual transition observed in the top 2 ft (610 mm) of the steel web. The maximum teperature recorded for the deck concrete was 116° F (47° C), which was about 40° F (22° C) higher than the air temperature recorded at the same time.

Mechanical Strain Measurement.—The many mechanical strain measurements were evaluated by computer. All the mechanical readings were punched on computer cards, together with the temperature readings, and the net strain was determined by, first, calculating the total strain and, then, correcting for the free temperature strain. As mentioned before, the strains due to temperature-induced stresses could not be eliminated.

Strain Distribution in Two Typical Cross Sections.—The results of the strain measurements across the steel box are shown in Fig. 11 for the section near support C (station 5) and for the middle span BC (station 3). At station 3,

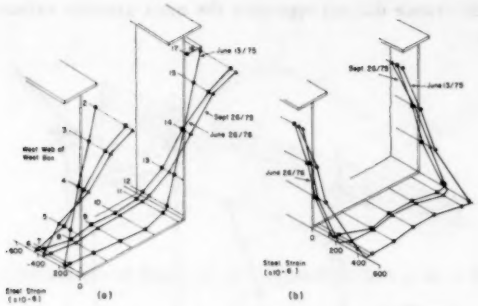

FIG. 11.—Steel Strain Distributions for Different Stages of Construction: (*a*) Station 5W; (*b*) Station 3W

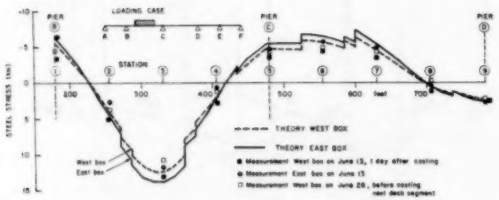

FIG. 12.—Comparison of Theoretical with Measured Steel Stresses along Bottom of Steel Girders; 1 ft = 0.305 m; 1 ksi = 6.89 MPa

the maximum strains in the bottom flange occurred after casting of the concrete deck in that span. The subsequent casting of the deck in the adjacent span reduced the strains in the bottom flange considerably. After the concrete in the two main spans had been poured, the strains did not change. From Fig. 11(*a*), it is also obvious that the location of zero strain changed considerably during the various stages of construction. This was a result of the increase in flexural rigidity after casting of the deck, shrinkage of the deck concrete and changes of temperature. From the figures it can be concluded that the strain distribution in the webs was nearly linear, and the strains were almost uniformly distributed across the bottom plate. This justifies the assumption

that the flexural stresses can be computed using conventional beam theory for this type of structure.

Strains and Stress in Steel Boxes.—Fig. 12 shows the steel stresses in the bottom plates of the boxes of stations 1–9 after casting of deck segment 7. The values shown at each station are the average of the five target points 7–11 measured on the bottom plate of each steel box. For the west box two sets of values are plotted, one, recorded the day after pouring the deck (June

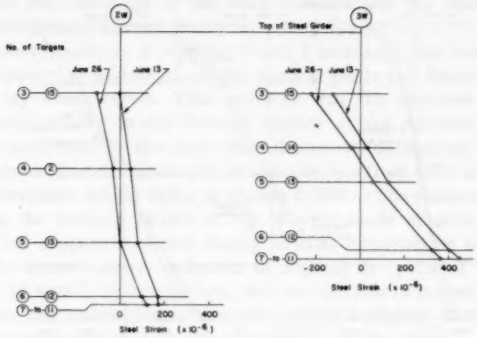

FIG. 13.—Temperature Induced Strains (West Box)

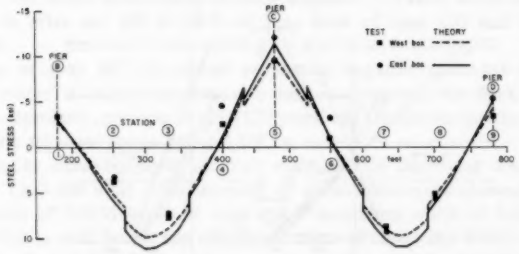

FIG. 14.—Measured Distribution of Bottom Fiber Stress along Girders and Comparison with Theoretical Stresses for Loading Stage 3 (after Completion of Bridge—Sept. 26, 1975); 1 ft = 0.305 m; 1 ksi = 6.89 MPa

13), and, the other, two weeks later (June 26), before pouring the next segment of the deck slab. The difference in stress, which amounts to a maximum of about 2.5 ksi (17.24 MPa) at station 3, is the result of the cooling and the early shrinkage of the deck concrete. Comparison with the measured stresses shows that overall, they agree reasonably well with theoretical ones. In Fig. 13, the strain distributions for sections 2W and 3W from shortly after pouring the deck to 13 days after are plotted. Cooling and shrinkage of the deck concrete introduced an almost uniformly distributed axial strain of about -80×10^{-6},

which corresponds to a compressive stress in the steel box of approx 2.5 ksi (17.24 MPa). The corresponding tensile stress in the concrete is approx 500 psi (3.45 MPa).

Fig. 14 shows the distribution of bottom fiber stresses along the steel boxes after completion of the concrete deck. Comparing theoretical and observed stresses, one can conclude that the negative moments are higher than the positive ones, which is explained by the more extensive cracking of the positive moment

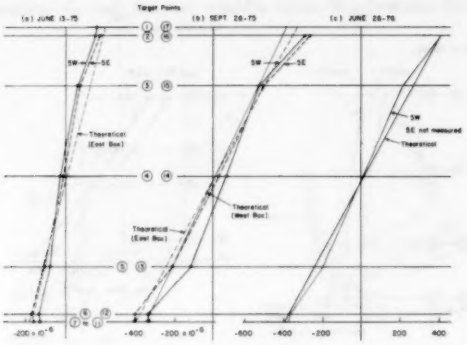

FIG. 15.—Comparison of Strain Distribution between West, W, and East, E, Boxes at Station 5

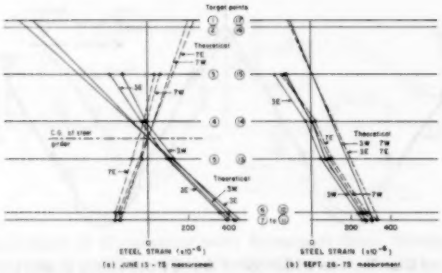

FIG. 16.—Comparison of Strain Distribution between the East, E, and West, W, Boxes (Stations 3 and 7) for Loading Cases 1 and 3

zones and the resulting loss of stiffness. The shrinkage and creep effects on one hand and the cracking of parts of the deck concrete on the other, make analysis of such a structure extremely complex, and the analysis with an effective modulus of elasticity does not represent these effects. A comparison of the measured and calculated strain distribution across sections 5W and 5E (over support) shows that for all three cases presented in Fig. 15, agreement is surprisingly good. As expected, the strains in the east box are slightly higher

than in the west box. The agreement is less satisfactory at the middle of the two spans Fig. 16. While the measured bottom fiber strains still agree reasonably well with the theoretical values, the distribution across the section deviates significantly from the anticipated linear distribution. The heat of hydration in the concrete deck on June 13, 1975 is responsible for the nonlinear strain distribution at that date.

The strains recorded on September 26, 1975 (Fig. 16(*b*)), after completion of the deck also deviate from the theoretical values above the bottom fibers. It is assumed that shrinkage of the deck concrete and the resulting cracking caused the difference between theory and observation.

The September readings at stations 3 and 7 indicated that the level of zero stress was approx at mid-depth of the section while the theoretical point of zero stress lay much higher. This indicated that the concrete deck did not contribute substantially to the flexural rigidity at the midspan section. This statement is confirmed by the larger than theoretical deflections of Fig. 8. The strains remained virtually unchanged during the 3 yr from 1976 until 1979.

Slip Measurements Across Splice at Station 5/6W.—The measurements across the splice at the location shown in Fig. 4 were made in order to determine whether or not slippage occurred during or after construction of the concrete deck. Of the measurements indicated in Fig. 6, the pairs of measurements numbered 6–13 would, by comparison, indicate whether or not relative deformation between the splice plates and the bridge segments occurred. All the measurements indicated that no slip occurred across the splice.

Cracks.—The high shrinkage, the temperature, and the sequence of casting chosen for the production of the deck resulted in the formation of numerous cracks in the deck, particularly in deck segment 7. Crack width measurement were taken after the 180 ft (54.9 m) long deck of span CD had been poured on July 4.

Pouring of span BC introduced substantial negative moments in span AB, which resulted in tensile stresses in, and cracking of, the deck concrete in that span. Similarly, pouring of span CD produced tensile stresses in the concrete deck in the adjacent spans BC and DE.

The cracks extended over the full width of the deck and were spaced at 12–16 in. (300–400 mm). Measurement of about 200 cracks showed an average crack width of 0.0035 in. (0.09 mm) and a maximum width of 0.0087 in. (0.22 mm), which is well below the maximum value of 0.013 in., which corresponds to the Z value of 175 for exterior exposure, given by the American Concrete Institute, ACI Code 318-77 (2).

Conclusions

Temperature.—The most important finding in this study is the large temperature difference of 73° F (41° C) between the concrete deck and the steel box exposed to the sunlight. This temperature difference developed in less than 2 hr.

The box-type bridge with a composite deck appears to generate high temperature differences because of the enclosed air space inside the box, which seems to warm up quickly. It may be assumed that the dark color of the corrosion resistant steel accelerates the heating process.

It must be emphasized that the measured value of 73° F (41° C) does not

represent a maximum value. Values of 90° F (50° C) and more must be expected under extreme conditions. It is recommended that differential thermal stresses be considered in the design of composite box girder bridges. Several analytical methods are available for calculating such stresses (4, 8, 9, and 10).

According to the present American Association of State Highway and Transportation Officials, AASHTO, specification (1), there is no requirement to design for thermal gradients.

Concrete Deck.—Cracking of the concrete deck is to be attributed to the following causes: (1) Temperature developed in concrete deck shortly after casting; (2) sequence of casting; (3) shrinkage of deck concrete; and (4) rapid heating of the steel boxes exposed to direct sunlight.

The concrete deck was subjected to tensile stresses from the beginning. The heat of hydration and the sunlight caused the deck concrete to develop a temperature about 45° F (25° C) higher than that of the steel boxes. As this temperature difference is maintained until after the deck concrete has hardened, the concrete will be subjected to substantial tensile stresses at a rather early age when cooling of the deck occurs. Controlling the heat of hydration would greatly reduce these temperature stresses.

The second substantial source of tensile stresses was the result of the sequence of construction. Casting large segments of the concrete deck in the various pans led to negative moments in the adjacent spans, causing tension in the concrete deck. This effect would have been less pronounced if smaller sections of the deck concrete had been poured alternatively in adjacent spans.

Shrinkage of the deck concrete is the third major source of tensile stresses. With a free shrinkage of approximately 410×10^{-6} determined for the deck concrete, considerable tension must be introduced. The shrinkage-induced compression in the steel box led to a measured strain of about -80×10^{-6} corresponding to a tensile stress in the concrete of nearly 500 psi (3.45 MPa) which is in excess of the tensile strength of the concrete. To decrease these high stresses, shrinkage should be reduced as much as possible.

Finally, there was the temperature difference of 73° F (41° C) between the sunlit web of the west steel box and the concrete deck. This temperature difference alone would have been large enough to cause cracking of the concrete deck. The maximum and average recorded crack width is 0.0087 in. (0.22 mm) and 0.0035 in. (0.09 mm), respectively. The only way cracking can be prevented is by prestressing the deck slab.

Strain Distribution.—With regard to the variation of strains across the box, it can be stated that the strain distribution is more or less linear over the depth of the web plates and the width of the bottom plates. The linearity of the strain distribution confirms that the beam theory can be applied with confidence for the analysis of structures of this type. Strain measurements across a field splice indicate that no slip occurred at the splice. Other measurements confirmed that no slip occurs between the concrete deck and the steel girders.

Stiffness and Deflection.—Cracking of the deck concrete resulted in a reduction of the stiffness of the structure. However this seems to have little effect on live load capacity of the bridge at service load level (5).

Acknowledgment

The writers wish to express their gratitude to J. Quong and D. W. Anderson,

Public Works Canada, Whitehorse Office, for their assistance in the fieldwork and to T. Baker, Public Relations and Information Services, Public Works Canada, for his contributions during the preparation of this paper.

APPENDIX.—REFERENCES

1. American Association of State Highway and Transportation Officials, "Standard Specifications for Highway Bridges," 12th ed., Washington, D.C., 1977, p. 496.
2. American Concrete Institute, "Building Code Requirement for Reinforced Concrete," ACI Standard 318-77, Dec., 1977, p. 102.
3. Berwanger, C., and Sarkar, A. F., "Effect of Temperature and Age on Thermal Expansion and Modules of Elasticity of Concrete," *The Behavior of Concrete under Temperature Extremes*, ACI publication SP39, 1973, pp. 1–22.
4. Berwanger, C., and Symko, Y., "Thermal Stresses in Steel-Concrete Composite Bridges," *Canadian Journal of Civil Engineering*, Vol. 2, No. 1, March, 1975, pp. 66–84.
5. Cheung, M. S., and Chan, M. Y. T., "Live Load Field Testing on the Muskwa River Bridge," *Canadian Journal of Civil Engineering*, Vol. 5, No. 2, 1978, pp. 186–201.
6. Comité Euro-International du Béton-Federation Internationale de la Précontrainte, "Model Code for Concrete Structures," Paris, 1978, p. 348.
7. Dilger, W. H., and Ghali, A., "Field Measurements on the Muskwa River Bridge," Research Report Submitted to Public Works Canada, March, 1977, p. 76.
8. Dilger, W. H., and Ghali, A., "Temperature Induced Stresses in Composite Box Girder Bridges," Research Report Submitted to Public Works Canada, Oct., 1980, p. 179.
9. Emanuel, J. H., and Hulsey, J. L., "Temperature Distributions in Composite Bridges," *Journal of the Structural Division*, ASCE, Vol. 104, No. ST1, Proc. Paper 13474, Jan., 1978, pp. 65–78.
10. Hunt, B., and Cooke, N., "Thermal Calculations for Bridge Design," *Journal of the Structural Division*, ASCE, Vol. 101, No. ST9, Proc. Paper 11545, Sept., 1975, pp. 1763–1781.

PREDICTION OF TEMPERATURES IN CONCRETE BRIDGES

By Allan Churchward,[1] and Yehuda J. Sokal,[2] M. ASCE

INTRODUCTION

Concrete bridges are subjected to continuous heating and cooling from the environment and solar radiation. This may cause undesired deformations and stresses. The main types of deformations are longitudinal expansion, and contraction and vertical deflections. The first is caused by changes in average temperature within the bridge sections, while the second results from a vertical temperature gradient across sections. Knowledge of the vertical temperature profile gives information on both types of deformations. This paper includes the description of the experimental program aimed at collecting data on temperature distributions in a poststressed concrete bridge section, and the processing of the recorded temperatures to yield information for the possible analytical prediction of the temperature distribution in similar sections, with minimum necessity for repetition of measurements. This paper is based on research performed by the Main Roads Department, Queensland, and the University of Queensland (5). Unless otherwise specified, the temperatures throughout the paper are given in degrees Celsius (°C).

GENERAL EFFECT OF TEMPERATURES ON BRIDGES

Figs. 1 and 2 show the decomposition of the temperature strain across the section to uniform, linear, and nonlinear components. In that decomposition, each component is responsible for a different type of deformation.

In simple supported beams, stress is induced from the nonlinear component, STS only. In continuous beams, stress is induced from all three components, with major contributions from Curvature Inducing Strain Component, CURS, and Stress Inducing Strain Component, STS.

It is important to emphasize that the magnitude of the temperatures to be used in the design must be relative to the reference magnitude at the time that thermal restraint occurred.

[1]Engr., Main Roads, Dept., Brisbane, Queensland, Australia.
[2]Lect. in Civ. Engrg., Univ. of Queensland, Brisbane, Queensland, Australia.

Note.—Discussion open until April 1, 1982. To extend the closing date one month, a written request must be filed with the Manager of Technical and Professional Publications, ASCE. Manuscript was submitted for review for possible publication on July 14, 1980. This paper is part of the Journal of the Structural Division, Proceedings of the American Society of Civil Engineers, ©ASCE, Vol. 107, No. ST11, November, 1981. ISSN 0044-8001/81/0011-2163/$01.00.

Aim of Investigation

The present investigation aimed at establishing a mathematical model for the prediction of the temperature distribution from the knowledge of several environ-

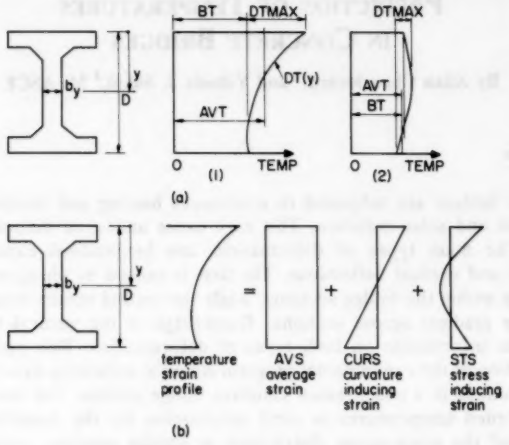

FIG. 1.—Temperature and Strain Distribution in Section: (*a*) Temperature Variables; (*b*) Temperature Induced Strains

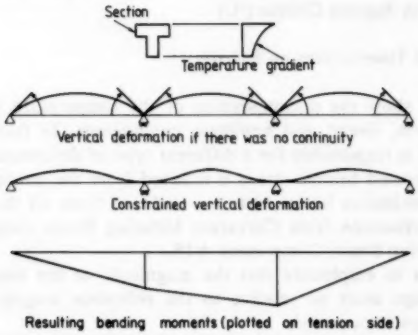
Section
Temperature gradient
Vertical deformation if there was no continuity
Constrained vertical deformation
Resulting bending moments (plotted on tension side)

FIG. 2.—Development of Temperature Bending Moments in Continuous Bridge

mental parameters, such as ambient temperatures, solar radiation, wind velocity, and hours of sunshine, and from the temperature on the top surface of the section.

Experimental Program

A section of a recently completed bridge had been instrumented with copper

constantan thermocouples and measurements were made continuously throughout a three-year period. Figs. 3 and 4 show a typical cross section of the bridge and the particular section investigated, together with positioning of the thermo-

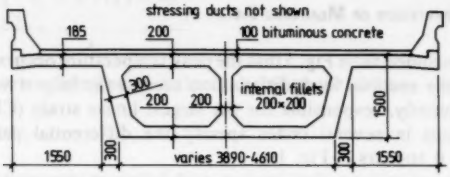

FIG. 3.—Detail of Investigated Section

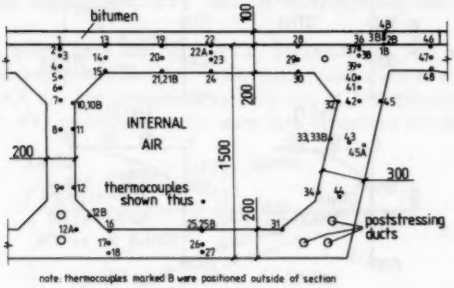

FIG. 4.—Positioning of Thermocouples

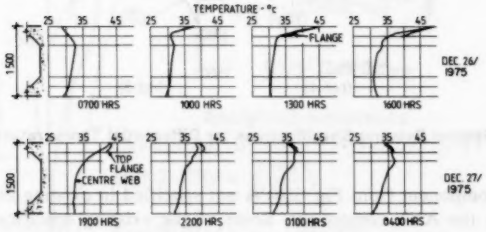

FIG. 5.—Temperature Profiles at Various Times of Day

couples. Simultaneously with temperatures, the following environmental parameters have been recorded:

1. Minimum and maximum ambient air temperatures in degrees C° (AMIN and AMAX).
2. Solar radiation (insolation) in Joules/M × Day.
3. Hours of sunshine per day (HS).

It was found that the temperature distribution in all webs is almost identical, while there is a small variation across the flange, which shows the recorded temperature profiles at different times Fig. 5.

Means of Interpretation of Measured Data

It may be concluded from Fig. 5 that the peak temperature occurs predominantly on the top of the section. Such distribution creates the largest vertical gradient and is, consequently, responsible for the largest linear strain (CURS). Existing recommendations in several codes specify the differential part only of the distribution as it appears in Fig. 1.

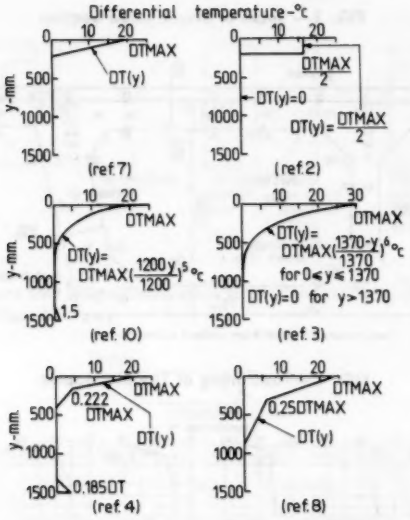

FIG. 6.—Several Existing Specifications for Differential Temperature Gradient

The BT component from Fig. 1(*a*) is not specified in existing codes; instead, they specify the AVT component. Some of the existing specifications for the differential part DT(y) are shown in Fig. 6.

The interpretation of the measured data has been directed towards a similar representation. Previous investigators (11,9) have indicated that the lower part of the temperature distribution is negligibly affected by daily changes in atmospheric conditions, and is also independent of the depth of the section below approx 3.28 ft (1 m) depth. If the last statement can be generally accepted, then the data from this particular investigation could be used directly in the design of some other bridges in similar environments. For the purpose of this investigation, the average value from thermocouples No. 9 and 12 (Fig. 4) has been used as a representative for that temperature subsequently defined as

Base Temperature (BT). This means that AVT component (Fig. 1) can be computed from BT and DT(y) by simple addition and integration:

$$AVT = BT + \frac{\int_0^D b_y \times DT(y) \times dy}{A} \quad \ldots\ldots\ldots\ldots\ldots\ldots\ldots\ldots\ldots\ldots (1)$$

BT and DT(y) are subsequently defined as design variables.

Processing of Data

From the continuously recorded data, several daily profiles have been selected at specific times of the day. The chosen times correspond to the occurrence to the maximum differential temperature on the top, DTMAX, maximum and minimum average temperature, AVT, and the corresponding base temperature, BT.

It should be noted here that like AVT, DTMAX has two extreme daily occurrences: maximum and minimum. In this paper, temperatures with a minimum value of DTMAX are not presented as they are of little importance for the Brisbane region. The recorded profiles were then processed for the following:

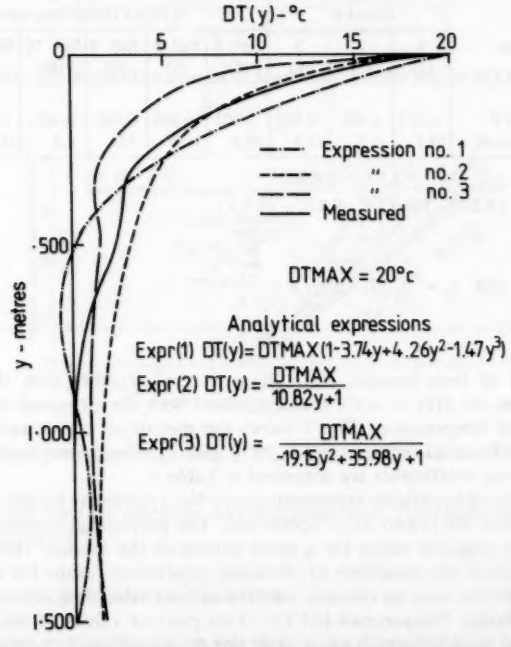

FIG. 7.—Plot of Measured and Calculated Curves for DT(y)

1. Least squares curve fitting for the establishment of an analytical expression to define the profile DT(y).
2. Extraction of BT.
3. Correlation between BT, DTMAX, and AVT.
4. Relation with environmental parameters as stated before.

Presentation of Results

Differential Temperature Profile [DT(y)].—Several analytical profiles for DT(y) were attempted. All of these were of the form similar to the existing specifications, i.e., function of the depth $f(y)$ multiplied by DTMAX in which y is measured from the top. The attempted expressions were calculated using

TABLE 1.—Correlation Coefficients and Error Coefficients for Suggested and Existing Curves DT(y)

	TEMPERATURE GRADIENT DT(y)								
	Developed in This Investigation Number			From Other Sources					
Number (1)	1 (2)	2 (3)	3 (4)	Ref. 8 (5)	Ref. 4 (6)	Ref. 3 (7)	Ref. 10 (8)	Ref. 7 (9)	Ref. 2 (10)
Correlation coefficient $\bar{r}$	0.971	0.992	0.929	0.971	0.949	0.983	0.980	0.951	0.830
Error coefficient $\bar{e}$	10.1	6.5	12.7	10.8	11.8	7.0	8.3	14.1	24.1

Note: $r_k = \dfrac{N\Sigma T_i t_i - \Sigma T_i \Sigma t_i}{(N\Sigma t_i^2 - (\Sigma t_i)^2)^{1/2}\,(N\Sigma T_i^2 - (\Sigma T_i)^2)^{1/2}}$;

$\bar{r} = \dfrac{\sum_{k=1}^{K} r_k}{K}$; and $e_k = \sum_{i=1}^{N} |T_i - t_i|$; $\bar{e} = \dfrac{\sum_{i=1}^{K} e_k}{K}$

the method of least squares (12). These curves, together with the existing specifications for DT(y), were then correlated with the measured data for the magnitude of temperatures. Fig. 7 shows the plot of all curves calculated for DTMAX (differential temperature) = 20° C (36° F). The corresponding correlations and error coefficients are presented in Table 1.

The calculated hyperbolic expression (curve No. 2) gives the highest correlation coefficient and the lowest error coefficient. The polynomial expression (curve No. 1) gives negative values for a small portion of the section. However, this does not exclude the possibility of obtaining satisfactory results for structurally important effects, such as stresses, curvatures, and axial elongations.

Average Bridge Temperature (AVT).—Two pairs of values of maximum BT and DTMAX were chosen on the straight line drawn arbitrarily across the upper boundary of the plot of coexisting occurrences shown in Fig. 8. The chosen

values were then used to calculate AVT using Eq. 1 in which DT(y) was taken from Figs. 6 and 7. The calculated values of max AVT are plotted in Fig. 9.

Fig. 9 allows drawing the following two conclusions:

1. The good correlation between the measured AVT and BT indicates that the component of DT(y) in AVT is significant (approx 17% in Fig. 9).
2. The differential temperature component in the maximum value of AVT can be safely computed from almost all available DT(y) curves.

As for the minimum AVT, it was found that the DT(y) component is very

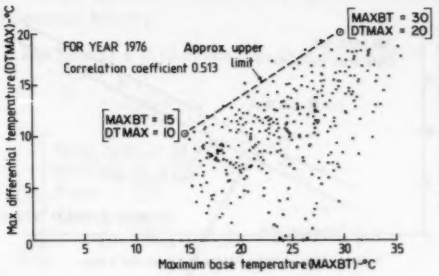

FIG. 8.—Mutual Occurrence of Measured DTMAX and of MAXBT

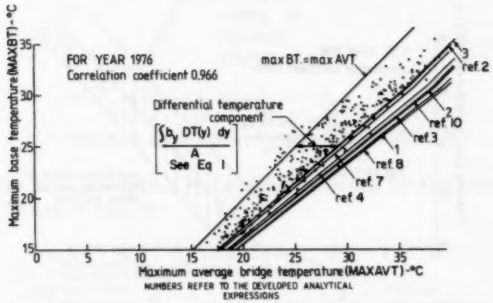

FIG. 9.—Mutual Occurrence of Measured MAXBT and of MAXAVT

small, and for practical purposes may be disregarded. Therefore, minimum AVT equals minimum BT.

Correlation with Environmental Parameters

Correlation was attempted for two design variables, DTMAX and BT, using linear relationships only. For DTMAX reasonably good correlation was obtained

with insolation (I). Fig. 10 shows the plot of the mutual occurrence of DTMAX and of insolation. The highest correlation coefficient of 0.912 is given by the equation

$$\text{DTMAX} = 0.6278 \times I - 1 \quad \ldots\ldots (2)$$

while 90% of measured data lies beneath the line given by the equation

$$\text{DTMAX} = 0.6278 \times I + 1 \quad \ldots\ldots (3)$$

Values of maximum BT are well correlated with maximum ambient temperature

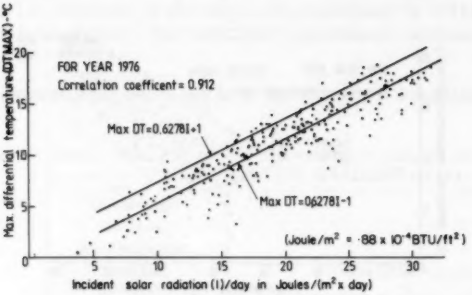
Max. differential temperature(DTMAX) - °C
FOR YEAR 1976
Correlation coefficent = 0.912
Max DT=0.6278I+1
Max DT=0.6278I-1
(Joule/m² = ·88 x 10⁻⁴BTU/ft²)
Incident solar radiation (I)/day in Joules/(m² x day)

FIG. 10.—Mutual Occurrence of Measured MAXDT and I

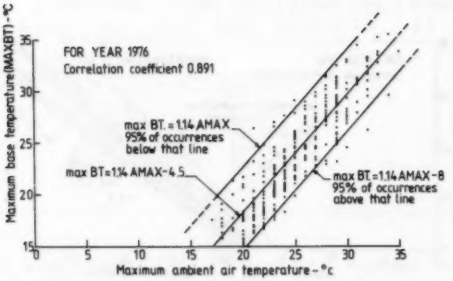

FIG. 11.—Mutual Occurrence of Measured Maximum Base Temperature and of Maximum Ambient Air Temperature

AMAX (Fig. 11). This relationship can be represented by the following two equations:

$$\text{BT} = 1.14\,\text{AMAX} \quad \ldots\ldots (4)$$

gives 5% only of measured occurrences exceeding BT, and

$$\text{BT} = 1.14\,\text{AMAX} - 8 \quad \ldots\ldots (5)$$

gives 95% of measured occurrences exceeding BT. Good correlation was also

obtained between BT and the temperature history, i.e., with ambient temperatures recorded during the previous days, proving that BT is less affected by instantaneous temperature changes, or by direct solar radiation on that particular day. This relationship is presented in the following equation

$$BTMAX = 0.48\ AMAX + 0.43\ AMIN + 0.46\ AMAX\ (-1) - 0.14\ AMIN\ (-1) - 4.7 \quad (6)$$

in which (-1) signifies the temperature recorded one day prior to the recording of the BT. The correlation coefficient for this relationship was 0.956. The interesting feature in this relationship is the almost equal coefficients in the first three terms. For the minimum value of BT, good correlation was obtained using longer temperature history.

$$BTMIN = 0.47\ AMAX\ (-1) + 0.18\ AMAX\ (-2) + 0.74\ AMIN - 0.17\ AMIN\ (-1) - 2 \quad (7)$$

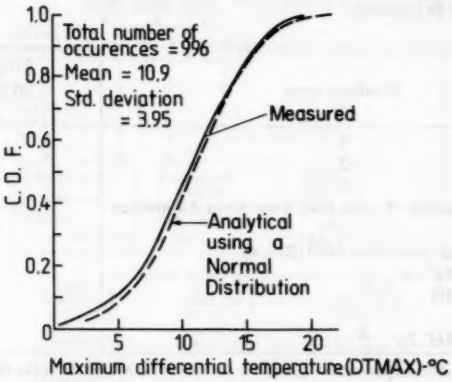

FIG. 12.—Three Years Cumulative Probability Distribution for Maximum Differential Temperature on Top of Section

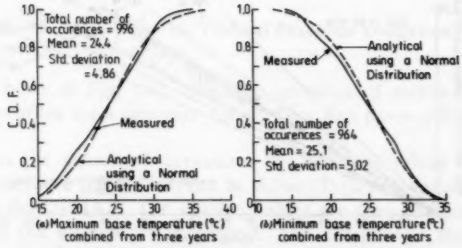
Total number of occurences = 996
Mean = 24.4
Std. deviation = 4.86
Measured
Analytical using a Normal Distribution
C. D. F.
(a) Maximum base temperature (°C) combined from three years
Analytical using a Normal Distribution
Measured
Total number of occurences = 964
Mean = 25.1
Std. deviation = 5.02
(b) Minimum base temperature (°C) combined from three years

FIG. 13.—Three Years Cumulative Distribution of Maximum and Minimum Base Temperatures

The correlation coefficient for this relationship was 0.94. The interesting feature in this equation is the relatively large coefficients for the minimum temperature, AMIN, and the previous day's maximum temperature, AMAX (−1). Hours of sunshine (HS) gave, in general, poor correlation.

Probability Distributions

Tests were performed to check the probability distributions of the maximum and minimum values of the design variables DTMAX and BT. It is believed that the knowledge of the probability of occurrence of these variables could be helpful in the choice of the design values. For that purpose, cumulative distributions of the recorded values were plotted, together with the theoretical normal cumulative distributions for the same values of the mean and standard deviations. Plots of both distributions are in Figs. 12 and 13.

TABLE 2.—Percent Differences in Curvatures Calculated from Measured Data and from Analytical Expressions

Gradient type (1)	Differences in percent (2)
1	+1[a]
2	−17
3	−45
National Association of Australian State Road Authorities (Ref. 8)	+25
British Standards Institution 5400 (Ref. 4)	−18
New Zealand (Ref. 3)	+7
Priestley (Ref. 10)	0
Maher (Ref. 7)	−16
New Zealand (Ref. 2)	−30

[a]+1 indicates that Expression 1 gives curvatures which overestimate the average upper limit of curvatures from measured gradients by 1%.

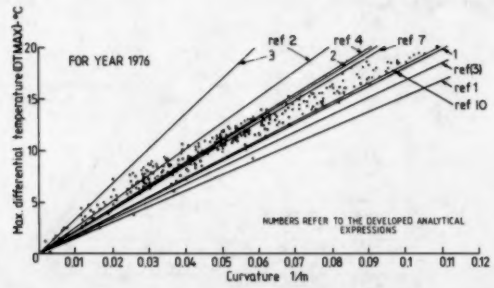

FIG. 14.—Calculated Curvatures Using Measured and Calculated Temperature Gradients

Visual inspection of these figures shows a reasonably good agreement. Theoretical distributions tend to be more conservative for extremely higher and extremely lower temperatures.

Curvatures Determined from Empirical Distributions

The curvatures generated by differential temperature gradient may be used as an indication of the resulting deformations and stresses in continuous bridge structures. For that purpose, all aforementioned empirical gradients (existing and new) have been processed to yield the curvature which generated linear

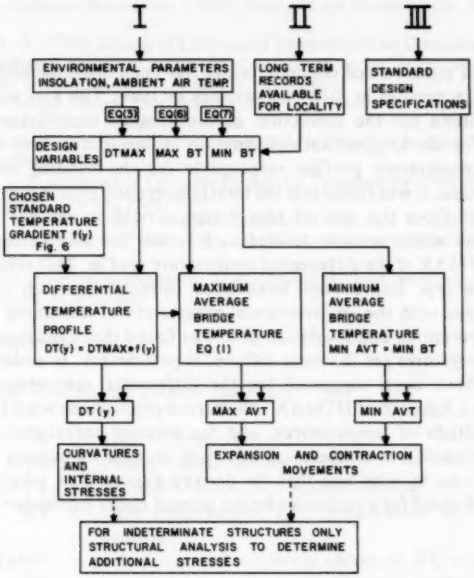

FIG. 15.—Flow Chart for Thermal Response Evaluation

strain CURS, shown in Fig. 1(*b*), using the investigated section from Fig. 3. The measured profiles for a one-year period were also processed and are used in comparison.

Fig. 14 shows the calculated curvatures for different values of maximum differential temperature DTMAX. It can be shown (5) that curvatures are always proportional to the DTMAX. The relative values are then computed in Table 2, which shows the differences in percent. The comparison shows that the empirical expression from Ref. 10 gave the best correlation, while the newly derived expression No. 2, which gave the best correlation for temperature magnitudes, underestimates curvatures.

Implementation in Analysis and Design

The method involved in determining the thermal effects, either for design purposes or for a response, is shown in Fig. 15. The flow chart represents several approaches to the evaluation of response depending on available information and desired accuracy.

The most complete approach would consist of obtaining data from long-term temperature records, and this is shown in approach II. Approach I requires data on environmental parameters and their history, but eliminates the necessity for long-term temperature measurements. If a crude approximation is satisfactory, then approach III may be sufficient, subject to availability of design specifications.

Conclusions

A section of poststressed concrete bridge has been instrumented for recording of temperature profiles at different instants of time. The aim was to establish analytical criteria for the prediction of the average temperatures, which are responsible for the longitudinal deformation of the bridge, and of the vertical differential temperature profiles responsible for the bending deformations in the vertical plane. It was found that the total temperature profile may be reasonably well predicted from the sum of two design variables: one having a constant value over the whole section defined as BT, and the second representing the maximum DTMAX of the differential temperature profile. This ordinate generally occurs at the top. Expressions have been formulated which correlate these design variables with the environmental parameters of maximum and minimum ambient temperatures and insolation as it was found that insolation and extreme ambient temperatures are the most influential parameters. In addition, analytical expressions have been suggested for the differential temperature profile, all of them being a function of DTMAX. All derived expressions were then correlated for the magnitude of temperatures, and for induced curvatures. It was found that good correlation in temperature does not necessarily happen in curvatures. It should be kept in mind also that the derived expressions, whether successful or not, were derived for a particular bridge section under particular environmental conditions.

Suggestions for Future Research

It is recommended that temperature recordings of similar bridges and of other types of bridges be accompanied by the measurements of stresses and deformations. Temperature affects structures through the difference in its magnitude; therefore, the choice of the datum temperature for each particular case also must be investigated.

Acknowledgments

The writers wish to thank the Commissioner of Main Roads, Queensland, Australia, and the Executive Director, Australian Road Research Board, for the funding of this project and for permission to publish this paper.

Appendix I.—References

1. Ang, A. H. S., and Tang, W. H., "Probability Concepts in Engineering Planning and Design," John Wiley and Sons, Inc., New York, N.Y., 1975.
2. "Bridge Design—Temperature Gradient," Ministry of Works, Civil Engineering Division, MOW, New Zealand, 1970.
3. "Bridge Design—Temperature Gradients," Ministry of Works, Civil Engineering Division, MOW, New Zealand, 1974.
4. British Standards Institution, "BS 5400: Part 1: 1978," London, England, 1978.
5. Churchward, A., "Thermal Response of a Concrete Box Girder Bridge," thesis presented to the University of Queensland, at Queensland, Australia, in 1979, in partial fulfillment of the requirements for the degree of Master of Science.
6. Emerson, M., "Bridge Temperatures and Movements in the British Isles," *Road Research Laboratory Report No. LR228*, Dept. of the Environment, England, 1968, 39 pp.
7. Maher, D. R. H., "The Effects of Differential Temperature on Continuous Prestressed Concrete Bridges," presented at the 1969 Conference on the Deformation of Concrete and Concrete Structures, held at Brisbane, Australia.
8. "NAASRA Bridge Design Specification, 1976," National Association of Australian State Road Authorities, Sydney, Australia.
9. Priestley, M. J. N., "Design Thermal Gradients for Concrete Bridges," *New Zealand Engineering*, Sept., 1976.
10. Priestly, M. J. N., "Design of Concrete Bridges for Temperature Gradients," *American Concrete Institute Journal*, May, 1978.
11. Radolli, M., and Green, R., "Thermal Stresses in Concrete Bridge Superstructures under Summer Conditions," *Transportation Research Record*, Washington, D.C., No. 547, pp. 23–35, 1976.
12. Young, H. D., *Statistical Treatment of Experimental Data*, McGraw-Hill Book Co., Inc., New York, N.Y., 1962.

Appendix II.—Notation

The following symbols are used in this paper:

A = area of cross section;
AVS = average strain across section;
AVT = average temperature across section;
BT = base temperature, i.e., temperature at lower part of section;
BTMAX, BTMIN = maximum and minimum values of BT, respectively;
CT = constant temperature across cross section;
CURS = curvature inducing strain component;
D = depth of section;
DT(y) = differential temperature magnitude at top of section;
DTMAX = differential temperature magnitude at top of section;
e_k = error coefficient calculated for one particular profile of temperature gradient;
$\bar{e}$ = overall error coefficient;
I = incident solar radiation (insolation) in Joules/(m^2/day);
i = lower suffix used as counter indicator in summations;
K = total number of temperature profiles involved in calculation or error correlation coefficients;
k = lower suffix to denote that error or correlation coefficient is for one particular profile of temperature gradient;

M = number of design variables used in calculation of probability distributions;
N = number of nodal points along vertical axis of bridge section where temperature has been measured and correlated;
r_k = correlation coefficient calculated for one particular profile of temperature gradient;
$\bar{r}$ = overall correlation coefficient;
STS = stress inducing strain component;
T_i = calculated temperature at node i;
t_i = measured temperature at node i along vertical axis of web; and
Σ = (Greek sigma) denotes sum of.

DISCRETE STRUCTURAL OPTIMIZATION

By Judith S. Liebman,[1] Narbey Khachaturian,[2] F. ASCE, and Visarn Chanaratna[3]

INTRODUCTION

Optimization problems in structural design are predominantly of a discrete type in which the variables can assume only certain predetermined quantities. Among the problems that commonly arise in structural design is the selection of standard steel sections for continuous, or frame structures. The design of reinforced or prestressed concrete structures represents another example in which both the amount of steel and the dimensions of concrete are discrete variables. The amount of reinforcement is determined on the basis of the standard sizes available, and the dimensions of concrete used in practice are usually within the nearest half-inch. Thus, from a practical standpoint it is more convenient to formulate the design problem with discrete variables than it would be if the variables were assumed to be continuous.

Several researchers have attempted to develop methods for discrete optimization of structures (6,8,9). Toakley (8) formulated the optimal plastic design of frame structures as a discrete problem, in which the solution space consisted of the available standard sections, and solved it by using a mixed integer-continuous programming algorithm. Lai and Achenbach (6) presented a direct search algorithm to solve nonlinear optimization problems in which the variables were discrete. Twisdale and Khachaturian (8) developed a dynamic programming approach which is efficient for certain classes of problems but which has the usual limitations associated with dimensionality.

The method presented here is based on a search technique developed by Glankwahmdee, Liebman and Hogg (4) specifically for nonlinear discrete unconstrained optimization problems. The method is adapted to problems of structural optimization which are mostly constrained by using interior penalty functions (3,5). The method is reasonably efficient and is convenient, since it utilizes concepts developed for problems with continuous variables to solve problems with discrete variables. In the following paragraphs the method is presented,

[1]Assoc. Prof. of Operations Research, Dept. of Mechanical and Industrial Engrg., Univ. of Illinois at Urbana-Champaign, Urbana, Ill. 61801.

[2]Prof. of Civ. Engrg., Univ. of Illinois at Urbana-Champaign, Urbana, Ill. 61801.

[3]Dept. of Engrg., Chulachomklao Royal Military Academy, Bangkok, Thailand.

Note.—Discussion open until April 1, 1982. To extend the closing date one month, a written request must be filed with the Manager of Technical and Professional Publications, ASCE. Manuscript was submitted for review for possible publication on November 9, 1979. This paper is part of the Journal of the Structural Division, Proceedings of the American Society of Civil Engineers, ©ASCE, Vol. 107, No. ST11, November, 1981. ISSN 0044-8001/81/0011-2177/$01.00.

and several examples are included to illustrate the method. Computational problems are also described.

Discrete Programming Problems

In general, a constrained optimization problem subject to inequality and equality constraints can be expressed as:

$$\min F(X) \quad \ldots\ldots (1)$$

$$\text{subject to} \quad \phi_i(X) \geq 0 \quad i = 1, 2, \ldots, m \quad \ldots\ldots (2)$$

$$\psi_j(X) = 0 \quad j = 1, 2, \ldots, p \quad \ldots\ldots (3)$$

$$\mathbf{X} \geq 0 \quad \ldots\ldots (4)$$

in which $\mathbf{X}$ = the N-dimensional independent design variable vector; $F(X)$ = the objective function; $\phi_i(X)$ are the inequality constraints imposed upon $\mathbf{X}$, and $\psi_j(X)$ are the equality constraints imposed upon $\mathbf{X}$.

When there are no restrictions upon $\mathbf{X}$, except the conditions of non-negativity, the problem may be treated as an unconstrained optimization problem. When the variables $\mathbf{X}$ are assumed to have continuous values, there are many methods of solutions available. However, when $\mathbf{X}$ may only assume discrete values, $F(X)$ and all of the constraint functions exist only at discrete points. Among the several search methods for discrete unconstrained problems, the method of integer gradient direction (4) is particularly promising for structural design problems.

The general procedure of the method of integer gradient directions is as follows:

1. Select an initial feasible base point (XB).
2. Generate the integer gradient direction $GM(XB)$:
   (a) Calculate $G(XB)$, the approximate gradient at (XB):

$$G(XB) = \frac{[F(x + \Delta x) - F(x - \Delta x)]}{2\Delta x}, \quad \text{or}$$

$$G(XB) = \frac{(F(x + \Delta x) - F(x))}{\Delta x}$$

   (b) Calculate $S(XB)$, the normalized gradient direction at XB:

$$\frac{S(XB) = -G(XB)}{\|G(XB)\|}$$

   (c) Calculate $DR(XB)$, the relative gradient direction at XB: $DR(XB) = S(XB)/s$, where s is the smallest (in absolute value) element of S.
   (d) Calculate $GM(XB)$, the integer gradient direction vector at XB by changing values in $DR(XB)$ to the nearest integer value.
3. Perform a one-dimensional search along the direction $GM(XB)$ until the best improved objective function is found. Any discrete point, XT, along the direction of $GM(XB)$ can be generated from the equation

$$(XT) = (XB) + \lambda \cdot (\Delta x) \cdot GM(XB) \quad \ldots\ldots (5)$$

in which λ represents the position number of all the discrete points (XT) in the direction $GM(XB)$ starting from (XB) and can be any integer; Δx is a diagonal matrix of discrete step sizes in which the ith diagonal component is the step size of the ith design variable.

4. Redefine (XB) to be the just-found best improved solution point and generate the new search direction $GM(XB)$. If (XB) is local optimum, stop. Otherwise go to step 3.

One way by which constrained problems can be solved is converting them into a sequence of unconstrained problems by use of penalty functions. Each unconstrained problem in the sequence can then be solved by the aforementioned method. The problem formulation becomes

$$\min P(X,r) \equiv F(X) + r\,I(X) \quad \ldots\ldots\ldots\ldots\ldots\ldots\ldots\ldots\ldots\ldots (6)$$

in which $P(X,r)$ = the parametric objective function; r = the penalty function parameter; and $I(X)$ = an interior penalty function of the original inequality design constraints $\phi_i(X)$. The original equality constraints, $\psi_j(X)$, in structural optimization represent limitations imposed by stresses or deformations of various elements of the structural systems. The equality constraints are the equations used to analyze the structure. For small problems, these equalities can be used directly to reduce the size of the problem. For larger problems, the structure can be analyzed in each step to obtain the forces and the stresses that are necessary for the evaluation of the inequality constraints. This approach limits the formal expression of the problem to inequality constraints only.

The second term on the right-hand side of Eq. 6 is the penalty term, in which $I(X)$ can be one of several functional forms. For a sequence of gradually decreasing positive values of the penalty function parameter r, Eq. 6 can be visualized as a sequence of unconstrained optimization problems which converge to a discrete locally optimal solution of the original constrained problem.

The following terminology and definitions will conveniently be employed in the review of the constrained problem.

A *principal axis* is a coordinate axis, and Δx_i is the shortest distance between two discrete points on a line parallel to x_i-axis. A *unit neighborhood*, N1(X) of the discrete point X contains all the points whose components do not differ more than $\pm\Delta x_i$ from $X = x_i$, $i = 1, 2, \ldots n$. We will designate $\bar{S}$ as the set of all feasible points, that is

$$\bar{S} = \{X | \phi_i(X) \geq 0,\ i = 1, 2, \ldots, m \quad \text{and} \quad \psi_j(X) = 0,\ j = 1, 2, \ldots, p\}$$

We will designate $\bar{S}_B$ as the set of all discrete boundary points in $\bar{S}$ whose principal neighborhood contains points that violate one or more constraints, and $\bar{S}_I$ is the set of all discrete interior points which includes all points that lie in $\bar{S}$ but not in $\bar{S}_B$.

For structural optimization problems, in which the objective function is the cost or the weight, the discrete optimal solution will be a point in $\bar{S}_B$ and not $\bar{S}_I$. This is true because, if the constraints specifying the structural requirements are ignored, the minimum weight or minimum cost solution is a structure violating the requirements. However, these discrete boundary points need not lie on the boundary of the corresponding continuous problem. Thus, a discrete optimal

solution of Eqs. 1–4 may not satisfy any of the inequality constraints 2 exactly. In fact, it is unlikely to do so.

The interior penalty function, $I(X)$, of the unconstrained problem of Eq. 6 must be in a form such that its value is non-negative at every point in the feasible set $\bar{S}$ and increases to a large number as a discrete boundary point is approached. Thus, the primary role of the interior penalty function is to insure that the discrete optimal solution of the unconstrained problem seen in Eq. 6 is feasible to the constrained problem found in Eqs. 1–4. The function $I(X)$ adopted in this study is a modification of the one first introduced by Carroll (2) and used frequently by others:

$$I(X) = \sum_{i=1}^{m} \frac{1}{\phi_i(X) + \epsilon\delta_i} \quad \ldots\ldots\ldots\ldots\ldots\ldots\ldots\ldots\ldots\ldots\ldots\ldots\ldots\ldots (7)$$

in which ϵ is some very small quantity; and δ_i is 1 if the constraint is satisfied exactly and 0 otherwise.

Our modification is the addition of the $\epsilon\delta_i$ term which is necessary with discrete variables. In the use of penalty functions with continuous variables, the constraint boundaries are approached smoothly but never reached exactly. With the discrete variables however, points that exactly satisfy one of the inequality constraints, that is, for which $\phi_i(X) = 0$, may well be evaluated during the discrete search process. From Eq. 7, as long as the direct search remains in $\bar{S}$, the value of $I(X)$ is non-negative, and has a relatively small value at a solution that is far from the boundaries, and becomes larger as the boundaries are approached.

In order for the penalty function approach to reach a locally optimal solution, the penalty function parameter r in Eq. 6 must assume a monotonically decreasing sequence of positive numbers, approaching zero in the limit. In this study a sequence of the r values is chosen such that

$$r_2 = \frac{r_1}{a},\ r_3 = \frac{r_2}{a},\ \ldots\ r_{k+1} = \frac{r_k}{a} \quad \ldots\ldots\ldots\ldots\ldots\ldots\ldots\ldots\ldots\ldots\ldots\ldots (8)$$

in which a = a constant number.

In order to begin the solution, values of the parameters r_1 and a, and the starting point $\mathbf{X}_0$, must be selected. In the problems described in this paper, r_1 was chosen for a starting point $\mathbf{X}_0$ so that initially the penalty term $r_1 I(x)$ did not dominate the problem. For the reduction factor a, a value of 10 was satisfactory for the smaller example problems, but it was necessary to have $a = 4$ to obtain convergence on larger and more complex problems.

In the examples that follow, in order to begin with an initial feasible solution, the algorithm was started with an obviously conservative design. This approach was used to demonstrate the convergence of the method as well as its generality. In a practical situation it is possible to estimate an initial feasible solution that is closer to the optimal design.

Although in theory this approach requires only that the values of r converge to zero, it is crucial to select an initial value for r and a rate of reduction for r that provides a relatively well-behaved sequence of unconstrained optimization problems. These choices, therefore, are fairly problem-dependent.

Simple Example

In this section, the discrete optimal design of a simple reinforced concrete structure is illustrated. The area of the reinforcement A_s and the width of the beam b are taken as discrete design variables, and the objective function is the total cost of concrete and reinforcing steel.

The beam considered is shown in Fig. 1. The beam is assumed to be simply-supported with a span of 30 ft and an overall depth of 30 in. It is subjected to a live load of 2.0 klf and a dead load of 1.0 klf which includes the weight of the beam. The strength of concrete f'_c is 5 ksi, the yield point stress of the reinforcing steel f_y is 50 ksi, and the effective depth d is assumed to be 24 in. The cost of concrete is \$0.02/sq in./lin. ft and the cost of steel is \$1.00/sq in./lin. ft. It is intended to determine the cross-sectional area of the reinforcing steel and the width of the beam such that the total cost of the structure is minimum. The structure should be proportioned to have a required strength based upon the ACI Building Code 318-77 (1) as follows:

$$M_u = 0.9A_s f_y d\left(1 - 0.59\frac{A_s f_y}{bd f'_c}\right) \geq 1.4M_d + 1.7M_l \quad \ldots\ldots\ldots\ldots (9)$$

in which M_u = the flexural strength of the beam; and M_d and M_l = the dead

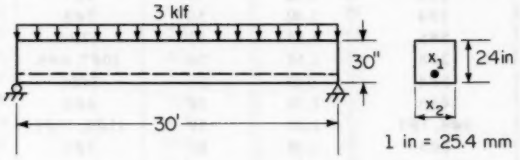

FIG. 1.—Reinforced Concrete Beam

load and live load moments, respectively. For this example, M_d = 1,350 in k and M_l = 2,700 in k. Denoting $A_s = x_1$ and $b = x_2$, the optimization problem can be stated in a simplified form as follows:

$$\text{Min } F(X) \equiv 29.4x_1 + 18x_2 \quad \ldots\ldots\ldots\ldots\ldots\ldots\ldots\ldots\ldots\ldots (10)$$

$$\text{subject to } \quad \phi(X) \equiv x_1 - 0.2458\frac{x_1^2}{x_2} - 6 \geq 0 \quad \ldots\ldots\ldots\ldots\ldots\ldots (11)$$

Before the optimization procedure is started, a discrete solution space must be established. For simplicity it is assumed that the reinforcement is made up of #4 through #9 bars, and that only bars of the same size are allowed. The available values of x_1 are tabulated and numbered in the order of increasing cross-sectional area in Table 1. For this particular problem, there are a total of 77 available values of x_1. Thus, x_1 is now represented by a number with the corresponding cross-sectional area of the steel from the table.

In practice, the width of the beam is allowed to vary discretely, usually, in half-inch increments. For this particular problem, the available solutions for x_2 are tabulated in Table 2. Thus, x_2 is represented by a number which corresponds

TABLE 1.—Design Space for Reinforcing Bars

Design number x_i (1)	Bar type (2)	Area, in square inches (3)	Design number x_i (4)	Bar type (5)	Area, in square inches (6)
1	1#4	0.20	40	5#8	3.95
2	1#5	0.31	41	9#6	3.96
3	2#4	0.40	42	4#9	4.00
4	1#6	0.44	43	13#5	4.03
5	3#4, 1#7	0.60	44	7#7	4.20
6	2#5	0.62	45	14#5	4.34
7	1#8	0.79	46	10#6	4.40
8	4#4	0.80	47	15#5	4.65
9	2#6	0.88	48	6#8	4.74
10	3#5	0.93	49	8#7	4.80
11	5#4, 1#9	1.00	50	11#6	4.84
12	6#4, 2#7	1.20	51	5#9	5.00
13	4#5	1.24	52	12#6	5.28
14	3#6	1.32	53	9#7	5.40
15	7#4	1.40	54	7#8	5.53
16	5#5	1.55	55	13#6	5.72
17	2#8	1.58	56	10#7, 6#9	6.00
18	8#4	1.60	57	14#6	6.16
19	4#6	1.76	58	8#8	6.32
20	9#4, 3#7	1.80	59	15#6, 11#7	6.60
21	6#5	1.86	60	7#9	7.00
22	10#4, 2#9	2.00	61	9#8	7.11
23	7#5	2.17	62	12#7	7.20
24	11#4, 5#6	2.20	63	13#7	7.80
25	3#8	2.37	64	10#8	7.90
26	12#4, 4#7	2.40	65	8#9	8.00
27	8#5	2.48	66	14#7	8.40
28	13#4	2.60	67	11#8	8.69
29	6#6	2.64	68	15#7	9.00
30	9#5	2.79	69	12#8	9.48
31	14#4	2.80	70	13#8	10.27
32	15#4, 5#7, 3#9	3.00	71	11#9	11.00
33	7#6	3.08	72	14#8	11.06
34	10#5	3.10	73	15#8	11.85
35	4#8	3.16	74	12#9	12.00
36	11#5	3.41	75	13#9	13.00
37	8#6	3.52	76	14#9	14.00
38	6#7	3.60	77	15#9	15.00
39	12#5	3.72			

Note: 1 in. = 25.4 mm; 1 in.^{2} = 645.16 mm^2.

to a specific value of the width of the beam (because of this transformation; $\Delta x_1 = \Delta x_2 = 1$).

The problem described by (10) and (11) must be transformed into a sequence of discrete unconstrained optimization problems, the k-th of which is of the form

$$\text{Min } P(X, r_k) \equiv F(X) + \frac{r_k}{\phi(X) + \epsilon\delta} \quad \ldots\ldots\ldots\ldots\ldots\ldots\ldots\ldots \quad (12)$$

A sequence of unconstrained discrete optima obtained by solving the above unconstrained optimization problems by the method of integer gradient direction will converge to the discrete optimum of the original constrained optimization problem.

A relatively large value must be assigned to the penalty function parameter

TABLE 2.—Design Space for Widths of Beam

Design number x_2 (1)	Beam width, in inches (2)	Design number, x_2 (3)	Beam width, in inches (4)
12	6.0	27	13.5
13	6.5	28	14.0
14	7.0	29	14.5
15	7.5	30	15.0
16	8.0	31	15.5
17	8.5	32	16.0
18	9.0	33	16.5
19	9.5	34	17.0
20	10.0	35	17.5
21	10.5	36	18.0
22	11.0	37	18.5
23	11.5	38	19.0
24	12.0	39	19.5
25	12.5	40	20.0
26	13.0		

Note: 1 in. = 25.4 mm.

of the first unconstrained problem in the sequence. This value should be large but yet it should not let the penalty term dominate the problem. If we begin the initial feasible solution at point $(XB)_1 = \begin{vmatrix} 74 \\ 24 \end{vmatrix}$ in which $x_1 = 12.00$ in.[2] and $x_2 = 12$ in. If we let $r_1 = 100$; then $F(XB)_1 = 568.60$ dollars; $(XB)_1 = 3.0504$, $r_1/\phi(XB) = 32.78$; and $P(XB, r_1) = 601.58$.

From the foregoing values, we can see that r_1 is relatively large, and the penalty term $r_1/\phi(XB)$ does not dominate $P(XB, r_1)$. A wide range of values could have been assigned to r_1, but a value of 100 was chosen for convenience. A reduction factor of $a = 10$ was used to obtain the value of the succeeding values of r.

A two-sided gradient approximation was used in this example. For point $(XB)_1$,

letting PF be the parametric function value, the necessary computations before approximating the gradient are summarized in Table 3.

$$\text{Then} \quad G(XB)_1 = \left| \begin{array}{c} \dfrac{PF(75,24) - PF(73,24)}{2} \\ \dfrac{PF(74,25) - PF(74,23)}{2} \end{array} \right| = \left| \begin{array}{c} 14.22 \\ 7.67 \end{array} \right|.$$

$$\text{Therefore} \quad GM(XB)_1 = \left| \begin{array}{c} -2 \\ -1 \end{array} \right|$$

Discrete points along an integer gradient direction were generated by Eq. 5. For the first iteration of the search, the best point is located at the third discrete

TABLE 3.—Penalty Function Calculations for XB_1 and Its Principal Neighborhood

(X) (1)	$F(X)$ (2)	$\phi(X)$ (3)	$PF(X) = P(X, r_1)$ (4)
(74,24)	568.80	3.0504	601.58
(75,24)	598.20	3.5383	626.46
(73,24)	564.39	2.9737	598.02
(74,25)	577.80	3.1684	609.36
(74,23)	599.80	2.9222	594.02

TABLE 4.—Summary of First Iteration

λ (1)	(XT) (2)	$F(XT)$ (3)	$\phi(XT)$ (4)	$PF(XT)$ (5)
1	(72,23)	532.16	2.4455	573.05
2	(70,22)	499.94	1.9132	552.21
3	(68,21)	543.60	1.1038	544.19
4	(66,20)	426.96	0.6656	577.19

point form point $(XB)_1$ in which $\lambda = 3$. Results from the first iteration of the search are summarized in Table 4. A total of three iterations of discrete searches were necessary to reach the discrete optimum of the first unconstrained optimization problem in the sequence. This point is designated as point (X^*, r_1), for which

$$(X^*, r_1) = \left| \begin{array}{c} 69 \\ 19 \end{array} \right|; \quad F(X^*, r_1) = \$449.71;$$

$\phi(X^*, r_1) = 1.1547$; and $P(X^*, r_1) = 536.31$.

A discrete optimal solution of the original constrained optimization problem was reached at the discrete optimal solution of the fourth unconstrained problem in the sequence, in which $k = 4$ and $r_4 = 0.1$. A total of seven iterations of discrete searches were necessary from the initial feasible solution to reach

that point. Fig. 2 shows how the search progressed, and Fig. 3 shows profiles of the values of PF-function and F-function at each iteration of the search. The sequence of discrete unconstrained optima with other corresponding values are summarized in Table 5.

From Table 5 it is evident that a discrete local optimum of the original constrained problem is at point (X^*, r_4). The optimal solutions of the remaining unconstrained problems in the sequence, in which $k = 5, 6 \ldots$, remain at this point while the values of P-function become closer to the value of the locally optimal objective function of the constrained problem. It can be seen that at the optimal solution X^*, the cross-sectional area of the reinforcing steel is

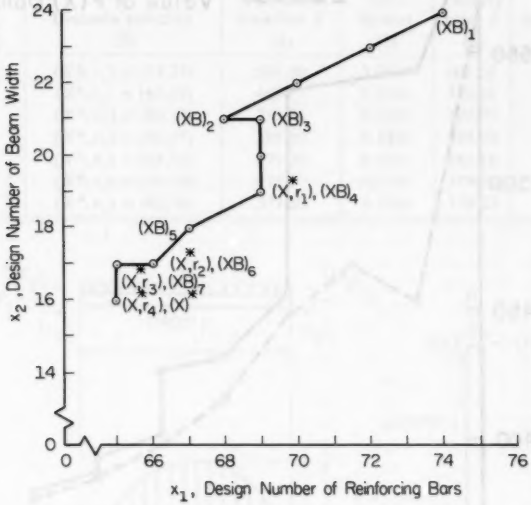

FIG. 2.—Search Process Leading to Optimal Solution

8.00 sq in. or 8-#9 bars, the width of the beam is 8.0 in., $F(X)^* = \$379.20$, and $\phi(X)^* = 0.0336$.

Discrete Optimization of Steel Building Frames

The approach presented above is applied to the design of steel building frames in which the beams and columns are prismatic and are made of standard sections. It is assumed that the geometric configuration of the structure is given, that the loads are static and deterministic, and that the constraints are based on the AISC Specifications (7). The objective function is the total weight of the structure. The constraints limit the maximum stress due to the combination of bending moment and axial force, taking the slenderness of the members into account. Sidesway can conveniently be constrained, however, it has not been considered in the examples presented.

Since the allowable stresses are provided in accordance with the type of loading, the constraint functions are formulated for a typical beam and a typical column under different loading conditions in accordance with the AISC Specifications. There is one constraint for each member for each load. Thus, ϕ_j indicates

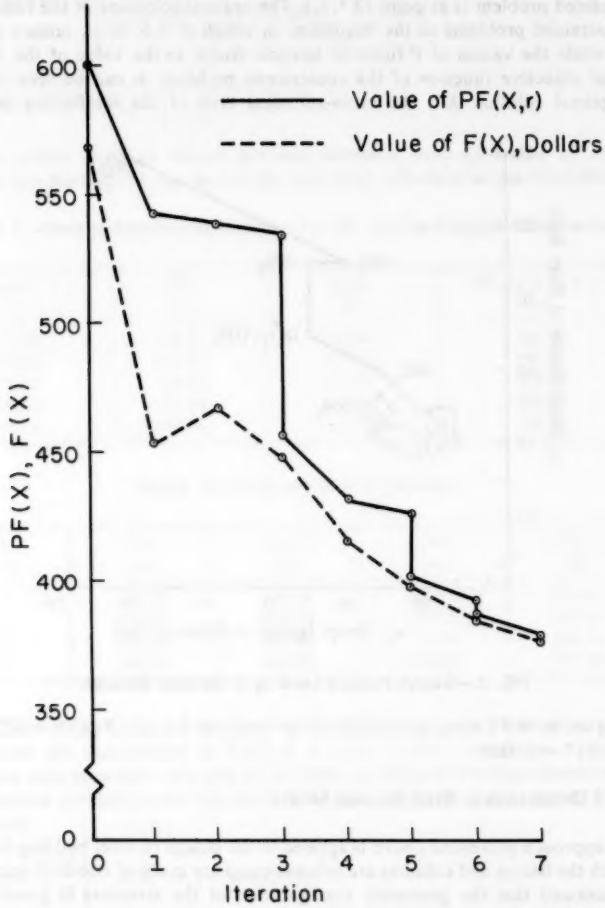

FIG. 3.—Profiles of Values of PF(X,r) and $F(x)$

the constraint corresponding to the jth member when the structure is subjected to only one load. Where there are more than one loading conditions acting alternately on the structure, $\phi_{N(l-1)+j}$ indicates the constraint corresponding

to the j-th member subjected to loading condition i, where N is the total number of members.

The gravity loads consist of the dead and live loads, and for simplicity we will assume that the live load acts on all floors with the dead load. A typical beam j of a steel building frame subjected to a uniformly distributed load of intensity w_j has three joint forces at each end as shown in Fig. 4(a). However, in formulating the constraint function for the beam, the axial force has been

TABLE 5.—Sequence of Discrete Unconstrained Optima

k (1)	r_k (2)	Discrete solution (3)	Objective function F (4)	Constraint (5)	Penalty term P (6)	Penalty function PF (7)
1	10^2	$(XB, r_1) = (74,24)$	568.80	3.0504	601.58	
1	10^2	$(X^*, r_1) = (69,19)$	449.71	1.1547	536.31	86.60
2	10	$(X^*, r_2) = (66,17)$	399.96	0.3596	427.77	27.81
3	1	$(X^*, r_3) = (65,17)$	388.20	0.1493	394.90	6.70
4	10^{-1}	$(X^*, r_4) = (65,16)$	379.20	0.0336	382.18	2.98
5	10^{-2}	$(X^*, r_5) = (65,16)$	379.20	0.0336	379.50	0.30
6	10^{-3}	$(X^*, r_6) = (65,16)$	379.20	0.0336	379.23	0.03

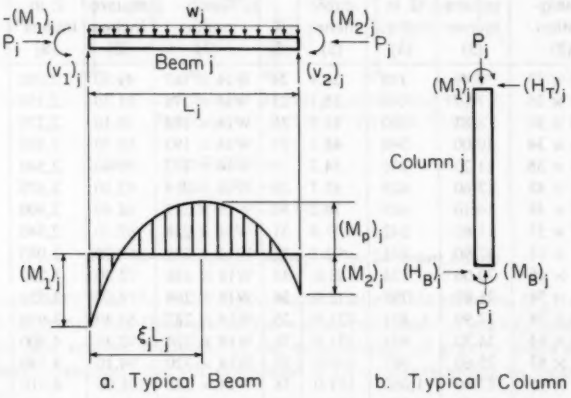

FIG. 4.—Typical Building Beam and Column

neglected. From Fig. 4(a) it can be seen that the governing moment $(M_{\max})_j$, is the largest of the three moments $(M_1)_j$, $(M_p)_j$ and $(M_2)_j$. The jth constraint can be expressed as follows

$$\phi_j(X) \equiv 1 - \frac{(M_{\max})_j}{F_b S_j} \geq 0 \quad \ldots \ldots \ldots \ldots \ldots \ldots \ldots \ldots \ldots \ldots \quad (13)$$

in which F_b = the allowable stress in steel which is taken as 66% of the yield

point stress of steel; and S_j = the section modulus of beam j.

In accordance with the AISC Specifications in the similar fashion from Fig. 4(*b*) the column constraints can be expressed as follows:

$$\phi_j(X) \equiv 1 - \frac{(f_a)_j}{(F_a)_j} - \frac{(f_b)_j}{F_b} \geq 0; \quad \text{when} \quad \frac{(f_a)_j}{(F_a)_j} \leq 0.15 \quad \ldots\ldots\ldots\ldots (14)$$

$$\text{or} \quad \phi_j(X) \equiv \min \left[1 - \frac{(f_a)_j}{(F_a)_j} - \frac{C_m(f_b)_j}{\left(1 - \dfrac{(f_a)_j}{(F_e)_j}\right) F_b}; \quad 1 - \frac{(f_a)_j}{0.6\,F_y} - \frac{(f_b)_j}{F_b} \right] \geq 0;$$

$$\text{when} \quad \frac{(f_a)_j}{(F_a)_j} > 0.15 \quad \ldots\ldots\ldots\ldots\ldots\ldots\ldots\ldots\ldots\ldots\ldots\ldots (15)$$

in which $(f_a)_j$ and $(F_a)_j$ = the computed and the allowable stresses in column j, respectively; $(F_e)_j$ = the Euler critical stress in column j; and C_m = a coefficient applied to the bending term.

TABLE 6.—Design Space for One-Story Four-Bay Unsymmetrical Frame

X (1)	Designation (2)	A, in square inches (3)	I, in inches^4 (4)	S, in cubic inches (5)	X (6)	Designation (7)	A, in square inches (8)	I, in inches^4 (9)	S, in cubic inches (10)
1	W14 × 22	6.49	198	28.9	24	W14 × 167	49.10	2,020	267.0
2	W14 × 26	7.67	244	35.1	25	W14 × 176	51.70	2,150	282.0
3	W14 × 30	8.83	290	41.9	26	W14 × 184	54.10	2,270	296.0
4	W14 × 34	10.00	340	48.6	27	W14 × 193	56.70	2,400	310.0
5	W14 × 38	11.20	386	54.7	28	W14 × 202	59.40	2,540	325.0
6	W14 × 43	12.60	429	62.7	29	W14 × 211	62.10	2,670	339.0
7	W14 × 48	14.10	485	70.2	30	W14 × 219	64.40	2,800	353.0
8	W14 × 53	15.60	542	77.8	31	W14 × 228	67.10	2,940	368.0
9	W14 × 61	17.90	641	92.2	32	W14 × 237	69.70	3,080	382.0
10	W14 × 68	20.00	724	103.0	33	W14 × 246	72.30	3,230	397.0
11	W14 × 74	21.80	797	112.0	34	W14 × 264	77.60	3,530	427.0
12	W14 × 78	22.90	851	121.0	35	W14 × 287	84.40	3,910	465.0
13	W14 × 84	24.70	928	131.0	36	W14 × 314	92.30	4,400	512.0
14	W14 × 87	25.60	967	138.0	37	W14 × 320	94.10	4,140	493.0
15	W14 × 95	27.90	1,060	151.0	38	W14 × 342	101.00	4,910	559.0
16	W14 × 103	30.30	1,170	164.0	39	W14 × 370	109.00	5,450	608.0
17	W14 × 111	32.70	1,270	176.0	40	W14 × 398	117.00	6,010	657.0
18	W14 × 119	35.00	1,370	189.0	41	W14 × 426	125.00	6,610	707.0
19	W14 × 127	37.30	1,480	202.0	42	W14 × 455	134.00	7,220	758.0
20	W14 × 136	40.00	1,590	216.0	43	W14 × 500	147.00	8,250	840.0
21	W14 × 142	41.80	1,670	227.0	44	W14 × 550	162.00	9,450	933.0
22	W14 × 150	44.10	1,790	240.0	45	W14 × 605	178.00	10,900	1,040.0
23	W14 × 158	46.50	1,900	253.0	46	W14 × 665	196.00	12,500	1,150.0
					47	W14 × 730	215.00	14,400	1,280.0

Note: 1 in. = 25.4 mm; 1 in.^{2} = 645 mm^2; 1 in.^{3} = 16,400 mm^3; and 1 in.^{4} = 416,200 mm^4.

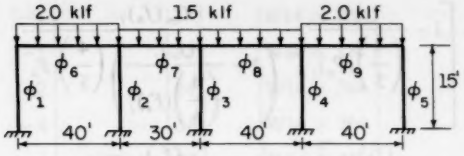

(a) Gravity Loads Only

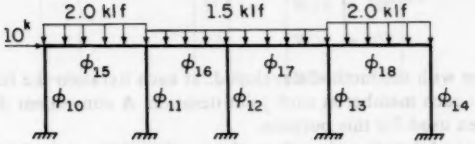

(b) Combined Gravity Loads and the Wind Load Acting from the Left

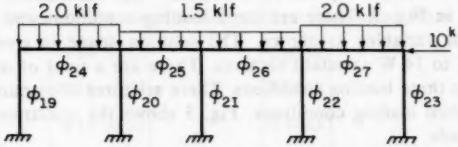

(c) Combined Gravity Loads and the Wind Load Acting from the Right

Note: 1 ft = 0.305 m
1 kip = 4.45 kN
1 kip/ft = 14.59 kn/m

FIG. 5.—Constraint Numbers for Different Loads

In accordance with the AISC Specification, allowable stresses, $(F_a)_j$ and $(F_b)_j$ may be increased one-third above the values provided for gravity loads. Thus, for wind and seismic loadings, or the combination of gravity loads and wind and seismic loadings, the jth constraint $\phi_j(X)$ corresponding to beam j is as follows:

$$\phi_j(X) \equiv 1 - \frac{(M_{\max})_j}{\left(\frac{4}{3}\right) F_b S_j} \geq 0 \quad \ldots \ldots \ldots \ldots \ldots \ldots \ldots \ldots \quad (16)$$

and the jth constraint $\phi_j(X)$ corresponding to column j is as follows:

$$\phi_j(X) \equiv 1 - \frac{(f_a)_j}{\left(\frac{4}{3}\right)(F_a)_j} - \frac{(f_b)_j}{\left(\frac{4}{3}\right) F_b} \geq 0, \quad \text{when} \quad \frac{(f_a)_j}{(F_a)_j} \leq 0.15 \quad \ldots \ldots \quad (17)$$

$$\phi_j(X) \equiv \min \left[1 - \frac{(f_a)_j}{\left(\frac{4}{3}\right)(F_a)_j} - \frac{C_m(f_b)_j}{\left(1 - \frac{(f_a)_j}{\left(\frac{4}{3}\right)(F_e)_j}\right)\left(\frac{4}{3}\right)F_b}; \right.$$

$$\left. 1 - \frac{(f_a)_j}{\left(\frac{4}{3}\right)0.6\,F_y} - \frac{(f_b)_j}{\left(\frac{4}{3}\right)F_b} \right] \geq 0; \quad \text{when} \quad \frac{(f_a)_j}{(F_a)_j} > 0.15 \quad \ldots\ldots\ldots \quad (18)$$

In accordance with the method developed, at each iteration the forces should be calculated at each member at each joint iteration. A convenient displacement method has been used for this purpose.

Several large steel structures have been designed by this approach. Specifically, two examples will be reported, namely, a one-story four-bay unsymmetrical frame and an eight-story three-bay symmetrical frame.

One-Story Four-Day Unsymmetrical Frame.—The dimensions and the loads are as shown in Fig. 5. There are three loading conditions and nine members or nine design variables as shown. The solution space is given in Table 6, and is limited to 14 W standard sections. There are a total of nine constraints for each of the three loading conditions. There are three constraints per member for the combined loading conditions. Fig. 5 shows the constraint numbers for the various loads.

We will first solve the problem for the gravity loads only and will start from the following initial point:

$$(XB)_1 = \begin{vmatrix} 40 \\ 40 \\ 40 \\ 40 \\ 40 \\ 40 \\ 40 \\ 40 \\ 40 \end{vmatrix} = \begin{vmatrix} \text{W14} \times 398 \\ \text{W14} \times 398 \\ \text{W14} \times 398 \\ \text{W14} \times 398 \\ \text{W14} \times 398 \\ \text{W14} \times 398 \\ \text{W14} \times 398 \\ \text{W14} \times 398 \\ \text{W14} \times 398 \end{vmatrix}; \quad \phi(XB)_1 = \begin{vmatrix} 0.8116 \\ 0.8746 \\ 0.9256 \\ 0.9213 \\ 0.8180 \\ 0.7805 \\ 0.8718 \\ 0.8037 \\ 0.7637 \end{vmatrix} \quad \ldots\ldots\ldots\ldots \quad (19)$$

The objective function value of the initial design is 89,550 lb. With the first penalty function parameter $r_1 = 8{,}333.46$, the PF-function value of the base point is 179,100. Using one-sided gradient approximations, the integer gradient direction at the base point is generated. The integer gradient direction vector and the best integer point obtained from the search in the direction of the integer gradient are as follows:

$$GM(XB)_1 = \begin{vmatrix} -1 \\ -1 \\ -2 \\ -2 \\ -1 \\ -4 \\ -3 \\ -4 \\ -4 \end{vmatrix}; \quad (XT) = \begin{vmatrix} 37 \\ 37 \\ 34 \\ 34 \\ 37 \\ 28 \\ 31 \\ 28 \\ 28 \end{vmatrix} = \begin{vmatrix} \text{W14} \times 320 \\ \text{W14} \times 320 \\ \text{W14} \times 264 \\ \text{W14} \times 264 \\ \text{W14} \times 320 \\ \text{W14} \times 202 \\ \text{W14} \times 228 \\ \text{W14} \times 202 \\ \text{W14} \times 202 \end{vmatrix} \quad \lambda = 3 \quad \ldots\ldots\ldots (20)$$

The best point along the integer gradient direction $GM(XB)_1$ is located at the 4th integer point; that is, $\lambda = 4$. The PF-function value is 155,934 which corresponds to the objective function value of 53,400 lbs. The total weight of the structure is reduced by a magnitude of 36,150 lbs in the first iteration. The optimal solution of the constrained problem is reached when $r = 0.00012$:

$$(X)^* = \begin{vmatrix} 12 \\ 6 \\ 1 \\ 1 \\ 10 \\ 11 \\ 7 \\ 12 \\ 13 \end{vmatrix} = \begin{vmatrix} \text{W14} \times 78 \\ \text{W14} \times 43 \\ \text{W14} \times 22 \\ \text{W14} \times 22 \\ \text{W14} \times 68 \\ \text{W14} \times 74 \\ \text{W14} \times 48 \\ \text{W14} \times 78 \\ \text{W14} \times 84 \end{vmatrix}; \quad \phi(X)^* = \begin{vmatrix} 0.0532 \\ 0.0817 \\ 0.1683 \\ 0.0081 \\ 0.0373 \\ 0.0002 \\ 0.0076 \\ 0.0158 \\ 0.0078 \end{vmatrix} \quad \ldots\ldots\ldots\ldots (21)$$

The optimal PF-function value is 14,375.64 and the optimal objective function value is 14,375 lb. Fig. 6 shows the optimal solution. It took 45 iterations from the initial base point to the optimal solution. Member end moments and member axial forces of the least weight structure are summarized in Table 7. In this case all the constraints are nearly active except the constraint corresponding to the third column.

We will consider next the alternate loading condition in which the gravity loads and the wind load act alternately as shown in Fig. 5. In this case there are a total of 27 constraints. The initial base point is $(XB)_1^T$ = (35,35,35,35,35,35, 35,35,35), or W14 × 287 is the section selected for all nine members of the frame. The initial objective function value is 64,575 lb with R_1 = 1,952.56, and $PF(XB)_1$ = 129,150. Using one-sided gradient approximations, the integer gradient direction vector and the best integer point obtained from the search are as follows:

TABLE 7.—Member Forces for Optimal Design of One-Story Four-Bay Frame Subjected to Various Loads

Member (1)	Axial Force, in kips (+ tension) Load 1 (2)	Load 2 (3)	Load 3 (4)		Moment, in inch-kips (+ clockwise) Load 1 (5)	Load 2 (6)	Load 3 (7)
1	−41.0	−40.3	−41.6	T	+2,759	+2,592	+2,909
				B	+1,370	+1,007	+1,694
2	−66.2	−66.6	−66.0	T	−1,128	−1,316	−952
				B	−549	−777	−333
3	−50.8	−50.9	−50.7	T	+355	+258	+453
				B	+191	+82	+301
4	−78.4	−78.1	−78.6	T	+290	+179	+410
				B	+165	+51	+289
5	−39.4	−39.9	−38.9	T	−2,367	−2,508	−2,206
				B	−1,085	−1,368	−764
6	−23.0	−30.0	−25.6	L	−2,759	−2,592	−2,909
				R	+2,986	+3,112	+2,870
7	−13.6	−18.4	−18.4	L	−1,858	−1,797	−1,918
				R	+1,457	+1,509	+1,404
8	−16.7	−20.3	−22.6	L	−1,812	−1,767	−1,857
				R	+3,176	+3,206	+3,145
9	−19.2	−21.5	−26.5	L	−3,466	−3,386	−3,555
				R	+2,367	+2,508	+2,206

Note: 1 kip = 4.45 kN; 1 inch-kip = 0.113 kNm.
Load 1 Gravity Load Only.
Load 2 Gravity and Wind.
Load 3 Alternate Loads.

$$GM(XB)_1 = \begin{vmatrix} -1 \\ -2 \\ -2 \\ -2 \\ -1 \\ -4 \\ -4 \\ -5 \\ -4 \end{vmatrix}; \quad (XT)_{\lambda=3} = \begin{vmatrix} 32 \\ 29 \\ 29 \\ 29 \\ 32 \\ 23 \\ 23 \\ 20 \\ 23 \end{vmatrix} = \begin{vmatrix} \text{W14} \times 237 \\ \text{W14} \times 211 \\ \text{W14} \times 211 \\ \text{W14} \times 211 \\ \text{W14} \times 237 \\ \text{W14} \times 158 \\ \text{W14} \times 158 \\ \text{W14} \times 136 \\ \text{W14} \times 158 \end{vmatrix} \quad \ldots\ldots\ldots (22)$$

The objective function value of the best point is 39,425 lb; a reduction of 38.9% from the initial design weight. The optimal solution of the constrained problem is obtained at the 34th iteration, and the least weight structure is 14,375 lbs, with $r = 0.00012$ and $PF(X)^* = 14{,}375.61$. The optimal solution is shown in Fig. 6 and is also listed below:

$$(X)^* = \begin{vmatrix} 12 \\ 6 \\ 1 \\ 1 \\ 10 \\ 11 \\ 7 \\ 12 \\ 13 \end{vmatrix} = \begin{vmatrix} \text{W14} \times 78 \\ \text{W14} \times 43 \\ \text{W14} \times 22 \\ \text{W14} \times 22 \\ \text{W14} \times 68 \\ \text{W14} \times 74 \\ \text{W14} \times 48 \\ \text{W14} \times 78 \\ \text{W14} \times 84 \end{vmatrix} \quad \ldots\ldots\ldots\ldots\ldots\ldots\ldots\ldots\ldots\ldots \quad (23)$$

From those values, it can be seen that the gravity loads govern the optimal design; that is, eight out of nine gravity load constraints are nearly active at the optimal solution while the rest of the constraints are far from being active. It is also important to note that the optimal solutions of the frame subjected to gravity loads only and the frame subjected to three alternate loads are identical.

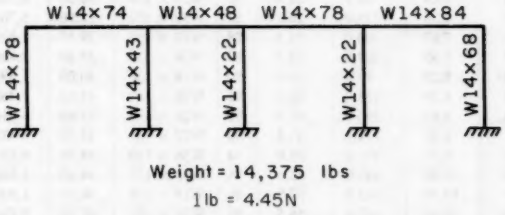

FIG. 6.—Optimal Solution

Member end forces of the least weight structure are summarized in Table 7. Sidesway of the least weight frame is 0.17 in.

Eight-Story Three-Bay Symmetrical Frame.—Dimensions and all possible design loads for the eight-story three-bay symmetrical frame with fixed bases are shown in Fig. 7(*a*). There are 56 members in the frame with 32 colums and 24 beams. However, there are only 16 variables, since it is assumed that the beam sections are the same in each floor, and the column sections are the same for two consecutive stories. A total of 137 standard W sections are available for the design, and are listed in Table 8. There is no sidesway limitation to this problem, and the effective length factor for all columns is assumed to be 2.5. There are two different loads acting on the frame, namely, gravity loads only, and combined gravity and wind loads. These two loading conditions are treated as the independent alternate loads acting on the frame. There are a total of 112 constraints in this problem. Fig. 7(*a*) shows the numbers assigned to each of the 16 variables.

The initial base point is $(XB)_1^T$ = (120,120,120,120,120,120,120,120,130,130, 130,130,130,130,130,130) which corresponds to W14 × 246 for all columns, and W14 × 398 for all beams. The objective function value of the initial design

TABLE 8.—Design Space for Eight-Story Three-Bay Frame

X (1)	Designation (2)	A, in square inches (3)	I, in inches^4 (4)	S, in cubic inches (5)	X (6)	Designation (7)	A, in square inches (8)	I, in inches^4 (9)	S, in cubic inches (10)
1	W6 × 8.5	2.51	14.8	5.1	70	W24 × 100	29.50	3,000.0	250.0
2	W8 × 10	2.96	30.8	7.8	71	W27 × 102	30.00	3,610.0	267.0
3	W10 × 11.5	3.39	52.0	10.5	72	W14 × 103	30.00	1,170.0	164.0
4	W6 × 12	3.54	21.7	7.3	73	W18 × 105	30.90	1,850.0	202.0
5	W8 × 13	3.83	39.6	9.9	74	W12 × 106	31.20	931.0	145.0
6	W12 × 14	4.12	88.0	14.8	75	W30 × 108	31.80	4,470.0	300.0
7	W10 × 15	4.41	68.9	13.8	76	W24 × 110	32.50	3,330.0	276.0
8	W6 × 15.5	4.56	30.1	10.0	77	W14 × 111	32.70	1,270.0	176.0
9	W6 × 16	4.72	31.7	10.2	78	W21 × 112	33.00	2,620.0	250.0
10	W12 × 16.5	4.87	105.0	17.6	79	W27 × 114	33.60	4,090.0	300.0
11	W10 × 17	4.99	81.9	16.2	80	W30 × 116	34.20	4,930.0	329.0
12	W5 × 18.5	5.43	25.4	9.9	81	W33 × 118	34.80	5,900.0	359.0
13	W12 × 19	5.59	130.0	21.3	82	W14 × 119	35.00	1,370.0	189.0
14	W8 × 20	5.89	69.4	17.0	83	W24 × 120	35.40	3,650.0	300.0
15	W10 × 21	6.20	107.0	21.5	84	W40 × 124	36.50	5,360.0	355.0
16	W14 × 22	6.49	198.0	28.9	85	W21 × 127	37.40	3,020.0	284.0
17	W8 × 24	7.06	82.5	20.8	86	W33 × 130	38.30	6,710.0	406.0
18	W10 × 25	7.36	133.0	26.5	87	W30 × 132	38.90	5,760.0	380.0
19	W16 × 26	7.67	300.0	38.3	88	W12 × 133	39.10	1,220.0	183.0
20	W12 × 27	7.95	204.0	34.2	89	W36 × 135	39.80	7,820.0	440.0
21	W8 × 28	8.23	97.8	24.3	90	W14 × 136	40.00	1,590.0	216.0
22	W10 × 29	8.54	158.0	30.8	91	W33 × 141	41.60	7,460.0	448.0
23	W14 × 30	8.83	290.0	41.9	92	W21 × 142	41.80	3,410.0	317.0
24	W16 × 31	9.13	374.0	47.2	93	W27 × 145	42.70	5,430.0	404.0
25	W10 × 33	9.71	171.0	35.0	94	W36 × 150	44.20	9,030.0	504.0
26	W14 × 34	10.00	340.0	48.6	95	W33 × 152	44.80	8,160.0	487.0
27	W18 × 35	10.30	513.0	57.9	96	W14 × 158	46.50	1,900.0	253.0
28	W16 × 36	10.60	447.0	56.5	97	W36 × 160	47.10	9,760.0	542.0
29	W14 × 38	11.20	386.0	54.7	98	W12 × 161	47.40	1,540.0	222.0
30	W10 × 39	11.50	210.0	42.2	99	W14 × 167	49.10	2,020.0	267.0
31	W18 × 40	11.80	612.0	68.4	100	W36 × 170	50.00	10,500.0	580.0
32	W14 × 43	12.60	429.0	62.7	101	W30 × 172	50.70	7,910.0	530.0
33	W21 × 44	13.00	843.0	81.6	102	W14 × 176	51.70	2,150.0	282.0
34	W18 × 45	13.20	705.0	79.0	103	W27 × 177	52.20	6,740.0	494.0
35	W14 × 48	14.10	485.0	70.2	104	W36 × 182	53.60	11,300.0	622.0
36	W21 × 49	14.40	971.0	93.3	105	W14 × 184	54.10	2,270.0	296.0
37	W18 × 50	14.70	802.0	89.1	106	W30 × 190	56.00	8.850.0	587.0
38	W14 × 53	15.60	542.0	77.8	107	W14 × 193	56.70	2,400.0	310.0
39	W10 × 54	15.90	306.0	60.4	103	W36 × 194	57.20	121,00.0	665.0
40	W24 × 55	16.20	1,340.0	114.0	109	W33 × 200	58.90	11,100.0	671.0
41	W16 × 58	17.10	748.0	94.4	110	W14 × 202	59.40	2,540.0	325.0
42	W18 × 60	17.70	986.0	108.0	111	W30 × 210	61.90	9,890.0	651.0
43	W24 × 61	18.00	1,540.0	130.0	112	W14 × 211	62.10	2,670.0	339.0
44	W21 × 62	18.30	1,330.0	127.0	113	W14 × 219	64.40	2,800.0	353.0
45	W18 × 64	18.90	1,050.0	118.0	114	W33 × 220	64.80	12,300.0	742.0
46	W12 × 65	19.10	533.0	88.0	115	W14 × 228	67.10	2,940.0	368.0
47	W10 × 66	19.40	382.0	73.7	116	W36 × 230	67.70	15,000.0	837.0
48	W8 × 67	19.70	272.0	60.4	117	W14 × 237	69.70	3,080.0	382.0
49	W24 × 68	20.00	1,820.0	153.0	118	W33 × 240	70.60	13,600.0	813.0
50	W18 × 70	20.60	1,160.0	129.0	119	W36 × 245	72.10	16,100.0	894.0
51	W16 × 71	20.90	841.0	116.0	120	W14 × 246	72.30	3,230.0	397.0
52	W12 × 72	21.20	597.0	97.5	121	W36 × 260	76.50	17,300.0	952.0

TABLE 8.—*Continued*

(1)	(2)	(3)	(4)	(5)	(6)	(7)	(8)	(9)	(10)
53	W21 × 73	21.50	1,600.0	151.0	122	W14 × 264	77.60	3,530.0	427.0
54	W14 × 74	21.80	797.0	122.0	123	W36 × 280	82.40	18,900.0	1,030.0
55	W24 × 76	22.40	2,100.0	176.0	124	W14 × 287	84.40	3,910.0	465.0
56	W18 × 77	22.70	1,290.0	142.0	125	W36 × 300	88.30	20,300.0	1,110.0
57	W16 × 78	23.00	1,050.0	128.0	126	W14 × 314	92.30	4,400.0	512.0
58	W12 × 79	23.20	663.0	107.0	127	W14 × 320	94.10	4,140.0	493.0
59	W21 × 82	24.20	1,760.0	169.0	128	W14 × 342	101.00	4,910.0	559.0
60	W27 × 84	24.80	2,830.0	212.0	129	W14 × 370	109.00	5,450.0	608.0
61	W18 × 85	25.00	1,440.0	157.0	130	W14 × 398	117.00	6,010.0	657.0
62	W14 × 87	25.60	967.0	138.0	131	W14 × 426	125.00	6,610.0	707.0
63	W16 × 88	25.90	1,220.0	151.0	132	W14 × 455	134.00	7,220.0	758.0
64	W10 × 89	26.20	542.0	99.7	133	W14 × 500	147.00	8,250.0	840.0
65	W12 × 92	27.10	789.0	125.0	134	W14 × 550	162.00	9,450.0	933.0
66	W27 × 94	27.70	3,270.0	243.0	135	W14 × 605	178.00	10,900.0	1,040.0
67	W14 × 95	27.90	1,060.0	151.0	136	W14 × 665	196.00	12,500.0	1,150.0
68	W21 × 96	28.30	2,100.0	198.0	137	W14 × 730	215.00	14,400.0	1,280.0
69	W30 × 99	29.10	4,000.0	270.0					

Note: 1 in. = 25.4 mm; 1 in.^{2} = 645 mm^2; 1 in.^{3} = 16,400 mm^3; 1 in.^{4} = 416,200 in.^{4}

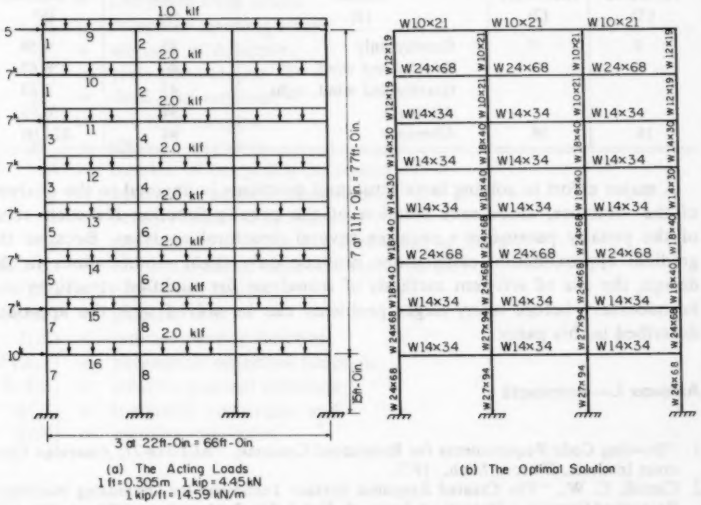

(a) The Acting Loads
1 ft=0.305m 1 kip=4.45 kN
1 kip/ft=14.59 kN/m

(b) The Optimal Solution

FIG. 7.—Eight-Story Three-Bay Symmetrical Frame

is 300,672 lbs with the initial R = 2,354, and the PF-function value of 601,344.

The optimal solution is reached when the penalty function parameter has been reduced to 0.0006. The optimal *PF* and objective functions are 39,598 and 39,598 lb, respectively. At optimal design, the maximum sidesway is 2.50 in. The optimal solution is presented in Fig. 7(*b*).

Computer Program

A FORTRAN program was developed to carry out the computations involved in the aforementioned problems. The input information was the geometry of the structure, the available discrete solutions, loads and the design constraints.

There are two levels of convergence in the penalty function approach. The first level is the convergence of reaching the optimal P function with a given parameter r. The second level is the convergence of the locally optimal solutions of the sequence of unconstrained problems to a locally optimal solution of the constrained problem. For large structures it is computationally advisable to reduce r as soon as the first level convergence becomes relatively slow.

The total number of searches increases progressively as the size of the structure increases. Table 9 summarizes the total number of searches and computer time necessary to solve the structural problems discussed in this paper.

TABLE 9.—Summary of Computational Effort

Number of variables (1)	Number of members (2)	Loads (3)	Total number of searches (4)	Computer time, in seconds (5)
9	9	Gravity only	45	6.58
		Gravity and wind, left	46	6.67
		Gravity and wind, right	45	6.63
		Alternate	34	6.95
16	56	Alternate	94	224.00

A major effort in solving large structural problems is devoted to the analysis of the structure, since each solution of the penalty function for each value of the penalty parameter r requires several structural analyses. Because the gradient approximation calculations produce only slight modifications in the design, the use of efficient methods of reanalysis for modified structures will be necessary before many larger problems can be solved with the approach described in this paper.

Appendix I.—References

1. "Building Code Requirements for Reinforced Concrete," ACI 318-77, American Concrete Institute, Detroit, Mich., 1977.
2. Carroll, C. W., "The Created Response Surface Technique for Optimizing Nonlinear Restrained Systems," *Operations Research*, Vol. 9, No. 2, Mar.–Apr., 1961, pp. 196–184.
3. Chanaratna, V., "Discrete Structural Optimization," thesis presented to the University of Illinois, at Urbana-Champaign, Ill., in 1977, in partial fulfillment of the requirements for the degree of Doctor of Philosophy.
4. Glankwahmdee, A., Liebman, J. S., and Hogg, G. L., "Unconstrained Discrete Nonlinear Programming," *Engineering Optimization*, Vol. 4, 1979, pp. 95–107.
5. Liebman, J. S., Chanaratna, V., and Khachaturian, N., "Discrete Optimization in Structural Design," *Proceedings of the Symposium on Applications of Computer Methods in Engineering*, Vol. 1, 1977, pp. 553–562.
6. Lai, Y. S., and Achenbach, J. D., "Direct Search Optimization Method," *Journal*

of the Structural Division, ASCE, Vol. 98, No. ST1, Proc. Paper 9470, Jan., 1973, pp. 119–31.
7. "Manual of Steel Construction," Seventh ed., American Institute of Steel Construction, New York N.Y., 1973.
8. Toakley, A. R., "Optimum Design Using Available Sections," *Journal of the Structural Division*, ASCE, Vol. 94, No. ST5, Proc. Paper 5960, May, 1968, pp. 1219–1241.
9. Twisdale, L. A., and Khachaturian, N., "Optimization of Structures by Dynamic Programming," *Journal of the Structural Division*, ASCE, Vol. 101, No. ST5, Proc. Paper 11297, May, 1975, pp. 1000–1019.

Appendix II.—Notation

The following symbols are used in this paper:

A_s = area of reinforcement;
b = width of beam;
C_m = coefficient;
d = effective depth of beam;
F_a = allowable axial stress;
F_b = allowable bending stress;
F_e = Euler critical stress;
f_a = computed axial stress;
f_b = computed bending stress;
f'_c = strength of concrete;
f_y = yield point stress;
M_d = dead load moment;
M_ℓ = live load moment;
M_u = ultimate moment;
m = number of inequality constraints;
p = number of equality constraints;
r = penalty function parameter;
s = smallest (in absolute value) element of $S(XB)$;
$\mathbf{DR}(XB)$ = relative gradient direction vector at SB;
$F(X)$ = objective function;
$G(XB)$ = gradient at B;
$I(X)$ = interior penalty function;
$P(X,r)$ = parametric objective function;
$S(XB)$ = relative gradient direction;
$\phi(X)$ = inequality constraint; and
$\psi(X)$ = equality constraint.

RESPONSE MEASUREMENTS FOR GLASS CLADDING PANELS

By James I. Craig[1] and Barry J. Goodno,[2] M. ASCE

INTRODUCTION

In the past, greater analytical attention has been paid to major building components (foundation, frame) than to architectural details such as the cladding or window systems. The principal reason is, of course, that the failure of a major component would be catastrophic. However, the increasingly frequent failure of windows and cladding to perform as intended has noticeably increased the economic risk of advanced design concepts. Clearly, many of the failures of windows and cladding assemblies, reported or not, can be generally attributed to improper design. The solution to these problems is not always so direct, however. While all important factors may not have been considered, it is also possible that some factors were previously unknown. The use of new materials and advanced construction techniques makes it imperative that not only all significant loads are defined, but also that the various response patterns are properly identified and understood.

A rational methodology for designing building cladding, and windows in particular, has lagged behind other areas of structural design, and only recently have attempts been made to characterize the nature of localized loadings (1,7,10,12). There have been scattered attempts to ascertain the localized structural response to these forces (6), and at least one experimental facility has been built to simulate the anticipated conditions (8).

As far as response characteristics or failure modes are concerned, there is much conjecture but little hard evidence. It has been observed that pressure loads may, in certain circumstances, cause window panes actually to be ejected from their glazing, but it is often assumed that the force responsible for this is a quasi-static pressure load due largely to wind suction effects. Instances are often recorded, in which the light does not appear to fracture before leaving the glazing, and consequently it can be assumed that glass fracture by itself is not the sole consideration. There has been no real attention directed toward

[1]Assoc. Prof., School of Aerospace Engrg., Georgia Inst. of Tech., Atlanta, Ga. 30332.
[2]Assoc. Prof., School of Civ. Engrg., Georgia Inst. of Tech., Atlanta, Ga. 30332.

Note.—Discussion open until April 1, 1982. To extend the closing date one month, a written request must be filed with the Manager of Technical and Professional Publications, ASCE. Manuscript was submitted for review for possible publication on March 7, 1980. This paper is part of the Journal of the Structural Division, Proceedings of the American Society of Civil Engineers, ©ASCE, Vol. 107, No. ST11, November, 1981. ISSN 0044-8001/81/0011-2199/$01.00.

possible dynamic mechanisms which might play a role in this ejection type failure of lights.

An interesting failure mode involving excessive deflection, coupled with dynamic response, has been suggested in windows that are doubly glazed. The proposed failure mode, particularly for those windows incorrectly or incompletely installed, involves a sharp transient vibration of the panes in which each moves out of phase with the other. If sufficient amplitude is developed, the panes might actually come into contact, and while the ultimate failure is due to breakage, the initiation might be the result of dynamic response of the window.

Dynamic processes would be present to some degree in curtain wall windows of all sizes, but the effects may become more pronounced in larger windows. In these cases, the natural frequencies are lower and the vibrations are often of higher amplitude. Since pressure loading increases as the square of the dimensions, the restraint forces per unit length along the boundaries are increased in direct proportion to the edge dimensions. This requires correspondingly heavier glazing and magnifies dynamic effects.

In examining the overall design of curtain walls, it appears reasonable to inquire as to the possible effects of the vibration behavior of lights, as well as other component panels, on the structural performance of the assembly. The work reported here is part of a recently completed study to assess the nature of cladding loads, and to predict the response to these loads (2). This study involved both field measurements of local pressure loads on a 29 story high-rise building in Atlanta, as well as design and construction of a laboratory test facility capable of simulating normal and extreme dynamic pressure loads on full-scale cladding assemblies. The models and the substantiating experimental testing are based on the cladding actually employed in the building. While somewhat specific in application, the methodology and much of the results are generally applicable to lightweight cladding systems.

Analytical Studies

Cladding Description.—A typical portion of the glass cladding between story levels in the prototype structure is shown in Fig. 1. The curtain wall is composed of a single-glazed spandrel panel, and a double-glazed insulating window supported by neoprene gaskets in an extruded aluminum framework. The mullions are pin-supported at floor levels, as shown in Fig. 2, and are spliced near the anchor points at two-story intervals. The double-glazed window itself is detailed in a later section on testing. Finite element and continuum models of the cladding were developed and used in static and dynamic analyses of the window-framework assembly.

Finite Element Model.—The frame-finite element model in Fig. 3 is a representation of the window-frame subsystem. Two-dimensional stretching and bending elements (3) were used to model the glass panel, space frame elements with elastic connections were employed to account for the stiffness of the framework, and linear springs were used to connect panel and frame nodes in the model in place of the continuous neoprene gasket. The gasket springs in Fig. 3 account for the resistance on the boundary to in-plane motions, either parallel, k_L, or perpendicular k_P, to the panel edge, and to out-of-plane motions, either normal, k_N, to the panel or due to relative rotation, k_R, between the

panel and frame. Spring stiffnesses were determined from simple laboratory static tests (2). Gasket and other model properties are summarized in Table 1.

Panel, frame, and spring elements were assembled to form consistent stiffness

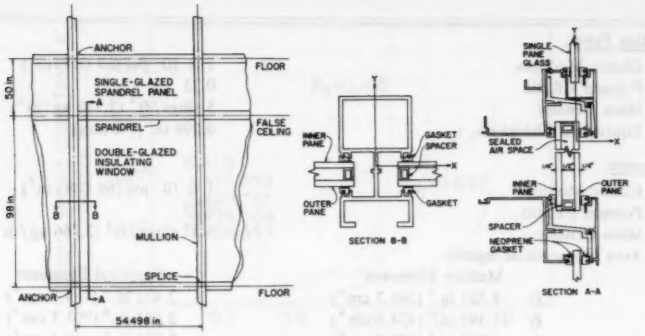

FIG. 1.—Cladding System (1 in. = 25.4 mm)

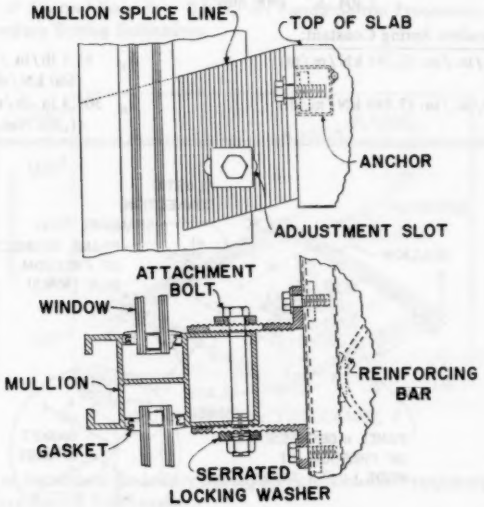

FIG. 2.—Mullion-Slab Connection

and mass properties for the total structure model. Extraneous degrees of freedom on the panel and frame were eliminated using a two-stage condensation procedure. Details of the model and the analysis procedure have been presented elsewhere (3,5) and will not be repeated.

Model properties were adjusted until displacements and frequencies were reasonably close to measured laboratory values. System properties which had

TABLE 1.—Model Properties

Glass Panel:		
Elastic Modulus		1×10^7 psi (69 GN/m^2)
Poisson's Ratio		0.23
Mass Density		5 slugs/ft^3 (2,575 kg/m^3)
Equivalent Thickness, t_p		0.298 in. (7.6 mm)
Frame:		
Elastic Modulus		1×10^7 psi (69 GN/m^2)
Poisson's Ratio		0.25
Mass Density		5.37 slugs/ft^3 (2,766 kg/m^3)
Area Moments of Inertia		
	Mullion Elements	Spandrel Elements
Ix	8.321 in.^{4} (346.3 cm^4)	3.452 in.^{4} (143.7 cm^4)
Iy	11.390 in.^{4} (474.1 cm^4)	2.481 in.^{4} (103.3 cm^4)
Iz	3.069 in.^{4} (127.7 cm^4)	0.971 in.^{4} (40.4 cm^4)
Cross-sectional Areas		
Mullion	2.613 in.^{2} (1,686 mm^2)	
Spandrel	1.404 in.^{2} (906 mm^2)	
Gasket Equivalent Spring Constant:		
k_L	318.0 lb/in./in. (2,194 kN/m/m)	k_P 81.1 lb/in./in. (560 kN/m/m)
k_N	556.9 lb/in./in. (3,843 kN/m/m)	k_R 305.3 in.-lb/rad/in. (1,358 Nm/rad/m)

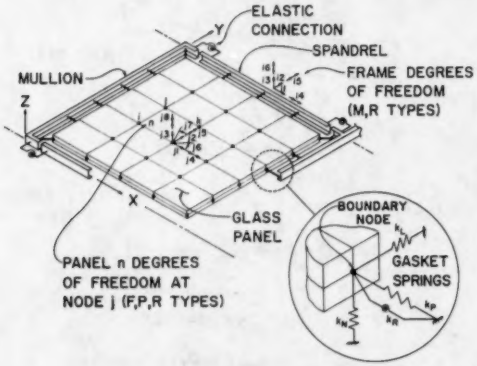

FIG. 3.—Finite Element Model

relatively more influence on the response were studied further for varying panel and support parameters. The following results of these sensitivity studies are

presented for comparison with the laboratory measurements.

Initially, the double-plate system was replaced by an equivalent single panel represented by a single-layer finite element model. This model assumed that both plates act together and vibrate in phase. Vibration frequencies, mode shapes,

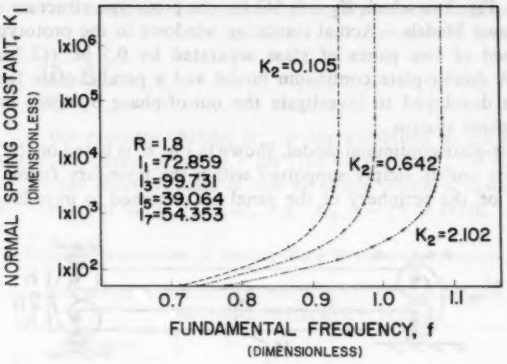

FIG. 4.—Effect of Normal Boundary Spring on Fundamental Frequency for Various Rotational Boundary Spring Stiffnesses

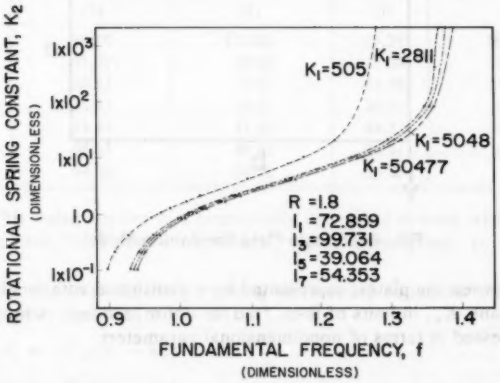

FIG. 5.—Effect of Rotational Boundary Spring on Fundamental Frequency for Various Normal Boundary Spring Stiffnesses

and response for in-phase motions were determined. The sensitivity of panel fundamental frequency to change in either k_N or k_R is summarized in Figs. 4 and 5, respectively. Variables K_i and I_i = dimensionless forms of the boundary spring constants and frame moments of inertia, respectively. Parameter f = the nondimensional frequency defined as the ratio of the natural frequency

of the model to that of a simply-supported plate. (The nondimensional ratios used are defined in the Appendix—Notation.) Fundamental frequency is seen to be insensitive to change in normal spring stiffness, k_N, in which the region of practical interest ($K_1 = 2{,}811$ for the prototype structure). However, an increase in gasket rotational stiffness, k_R, led to a notable increase in frequency, as shown in Fig. 5 in which $K_2 = 0.642$ for the prototype structure.

Double Panel Models.—Actual insulating windows in the prototype structure are composed of two panes of glass separated by 0.5 in. (12.7 mm) sealed air space. A double-plate continuum model and a parallel-plate finite element model were developed to investigate the out-of-phase dynamic properties of the double-panel system.

The double-plate continuum model, shown in Fig. 6, is based on the assumption that the glass unit is simply supported within the boundary frame. The metal spacer bars on the periphery of the panel are assumed to introduce rotational

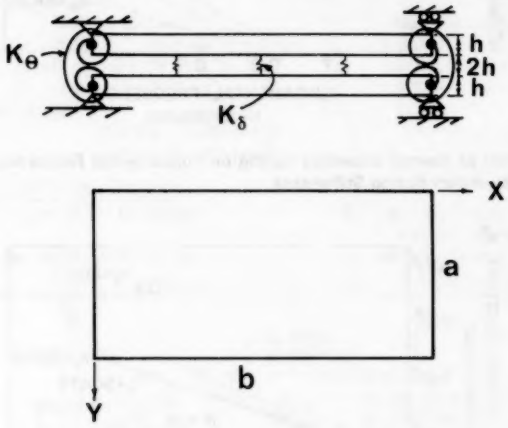

FIG. 6.—Double-Plate Continuum Model

coupling between the plates, represented by a distributed rotational spring with spring constant, K_θ, in units of lb-in./rad/in. (N-m/rad/m). A range of values of K_θ, expressed in terms of nondimensional parameters

$$\xi_B = \frac{2K_\theta b}{D} \quad \ldots\ldots\ldots\ldots\ldots\ldots\ldots\ldots\ldots\ldots\ldots\ldots\ldots\ldots\ldots\ldots\ldots\ldots \quad (1a)$$

$$\xi_A = \xi_B \frac{a}{b} \quad \ldots\ldots\ldots\ldots\ldots\ldots\ldots\ldots\ldots\ldots\ldots\ldots\ldots\ldots\ldots\ldots\ldots\ldots \quad (1b)$$

was used to approximate varying degrees of interplate connection on the boundary.

In modes of vibration in which volume change occurs, the air gap was modeled as a distributed linear spring with spring constant, K_δ, expressed in units of lb/in./in.^{2} (N/m/m^2), i.e., spring stiffness per unit area. To obtain estimates

of the natural frequencies, the distributed spring stiffness was taken to be a different constant in each mode of vibration. The stiffness, K_δ, for the entrapped air was determined by assuming adiabatic compression of the volume, and by neglecting resonances of the air mass. A linear relationship between volume change and pressure change was assumed to evaluate K_δ. Constant $K_{\delta mn}$ was computed for the *mn* mode as the pressure change per unit modal amplitude, namely,

$$K_{\delta mn} = \frac{\Delta p_{mn}}{a_{mn}} = \frac{\gamma p_o}{V_o} \frac{\Delta V_{mn}}{a_{mn}} \quad \ldots\ldots\ldots\ldots\ldots\ldots\ldots\ldots\ldots\ldots (2)$$

in which Δp_{mn} = the pressure change; a_{mn} = the amplitude in the *mn* mode; γ = the adiabatic exponent; p_o = 14.7 psi (101.4 kPa); ΔV_{mn} = the volume change; and V_o = the initial volume of the air space which is equal to 2,661 in.^{3} (4.36×10^{-2} m^3). For the (1, 1) mode, e.g., $K_{\delta 1,1}$ = 19.88 lb/in./in.^{2} (4,328 N/m/m^2). This value applies to a rotationally restrained system with K_θ equal to 256.2 lb-in./rad/in. (1,140 N-m/rad/m) which corresponds to $\xi_B = 2$ in Eq. 1*a*.

TABLE 2.—Natural Frequencies of Double-Plate System, Continuum Model

Mode Shape		NATURAL FREQUENCY, in Hertz			
		In Phase			
		Simply-supported boundary conditions	Out of Phase, K_θ and K_δ Included		
n (1)	*m* (2)	(3)	$\xi_B = 1 \times 10^{-10}$ (4)	$\xi_B = 2$ (5)	$\xi_B = 1 \times 10^{10}$ (6)
1	1	10.46	120.02	129.35	160.14
1	2	18.09	18.09	20.04	28.44
1	3	30.81	75.60	81.98	112.46
2	1	34.21	34.21	36.86	52.10
2	2	41.84	41.84	44.32	59.80
1	4	48.61	48.61	50.41	62.03
2	3	54.56	54.56	56.85	72.80

With K_θ and K_δ defined, the governing differential equations were written for the double plate model of Fig. 6 as

$$D\nabla^4 w_1 + \rho h \ddot{w}_1 = -K_\delta (w_1 - w_2) \quad \ldots\ldots\ldots\ldots\ldots\ldots\ldots\ldots (3a)$$

$$D\nabla^4 w_2 + \rho h \ddot{w}_2 = -K_\delta (w_2 - w_1) \quad \ldots\ldots\ldots\ldots\ldots\ldots\ldots\ldots (3b)$$

in which w_1 and w_2 = the displacement functions of the upper and lower plate, respectively. In-phase and out-of-phase vibration modes were considered separately in the solution of Eqs. 3*a* and 3*b* for frequencies and mode shapes. The results are summarized in Table 2.

The out-of-phase motions of the two glass panes in the insulating windows were also studied using a parallel-plate finite element model that is symmetric about the x-y plane. Discrete springs with spring constants k_N were attached between opposite interior panel nodes to account for the stiffness of the entrapped

air in the sealed space between the glass panels. Constants, k_N, were determined by multiplying air stiffness, $K_{\delta 1,1}$, by tributary panel area at each mode.

Normal springs on the panel boundary, representing the normal stiffness of the spacer bar between the glass plates, had spring constant, k_{NB}, which varied between soft, 8.85×10^3 lb/in. (1.55×10^3 kN/m), and hard 5×10^7 lb/in. (8.75×10^6 kN/m) values so that a range of frequencies for out-of-phase mode (1, 1) could be determined. The rotational spring on the panel boundary, representing the rotational stiffness of the spacer bar, had spring constant k_R with soft, intermediate, and hard values. Out-of-phase frequencies for mode (1, 1) are listed in Table 3 for various combinations of spring constants k_{NB} and k_R, and are compared with continuum model results.

TABLE 3.—Natural Frequencies of Double-Plate System, First Breathing Mode

Model (1)	Natural Frequency, in Hertz		
	$\xi_B = 1 \times 10^{-10}$ (2)	$\xi_B = 2$ (3)	$\xi_B = 1 \times 10^{10}$ (4)
Continuum[a]	120.02	129.35	160.14
Discrete, soft spring[b]	116.93	119.91	144.68
Discrete, hard spring[c]	118.44	122.28	156.89

[a]See Table 2.
[b]$k_{NB} = 8.85 \times 10^3$ lb/in. (1.55×10^3 kN/m).
[c]$k_{NB} = 5.0 \times 10^7$ lb/in. (8.76×10^6 kN/m).

Experimental Measurements

Experimental measurements of the window dynamic response were carried out in the laboratory using a full scale test fixture constructed expressly for this purpose (2,9). Basically, it consists of a robust vertical hardback capable of supporting a 16 ft × 8 ft (4.9 m × 2.5 m) section of cladding. The rear of the fixture is sealed tight around six large 15 ft^2 (1.4 m^2) pistons which are driven by servocontrolled hydraulic actuators to produce controlled fluctuating pneumatic pressures of up to 25 psf (1.2 kPa) amplitude, and 20 Hz frequency about mean pressures up to 50 psf (2.4 kPa). While this facility is capable of producing a variety of pressure loadings, its use in the present work was primarily as a window support fixture and a source of band-limited Gaussian amplitude pressure excitation. Fig. 7 shows the basic facility.

Test Window and Mounting Configuration.—A single story section of the cladding (Figs. 1, 2), including mullions, muntins, spandrel framing, glazing materials, and four double-pane vision lights, was obtained from the fabricator and installed in the test fixture. In actual service, the 24 ft (7.3 m) mullion sections are pinned to the floor slabs at a 12 ft (3.6 m) spacing with a splice every two stories. But in the present case a single story spliced configuration was constructed. The vision light was a 99 in. × 57 in. × 1 in. (2,515 mm × 1,448 × 25 mm) insulated silver reflective glass unit composed of two 0.24 in. (6.4 mm) thick panes bonded along their edges to a 0.5 in. (12.7 mm) thick square steel spacer. Plywood panels were installed around the window in the

same manner to simulate the effect of spandrel sections (single glazing in the field site) and adjacent windows. The window assembly was oriented with the normal "outside" surfaces facing outward so that building external suction (negative) pressures could be produced. However, the test fixture is capable of handling negative internal pressures and, only for convenience of sealing, was limited in these tests to positive pressures.

In the present study, two major parameters were considered:

1. Glazing support conditions—in particular, the effect of increased or decreased glazing support due to precompression of the neoprene glazing gasket.
2. Window integrity—the effect on deformation and stresses of maintaining a hermetically sealed volume (or gap) of gas between the two glass panes in an insulating window.

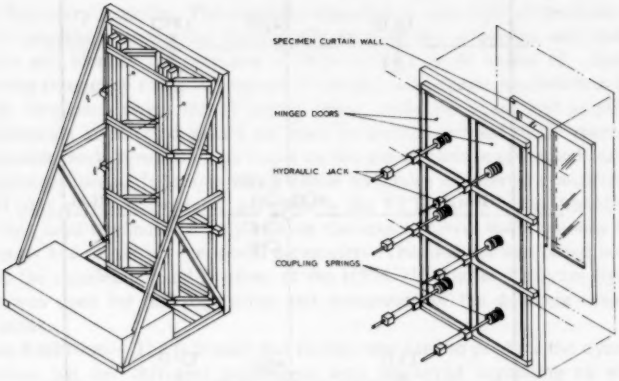

FIG. 7.—Laboratory Test Fixture

The first case is directly concerned with the effect of gasket support conditions on static response. Rather than consider the more complex case of variable structural geometry (which has been extensively explored in the analytical developments), the present tests were concerned with the effect on dynamic response when more or less gasket material is forced in the glazing, thus providing varying degrees of gasket precompression. This is typically the result of differences in glazing techniques and, for certain designs, the effect on performance may be substantial. The second case considers window performance when the seal between window panes is broken, either through aging or mechanical failure of the spacer and sealant.

The first case was simulated by using a standard glazing configuration in which the gasket length was cut exactly equal to the window perimeter. Then configurations with 10% less and 5% more gasket lengths were used. These values were the practical limits of the amounts of gasket that could be removed without leaving gaps, or the extra length that could be forced into the glazing. The "nominal" gasket configuration was quantatively evaluated in a series of

laboratory tests (4). Values for the out-of-plane, in-plane, and rotational boundary restraint stiffnesses, so determined, were used as nominal values in the analytical modelling.

The second case was simulated by boring four 3/8 in. (9.5 mm) holes through the insulating window spacer and into the internal volume. These were located

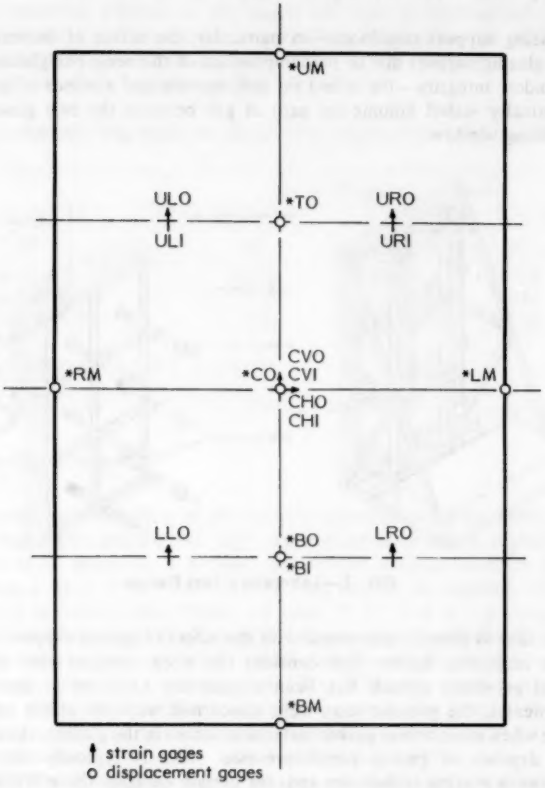

FIG. 8.—Reference Measurement Locations on Test Window

near each corner and were fitted with removable rubber plugs to allow simulation of either a "vented" or "sealed" configuration. One plug was fitted with a pressure tap to allow measurement of the internal pressure under "sealed" conditions.

The test window, with strain gages attached, was mounted in the framing and glazed with the specified amount of gasket material. The window was

supported on glazing blocks and carefully centered with a uniform penetration in the mullion and spandrel sections of approximately 0.5 in. (13 mm).

Measurement and Analysis Methodology.—The strain gage and linear variable differential transformer (LVDT) instrumentation, shown schematically in Fig. 8, was used for the dynamic response measurements. The output from the LVDT's is proportional to the transverse displacement of the glass at that point. The strain gage output is due to glass strain at the measurement point. For the range of deflections and loads used for the tests, the strain is due primarily to the plate curvature, and thus, the gage output can be directly related to the plate deflection. Strain gages are relatively inexpensive and simple to use and since, in contrast to the LVDT's, require no special reference mounting, they have been employed as the primary dynamic response transducers.

The primary objective of the dynamic response testing was to determine the basic modal characteristics of the window assembly for systematic variations in the boundary restraint. The classical approach to this type of problem has been to provide a means for dynamically exciting the structure, and then to measure and identify the response at each of the natural modes of vibration within the frequency range of interest. Typically, a harmonic excitation is used and the frequency swept slowly over a range, while the phase and amplitude measurements at selected points are used to identify normal mode response. The present work, however, was based on the use of both band-limited random and transient forcing functions which excite all modes of interest concurrently. Digital time series techniques, particularly the FFT (fast Fourier transform), were then used to simultaneously analyze the response over the frequency band of interest and to extract the modal parameters. The analysis was based largely around the capabilities and features of the HP5451B Fourier Analyzer System which was used for the acquisition and processing of the dynamic response time series.

Input Excitation.—The full-scale test facility was used to produce the dynamic excitation, but two different procedures were employed depending on which aspects of the response were being analyzed. The first procedure consisted of using the closed-loop servocontrolled hydraulic system to produce time varying pneumatic pressures across the test window. A time varying electrical signal was applied to the control system which in turn caused hydraulic actuators to displace two large doors, or pneumatic pistons, located on the rear side of the test fixture. The door motion produced corresponding time varying pressure fluctuations in the test facility and, thus provided the desired fluctuating differential pressure across the test window. Band-limited, Gaussian amplitude white noise was used as the excitation signal. This manner of excitation closely resembles the character of actual service conditions, but due to the window and test fixture symmetry, it was only possible to excite symmetric modes in this way.

An alternate method was developed to excite unsymmetric modes and was used along with the random excitation. This method was basically an impulse excitation applied unsymmetrically at a point on the window. Due to the relative inaccessibility of the window surface on the test chamber inside, a single input point was chosen and multiple response points were used. The impulse was applied by hand using a large mallet with a suitably cushioned head to provide the necessary impulse energy over the frequency range of interest.

Dynamic Response Results

The modal parameters were obtained from measured transfer functions by using the curve-fitting algorithms incorporated in the Modal Analysis software (11) on the HP5451B Analyzer. Each mode was identified by the phase relations between transfer functions at each of the measurement points. With reference to the arrangement of sensors shown in Fig. 8, it is possible in this way to detect modes with up to three nodes in the vertical and up to two nodes in the transverse directions (3-2 mode). For each test, ensemble averaging was used to reduce the variance to an acceptable level, and the transfer function data were rejected if the computed coherence function was of poor quality (below about 0.80).

Nominal Gasket.—Table 4 shows the modal frequencies and damping for the nominal gasket configuration. The results are shown for both the sealed and vented interpane void tests, and, for comparison, the continuous and discrete analytical predictions are also listed. Several points are noteworthy:

TABLE 4.—Frequencies and Damping for Nominal Gasket and Sealed Interpane Void

Source (1)	Parameter (2)	Mode 1-1 (3)	1-2 (4)	1′-2′ (5)	1-3 (6)	2-1 (7)	2′-1′ (8)
Measured	Frequency, in Hertz	10.2	19.4	19.6	28.6	32.8	42.3
	Damping, as a percent	6.0	3.3	1.8	10.9	7.6	1.1
Theory	Frequency, in Hertz	12.2[a]	18.2[b]	18.1–28.4[c]	34.7[a]	34.2[b]	34.2–52.1[c]

[a]Finite element model with measured properties.
[b]Continuum model for simple support.
[c]Continuum model, interplate restraint from 0 to infinite, out-of-phase modes involving opposing movement.

1. The experimental results identify not only the first four "classical" plate modes, but also the 1′-2′ and possibly the 2′-1′ modes. In the classical modes, the two plates move together and the window behaves like an equivalent single plate; while for the primed modes, the two plates move in opposite directions. This behavior may or may not involve a net interpane compression or breathing action, depending on the mode shape. The primed modes are of the even-odd type and thus do not involve a net void volume change (breathing). They do, however depend on the interplate rotational coupling at the edge. This coupling stiffness was not quantitatively assessed, but from the model results the 1′-2′ frequency could range from 18.09–22.44 Hz as the rotational stiffness, k_θ, varies from 0 to ∞. The observed frequency falls near the lower end of this range which indicates that this type of boundary coupling is not particularly strong for the present type of window. This kind of motion is perhaps of more interest analytically in the laboratory than it is in practice. For practical sized windows (areas less than about 60 ft^2 (6 m^2)), the critical frequencies are generally well above the frequency band containing most of the driving power in typical installations. Furthermore, these unsymmetric modes are driven most effectively by nonuniform pressure distributions across the window. For large, doubly glazed

windows in situations where significant variations in pressure distribution over the surface may exist, this type of behavior should be evaluated. Changes in boundary restraint do not appear to be very effective in changing the situation, but proper specification of the spacing of the panes should eliminate this factor.

2. The measured damping is in excess of 5% for most modes, which is somewhat large for metal or glass structures alone. This behavior is largely due to the viscoelastic properties of the boundary gasket, especially for the classical plate modes. The damping values for the primed modes are considerably smaller and reflect the reduced participation of the gasket in this type of response. From a design point of view, this suggests that glazing properties, through their viscoelastic behavior, might be used to control peak dynamic response in the classical plate modes, but would likely have little effect on the primed modes which could lead to the possibility of interplate contact, especially for very large panes with strong nonuniform pressure loadings.

TABLE 5.—Dependence of Modal Values on Gasket Restraint

Configuration (1)	1-1 Mode		1-2 Mode	
	Frequency, in Hertz (2)	Damping, as a percent (3)	Frequency, in Hertz (4)	Damping, as a percent (5)
		(*a*) Sealed		
−10%	10.18	5.7	17.54	3.5
0%	10.23	6.0	19.31	3.5
+5%	10.01	3.5	19.70	2.6
		(*b*) Vented		
−10%	9.95	5.7	17.49	3.1
0%	10.16	7.6	19.40	—
+5%	10.48	7.8	19.67	2.9
		(*c*) Average		
−10%	10.06	5.7	17.52	3.3
0%	10.20	6.8	19.36	3.5
+5%	10.25	5.8	19.68	2.8

3. The effect of interpane venting is essentially negligible for the present conditions. This is basically in agreement with the analysis since for the lower modes there should be no net interpane volume change. The effect would be a factor only for the breathing modes, the lowest of which is near 100 Hz, and at that frequency the present holes would be of insignificant size. In contrast, the static response is highly affected.

4. A clear normal mode response was not observed for some of the modes. This can be attributed in part to the high damping, but was largely due to the tendency of the two plates comprising the window to behave slightly differently rather than in unison for each mode. This effectively resulted in two very closely spaced modes which proved impossible to detect by hand and difficult at best to handle with the modal analysis software.

Boundary Gasket Effect.—The effect of variation in the boundary gasket support stiffness is shown in Table 5. The data cover the first two modes for both vented and sealed interpane conditions. As before, these data were obtained from transfer functions using the analytical curve-fitting software. Several features are noteworthy:

1. There is little difference between the vented and sealed interpane void data, as was anticipated and observed in the previous results. For clarity, these two cases have been averaged together and listed in the lower lines as the "average" modal values.
2. There is a consistent trend in which the frequencies increase as the boundary support is stiffened. This is seen most clearly in the "average" values and is most pronounced for the higher mode. This type of behavior is fully consistent with the analytical predictions.
3. The damping is not appreciably affected by alteration of the glazing gasket, as presently accomplished. However, as observed earlier, there is a substantial change in the damping from mode to mode.

Conclusions

Analytical studies have focused attention on the properties and behavior of a small segment of the exterior curtain wall encompassing the frame, gaskets, and a single or double-plate glass panel. The model is general in scope and permits a wide range of cladding configurations and loading types to be considered. Response was shown to be sensitive to gasket rotational stiffness and frame flexural stiffness. The analytical cladding model is compatible with existing three-dimensional multi-story building models, and is currently being used to study cladding-structure interaction in high-rise buildings.

The modal tests, using either impulse or uniform random pressure, have yielded frequencies, damping, and mode shapes for the double-glazed window when supported in a manner closely duplicating the actual service conditions. The measured frequencies agree reasonably well with analytical predictions, although sufficient experimental measurements were not made to adequately define those modes involving significant boundary movement. Damping values tended to be rather large for glass or metal structures, as a result of the viscoelastic boundary restraint provided by the glazing gaskets. However, variations in the amount of gasket material used in the glazing produced insignificant changes in damping.

The most significant result of the tests was the detection of the primed modes in which the two panes move in opposite directions. Since the damping was found to be relatively low in the lab tests, the possibility exists that these modes could be excited at relatively high amplitudes, especially in large windows where nonuniform pressure loading may occur. Finally, a major effort was made to closely simulate actual conditions, and this yielded results in close agreement with field and analytical studies, thus providing confidence in the analysis.

Acknowledgments

Support for this study, provided in part by National Science Foundation Grant

ENG73-04216, is greatefully acknowledged.

Appendix I.—References

1. Allen, D. E., and Dalgliesh, W. A., "Dynamic Wind Loads and Cladding Design," *The Preliminary Publication of the International Association of Bridge and Structural Engineering Symposium*, held at Lisbon, Portugal, 1973, pp. 279–285.
2. Craig, J. I., Goodno, B. J., and Deo, R. B., "Window and Curtain Wall Performance in Highrise Buildings," *Report No. GITAER-78-100/SCEGIT-78-170*, Schools of Aerospace and Civ. Engrg., Georgia Inst. of Tech., Atlanta, Ga., Mar., 1978.
3. Goodno, B. J., "Glass Curtain Wall Elements: Properties and Behavior," *Journal of the Structural Division*, ASCE, Vol. 105, No. ST6, Proc. Paper 14656, June, 1979, pp. 1121–1136.
4. Goodno, B. J., and Craig, J. I., "Response Studies of Glass Cladding Panels," *Proceedings*, International Symposium on Behavior of Building Systems and Building Components, held at Vanderbilt Univ., Nashville, Tenn., Mar. 8–9, 1979, pp. 137–158.
5. Goodno, B. J., Will, K. M., and Craig, J. I., "Analysis of Cladding on Tall Buildings," presented at the Oct. 1979 ASCE National Convention and Exposition, Session on Developments in Methods of Structural Analysis, held at Atlanta, Ga. (Preprint 3744).
6. Ida, M., Terayama, T., and Miyoshi, S., "Measurement of Natural Wind Pressure Acting on Glass Panels of Kasumigaseki High Rise Building in High Wind," *Research Report*, Asahi Glass Company, Tokyo, Japan, Vol. 20, No. 2, 1970, pp. 79–92.
7. Khan, F. R., "A Rational Method for the Design of Curtain Walls," *Proceedings*, Design Symposium on Wind Effects on Buildings, held at Northwestern Univ., Evanston, Ill., Mar. 23, 1970, pp. 145–174.
8. Miyoshi, S., and Miura, T., "Study of the Wind Resistance of Glass Panels (Part 2). Breaking Tests of Large Glass Panels by Means of Oscillatory Pressure," *Research Report*, Asahi Glass Company, Tokyo, Japan, Vol. 14, No. 2, 1964, pp. 82–92 (British Glass Industry Research Association Translation No. 660).
9. Palfery, J. G., and Craig, J. I., "Full-Scale Wind Pressure Simulation for Windows and Curtain Wall Structures," *Proceedings*, ASCE/EMD Specialty Conference on Dynamic Response of Structures, University of California at Los Angeles, Mar., 1976, pp. 380–390.
10. Peterka, Jon A., and Cermak, J. E., "Wind Pressures on Buildings: Probability Densities," *Journal of the Structural Division*, ASCE, Vol. 101, No. ST6, Proc. Paper 11373, June, 1975, pp. 1255–1267.
11. Richardson, M., and Potter, R. W., "Identification of the Modal Properties of an Elastic Structure from Measured Transfer Function Data," *Proceedings*, 20th Instrument Society of America Symposium, held at Albuquerque, N.M., May 21–23, 1974.
12. Sadeh, W. Z., and Cermak, J. E., "Turbulence Effect of Wall Pressure Fluctuations," *Journal of the Engineering Mechanics Division*, ASCE, Vol. 98, No. EM6, Proc. Paper 9445, Dec., 1972, pp. 1365–1379.

Appendix II.—Notation

The following symbols are used in this paper:

A_p = area of quarter panel ($ab/4$);
a_{mn} = amplitude of mn-th mode;
a, b, h = glass panel dimensions;
D = plate flexural rigidity;
f = dimensionless frequency;
I_x, I_y, I_z = area moments of inertia for frame elements;
I_1 = $2EI_x/bD$, mullion;
I_3 = $2EI_y/bD$, mullion;

I_5 = $2EI_y/aD$, spandrel;
I_7 = $2EI_x/aD$, spandrel;
K_1 = $k_N b^3/8D$;
K_2 = $k_R b/2D$;
K_θ, K_δ = boundary and air gap spring constants for double-plate model;
k_p, k_L, k_N, k_R = constants for gasket spring elements;
k_{NB} = air gap spring constant for discrete model;
p_o = atmospheric pressure;
V_o = initial interpane volume;
w_1, w_2 = lateral deflection of glass panels;
Δp_{mn} = interpane pressure change due to *mn*-th mode;
ΔV_{mn} = change in interpane volume due to *mn*-th mode;
γ = adiabatic exponent;
ξ_A, ξ_B = dimensionless form for K; and
ρ = mass per unit area of plate.

Extensions to Curved Prestressed Concrete Beams

By Carlo Pace[1] and Luigino Dezi[2]

Introduction

On continuous beams with straight centroidal axes, Guyon's theorem assures that when a steel profile is linearly transformed, the thrust line remains unchanged (8). (A linear transformation is a rotation of the line connecting the cable location at support points, keeping the two end points fixed. The curvature remains unchanged.)

This theorem permits appreciable simplifications in the study of thrust lines in continuous beams. In fact, starting from a cable line coincident with the thrust line (concordant), linear transformations can be made which result in a thrust line for a statically determinate structure.

In curved beams, this theorem no longer holds, as will be shown, because of the curvature in the horizontal plane which the cable must assume to follow the beam's centroidal axis.

In this paper, the theorem of Guyon is reconsidered for a continuous curved beam and those forces that invalidate the theorem are determined in terms of equivalent loads. For these loads, influence coefficients for stress resultants and rotations at the ends of each single span are obtained. These coefficients are used to determine the effect of a linear transformation in the two most common schemes used in continuous beams, and the results obtained are compared with those for straight beams.

Curved Beams

Consider a continuous curved beam supported by pairs of point supports which maintain torsional fixity while permitting relative deformation in the horizontal plane. In this way, no horizontal forces are induced so that the precompression is transferred to the structure without modification.

In order to realize the above support conditions in continuous beams, the

[1]Visiting Scholar, Dept. of Civ. Engrg. and Engrg. Mechanics, Columbia Univ., New York, N.Y. and Asst. Prof., Istituto di Tecnica delle Costruzioni, Ancona, Italy.

[2]Research Assoc., Istituto di Tecnica delle Costruzioni, Ancona, Italy.

Note.—Discussion open until April 1, 1982. To extend the closing date one month, a written request must be filed with the Manager of Technical and Professional Publications, ASCE. Manuscript was submitted for review for possible publication on March 11, 1980. This paper is part of the Journal of the Structural Division, Proceedings of the American Society of Civil Engineers, ©ASCE, Vol. 107, No. ST11, November, 1981. ISSN 0044-8001/81/0011-2215/$01.00.

roller supports must be oriented, in plan view, along the lines between them and the fixed support since it is along these lines that the beam shortens as a result of the compressive prestress. For a fuller discussion of this subject, see Ref. 5.

In what follows, the assumption usually made for beams with large span-to-depth ratios, that the supports are effectively at the centroid of the section instead of at the bottom, is implicitly made. The error introduced by this approximation is negligible, e.g., for bridge structures.

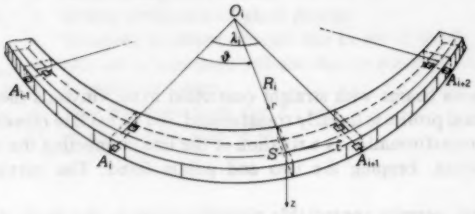

FIG. 1.—Curved Prestressed Beam on Several Supports

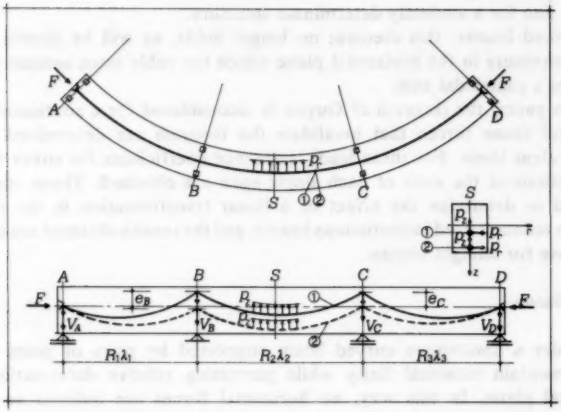

FIG. 2.—Three-Span Prestressed Beam with Two Cable Profiles—Plan and Elevation

The centroidal axis of the beam is referred to a system of polar coordinates, R and θ. At a generic section, $S(\theta)$, a local coordinate system, t, r, z, is defined, oriented as in Fig. 1, to which forces exerted between cable and concrete will be referred.

On such a beam, consider a prestressing cable laid out along the centroidal axis such that it has only a vertical eccentricity, denoted by $z(\theta)$. In the absence of external loads, the prestressing force, F, on the cable is constant over its entire length.

It is further assumed that the curve of the cable is sufficiently flat so that

the tangent can be approximated by its horizontal projection and the normal with its vertical projection.

Referring to a continuous three-span beam (Fig. 2), consider two cable profiles differing only by a linear transformation. The forces exerted by the cables on the concrete may be outlined as (10)

1. Horizontal forces, F, equal to the tension, applied at the two end sections.
2. Vertical forces, V, exerted on the supports, equal to the vertical component of the tension.
3. Vertical pressure, p_z, due to the vertical curvature of the cable, equal to $F\,Z''/R^2$, in which primes denote differentiation with respect to θ.
4. Radial pressure, p_r, produced because of the curvature of the beam, equal to F/R.
5. Distributed torsional couples, m_t, resulting from the eccentricity of the points of application of the radial pressure equal to $p_r z = Fz/R$.

As a result of the linear transformation, therefore, the force, F, and the pressures, p_z and p_r, remain unchanged. The forces, V, change because of the different slope of the cable, as do the torsional couples, m_t, since the eccentricity changes. While the forces, V, act directly on the supports, the couples, m_t, modify the state of stress in the structure.

This result makes Guyon's theorem invalid for curved beams. In these structures, when a linear transformation is performed, it is necessary to add the effects of the torsional couples.

Having effected a rigid body displacement of the cable, the distribution of couples is linear. Referring to Fig. 2, in which e_B and e_C are the displacements occurring at the intermediate supports (see Appendix I), the following expressions are obtained:

$$m_t(\theta) = \frac{F}{R_1} e_B \frac{\theta}{\lambda_1} \quad \text{in the first span} \qquad (1)$$

$$m_t(\theta) = \frac{F}{R_2}\left(e_B \frac{\lambda_2 - \theta}{\lambda_2} + e_C \frac{\theta}{\lambda_2}\right) \quad \text{in the second span} \qquad (2)$$

$$m_t(\theta) = \frac{F}{R_3} e_C \frac{\lambda_3 - \theta}{\lambda_3} \quad \text{in the third span} \qquad (3)$$

To evaluate the effects of these couples, a statically indeterminate problem must be solved. To this end, the beam may be cut at the supports and the bending moments M_B and M_C chosen as redundants, as shown in Fig. 3.

Continuity of flexural rotations at B and C require that

$$M_B(W^{I}_{BB} + W^{II}_{BB}) - M_C W^{II}_{BC} = W^{I}_{BO} - W^{II}_{BO} \qquad (4)$$

$$-M_B W^{II}_{BC} + M_C(W^{II}_{CC} + W^{III}_{CC}) = W^{II}_{CO} - W^{III}_{CO} \qquad (5)$$

in which W_{BB}, W_{CC}, and W_{BC} = flexibility coefficients; W_{BO} and W_{CO} = the rotation produced by the torsional couples, m_t; and I, II, III denote the spans (3).

The combination of the stresses produced by the couples, m_t, and by the

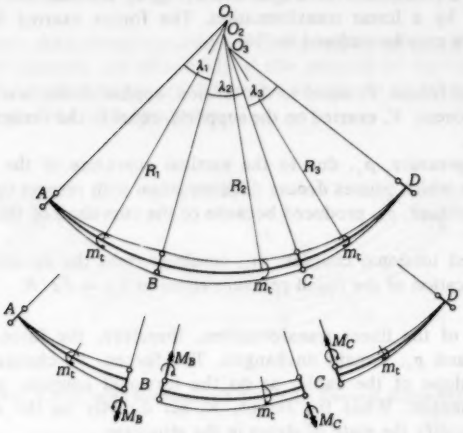

FIG. 3.—Redundants for Three-Span Prestressed Beam

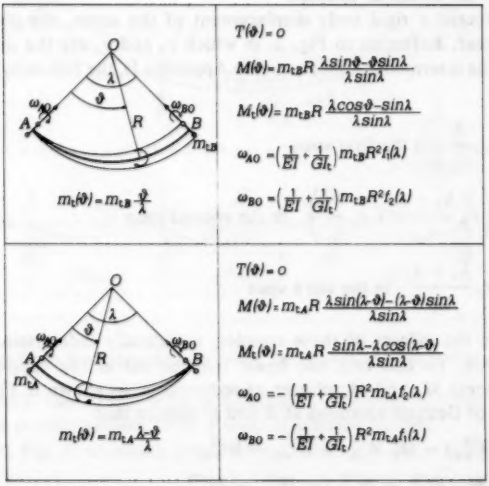

FIG. 4.—Stress Resultants and End Rotations Due to Twisting Couple Applied at Ends of Span

redundants M_B and M_C, constitute the effect of the linear transformation (Fig. 3).

In order to evaluate numerically these contributions, expressions for the stress resultants and for the end rotation are given for three possible distributions of twisting moments in Fig. 4. Only the results corresponding to the distributions of Eqs. 1 and 3 are exhibited because that of Eq. 2 may be obtained from these by superposition. In this table, m_{tA} and m_{tB} are the values of the applied distributed twisting couples at the supports and T, M, and M_t are the induced shear, bending moment, and twisting moment. The positive sense of the flexural rotations at the supports, W_{AO} and W_{BO} are indicated in the figures accompanying the table and EI and GI_t are the flexural and torsional stiffnesses, respectively.

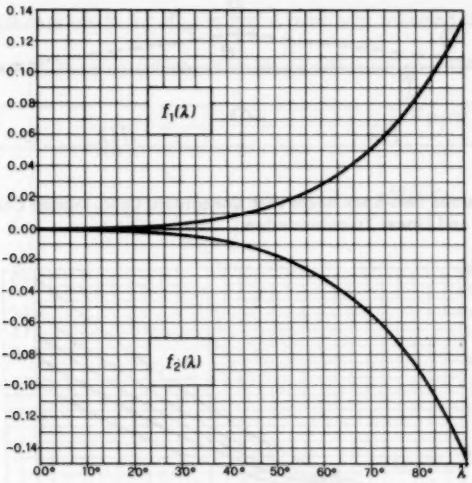

FIG. 5.—Plots of $f_1(\lambda)$ and $f_2(\lambda)$

The functions $f_1(\lambda)$ and $f_2(\lambda)$ appearing in Fig. 4 are given by

$$f_1(\lambda) = \frac{2\sin^2\lambda - \lambda\sin\lambda - \lambda^2\cos\lambda}{2\lambda\sin^2\lambda} \quad \ldots\ldots\ldots\ldots\ldots\ldots\ldots\ldots (6)$$

$$f_2(\lambda) = \frac{2\sin^2\lambda - \lambda^2 - \lambda\sin\lambda\cos\lambda}{2\lambda\sin^2\lambda} \quad \ldots\ldots\ldots\ldots\ldots\ldots\ldots\ldots (7)$$

and plotted in Fig. 5.

For small curvature, f_1 and f_2 approach zero and the effect of the couples, m_t, becomes negligible. In the limit as $\lambda \to 0$, the case of a straight beam is obtained for which $W_{AO} = W_{BO} = 0$.

Applications

By using the coefficients of Fig. 4, two applications are developed, and the

results obtained are compared with those of a straight beam.

The two most common cases of continuous beams, those with two or three spans, are considered. To reduce the number of variables, it is assumed that the spans are equal with equal curvature.

Furthermore, for simplicity the cable is taken to be initially straight, concordant and coincident with the centroidal axis. This choice does not limit validity of the results since the effects of a linear transformation are independent of the initial profile.

Referring to the beam of Fig. 6, consider a displacement, e, of the cable at the intermediate support. As established in the previous section, a distribution

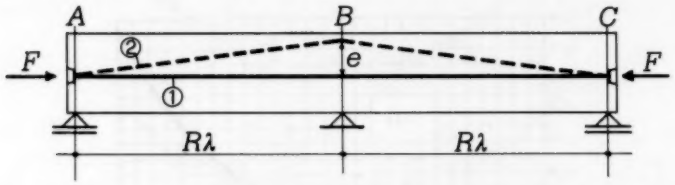

FIG. 6.—Continuous Two-Span Beam with Concordant Cable Initially Coincident with Centroidal Axis and Linear Transformation

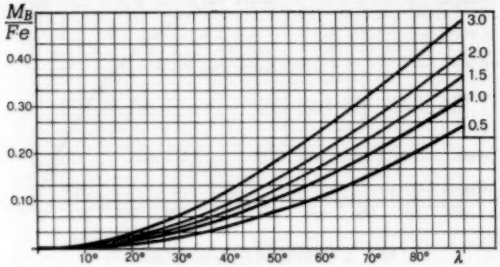

FIG. 7.—Plot of M_B for Beam of Fig. 5 for Various Values of EI/GI_t

of torsional couples is produced given by

$$m_t(\theta) = -\frac{F}{R} e \frac{\theta}{\lambda} \quad \text{in the first span} \quad \ldots\ldots\ldots\ldots\ldots\ldots\ldots\ldots (8)$$

$$m_t(\theta) = -\frac{F}{R} e \frac{\lambda - \theta}{\theta} \quad \text{in the second span} \quad \ldots\ldots\ldots\ldots\ldots\ldots\ldots (9)$$

To evaluate the effects of these couples, the structure is cut at B and the bending moment M_B is chosen as redundant. Eqs. 4 and 5 specialize to

$$M_B(W^{I}_{BB} + W^{II}_{BB}) = W^{I}_{BO} - W^{II}_{BO} \quad \ldots\ldots\ldots\ldots\ldots\ldots\ldots\ldots (10)$$

Since, from symmetry, $W^{II}_{BO} = -W^{I}_{BO}$ and $W^{I}_{BB} = W^{II}_{BB}$, the redundant is obtained as

$$M_B = \frac{W^1_{BO}}{W_{BB}} = -\frac{\left(\frac{1}{EI}+\frac{1}{GI_t}\right) f_2(\lambda)\, FeR}{\left(\frac{1}{EI}+\frac{1}{GI_t}\right) R \frac{\lambda - \sin\lambda\cos\lambda}{2\sin^2\lambda} - \frac{R}{GI_t}\frac{\sin\lambda - \lambda\cos\lambda}{\lambda\sin\lambda}}$$

$$= Fe \frac{\left(1+\frac{EI}{GI_t}\right)(2\sin^2\lambda - \lambda^2 - \lambda\sin\lambda\cos\lambda)}{\left(1+\frac{EI}{GI_t}\right)(\lambda^2 - \lambda\sin\lambda\cos\lambda) - \frac{EI}{GI_t}(2\sin^2\lambda - 2\lambda\sin\lambda\cos\lambda)} \quad \ldots (11)$$

using the first expression for W_{BO} in Fig. 4, with sign reversed, for W^1_{BO}.

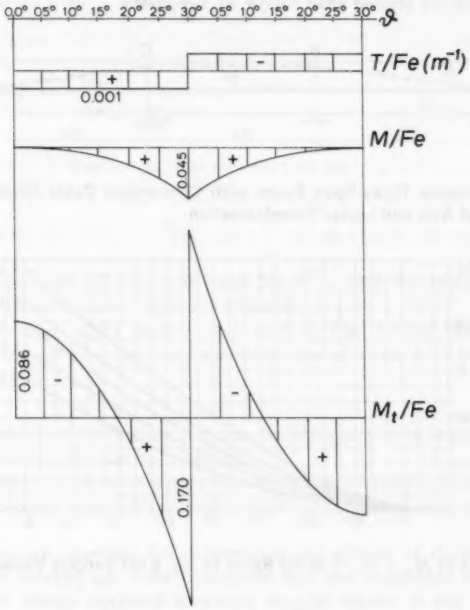

FIG. 8.—Shear, Bending Moment, and Twisting Moment Diagrams for Beam of Fig. 5

For straight beams, M_B would be zero. In Fig. 7, a plot of the nondimensional moment M_B/Fe as function of λ is shown for various values of EI/GI_t.

It is seen that, in accordance with the curve of $f_2(\lambda)$ plotted in Fig. 5, the value of M_B tends to zero as the angular opening λ decreases. There is seen to be a strong dependence on the ratio of flexural to torsional rigidity; M_B/Fe increasing with this ratio.

For the range of values encountered in practice, $1 \leq EI/GI_t \leq 2$ and λ

$< 40°$, it may be noted that the moment induced is less than 10% of the product Fe.

To complete the example, the stress resultant functions due to m_t and M_B are obtained for the first span as

$$T(\theta) = \frac{M_B}{R\lambda} \quad \ldots \quad (12)$$

$$M(\theta) = Fe\frac{\lambda \sin\theta - \theta \sin\lambda}{\lambda \sin\lambda} + M_B\frac{\sin\theta}{\sin\lambda} \quad \ldots \quad (13)$$

$$M_t(\theta) = -Fe\frac{\lambda\cos\theta - \sin\lambda}{\lambda \sin\lambda} - M_B\left(\frac{1}{\lambda} - \frac{\cos\theta}{\sin\lambda}\right) \quad \ldots \quad (14)$$

while those for the second span follow by symmetry.

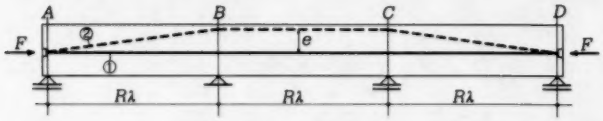

FIG. 9.—Continuous Three-Span Beam with Concordant Cable Initially Coincident with Centroidal Axis and Linear Transformation

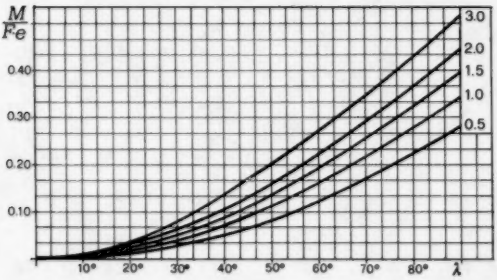

FIG. 10.—Plot of $M_B = M_C = M$ for Beam of Fig. 8 for Various Values of EI/GI_t

For the particular case $\lambda = 30°$, $R = 80$ m, $EI/GI_t = 1.5$, one obtains $M_B = 0.045\,Fe$ and the stress resultant diagrams of Eqs. 12, 13, and 14 are displayed in Fig. 8. The flexural moment has maximum value at the intermediate support, so that the graphs of Fig. 7 depict the controlling moment.

Curved beams must resist both flexural and torsional moments. The compressive prestress in a concordant cable is only partially effective because it cannot provide a resistant torsional couple (6). Fig. 8 shows, however, how an appropriate linear transformation may be used to provide such a capability.

In order to produce a distribution of torsional moments with sense opposite to those produced by the external loads, the designer must provide for an upward

displacement of the curve. A lowering of the cable would produce an undesirable contrary effect.

It is seen, then, that to produce a linear transformation favorable to torsional resistance, the concordant cable (position 1 in Fig. 6) must not have, with respect to the intermediate supports, the maximum eccentricity permitted by the cross section. This requires, however, a greater precompressive force in the cable than would be necessary if optimal eccentricity were used. This constitutes, therefore, a limitation or constraint on the procedure described above, to be weighed against the benefits obtained when torsion plays an important role.

Repeating the above procedure for a curved beam with three equal spans (Fig. 9), for which $M_B = M_C = M$, the equations of compatibility, Eqs. 4 and 5, reduce to

$$M(2W_{BB} - W_{BC}) = W'_{BO} - W''_{BO} \quad \ldots \ldots \ldots \ldots \ldots \ldots \ldots \quad (15)$$

so that $$M = FeR \frac{\frac{1}{EI} + \frac{1}{GI_t}[f_1(\lambda) - 2f_2(\lambda)]}{2W_{BB} - W_{BC}}$$

$$= \frac{\left(1 + \frac{EI}{GI}\right)(-2\sin^2\lambda + 2\lambda^2 + 2\lambda \sin\lambda \cos\lambda - \lambda \sin\lambda - \lambda^2 \cos\lambda)}{\left(1 + \frac{EI}{GI_t}\right)[\lambda \sin\lambda(1 - 2\cos\lambda) + \lambda^2(2\cos\lambda)] + \frac{EI}{GI}[2\lambda \sin\lambda(\cos\lambda - 1) - 2\sin^2\lambda]} \quad (16)$$

when the upper half of Fig. 4 is used for W'_{BO} and the sum of both W_{BO} for W''_{BO}. In all three cases, signs are changed.

The variation of M/Fe with λ is plotted in Fig. 10 for various value of EI/GI_t, illustrating behavior quite similar to that of a two-span beam.

Conclusions

Guyon's linear transformation theorem for straight beams is not strictly valid for curved beams and must be modified.

When a linear transformation is performed for such beams, a linear distribution of torsional couples is introduced which modifies the initial state of compressive prestress.

Expressions are obtained for determining the effects of these forces. Two examples are worked out which illustrate that the correction to the bending moments and shears obtained assuming straight beams is not too important and may be neglected in most cases.

As a result of a linear transformation, however, internal torsional moments of considerable magnitude can be produced by the precompression forces in the cable. With an appropriate selection of cable placement, these moments may be used to resist the torsion produced by the external loads.

Appendix I.—Derivation of Eqs. 1-3

As a result of the transformation in Fig. 2, internal torsional couples are created with the distribution

$$m_r(\theta) = p_r z(\theta) \quad \ldots \ldots \ldots

G = shear modulus;
I,II,III = superscripts denoting span number;
I = second moment of cross-sectional area;
I_t = polar moment of cross-sectional area;
M, M_t = bending and twisting moment;
m_t = distributed torsional couples;
p_r, p_z = radial and vertical cable pressures;
R = global radial coordinate of beam centroidal axis;
r = local radial coordinate;
S = denotes generic section of beam;
t = local tangential coordinate;
V = vertical support forces;
W_{BB}, W_{CC}, W_{BC} = flexibility coefficients;
W_{BO}, W_{CO} = rotations at sections B and C;
z = local vertical coordinate;
λ = included polar angle;
$\lambda_1, \lambda_2, \lambda_3$ = included angles in each of three spans; and
θ = polar angular coordinate.

SHEAR STRENGTH OF R/C BEAM-COLUMN CONNECTIONS

By Donald F. Meinheit[1] and James O. Jirsa,[2] Members ASCE

BACKGROUND

The first experimental tests on beam-column connections were conducted in the United States by the Portland Cement Association in the early 1960's and were published by Hanson and Conner (7) in 1967. These tests have become the standard reference for subsequent investigations. Hanson and Conner concluded that when the strength of the beam-column connection in shear was computed using equations developed for reinforced concrete beams, a satisfactory estimate of the response of the beam-column connection under repeated load was obtained.

Since the 1960's, other investigators have provided more data applicable to the beam-column connection design problem. However, in a recent report by ACI-ASCE Committee 352, Joints in Monolithic Reinforced Concrete Structures, additional areas of needed research on the behavior of beam-column connections were cited (18).

A review, chronologically, of other experimental investigations on beam-column connections is summarized in Table 1. While each research program had slightly different objectives, the thrust of the majority of the programs has been twofold: (1) To develop construction details to provide and maintain ductility under repeated loads on the beam-column connection; and (2) to provide anchorage for the beam reinforcement in an exterior connection where an unbalanced moment produces shear in the connection and aggravates the anchorage conditions.

In several investigations a simulated seismic loading history was applied to test specimens. Fig. 1 shows a sample of some of the loading histories. In most cases, the loading history was based on curvature or deflection ductility. Several investigators have considered the effect of the number of load reversals on behavior. The assortment of loading histories used in different test programs makes direct comparison of the experimental data difficult. In summary, there has been a major emphasis on seismic behavior and little concentration on

[1]Sr. Structural Engr., Wiss, Janney, Elstner and Assoc., Inc., Northbrook, Ill.
[2]Prof. of Civ. Engrg., Univ. of Texas at Austin, Austin, Tex.

Note.—Discussion open until April 1, 1982. To extend the closing date one month, a written request must be filed with the Manager of Technical and Professional Publications, ASCE. Manuscript was submitted for review for possible publication on January 23, 1981. This paper is part of the Journal of the Structural Division, Proceedings of the American Society of Civil Engineers, ©ASCE, Vol. 107, No. ST11, November, 1981. ISSN 0044-8001/81/0011-2227/$01.00.

the basic shear strength characteristics of beam-column connections in reinforced concrete.

Failure Modes in Region of Beam-Column Connection.—Five different modes of failure are possible in the beam-column connection region. The most desirable

TABLE 1.—Test Programs on R/C Beam-Column Connections

Date (1)	Authors (2)	Institution (3)	Connection type (4)	Reference (5)
1967	Hanson and Conner	PCA Labs, Skokie, Illinois	exterior	7
1969	Higashi and Ohwada	Tokyo Metropolitan Univ., Japan	interior	9
1971	Hanson	PCA Labs, Skokie, Illinois	interior and exterior	6
1971	Megget and Park	Univ. of Canterbury, New Zealand	exterior	14
1972	Hanson and Conner	PCA Labs, Skokie, Illinois	interior and exterior	8
1972	Kordina and Schaaff	Technical Univ.-Braunschweig, W. Germany	exterior	11
1972	Patton	Univ. of Canterbury, New Zealand	exterior	16
1972	Renton	Univ. of Canterbury, New Zealand	exterior	19
1972	Smith	Univ. of Canterbury, New Zealand	exterior	20
1974	Park and Thompson	Univ. of Canterbury, New Zealand	interior	15
1974	Uzumeri and Seckin	Univ. of Toronto, Canada	exterior	24
1975	Preistley	Ministry of Works, New Zealand	interior	17
1976	Gulkan	Mid. East Tech. Univ., Ankara, Turkey	interior	5
1977	Fenwick and Irvine	Univ. of Auckland, New Zealand	interior	4
1977	Lee, Wight, and Hanson	Univ. of Michigan, Ann Arbor	exterior	12
1977	Meinheit and Jirsa	Univ. of Texas at Austin	interior	13
1977	Townsend and Hanson	Univ. of Michigan, Ann Arbor	exterior	22
1977	Uzumeri	Univ. of Toronto, Canada	exterior	23
1978	Birss, Paulay, and Park	Univ. of Canterbury, New Zealand	interior	3
1978	Keong and Park	Univ. of Canterbury, New Zealand	interior	10
1980	Bertero, Popov, and Forzani	Univ. of California at Berkeley	interior	1

failure mode, Fig. 2(*a*), is a ductile flexural failure of the beams at the connection. Formation of hinges in the beams outside the connection allows for absorption of energy through large inelastic deformations without loss of strength. Although the mechanism is the same as beam hinging, hinging of the column is less

desirable than beam hinging. When columns hinge, Fig. 2(*b*), the frame may have a residual sway deflection and may be difficult to repair. Loss of the concrete cover over the reinforcement in the beam-column core, shown in Fig. 2(*c*), is undesirable since the column compressive load capacity may be reduced, especially in tied columns. The loss of anchorage of the reinforcement, Fig. 2(*d*), especially in exterior connections, is particularly undesirable because lateral shear can no longer be transmitted by the frame. Failure of the anchorage also causes a reduction in the energy absorbing ability of the structural system. The consequences of failure of the connection in shear, Fig. 2(*e*), are the same as loss of anchorage, an inability of the frame to transfer lateral shear and declining energy absorbing ability.

Current Design.—ACI-ASCE Committee 352 recommendations (18) for connection design are based on the addition of separate contributions of concrete and reinforcing steel in the connection to assess the strength or to proportion for the shear that exists (the addition rule).

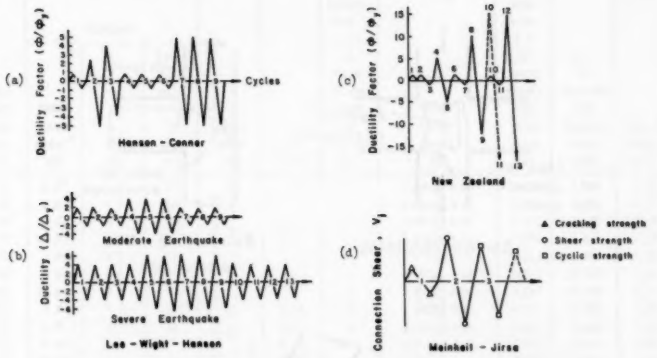

FIG. 1.—Experimental Loading Histories Simulating Earthquakes

The contribution of the concrete is taken as $V_c = 3.5\ \beta\gamma \sqrt{f_c'}(1 - 0.002N_u/A_g)$. The parameters β and γ modify the equation, originally intended for beams, and reflect values measured in beam-column connection tests. β reflects the type of design loading, and γ the confinement provided by transverse beams at the beam-column connection.

A contribution from closed hoop reinforcement is computed in the same manner as for reinforced concrete beams, $V_s = A_v f_y d/s$. The Committee report also made specific design and detailing recommendations for those connections required to carry seismic design forces.

Experimental Program

Scope and Objective.—The data obtained from tests listed in Table 1 are not sufficient to provide a basic shear strength value for beam-column connections. The programs listed in Table 1 have primarily been directed toward ensuring

that the connection failures shown in Figs. 2*c*, *d*, and *e* do not precipitate major structural damage or structural collapse.

The investigation reported herein was planned with the objective of examining methods of improving shear strength and measuring the basic shear strength characteristics of a reinforced concrete beam-column connection. The parameters

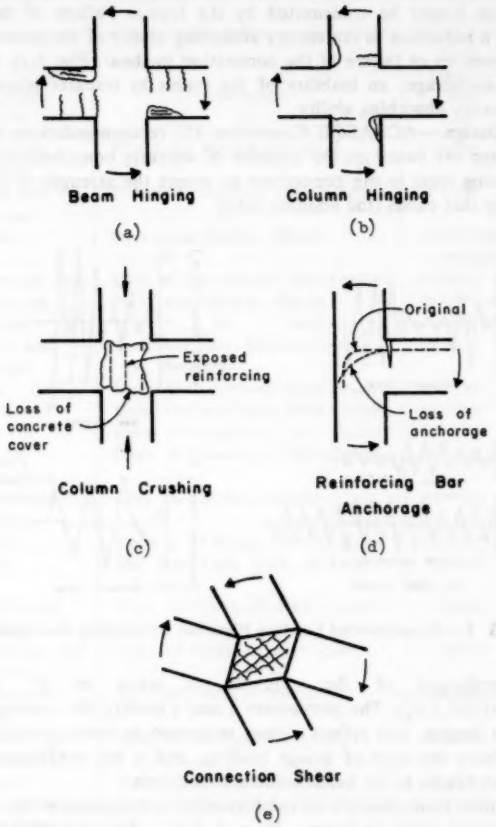

FIG. 2.—Possible Failure Modes for Beam-Column Connection

selected in this study provide information directed toward the needs expressed by ACI-ASCE Committee 352, and include the following (18): (1) The percentage of column reinforcement; (2) the nominal axial stress on the column; (3) the size and spacing of transverse (horizontal) hoop reinforcement in the connection core; (4) the effect of intersecting unloaded transverse beams; and (5) the aspect ratio (geometry) of the beam-column connection region.

Test Specimens.—Overall specimen dimensions are given in Fig. 3. The column was rectangular so that it could be loaded in bending about either of its principal bending axes (strong or weak). Details of the reinforcement and the sustained column axial load magnitude are summarized in Table 2.

State-of-the-art design recommendations (2,18) were used to proportion the member cross-sectional size and reinforcement. However, the majority of the specimens were specifically underdesigned in shear in the connection. Fabrication

TABLE 2.—Specimen Details

Specimen number (1)	Column			Main beam (5)	Transverse Beam		Connection Hoops		f_c', in pounds per square inch (10)	$\Sigma M_c / \Sigma M_g$ (11)
	Reinforcement[a] (2)	ρ_g (3)	Average axial load, in kips (4)		w_L/h_c (6)	Eccentricity of transverse beam, in inches (7)	Reinforcement (8)	Volumetric percentage with ρ = volume steel/volume core (9)		
I	8 #7	2.0	375	three #10 on top; three #8 on bottom; 2 in. clear cover on both top and bottom reinforcement	—	—	2 #4 @ 6 in.	0.011	3,800	1.00
II	8 #10	4.3	360		—	—	2 #4 @ 6 in.	0.011	6,060	1.72
III	10 #11	6.7	356		—	—	2 #4 @ 6 in.	0.011	3,860	1.64
IV	10 #9	4.3	363		—	—	2 #4 @ 6 in.	0.011	5,230	1.18
V	8 #10	4.3	48		—	—	2 #4 @ 6 in.	0.011	5,200	1.48
VI	8 #10	4.3	603		—	—	2 #4 @ 6 in.	0.011	5,330	1.55
VII	10 #9	4.3	597		—	—	2 #4 @ 6 in.	0.011	5,400	1.12
VIII	8 #10	4.3	355		0.83	0	2 #4 @ 6 in.	0.011	4,800	1.59
IX	8 #10	4.3	367		0.44	0	2 #4 @ 6 in.	0.011	4,500	1.54
X	8 #10	4.3	359		0.44	4	2 #4 @ 6 in.	0.011	4,290	1.50
XI	10 #9	4.3	365		0.46	0	2 #4 @ 6 in.	0.011	3,720	1.02
XII	8 #10	4.3	363		—	—	6 #5 @ 2 in.	0.052	5,100	1.63
XIII	8 #10	4.3	353		—	—	6 #4 @ 2 in.	0.033	5,990	1.71
XIV	10 #9	4.3	363		—	—	6 #4 @ 2 in.	0.033	4,810	1.14

[a]Summary of reinforcing bar yield strengths, in kips per square inch: bar size #4 = 59.3; #5 = 61.3; #7 = 66.3; #8 = 58.8; #9 = 63.5; #10 = 65.1; #11 = 58.3.

Note: 1 in. = 25.4 mm; 1 kip = 4.45 kN; 1 psi = 0.0069 MPa.

of test specimens was typical of that found in construction practice. Details can be found in Ref. (13).

Fig. 4 shows a specimen positioned in the loading frame ready for test. Arrows on Fig. 4 indicate the hardware for application of the column axial load, for the beam loads producing an unbalanced bending moment at the connection, and for the equilibrating shear forces necessary in the column. Beam loads were reversed by moving the beam loading mechanism to the opposite side of the beam. The applied loads, deflections, average curvatures in the beams and column near the connection, connection shear deformations, and reinforcing bar strains were measured.

Materials.—A concrete mix using Type I Portland Cement, Colorado River

Direction of Column Bending	Column		Main Beam		Transverse Beam		
	Width (b_c)	Depth (h_c)	Width (w_b)	Depth (h_b)	Width (w_L)	Depth (h_L)	w_L/h_c
Strong Axis (S)	13	18	11	18	0	0	0
					8	15	.44
					15	15	.83
Weak Axis (W)	18	13	16	18	0	0	0
					6	15	.46

All dimensions in inches 1 in. = 25.4 mm

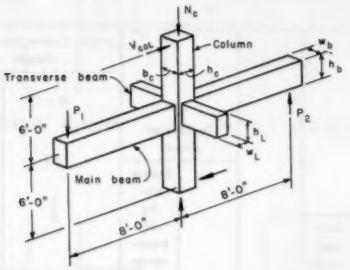

Note: 1 ft. = 0.305m; 1 in. = 25.4mm

FIG. 3.—Specimen Configuration

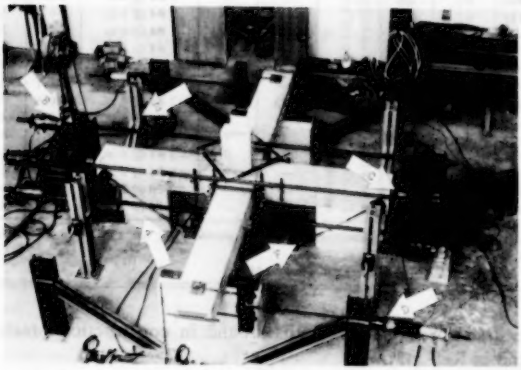

A. Supporting pedestals
B. Column load
C. Spherical pivot
D. Main beam frame
E. Column shear frame
F. Tension tie for unbalanced beam load

FIG. 4.—View of Test Specimen and Loading Equipment

Sand, and a graded 5/3 in. (16 mm) maximum size coarse aggregate was used for all test specimens. The concrete had a unit weight of about 145 lb/yd^3 (2,323 kg/m^3) and a slump of about 6 in. (152 mm) to ease placement. Compressive strengths for each test specimen are listed in Table 2. Reinforcing steel properties used in this investigation conformed to ASTM Designation A615 Grade 60 (21). Measured yield stresses are given in Table 2.

Test Procedure and Experimental Observations

Loading Sequence.—Several loading histories have been presented in Fig. 1.

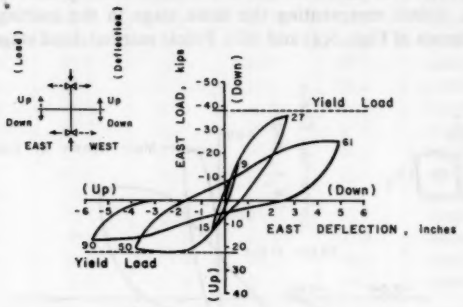

(a) East main beam load-deflection

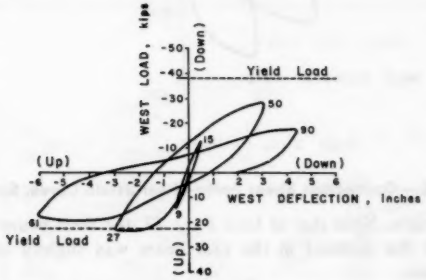

(b) West main beam load-deflection

Note: 1 in. = 25.4 mm; 1 kip = 4.45 kN

FIG. 5.—Typical Load-Deflection Curves, Specimen II

The diagram, as shown in Fig. 1(*d*), represents the loading used for the experimental tests reported herein. The first cycle was in the elastic range and the peak load was sufficient to cause inclined shear cracking of the beam-column connection. The first load cycle was applied to define the cracking shear strength

of the concrete in each direction. Subsequent cycles were applied to define the shear strength of the connection. Applied loads at the tips of the main beams were increased until either the connection was unable to accommodate an increasing unbalanced moment, or the beams formed hinges at the beam-column connection. The last loading consisted of two large inelastic deformation cycles.

Typical Specimen Behavior.—Top beam reinforcement was 60% greater in area than the bottom reinforcement. Because of the unsymmetrically reinforced sections, two separate load-deflection curves are necessary to describe the bending moments at the connection. The load-deflection response for Specimen II, under the imposed loading history of Fig. 1(*d*), is shown in Fig. 5. Similar plots are available in Ref. (13) for all specimens. Because the loading History was controlled by deflection, points representing the same stage in the loading history lie in opposite quadrants of Figs. 5(*a*) and 5(*b*). Points marked (load stage) 27 represent

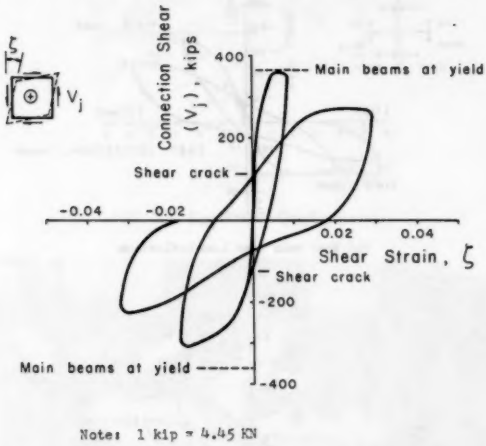

FIG. 6.—Connection Shear Force-Shear Strain Curve, Specimen II

one such example. Note that at load stage 27, the west beam reached the yield moment while the moment in the east beam was slightly less than the yield bending moment.

Behavior of the beam-column connection can be described by a plot of the connection shear versus the connection shear strain. Test results for Specimen II are plotted in Fig. 6. The horizontal dashed lines represent the shear level in the connection if both flexural members reach yield. At load stage 27, the maximum applied shear force is almost equal to that corresponding to yield. However, at other points in the loading history, the applied shear force is less than that which causes the main flexural members to yield. No column hinging or beam shear distress was observed, indicating a likely connection shear failure. A summary of the maximum applied connection shears and mode of failure for each specimen is found in Table 3.

The applied shear force at shear cracking is also shown for Specimen II

in Fig. 6. It is considerably less than the measured shear capacity. Adding the contribution of closed hoop reinforcement, calculated in accordance with

TABLE 3.—Measured Peak Connection Shear Stresses

Specimen number (1)	$v_{cr}/\sqrt{f_c'}$ (2)	$v_{j1}^{+}/\sqrt{f_c'}$ (3)	$v_{j1}^{-}/\sqrt{f_c'}$ (4)	$v_{j2}^{+}/\sqrt{f_c'}$ (5)	$v_{j2}^{-}/\sqrt{f_c'}$ (6)	Failure mode observed for column (3) (7)
I	7.3	19.8	18.8	18.9	15.4	connection shear
II	7.4	22.9	19.4	17.2	14.3	connection shear
III	8.3	22.0	19.5	20.3	17.1	connection shear
IV	9.4	23.9	21.5	22.7	18.7	connection shear
V	3.6	23.7	21.8	18.3	16.6	connection shear
VI	10.8	25.2	22.3	19.2	15.3	beam yielding
VII	13.0	23.8	21.8	19.6	17.3	connection shear
VIII	14.2	27.3	27.3	27.8	26.2	beam yielding
IX	8.2	26.6	25.9	24.9	20.7	connection shear
X	9.5	25.2	22.6	21.9	18.5	connection shear
XI	9.3	25.1	23.9	22.9	21.7	connection shear
XII	8.6	30.5	27.3	22.9	21.8	beam yielding
XIII	9.0	22.4	21.3	16.7	16.3	connection shear
XIV	9.7	26.4	24.8	21.7	18.2	connection shear

Note: v_{j1} = first inelastic deformation cycle; + = connection experiences positive shear deformation; v_{j2} = second inelastic deformation cycle; − = connection experiences negative shear deformation; v_{cr} = cracking shear.

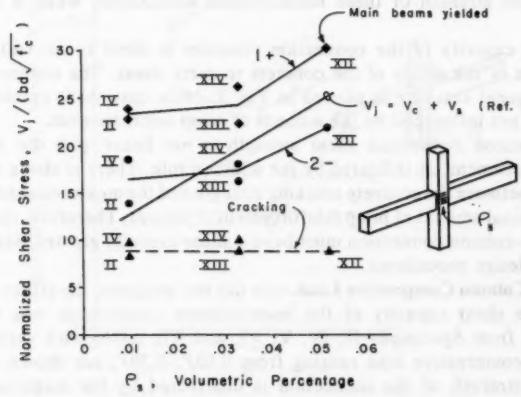

FIG. 7.—Transverse Hoop Reinforcement

the ACI-ASCE Committee 352 Recommendation (18), to the observed cracking shear, accounts for only 59% of the measured shear capacity. The behavior

of Specimen II is typical of those specimens in which the shear strength of the connection controlled the load carrying capacity.

Discussion of Results

Effect of Transverse Connection Hoop Reinforcement.—Horizontal closed hoop reinforcement is the most common approach for improving the strength of the beam-column connection. The results of five specimens in this test program provide data for evaluating the effect of connection hoop reinforcement. The amount of steel hoop reinforcement used in the connection core is described by the volumetric steel percentage. The definition of volumetric steel percentage is similar to the definition of the volume of transverse reinforcement in a spirally reinforced concrete column.

Plotted in Fig. 7 are the shear strength characteristics for the first and last load excursions reported in Table 3. The curve labeled 1^+ represents the monotonic strength shown as Load Stage 27 in Fig. 6, and 2^- represents the remaining capacity after two large deformation inelastic load cycles, shown in Fig. 6 as Load Stage 90.

Some improvement in the connection shear performance can be seen in Fig. 7 as the volumetric hoop reinforcement percentage increases. The connection shear strength was, in fact, larger than that corresponding to yielding of the main flexural reinforcement when the volumetric reinforcement percentage of the connection was 0.052.

Shown also in Fig. 7 is the relationship between shear strength and transverse reinforcement using ACI-ASCE 352 recommendations. The addition of concrete and steel shear contributions results in a much faster rate of strength increase with ρ_s than was observed from the tests. The addition rule conservatively predicted the strength of these beam-column connections when $\beta = 1.4$ and $\gamma = 1.0$.

Cracking capacity of the connection concrete in shear is currently used as the measure of the ability of the concrete to carry shear. The connection shear at first diagonal cracking is plotted in Fig. 7. Note that shear cracking of the concrete is not influenced by the amount of hoop reinforcement.

The measured connection shear strength is not linear with the amount of hoop reinforcement, as indicated by the addition rule. There is also a significant difference between the concrete cracking strength and the measured shear capacity when a nominal amount of hoop reinforcement is present. Therefore, the concrete in the beam-column connection must have a shear capacity greater than assumed in current design procedures.

Effect of Column Compressive Load.—In this test program, the effect of column load on the shear capacity of the beam-column connections was examined. The results from Specimens II, IV, V, VI, and VII tested with varying levels of column compressive load ranging from $0.03P_o$–$0.39P_o$ are shown in Fig. 8. The shear strength of the connection is unaffected by the magnitude of the column compressive load. However, shear cracking of the concrete is significantly affected by the column compressive load. The differences between curves in Fig. 8 marked 1^+ and 2^- indicate the deterioration of connection shear strength in two cycles of load. It is clear that the cracking shear does not represent the shear capacity of the concrete in the beam-column connection.

Effect of Column Vertical Reinforcement.—Shear forces in a beam-column connection are present on orthogonal planes in the connection. If reinforcing steel is assumed in accordance with ACI-ASCE Committee 352, closed hoops

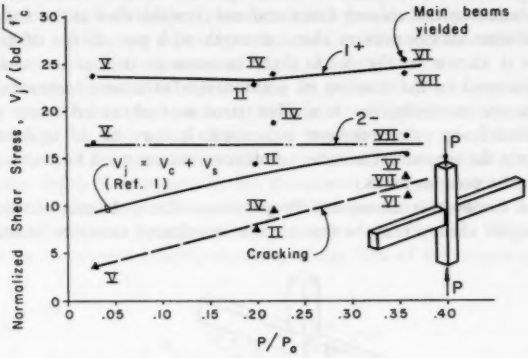

FIG. 8.—Column Load

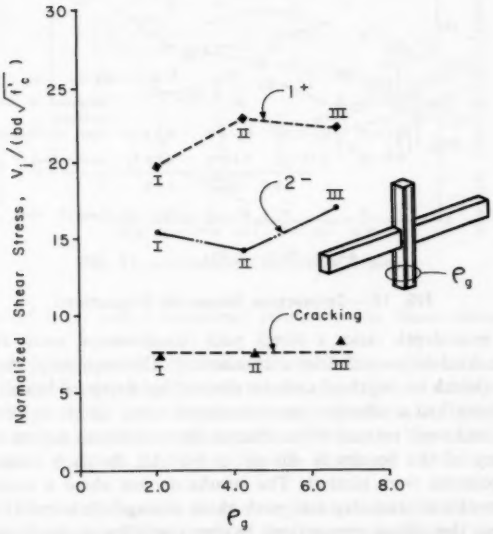

FIG. 9.—Column Percentage Reinforcement

should be provided in the vertical and horizontal planes of the connection. In most connections, the column reinforcement may serve this purpose. Additional

vertical hoop steel only adds to the congestion of reinforcement in the connection.

Three test specimens had significantly different percentages of column longitudinal steel. Specimen I had $\rho_g = 0.020$, Specimen II had $\rho_g = 0.043$, and Specimen III had $\rho_g = 0.067$. For each of these specimens, the column reinforcement was distributed on the column faces and not concentrated at the corners.

The variation of connection shear strength with percentage of column reinforcement is shown in Fig. 9. A slight increase in connection shear strength can be observed as the amount of column reinforcement increases; however, the results are inconclusive. A similar trend was observed when the amount of horizontal hoop reinforcement increased. It may be of interest in future tests to keep the amount of column reinforcement constant but vary the number of bars on the column faces.

Effect of Connection Geometric Proportions.—Deep beams characteristically develop higher shear strengths than slender reinforced concrete beams. Because

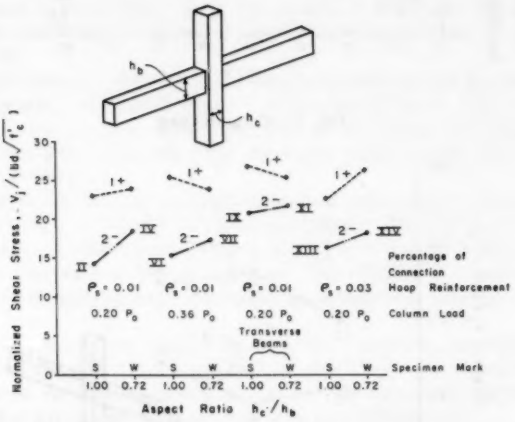

FIG. 10.—Connection Geometric Proportions

of the low span-depth ratio, a direct path (compression strut) for a portion of the shear load is provided in a connection. Consequently, the connection aspect ratio (width or depth of column divided by depth of beam) was varied. All the columns had a constant cross-sectional area, 13 in. × 18 in. (330 mm × 457 mm), and were rotated 90° to change the connection aspect ratio.

A summary of the results is shown in Fig. 10. In each case, results for pairs of specimens were plotted. The results do not show a consistent trend between connection geometry and peak shear strength (labeled 1^+). However, it does appear that those connections having a smaller aspect ratio performed better under large deformation load cycling (labeled 2^-).

During the testing of these specimens, major differences were observed in the inclination of the diagonal shear crack when the connection aspect ratio was changed. The shear cracks tended to propagate along lines parallel to the opposite corners of the beam-column connection. This means that, for tests

with aspect ratios smaller than 1.0, the cracks were inclined at an angle greater than 45°.

Effect of Unloaded Transverse Beams.—Early experimental results (6,8) showed that the behavior of the beam-column connection improved with the addition of unloaded beams on both sides of the connection perpendicular to the direction of applied shear. With one transverse beam, the shear characteristics were essentially the same as if no transverse beam existed.

In this study, the parameter representing an unloaded transverse beam was taken as the area of the connection covered (masked) by the transverse beam. The insert in Fig. 11 shows the dimensions used to define the masking ratio of the connection. All transverse beams had the same overall depth, 83% of the main beam depth. Consequently, the dimension changed in testing was the width of the transverse beam and its location with respect to the column centerline.

The results of six test specimens are compared in Fig. 11. These results show that wide transverse beams, covering about 70% of the connection area,

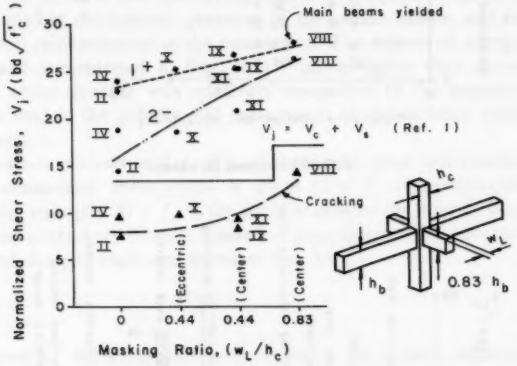

FIG. 11.—Unloaded Transverse Beams

masking ratio of 0.83, had a beneficial effect on the shear strength of the connection.

In The case of Specimen VIII, the wide transverse beam allowed the connection to develop a shear strength which permitted the main flexural members to reach yield. Smaller transverse beam sizes were not as effective, but did provide some improvement in the shear capacity of the connection. The cracking strength of the connection concrete, shown in Fig. 11, increased as the masking ratio increased.

The improvement in connection shear strength can be attributed to an increase in connection shear area. However, if the transverse beams were cracked flexurally, the shear behavior of the connection may still be improved, but perhaps not as significantly as measured in these tests.

Effect of Load Reversal.—Load reversals were applied to define the characteristics of behavior as the connection shear was reversed or repeated, or both. Figs. 5–11 have shown the effects of reversal and repeated loads. The peak

shear data for each cycle is summarized in Fig. 12. The majority of the test specimens were observed to fail in shear during the first half cycle of loading. The effect of reversing and repeating load is clearly indicated in Fig. 12 by the decaying (degrading) connection strength. Two specimens were observed

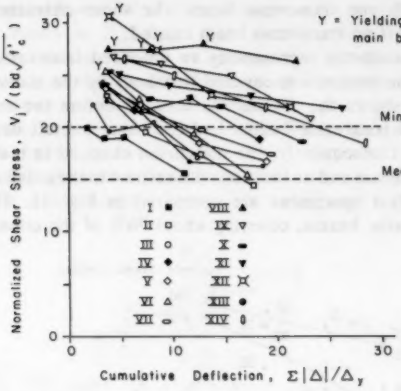

FIG. 12.—Load Reversal

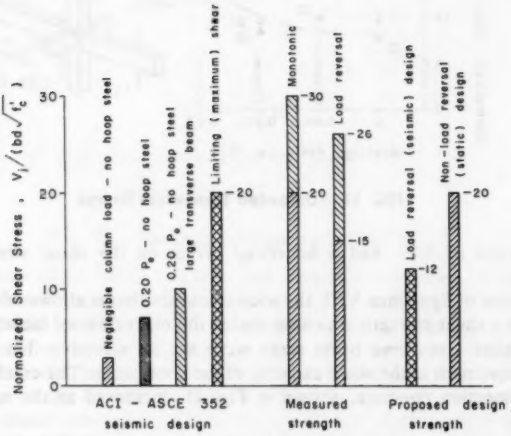
Normalized Shear Stress, $V_j/(bd\sqrt{f'_c})$
Negligible column load - no hoop steel
0.20 P_e - no hoop steel
0.20 P_e - no hoop steel large transverse beam
Limiting (maximum) shear
Monotonic
Load reversal
Load reversal (seismic) design
Non-load reversal (static) design
ACI - ASCE 352 seismic design
Measured strength
Proposed design strength

FIG. 13.—Comparison of Results and Design Approaches

to perform better than others in the load reversal tests: (1) Specimen XII, designed to resist cyclic loads by adding closed hoop reinforcement; and (2) Specimen VIII, the specimen with the large unloaded transverse beams.

There is a broad band of shear strength values plotted in Fig. 12. In all

cases, the specimens reached monotonic shear values of at least $20\sqrt{f_c'}$ during the static strength test. Under reverse cycling, the capacity remained above $15\sqrt{f_c'}$ through an imposed total deflection of nearly 20 times the yield deflection of the main flexural member.

An important result of the data summarized in Fig. 12 is that the initial (peak) connection shear strength can be improved; however, the shear strength always decayed. Since the slopes of the curves in Fig. 12 are nearly parallel, it appears that decay is a function of the concrete in the connection. Therefore, if the connection is to resist seismic forces, a larger connection shear area is necessary to keep the shear stresses low.

Test Result Comparisons and Design Suggestions

These test results can be compared with the present state-of-the-art design approach (18). The ACI-ASCE 352 design recommendations shown on the left side of Fig. 13 indicate that the strength of the connection varies depending on the axial load in the column, presence of transverse beams, and the amount of closed hoop reinforcement in the connection. The measured strengths shown in Fig. 12 and summarized in Fig. 13 are much higher than current design values. The shear strength was relatively insensitive to the magnitude of the compressive load in the column and the amount of closed hoop reinforcement in the connection.

A comparative analysis in Ref. (13) of these and other test results indicates that if the connection shear stress is about $12\sqrt{f_c'}$ (approximately 60% of the monotonic strength, $20\sqrt{f_c'}$), the performance of the interior beam-column connection is satisfactory when subjected to large deformation reversal loadings. The proposed design values are shown in Fig. 13.

Conclusions

The purpose of the program was to evaluate the factors influencing shear capacity of the beam-column connection. Several parameters were varied over relatively wide ranges in the investigation. The strength of the connection was governed primarily by the cross-sectional area of the joint. From the 14 specimens tested, the variation of the other test parameters can be summarized as follows:

1. Transverse reinforcement in the connection improved the shear capacity but not in the same ratio as indicated by the addition rule, $V_c + V_s$, for shear.
2. Column longitudinal percentage of reinforcement, ρ_g, increases did not produce similar increases in shear strength seen when transverse reinforcement increased.
3. Unloaded transverse beams improved the shear capacity. The largest increase, about 20%, was observed when the transverse beams masked most of the side face of the column.
4. Column axial load had no influence on ultimate shear capacity of the connection, but with higher axial compressive load, the shear at first cracking in the connection was increased.
5. Connection geometry had no influence on shear strength of the joint, as long as the shear area, bd, of the connection remained constant.

The test results provide an indication of the shear strength of the connection and the nature of shear degradation under repeated reversed loads. Under monotonic loading, the connections carried shear stresses of $20\sqrt{f_c'}$ with several carrying stresses in excess of $25\sqrt{f_c'}$ and as high as $30\sqrt{f_c'}$. There was considerable variation of the shear capacity under load reversal. Although the shear strength decayed as the number of cycles increased, the connections could sustain shear stresses of at least $12\sqrt{f_c'}$ without large percentages of transverse reinforcement. It appears that if the connection were designed so that shear stress did not exceed $12\sqrt{f_c'}$, the connection would perform satisfactorily under reversed loading. Unloading transverse beams could increase the design shear stress to about $15\sqrt{f_c'}$.

Acknowledgments

Support for this research by the National Science Foundation under Grant Number GK-40289 is gratefully acknowledged. The authors would also like to recognize the contributions of Marisol Abad de Aleman, John W. Woollen, and the technical staff of the Phil M. Ferguson Structural Research Laboratory at The University of Texas at Austin, Department of Civil Engineering, Austin, Tex.

Appendix I.—References

1. Bertero, V. V., Popov, E. P., and Forzani, B., "Seismic Behavior of Lightweight Concrete Beam-Column Subassemblages," *American Concrete Institute Journal*, Proceedings, Vol. 77, No. 1, Jan.–Feb., 1980, pp. 44–52.
2. *Building Code Requirements for Reinforced Concrete (ACI 318-71)*, American Concrete Institute, Committee 318, American Concrete Institute, Detroit, Mich., 1971, pp. 78.
3. Birss, G. R., Paulay, T., and Park, R., "The Elastic Behavior of Earthquake Resistant R. C. Interior Beam-Column Joints," *Report 78-13*, Univ. of Canterbury, Dept. of Civ. Engrg., Christchurch, New Zealand, Feb., 1978.
4. Fenwick, R. C., and Irvine, H. M., "Reinforced Concrete Beam-Column Joints for Seismic Loading," *Report No. 142*, Univ. of Auckland, Auckland, New Zealand, Mar., 1977.
5. Gulkan, P., "The Inelastic Response of Repaired Reinforced Concrete Beam-Column Connections," *Report on Project M46-372*, Middle East Technical Univ., Ankara, Turkey, 1976.
6. Hanson, N. W., "Seismic Resistance of Concrete Frames with Grade 60 Reinforcement," *Journal of the Structural Division*, ASCE, Vol. 97, No. ST6, June, 1971, pp. 1685–1700.
7. Hanson, N. W., and Conner, H. W., "Seismic Resistance of Reinforced Concrete Beam-Column Joints," *Journal of the Structural Division*, ASCE, Vol. 93, No. ST5, Oct., 1967, pp. 533–560.
8. Hanson, N. W., and Conner, H. W., "Tests of Reinforced Concrete Beam Column Joints under Simulated Seismic Loading," *RD012.01D*, Portland Cement Association, Skokie, Illinois, 1972.
9. Higashi, Y., and Ohwada, Y., "Failing Behaviors of Reinforced Concrete Beam-Column Connections Subjected to Lateral Loads," *Memoirs of Faculty of Technology, No. 19*, Tokyo Metropolitan Univ., Tokyo, Japan, 1969.
10. Keong, Y. S., and Park, R., "Prestressed Concrete Beam-Column Joints," *Report 78-2*, Univ. of Canterbury, Dept. of Civ. Engrg., Christchurch, New Zealand, Feb., 1978.
11. Kordina, K., and Schaaff, E., *Tragverbalten von Rahmenknoten bei herabgesetzter Verankerungslange der Anschlusbewehrung unter Berucksichtigung der Bewehrungs-*

fuhrung, Technical Univ. of Braunschweig, Braunschweig, W. Germany, No. 3263, 1972.
12. Lee, D. L. N., Wight, J. K., and Hanson, R. D., "RC Beam-Column Joints under Large Load Reversals," *Journal of the Structural Division,* ASCE, Vol. 103, No. ST12, Dec., 1977, pp. 2337–2350.
13. Meinheit, D. F., and Jirsa, J. O., "The Shear Strength of Reinforced Concrete Beam-Column Joints," *Report No. 77-1,* Dept. of Civ. Engrg., Structures Res. Lab., Univ. of Texas at Austin, Jan., 1977.
14. Megget, L. M., and Park, R., "Reinforced Concrete Exterior Beam-Column Joints under Seismic Loading," *New Zealand Engineering,* 15 Nov., 1971, pp. 341–353.
15. Park, R., and Thompson, K. J., "Behavior of Prestressed, Partially Prestressed, and Reinforced Concrete Interior Beam-Column Assemblies under Cyclic Loading: Test Results of Units 1 to 7," *Research Report 74-9,* Dept. of Civ. Engrg., Univ. of Canterbury, Christchurch, New Zealand, 1974, pp. 42.
16. Patton, R. N., "Behavior under Seismic Loading of Reinforced Concrete Beam-Column Joints with Anchor Blocks," *Master of Engrg.* Report, Univ. of Canterbury, Christchurch, New Zealand, 1972, 103 pp.
17. Priestley, M. J. N., "Testing of Two Reinforced Concrete Beam-Column Assemblies under Simulated Seismic Loading," *Report 5-75/1,* New Zealand Ministry of Works and Development, 1975.
18. "Recommendations for Design of Beam-Column Joints in Monolithic Reinforced Concrete Structures," ACI-ASCE Joint Committee 352, *Journal of the American Concrete Institute, Proceedings,* Vol. 73, No. 7, July, 1976, pp. 375–393.
19. Renton, G. W., "The Behavior of Reinforced Concrete Beam-Column Joints under Cyclic Loading," thesis submitted to the Univ. of Canterbury, at Christchurch, New Zealand, in 1972, in partial fulfillment of the requirements for the degree of Master of Engineering in Civil Engineering.
20. Smith, B. J., "Exterior Reinforced Concrete Joints with Low Axial Load under Seismic Loading," report submitted to the Univ. of Canterbury, at Christchurch, New Zealand, in 1972, in partial fulfillment of the requirements for the degree of Master of Engineering, 103 pp.
21. "Standard Specifications for Deformed and Plain Billet-Steel Bars for Concrete Reinforcement," ASTM Designation: A615-72 *ASTM Standards,* Part 4, Philadelphia, Pa., 1974.
22. Townsend, W. H., and Hanson, R. D., "Reinforced Concrete Connection Hysteresis Loops," *Symposium on Reinforced Concrete Structures in Seismic Zones, ACI SP-53,* American Concrete Institute, Detroit, Mich., 1977, pp. 351–370.
23. Uzumeri, S. M., "Strength and Ductility of Cast-In-Place Beam-Column Joints," *Symposium on Reinforced Concrete Structures in Seismic Zones, ACI SP-53,* American Concrete Institute, Detroit, Mich., 1977, pp. 293–350.
24. Uzumeri, S. M., and Seckin, M., "Behavior of Reinforced Concrete Beam-Column Joints Subjected to Slow Load Reversals," *Report 74-05,* Dept. of Civ. Engrg., University of Toronto, Toronto, Ont., Canada, Mar., 1974.

APPENDIX II.—NOTATION

The following symbols are used in this paper:

A_g = gross area of column cross section;
A_v = area of shear reinforcement;
b, b_c = width of compressive face of column;
d = distance from extreme compressive fiber to centroid of tensile force;
f_c' = concrete compressive strength;
f_v = yield strength of shear reinforcement;
h_b = depth of main beam;

h_c = depth of column;
h_L = depth of transverse beam;
M_B = yield bending moment of main beam;
M_c = yield bending moment of column;
N_c, N_u, P = column compressive load;
P_o = concentric column strength;
P_1, P_2 = concentrated loads applied to main beams;
s = spacing of closed hoop reinforcement in connection;
V_c = shear force carried by concrete;
V_{col} = shear force in column;
V_j = shear force in connection;
V_s = shear force carried by steel reinforcement;
v_{cr} = shear stress at diagonal cracking of concrete;
v_j, v_{j1}, v_{j2} = nominal connection shear stress;
w_b = width of main beam;
w_L = width of transverse beam;
β = factor reflecting amount of energy absorbing capacity or type of loading imposed on beam-column connection;
γ = factor reflecting existence of transverse members perpendicular to plane of connection shear;
Δ = frame sway deflection or beam deflection;
Δ_y = deflection at yield;
ζ = shear strain;
ρ_g = column percentage of reinforcement;
ρ_s = ratio of volume of connection hoop reinforcement to enclosed volume of concrete core;
ϕ = curvature; and
ϕ_y = curvature at yield.

FUNDAMENTAL ANALYSIS OF AGGREGATE INTERLOCK[a]

By Joost C. Walraven[1]

INTRODUCTION

The capacity of cracks in concrete to transmit shear forces is of vital importance in many structures. Cracks, which occurred as a consequence of bending moments, can be subjected to shear forces as a result of other loading configurations. Such a situation occurs, for instance, in long bridges, supported by hinged columns in the longitudinal axis, where the torsional moments have to be resisted by the abutments. In order to guarantee the full bearing capacity of the structure, open cracks have to transmit shear stresses. In fully prestressed concrete this applies to the ultimate loading state, but in partially prestressed concrete this mechanism will already occur under serviceability conditions.

Shear forces in cracks can also occur due to other reasons. The anisotropical properties of cracked reinforced concrete itself can directly give rise to shear forces in cracks; this is the case, for instance, in beams without shear reinforcement, the shear resistance of which relies, by virtue of redistribution of forces, for a considerable part on the resistance of the crack faces to shear displacements (8,22,23).

In the design of relatively simple structural elements subjected to shear, the shear capacity of the cracks can be used as an active component by applying the shear friction analogy (3,7,15,16,17). The shear friction concept, however, applies only to the ultimate loading state and does not relate the stresses on and the displacements of the crack faces. The interest in the constitutive relations of cracks in concrete was considerably enhanced during the development of modern numerical calculation programs, which enable the analysis of the behavior of structures during the whole loading history, provided that adequate formulations of the basic material properties are available. Because of the lack of a satisfactory model for the behavior of cracks in concrete subjected to shear forces, widely varying formulations are encountered. Most authors characterize the shear resistance of cracks in their finite element analyses by simply reducing the

[a]Presented at the April 18, 1980, ASCE Convention and Exposition and Education Program, held at Portland, Oreg. (Preprint No. 80-011).

[1]Sr. Research Engr., Univ. of Technology, Delft, The Netherlands.

Note.—Discussion open until April 1, 1982. To extend the closing date one month, a written request must be filed with the Manager of Technical and Professional Publications, ASCE. Manuscript was submitted for review for possible publication on December 30, 1980. This paper is part of the Journal of the Structural Division, Proceedings of the American Society of Civil Engineers, ©ASCE, Vol. 107, No. ST11, November, 1981. ISSN 0044-8001/81/0011-2245/$01.00.

shear modulus G, after cracking, by a factor α_s ($0 < \alpha_s < 1$). Sometimes a constant value is chosen for α_s (5,11,14), while in other cases α_s is defined to be a function of one or more parameters, such as, for instance, the strain normal to the direction of the cracks, the level of the shear stress, the concrete quality, and the distribution of crack widths and distances (6,9,20,21).

However, hardly any attention has been paid to the fundamental property that shear displacement of crack faces at constant crack width inevitably provokes stresses normal to the crack due to wedging action of the irregular crack faces. Only recently Bazant and Tsubaki (2) pointed out that if this effect is disregarded, an unsafe design of structures may result.

Therefore, it should be emphasized that the mechanism may not be represented by the traditional relation, $\tau = B_{tt}\,\Delta$, in which τ = the shear stress; Δ = the shear displacement; and B_{tt} = a constant, but that both the shear stress and the normal stress always have to be taken into account as essential components. Assuming that the irregular faces of a crack can be deformed, both the shear stress, τ, and the normal stress, σ, are functions of the crack width, w, and the shear displacement, Δ:

$$\tau = f_t(w,\Delta) \quad \text{and} \quad \sigma = f_n(w,\Delta) \qquad (1)$$

The constitutive equations for a single crack can, for instance, be formulated in an incremental way as proposed by Bazant and Gambarova (1):

$$\begin{Bmatrix} d\tau \\ d\sigma \end{Bmatrix} = \begin{bmatrix} B_{nn} & B_{nt} \\ B_{tn} & B_{tt} \end{bmatrix} \begin{Bmatrix} dw \\ d\Delta \end{Bmatrix} \qquad (2a)$$

in which B_{nn}; B_{nt}; ... = the crack stiffness coefficients. Differentiating Eq. 1 and comparing the result with Eq. 2, it is concluded that

$$B_{nn} = \frac{\partial f_n}{\partial w}; \quad B_{nt} = \frac{\partial f_n}{\partial \Delta}; \quad B_{tn} = \frac{\partial f_t}{\partial w}; \quad B_{tt} = \frac{\partial f_t}{\partial \Delta} \qquad (2b)$$

The basic problem is the formulation of Eq. 1. In this paper a fundamental model is developed, based on a statistical analysis of the crack structure and the associated contact areas between the crack faces as a function of the displacements, w and Δ, and the composition of the concrete mix. Dowel action can be shown to be of minor importance in practical circumstances (26) and is therefore neglected; so this study concentrates on the mechanism which is generally denoted by the term *aggregate interlock*.

Fundamentals

Concrete can be represented as a two-phase system: In a matrix (hardened cement paste) a collection of aggregate particles are embedded. Generally the strength and stiffness of the aggregate particles are greater than those of the matrix. However, the contact area between both materials, the bond zone, is the weakest link of the system. Therefore, cracking occurs commonly through the matrix, but along the periphery of the aggregate particles. These particles are simplified as spheres, which can be intersected by the crack plane at all depths with the same probability. This results in a crack structure, as shown in Fig. 1.

Considering this figure and taking into account that the size of most particles is considerably greater than the crack width, it can be concluded that the *microroughness* of the crack, caused by the aggregate particles projecting from the crack plane, dominates the *macroroughness*, due to overall undulations of the crack faces. Therefore, the overall crack plane is assumed to be a flat plane.

Hardened cement paste is a viscoelastic material; the deformations provoked by stresses are only partially elastic, for the other part plastic (13). Under multiaxial stresses, as in the area between the aggregate particles in concrete, large plastic deformations can occur as a result of pore-volume reduction. Since the plastic deformations are expected to dominate the elastic deformations, the stress-strain relation of the matrix material, consisting of hardened cement

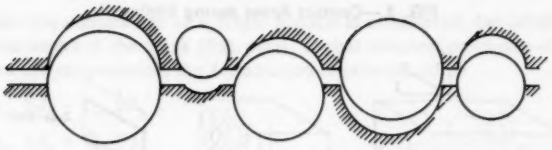

FIG. 1.—Generally Observed Structure of Crack Plane

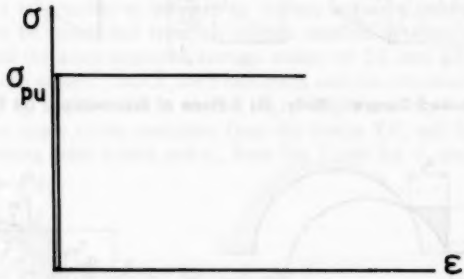

FIG. 2.—Rigid-Plastic Stress-Strain Relation for Matrix Material

paste with aggregate particles smaller than 0.25 mm (an arbitrary limit between the two phases), is assumed to be rigid-plastic, as shown in Fig. 2.

The stress at which plastic deformation occurs is denoted as σ_{pu}. Thus, it can be expected that, during shear displacement of the crack faces, contact areas develop on the surface of the particles, due to plastic deformation of the matrix. Fig. 3 shows the formation of this type of area as a result of a shear displacement in the direction of the x-axis. The stresses at these contact areas produce reactions in the directions of all principal axes. As a result of the assumption of spherical particles, the resulting component in the Z direction is zero, just as for a real crack face, if the crack area is not too small. As a result it is possible to consider a cracked concrete body, as shown in Fig. 4(*a*), as an assemblage of a large number of slices each of finite width [Fig. 4(*c*)], and it is possible to derive the overall behavior of the crack by first

studying the properties of this thin slice.

Fig. 5 shows a cross section through a particle lying in a Z-plane in which there is a line of contact between the opposite crack faces. The projections of this line of contact on the x and y directions are a_x and a_y. The shaded area represents that part of the matrix where plastic deformation has occurred.

FIG. 3.—Contact Areas during Sliding

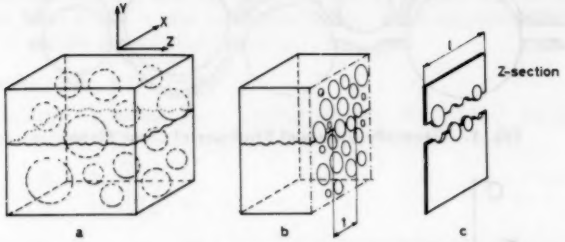

FIG. 4.—(*a*) Cracked Concrete Body; (*b*) Z-Plane of Intersection; (*c*) Representative Slice

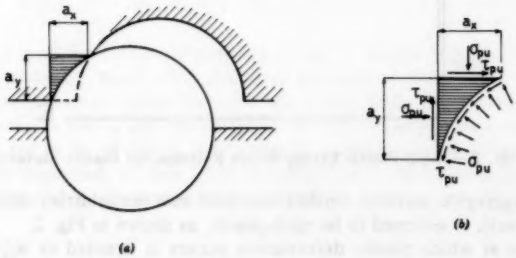

FIG. 5.—(*a*) Contact Area between Matrix and Aggregate; (*b*) Stress Conditions

If the shear load on the plane of cracking is increased and the crack opening is counteracted by restraining forces, a mechanism will develop which can be described as follows. The contact areas tend initially to slide; as a result of this sliding, the contact area is reduced, which results in too high contact stresses. Thus, further plastic deformation occurs, until equilibrium of forces is obtained in the x and y directions.

The stresses at the contact area are resolved into a stress, σ_{pu}, normal to

the contact area and a stress, τ_{pu}, tangential to this area. The stresses, σ_{pu} and τ_{pu}, are interrelated by the condition that the contact areas are about to slide. Therefore the equilibrium conditions are formulated, based on a uniform critical stress combination, (σ_{pu}, τ_{pu}), with

$$\tau_{pu} = \mu \cdot \sigma_{pu} \quad \ldots \quad (3)$$

Next, the components of the contact forces in the x and y directions can be derived, based on the previous assumptions. Fig. 5(*b*) shows the equilibrium conditions at a particle surface. The reactions in the x and y direction can be formulated as

$$F_y = \sigma_{pu} \cdot a_x - \tau_{pu} \cdot a_y \quad \ldots \quad (4a)$$

$$F_x = \sigma_{pu} \cdot a_y + \tau_{pu} \cdot a_x \quad \ldots \quad (4b)$$

If not only the contact line of a single particle is considered, but of all particles over a unit length of the crack [Fig. 4(*b*)], so that intersection circles of different diameters are encountered, the formulation is generalized to

$$\Sigma F_y = \sigma_{pu} \Sigma \bar{a}_x - \tau_{pu} \Sigma \bar{a}_y \quad \ldots \quad (5a)$$

$$\Sigma F_x = \sigma_{pu} \Sigma \bar{a}_y + \tau_{pu} \Sigma \bar{a}_x \quad \ldots \quad (5b)$$

in which $\Sigma \bar{a}_x$, $\Sigma \bar{a}_y$ = the most probable, average projected contact lengths over the unit crack length [Fig. 4(*b*)] considered. If the lengths, $\Sigma \bar{a}_x$ and $\Sigma \bar{a}_y$, are known, it is possible to proceed to surface areas: a unit surface can be considered to be composed from an infinite number of lines of unit length, which have all the same expected average values of $\Sigma \bar{a}_x$ and $\Sigma \bar{a}_y$. So the most probable contact areas $\bar{A}_x$ and $\bar{A}_y$ for a unit crack area are obtained by multiplying $\Sigma \bar{a}_x$ and $\Sigma \bar{a}_y$ by a unit width l, so that $\bar{A}_x = \Sigma \bar{a}_a \cdot l$ and $\bar{A}_y = \Sigma \bar{a}_y \cdot l$. Similar considerations apply to the transition from the forces ΣF_y and ΣF_x to stresses, σ and τ. Inserting these values and τ_{pu} from Eq. 3 into Eq. 5, we can write

$$\sigma = \sigma_{pu}(\bar{A}_x - \mu \bar{A}_y) \quad \ldots \quad (6a)$$

$$\tau = \sigma_{pu}(\bar{A}_y + \mu \bar{A}_x) \quad \ldots \quad (6b)$$

Calculation of Projected Contact Areas $\bar{A}_x$ and $\bar{A}_y$

At first the distribution of the circle diameters in a Z-plane, crossed by the crack, is established. To be able to calculate the distribution of the diameters of the intersected circles in the Z-plane, a Fuller curve is adopted for the distribution of the aggregate particles. This cumulative distribution function is represented by

$$p = \sqrt{\frac{D}{D_{\max}}} \quad \ldots \quad (7)$$

in which p = the fraction, passing a sieve with an opening diameter D; and $D_{\max}$ = the diameter of the greatest aggregate particle. The probability that an arbitrary point in the concrete is located in an aggregate particle is denoted with $p = p_k$. Properly, p_k is the ratio between the total volume of the aggregate and the concrete volume. The probability that a point, if located in a particle,

lies also in a particle with a diameter smaller than an arbitrary choosen value, D_x, can be expressed, using Eq. 7, as

$$p(D < D_x) = p_k \left(\frac{D_x}{D_{max}} \right)^{1/2} \quad \ldots\ldots\ldots\ldots\ldots\ldots\ldots\ldots\ldots\ldots (8)$$

By differentiation of this function the probability density function $p'(D_x)$ is obtained:

$$p'(D_x) = \frac{\partial\, p(D < D_x)}{\partial D_x} = \frac{1}{2} p_k \left(\frac{D_x}{D_{max}} \right)^{-1/2} \cdot \frac{1}{D_{max}} = C \cdot D_x^{-1/2} \quad \ldots\ldots\ldots (9)$$

with $C = \frac{1}{2} \cdot p_k \cdot D_{max}^{-1/2}$

Subsequently an analysis is made of the probability that an arbitrary point in a Z-plane lies in an intersection circule with a certain diameter, D_0. The probability that a point, if located in a particle with a diameter D_x, lies also in an intersection circle with a diameter $> D_0 (D_0 < D_x)$, is equal to the ratio between the volume of the sphere section A (Fig. 6) and the volume of the hemisphere. The volume of the sphere section B is equal to

$$V_B = \frac{1}{6} \pi\, h(3a^2 + h^2) \quad \text{with} \quad h = \frac{1}{2} D_x - \sqrt{\frac{1}{4} D_x^2 - a^2} \quad \ldots\ldots\ldots (10a)$$

while the volume of the hemisphere is

$$V = \frac{1}{12} \pi\, D_x^3 \quad \ldots\ldots\ldots\ldots\ldots\ldots\ldots\ldots\ldots\ldots\ldots\ldots (10b)$$

The probability that a point in this sphere lies in an intersection circle with $D > D_0$ is equal to

$$P_{D_x}(D > D_0) = \frac{(V - V_B)}{V} \quad \ldots\ldots\ldots\ldots\ldots\ldots\ldots\ldots\ldots\ldots\ldots (11)$$

Substitution of Eqs. 10*a* and 10*b* into Eq. 11 and elaboration results in

$$P_{D_x}(D > D_0) = \left(1 + \frac{1}{2} \frac{D_0^2}{D_x^2} \right) \sqrt{1 - \left(\frac{D_0}{D_x} \right)^2} \quad \ldots\ldots\ldots\ldots\ldots\ldots (12)$$

So the probability that an arbitrary point in a Z-plane [Fig. 4(*b*)] lies in an intersection circle with a diameter, $D > D_0$, is obtained by integrating the product of Eqs. 9 and 12 over the interval D_0–D_{max}:

$$p_c(D > D_0) = \int_{D_0}^{D_{max}} p'(D_x) \cdot P_{D_x}(D > D_0)\, dD_x \quad \ldots\ldots\ldots\ldots\ldots\ldots (13)$$

Inversely, the probability that an arbitrary point in the Z-plane is located in an intersection circle with a diameter, $D < D_0$, is obtained from Eq. 13 as

$$p_c(D < D_0) = 1 - p_c(D > D_0) \quad \ldots\ldots\ldots\ldots\ldots\ldots\ldots\ldots\ldots\ldots\ldots (14)$$

Substitution of Eqs. 9 and 12 into Eq. 13, integration of this expression and substitution of the result into Eq. 14 yields (26)

$$p_c(D < D_0) = p_k(1.065\, D_0^{0.5} D_{max}^{-0.5} - 0.053\, D_0^4 D_{max}^{-4} - 0.012\, D_0^6 D_{max}^{-6} - 0.0045\, D_0^8 D_{max}^{-8} - 0.0025\, D_0^{10} D_{max}^{-10}) \quad (15)$$

This function is shown in Fig. 7. The density function for the probability that an arbitrary point in the concrete body, laying in a Z-plane of intersection, is situated in an intersection circle with a diameter $D = D_0$ is obtained by differentiation of 15 to D_0:

$$p'_c(D_0) = p_k(0.532\, D_0^{-0.5} D_{max}^{-0.5} - 0.212\, D_0^3 D_{max}^{-4} - 0.075\, D_0^5 D_{max}^{-6} - 0.036\, D_0^7 D_{max}^{-8} - 0.025\, D_0^9 D_{max}^{-10}) \quad (16)$$

Since the distribution of circles of intersection in the Z-plane is now known, it is possible to establish the frequency of circles which both lie in the Z-plane

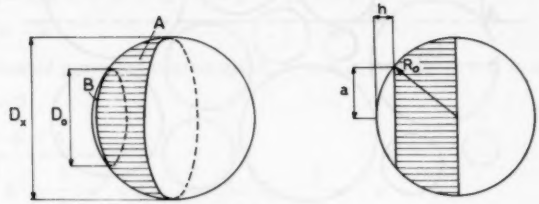

FIG. 6.—Intersection Circle with Diameter, D_0, on Particle with Diameter, D_x

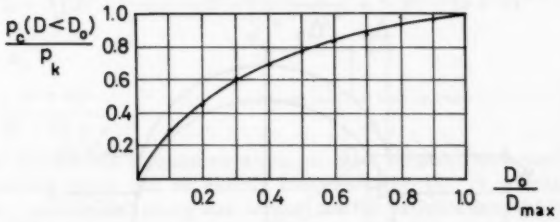

FIG. 7.—Cumulative Distribution Function for Diameter of Intersection Circles

and are crossed by the crack [Figs. 4(*b*) and 8]. The average length $\bar{s}$ of the intersection line, AB, for a circle with a diameter, D_0, crossed by the crack is

$$\bar{s} = \frac{\pi D_0}{4} \quad (17)$$

Considering a crack section [intersection of the crack plane and the Z-plane, Fig. 4(*c*)] with a unit length, the probability density function for the expected part of that length, containing merely points which are located in an intersection circle with a diameter, D_0, can be obtained by multiplying this unit length with $p'(D_0)$ (Eq. 16), so that

$$1(D_0) = p'(D_0) \cdot 1 = p'(D_0) \quad (18)$$

Consequently, the probability density function for the expected number of intersection circles with a diameter, D_0 in the Z-plane, which intersect also the unit crack length, can be obtained from Eqs. 17 and 18 as

$$n(D_0) = \frac{p'(D_0)}{0.25\pi\ D_0} \quad \ldots\ldots\ldots\

line is denoted as u (Fig. 9). This value is assumed to be a random variable in the interval $0 \le u \le R$. For $-R \le u \le 0$ the circle is in the opposite crack face, for which the same considerations are valid. If $w + u > R$, then for no value of the shear displacement, Δ, any contact area is formed. If $w + u < R$, then two characteristic values for Δ can be found. For $\Delta < \Delta_0$ no contact area is found [see also Fig. 10(*a*)]. If $\Delta_0 < \Delta < \Delta_b$, a contact area is obtained, which increases for increasing value of Δ. This phase is denoted as the *growing contact phase* [Fig. 10(*b*)]. If $\Delta > \Delta_b$, no increase of contact area by further shear displacement can be obtained. This phase is denoted as the maximum contact phase [Fig. 10(*c*)]: (1) Phase no contact ($0 < \Delta < \Delta_0$); (2) Phase growing contact ($\Delta_0 < \Delta < \Delta_b$); and (3) Phase maximum contact ($\Delta_b < \Delta$). The values Δ_0, Δ_b are determined with the help of Fig. 9:

$$\Delta_0 = \mathrm{OA} - \mathrm{OB} = \sqrt{R^2 - u^2} - \sqrt{R^2 - (u + w)^2} \quad \ldots\ldots\ldots\ldots \quad (20a)$$

$$\Delta_b = 2Rw - w^2 \quad \ldots\ldots\ldots\ldots \quad (20b)$$

The associated projected contact areas, a_x and a_y, are for $0 < \Delta < \Delta_0$

$$a_x = a_y = 0 \quad \ldots\ldots\ldots\ldots \quad (20c)$$

for $\Delta_0 < \Delta < \Delta_b$

$$a_y = \sqrt{R^2 - \frac{1}{4}(w^2 + \Delta^2)}\,\frac{\Delta}{\sqrt{w^2 + \Delta^2}} - \frac{1}{2}w - u \quad \ldots\ldots\ldots\ldots \quad (20d)$$

$$a_x = \frac{1}{2}\Delta - \sqrt{R^2 - \frac{1}{4}(w^2 + \Delta^2)}\,\frac{w}{\sqrt{w^2 + \Delta^2}} + \sqrt{R^2 - (u + w)^2} \quad (20e)$$

for $\Delta > \Delta_b$

$$a_y = R - (u + w) \quad \ldots\ldots\ldots\ldots \quad (20f)$$

$$a_x = \sqrt{R^2 - (u + w)^2} \quad \ldots\ldots\ldots\ldots \quad (20g)$$

Eqs. 20 contain the embedment depth, u, as a variable. However, in order to get results which can be directly combined with Eq. 19, average values, a_y and a_x, are needed, taking into account the full variation interval of u.

An intersection circle must be taken into account if it offers a contact area in its most favorable position. It is evident that the most favorable position is obtained if the embedment depth u is zero. If a circle even in this extreme position is not in contact with the opposite crack face, it may be excluded from the calculation. The first demand, if contact is requested, is that $R > w$; if $R < w$, there is no contact for any value of Δ, even in the extreme case that $u = 0$.

If contact is possible in advance, so that $R > w$, an analysis has to be made of how the circles contribute to the total contact area, taking into account the different modes of contact shown in Fig. 10. The value R_1, up to which the radius of the intersection circle has to grow (Fig. 11) to provide at least one point of contact, can be calculated from Eq. 20*a*.

For $u = 0$ one can derive that only one point of contact is obtained:

$$R_1 = \frac{w^2 + \Delta^2}{2\Delta} \quad \ldots\ldots\ldots\ldots \quad (21)$$

The value R_2, providing an upper limit for the range in which maximum contact (Fig. 10) is obtained, is found from Eq. 20*b*:

$$R_2 = \frac{w^2 + \Delta^2}{2w} \quad \ldots\ldots\ldots\

The fundamental cases A and B have to be distinguished, establishing the average expected contributions of the intersection circles to the contact area. This is done in the following derivation.

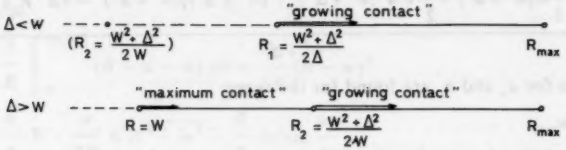

FIG. 12.—Schematical Representation of Fundamental Contact Modes for Varying Values of Radius, R, of Intersection Circles

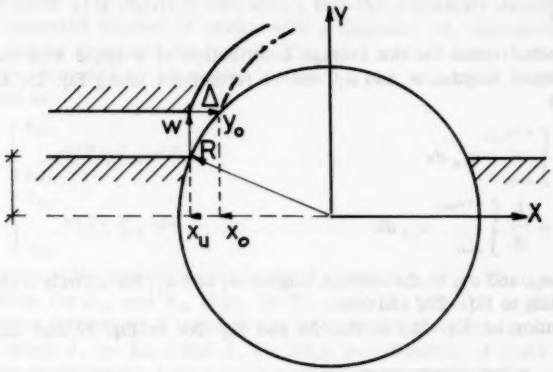

FIG. 13.—Calculation of Maximum Embedment Depth, u_{max}, for Which Still Contact Exists

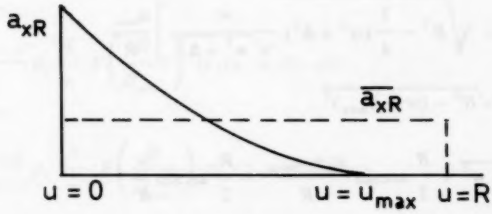

FIG. 14.—Calculation of Average Contribution of Circle with Radius, R, to Contact Length, a_{xR}

Case *A*: $\Delta < w$.—If there is any contact area, this is at least the case for the minimum embedment depth, $u = 0$. Solutions are found up to an upper bound, u_{max}, derived using Fig. 13. For constant values of Δ, w and R, the variable u is increased so far that only a single point of contact remains: in

that stage u_{max} is reached. With the help of Fig. 13 one can derive this value u_{max} to be equal to

$$u_{max} = \frac{-\frac{1}{2}w(w^2+\Delta^2) + \frac{1}{2}\sqrt{w^2(w^2+\Delta^2)^2 - (w^2+\Delta^2)[(w^2+\Delta^2)^2 - 4\Delta^2 R^2]}}{w^2+\Delta^2} \quad (23)$$

So values for a_x and a_y are found for the range

$$0 < u < u_{max} \quad (24)$$

The probability density function for the occurrence of a value, u, is assumed to be equal to

$$p(u) = \frac{1}{R} \quad (25)$$

The expected value for the average contribution of a circle with radius, R, to the contact lengths, a_x and a_y, can be formulated, using Eq. 25, as shown in Fig. 14

$$\bar{a}_{yR} = \frac{1}{R}\int_{u=0}^{u=u_{max}} a_{yR}\, du \quad (26)$$

and $$\bar{a}_{xR} = \frac{1}{R}\int_{u=0}^{u=u_{max}} a_{xR}\, du \quad (27)$$

in which a_{yR} and a_{xR} = the contact lengths, a_y and a_x, for a circle with radius, R, according to Eqs. 20*d* and 20*e*.

Substitution of Eq. 20*d* in Eq. 26 and Eq. 20*e* in Eq. 27 and integration results in

$$\bar{a}_{yR} = \frac{1}{R}\sqrt{R^2 - \frac{1}{4}(w^2+\Delta^2)}\,\frac{\Delta}{\sqrt{w^2+\Delta^2}}\cdot u_{max} - \frac{1}{2}\frac{w}{R}u_{max} - \frac{1}{2}\frac{u_{max}^2}{R} \quad (28)$$

$$\bar{a}_{xR} = \left[\frac{1}{2}\Delta - \sqrt{R^2 - \frac{1}{4}(w^2+\Delta^2)}\,\frac{w}{\sqrt{w^2+\Delta^2}}\right]\frac{u_{max}}{R}$$

$$+ \frac{u_{max}+w}{2R}\sqrt{R^2-(w+u_{max})^2}$$

$$- \frac{w}{2R}\sqrt{R^2-w^2} + \frac{R}{2}\arcsin\frac{w+u_{max}}{R} - \frac{R}{2}\arcsin\frac{w}{R} \quad (29)$$

Case B: $\Delta > w$.—In Fig. 12 it is seen that for $R > (w^2+\Delta^2)/2w$ the calculation can be carried out in the same way as in case A. For the range

$$w < R < \frac{w^2+\Delta^2}{2w} \quad (30)$$

the maximum contact phase is valid. Similarly, as in the growing contact phase, a circle is in contact with the opposite crack face if the embedment depth,

u, is greater than zero and smaller than a certain upper bound. In Fig. 10(c) it can be seen that this upper bound is obtained for $u = u_{max} = R - w$. For values of R in the range indicated by Eq. 30, $\bar{a}_{yR}$ and $\bar{a}_{xR}$ are obtained by substitution of Eq. 20f in Eq. 26 and Eq. 20g in Eq. 27 and integration: This results in

$$\bar{a}_{yR} = \frac{1}{R}\int_0^{(R-w)} (R - u - w)\, du = \frac{1}{2R}(R - w)^2 \quad \ldots\ldots\ldots\ldots \quad (31)$$

$$\bar{a}_{xR} = \frac{\pi}{4}\cdot R - \frac{w}{2R}\sqrt{R^2 - w^2} - \frac{R}{2}\arcsin\frac{w}{R} \quad \ldots\ldots\ldots\ldots\ldots \quad (32)$$

For the range $R > (w^2 + \Delta^2)/2w$ Eqs 28 and 29 are valid.

For a unit length of the crack line, line of intersection of the crack plane and a Z-plane [Fig. 4(c)], it was shown that the probability density function for the expected number of circles with a diameter, D_0, intersected on this length, can be expressed by Eq. 19. The total contact areas in the X and y directions, provided by all circles intersecting the unit crack length, can be expressed as

$$\Sigma\bar{a}_{yR} = \int_{R_{min}}^{R_{max}} n(R)\cdot\bar{a}_{yR}\cdot dR \quad \ldots\ldots\ldots\ldots\ldots\ldots\ldots \quad (33)$$

$$\Sigma\bar{a}_{xR} = \int_{R_{min}}^{R_{max}} n(R)\cdot\bar{a}_{xR}\cdot dR \quad \ldots\ldots\ldots\ldots\ldots\ldots\ldots \quad (34)$$

Substitution of the concerning values for R_{min} and R_{max} (Fig. 12), the associated expressions for $\bar{a}_{yR}$ and $\bar{a}_{xR}$ (Eqs. 26–29) and $n(R)$ (Eq. 19) in Eqs. 33 and 34 and some rearranging of terms results in the final expressions for the projected contact areas $\bar{A}_y$ (= $\Sigma\bar{a}_y$) and $\bar{A}_x$ (= $\Sigma\bar{a}_x$), as a function of crack width, w, and shear displacement Δ for a crack area with a unit length and a unit width:

Case A: $\Delta < w$

$$\bar{A}_y = \frac{\int_{w^2+\Delta^2}^{D_{max}}}{\Delta} p_k\cdot\frac{4}{\pi}\cdot F\left(\frac{D}{D_{max}}\right)\cdot G_1(\Delta, w, D)\cdot dD \quad \ldots\ldots\ldots\ldots \quad (35)$$

$$\bar{A}_x = \frac{\int_{w^2+\Delta^2}^{D_{max}}}{\Delta} p_k\cdot\frac{4}{\pi}\cdot F\left(\frac{D}{D_{max}}\right)\cdot G_2(\Delta, w, D)\cdot dD \quad \ldots\ldots\ldots\ldots \quad (36)$$

Case B: $\Delta > w$

$$\bar{A}_y = \int_{2w}^{w^2+\Delta^2/w} p_k\cdot\frac{4}{\pi}\cdot F\left(\frac{D}{D_{max}}\right)\cdot G_3(\Delta, w, D)\cdot dD$$
$$+ \int_{w^2+\Delta^2/w}^{D_{max}} p_k\cdot\frac{4}{\pi}\cdot F\left(\frac{D}{D_{max}}\right)\cdot G_1(\Delta, w, D)\cdot dD \quad \ldots\ldots\ldots\ldots \quad (37)$$

$$\bar{A}_x = \int_{2w}^{w^2+\Delta^2/w} p_k \cdot \frac{4}{\pi} \cdot F\left(\frac{D}{D_{max}}\right) \cdot G_4(\Delta, w, D) \cdot dD$$

$$+ \int_{w^2+\Delta^2/w}^{D_{max}} p_k \cdot \frac{4}{\pi} \cdot F\left(\frac{D}{D_{max}}\right) \cdot G_1(\Delta, w, D) \cdot dD \quad \ldots\ldots\ldots\ldots\ldots (38)$$

with $$G_1(\Delta, w, D) = D^{-3}\left[\sqrt{D^2 - (w^2+\Delta^2)}\,\frac{\Delta}{\sqrt{w^2+\Delta^2}} \cdot u_{max} - w \cdot u_{max} - u_{max}^2\right]$$

$$G_2(\Delta, w, D) = D^{-3}\left[\Delta - \sqrt{D^2 - (w^2+\Delta^2)}\,\frac{w}{\sqrt{w^2+\Delta^2}} \cdot u_{max} + (u_{max} + w)\right.$$

$$\cdot \sqrt{\frac{1}{4}D^2 - (w + u_{max})^2} - w\sqrt{\frac{1}{4}D^2 - w^2} + \frac{1}{4}D^2 \arcsin\frac{w + u_{max}}{\frac{1}{2}D}$$

$$\left. - \frac{D^2}{4}\arcsin\frac{2w}{D}\right] dD \quad \ldots\ldots\ldots\ldots\ldots\ldots\ldots\ldots\ldots (39)$$

$$G_3(\Delta, w, D) = D^{-3}\left(\frac{1}{2}D - w\right)^2$$

$$G_4(\Delta, w, D) = D^{-3}\left(\frac{\pi}{8}D^2 - w\sqrt{\frac{1}{4}D^2 - w^2} - \frac{D^2}{4}\arcsin\frac{2w}{D}\right)$$

$$F\left(\frac{D}{D_{max}}\right) = 0.532\left(\frac{D}{D_{max}}\right)^{0.5} - 0.212\left(\frac{D}{D_{max}}\right)^4 - 0.072\left(\frac{D}{D_{max}}\right)^6$$

$$- 0.036\left(\frac{D}{D_{max}}\right)^8 - 0.025\left(\frac{D}{D_{max}}\right)^{10}$$

p_k = volume aggregate/volume concrete

u_{max} is expressed in Eq. 23

Integration of Eqs. 35–38 has been carried out in a numerical way with an Algol program (25).

Fig. 15 shows, as an example, the calculated relations for $\bar{A}_y$ and $\bar{A}_x$, or $\Sigma\bar{a}_y$ and $\Sigma\bar{a}_x$ for a unit crack area of 1 mm^2 (0.00155 in.^{2}), as a function of crack width, w, and shear displacement, Δ, for a concrete mixture with a maximum aggregate particle diameter of 32 mm (1.26 in.) and a p_k value of 0.75. The shear and normal stress across the crack faces are related to the contact areas

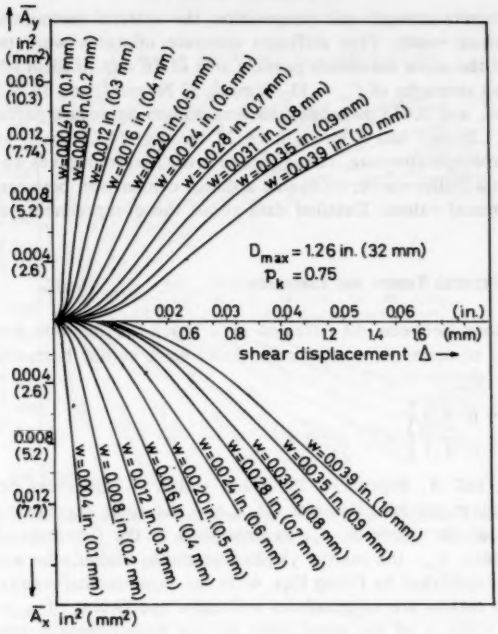

FIG. 15.—Total Projected Contact Areas, $\bar{A}_y$ and $\bar{A}_x$, for 1-mm² Crack Plane, as Function of Crack Width, w, and Shear Displacement, Δ, Calculated with Eqs. 35–38

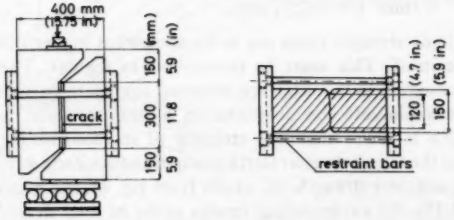

FIG. 16.—Pushoff Tests on Externally Restrained Specimens

$\bar{A}_y$ and $\bar{A}_x$ with Eq. 6. In order to evaluate the theory and to establish the material constants, σ_{pu} and μ, a number of experiments have been carried out.

Experiments

Tests were carried out on precracked pushoff specimens with external restraint bars of various stiffnesses (Fig. 16) [see also (25)]. The variables in the tests

were the concrete strength and composition, the external restraint stiffness and the initial crack width. Five different concrete mixtures were tested. Three of these had the same maximum particle size of 16 mm (0.63 in.) but different cube crushing strengths of $f'_{cc} = 13\ \text{N/mm}^2$, $37\ \text{N/mm}^2$, and $59\ \text{N/mm}^2$ (1,915 psi, 5,286 psi, and 8,428 psi), one had a maximum aggregate particle diameter of 32 mm (1.26 in.) and a strength of $33\ \text{N/mm}^2$ (4,714 psi), and one was a sanded lightweight concrete. The aggregate in the first four mixes was distributed according to a Fuller curve, to enable a direct comparison between theoretical and experimental values. Detailed data about these experiments are found in Ref. (25).

Comparison Between Theory and Experiments

The relations between the stresses in a crack on the one hand and the displacement components on the other hand have earlier been formulated as (see also Eq. 6)

$$\left.\begin{aligned}\sigma &= \sigma_{pu}(\bar{A}_x - \mu \cdot \bar{A}_y)\\ \tau &= \sigma_{pu}(\bar{A}_y + \mu \cdot \bar{A}_x)\end{aligned}\right\} \quad \ldots\ldots\ldots\ldots\ldots\ldots\ldots\ldots\ldots\ldots \quad (40)$$

in which A_x and A_y depend on the crack width, w, the shear displacement, Δ, the maximum particle diameter, D_{max} and the total aggregate volume per unit volume of the concrete, p_k, as expressed in the functions, Eqs. 35–38. The parameters, σ_{pu}, the matrix yielding strength, and μ, the coefficient of friction, are established by fitting Eqs. 40 to the experimental results. It appears that the best results are obtained for a friction coefficient of $\mu = 0.4$ for all mixes. This value is of the same order as was experimentally established by Weiss (27) in friction tests on concrete, mortar, and particle surfaces. The matrix yielding stress, σ_{pu}, which has to be inserted to get optimal fitting, is a function of the uniaxial concrete strength. The best results are obtained for

$$\sigma_{pu} = 6.39 f'^{\,0.56}_{cc}\ \text{N/mm}^2\ (56.7 f'^{\,0.56}_{cc}\ \text{psi}) \quad \ldots\ldots\ldots\ldots\ldots\ldots \quad (41)$$

The matrix yielding strength turns out to be somewhat higher than the strength of the concrete itself. This must be considered as regular: The weakest link of a hardened concrete is the interface between aggregate particles and matrix, where microcracks initiate the deterioration of the concrete; as a result the concrete strength is lower than the strength of its constituting components. Also the fact that the ratio between matrix strength and concrete strength decreases with increasing concrete strength, as results from Eq. 41, is a generally observed phenomenon (4,19). All experimental results could be well described with Eqs. 35–39 and the material constants, $\mu = 0.4$ and σ_{pu}, from Eq. 41. Examples are given for two mixtures (Figs. 17 and 18). It must be emphasized that, to fit Eqs. 40 to the experimental results, only two degrees of freedom exist, μ, σ_{pu}, so that only two lines per diagram (e.g., for $w = 1.0$ mm) can actually be fitted. The fact that automatically all other lines are found to fit the experimental results supports very well the validity of the theory.

Further Analysis of Aggregate Interlock

The model which has been developed is in adequate agreement with the

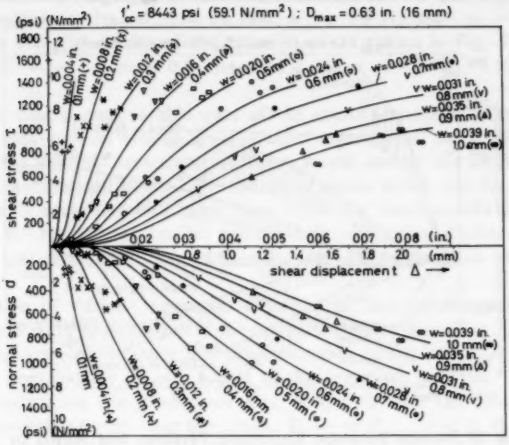

FIG. 17.—Comparison between Experimental Values for Concrete with f'_{cc} = 59 N/mm² (8,428 psi), D_{max} = 16 mm (0.63 in.), p_k = 0.75 and Theoretical Values, with σ_{pu} = 65 N/mm² (9,285 psi) and μ = 0.40

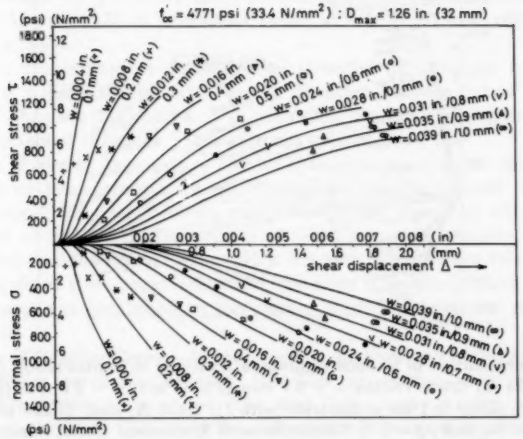
f'cc = 4771 psi (33.4 N/mm²) ; Dmax = 1.26 in. (32 mm)
(psi) (N/mm²)
shear stress τ
normal stress σ
shear displacement Δ
(in)
(mm)
w=0.004 in. 0.1 mm (+)
w=0.008 in. 0.2 mm (x)
w=0.012 in. 0.3 mm(*)
w=0.016 in. 0.4 mm (p)
w=0.020 in. 0.5 mm (o)
w=0.024 in./0.6 mm (o)
w=0.028 in./0.7 mm (•)
w=0.031 in./0.8 mm (v)
w=0.035 in./0.9 mm (Δ)
w=0.039 in./10 mm (■)

FIG. 18.—Comparison between Experimental Values for Concrete with f'_{cc} = 33.4 N/mm² (4,714 psi), D_{max} = 32 mm (1.26 in.), p_k = 0.75 and Theoretical Values, with σ_{pu} = 44 N/mm² (6,286 psi) and μ = 0.40

experimental results. As such it can be used for parameter studies, yielding a better insight into the fundamental mechanics of aggregate interlock.

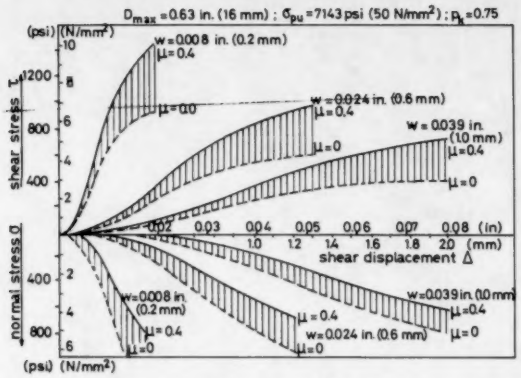
D_{max} = 0.63 in. (16 mm) ; σ_{pu} = 7143 psi (50 N/mm²) ; p_k = 0.75
(psi) (N/mm²)
w = 0.008 in. (0.2 mm)
μ = 0.4
μ = 0.0
w = 0.024 in. (0.6 mm)
w = 0.039 in. (1.0 mm)
shear stress τ
normal stress σ
0.02 0.03 0.04 0.05 0.06 0.07 0.08 (in)
1.0 1.2 1.4 1.6 1.8 2.0 (mm)
shear displacement Δ

FIG. 19.—Role of Friction between Aggregate Particles and Matrix in Transfer of Stresses across Crack, for Concrete with f'_{cc} = 40 N/mm² (5,714 psi), D_{max} = 16 mm (0.63 in.), and p_k = 0.75, Calculated with Theoretical Model

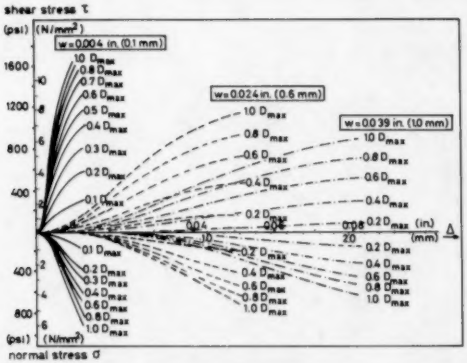

FIG. 20.—Contribution of Various Aggregate Fractions to Transmission of Stresses across Cracks for Crack Widths w = 0.1 mm (0.0039 in.); w = 0.6 mm (0.0236 in.); and 1.0 mm (0.039 in.) for a Concrete with f'_{cc} = 30 N/mm² (4,286 psi), D_{max} = 32 mm (1.26 in.) and p_k = 0.75 Calculated with Theoretical Model (Inserted Values σ_{pu} = 44 N/mm² (6,286 psi) and μ = 0.40)

Role of Friction between Aggregate and Matrix.—It was shown that equilibrium in the contact area was obtained by combinations of normal (yielding) stresses and shear (friction) stresses. It was shown that a friction coefficient equal to 0.4 resulted in the best fitting of the curves to the experimental results.

By conducting a calculation with a friction coefficient, $\mu = 0$, the influence of friction can be visualized. A calculation is carried out for a mixture with maximum aggregate size, $D_{max} = 16$ mm, $\sigma_{pu} = 50$ N/mm^2, $p_k = 0.75$, and $\mu = 0.0$ and 0.4. The results of the calculation are shown in Fig. 19 for some crack widths, $w = 0.2$ mm, 0.6 mm, and 1.0 mm (0.008 in., 0.024 in., and 0.039 in.).

It is seen that a considerable part of the shear resistance is provided by friction. If this friction would be eliminated e.g., by oil between the crack faces, and the external restraining stiffness would remain the same (compare equal σ-w combinations in Fig. 19), the shear stress which can be transferred is considerably smaller (even more than 100% for small crack widths), and equilibrium is obtained for smaller values of the shear displacement, Δ, which shows also that more overriding of particles and less deformation of the matrix will occur.

Contribution of Various Aggregate Fractions to Transmission of Stresses in Crack.—By a slight modification in the derivation of the equations, representing the relations between stresses and displacements in the crack, it is possible to find the contribution of only a part of the aggregate particles. Eq. 15 was found by integrating the product of Eqs. 9 and 12 over the interval, $D_0 \rightarrow D_{max}$. By integrating only over the range, $D_0 \rightarrow n \cdot D_{max}$, $n < 1$, the influence of aggregate fractions is visualized. An example is given in Fig. 20: With the modified expressions 35–38 the contribution of fractions has been established and represented for a small [0.1 mm (0.0039 in.)], an average [0.6 mm (0.0236 in.)], and a great [1 mm (0.039 in.)] crack width, for a mixture with a cube crushing strength of $f'_{cc} = 30$ N/mm^2 (4286 psi) and a maximum particle diameter of $D_{max} = 32$ mm (1.26 in.) (inserted values $\sigma_{pu} = 44$ N/mm^2 (6286 psi), $\mu = 0.40$, $p_k = 0.75$).

The lines, represented in these figures, describe the relations between σ, τ, w, and Δ if only the particles with a diameter between 0 and a varying fraction of D_{max} are considered. It is seen that the small aggregate fractions loose importance if the crack width becomes greater.

Influence of Size of Aggregate.—To obtain an impression about the influence of the size of the aggregate, two mixtures have been compared. Both have the same properties, except for the maximum particle diameter, which is once 16 mm and once 32 mm. The results of this comparison are shown in Fig. 21. It is seen that the normal stress, σ, is not very sensitive for this variation, but that the shear stress, τ, is influenced, the more if the crack width is greater. This tendency was confirmed by the results of the experimental part of this investigation.

Influence of Grading Curve.—In the previous analyses and in the experiments always a Fuller curve was adopted. However, in practice most codes allow a permissible grading curve region. The ideal Fuller curve is near to the lower boundary of this area. To study the influence of the grading curve a curve is chosen which approximates to the upper limit given in the Netherlands Code of Practice, the $VB'/4$, for $D_{max} = 16$ mm (0.63 in.).

The relations between stresses and displacements for the concrete confirming to the grading curve B were calculated, as shown in Fig. 22. Other values adopted were $p_k = 0.75$, $\mu = 0.40$, and $\sigma_{pu} = 44$ N/mm^2 (6,286 psi). Although this concrete has the same maximum particle diameter, D_{max}, as the comparable

Fuller mix, it contains a much higher proportion of sand particles.

The results previously obtained under the aforementioned section on the transmission of stresses, where the contribution of the individual aggregate fractions to the transfer of stresses in a crack was established, were used for

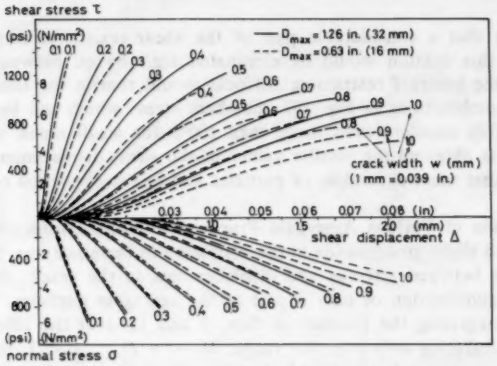

FIG. 21.—Influence of Size of Aggregate on Transmission of Stresses across Crack for Concretes with f'_{cc} = 30 N/mm² (4,286 psi), p_k = 0.75, D_{max} = 16 and 32 mm (0.63 in. and 1.26 in.), Calculated with Theoretical Model (Inserted Values σ_{pu} = 44 N/mm² (6,286 psi) and μ = 0.40)

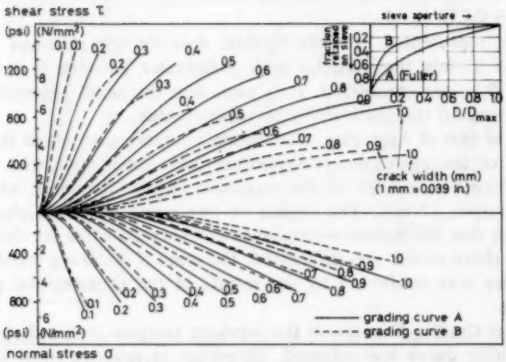

FIG. 22.—Influence of Grading Curve on Transfer of Stresses across Crack for Two Comparable Mixes Confirming to Different Grading Curves, Calculated with Theoretical Model (Inserted Values D_{max} = 32 mm (1.26 in.), p_k = 0.75, and μ = 0.40)

the calculations. The results for the concrete mix with the grading curve *B*, are shown in Fig. 22 by the dashed lines, and are compared with the results for the Fuller-type concrete, calculated earlier (Fig. 21).

It is seen that in both cases the influence of the sieve line on the normal stresses, σ, is not great, but is significant for the shear stresses. The most pronounced differences are obtained for greater crack widths. This can be expected, since the sand mixtures according to grading curve B provide a smaller potential contact area at greater crack width.

Cyclic Loading.—From tests (12) it is known that in the case of cyclic loading a considerable difference exists between the behavior of the crack plane during the first loading cycle and the subsequent cycles. The shear stress/shear displacement relation of the initial cycle is nearly linear, and after unloading a considerable amount of hysteresis is observed. The shear stress/shear displacement relationship for the later loading cycles is highly nonlinear and a hardening type of behavior is observed. This overall behavior can be explained with the theory.

This is done on basis of a fictitious specimen (Fig. 24) with a concrete (quality of $f'_{cc} = 33.4\ \text{N/mm}^2$ (4,770 psi) and a maximum aggregate particle diameter

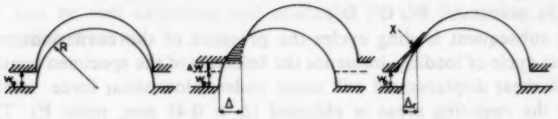

FIG. 23.—Three Characteristic Stages during First Loading Cycle: (*a*) Before Loading; (*b*) at Peak Shear Stress; (*c*) after Unloading

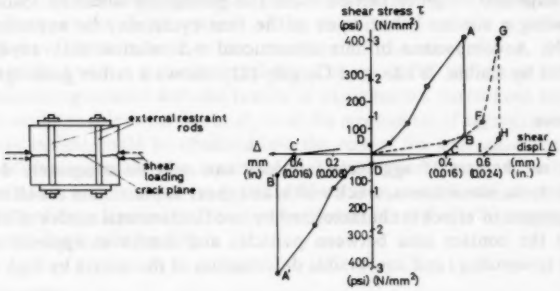

FIG. 24.—(*a*) Fictitious Specimen; (*b*) Calculated Response to Cyclic Loading

of 32 mm (1.26 in.), so that Fig. 18 can be used, a preset crack width of $w_0 = 0.5$ mm (0.020 in.), and external restraint bars, providing an equivalent restraint stress of $0.5\ \text{N/mm}^2$ (71 psi) for a crack width increment of $dw = 0.1$ mm (0.004 in.). The specimen is subjected to a maximum (cyclic) shear stress of $\tau = 3\ \text{N/mm}^2$ (430 psi). Fig. 23(*a*) shows the positions of the crack faces before loading. When the shear load is increased, the crack faces engage in contact, Fig. 23(*b*). The relation between τ, shear stress, and Δ, shear displacement, can be calculated using Fig. 18. If the maximum shear stress is reached, point A in Fig. 24(*b*), the friction between particles and matrix is still a maximum, $\mu = 0.40$. If the shear force is decreased, a relative movement

between the crack faces can only occur if the maximum amount of friction in the opposite direction is exceeded. With the theoretical model it was calculated that this point is reached when the shear stress is reduced to 0.50 N/mm^2 (71.4 psi), point B in Fig. 24(*b*). Fig. 23(*c*) shows that, after unloading, the no contact phase is reached before the shear displacement is back in the neutral position. This no contact phase is considered to be reached if in the most favorable case, $R = 1/2\ D_{max}$, $u = 0$, no contact exists any more. For the case considered it was calculated that the remaining shear displacement, Δ_r, is equal to 0.41 mm (0.016 in.), point C in Fig. 24(*b*).

To bring the two halves of the specimen back in their neutral position a small shear force may be necessary, since the rubble between the crack faces due to the deterioration of matrix material during loading, may cause some frictional resistance, point D in Fig. 24(*b*). If the shear force is applied in the opposite direction, the same type of behavior can be expected since those parts of the crack surfaces which get in touch in this reversed cycle are not yet damaged (Fig. 23). Thus, a similar loading and unloading curve can be expected (Fig. 24(*b*), points A′, B′, C′, D′).

In the subsequent loading cycles the presence of the cavitations, worn out in the first cycle of loading, influence the behavior of the specimen considerably. At first a shear displacement will occur under a low shear force, until contact between the opposing areas is obtained ($\Delta \geq 0.41$ mm, point E). Then in a short interval of Δ full contact between the cavitations will be obtained. In this short interval a proceeded wearing off will take place at places of high contact stresses, point x in Fig. 23(*c*). Hence a steeply ascending branch (EFG) may be expected, slightly shifted from the previously obtained loading line. At unloading a similar behavior as in the first cycle may be expected, GHI, Fig. 24(*b*). A comparison of this constructed τ-Δ relation with experiments, carried out by Laible, White, and Gergely (12), shows a rather good agreement.

Conclusions

1. The mechanism of aggregate interlock can only be adequately described if normal stress, shear stress, crack width, and shear displacement are all involved.
2. Aggregate interlock is characterized by two fundamental modes of behavior: sliding at the contact area between particles and matrix at opposite sides of the crack (*overriding*) and irreversible deformation of the matrix by high contact. stress.
3. The experimental results can be adequately described by a physical model, simplifying the aggregate particles to rigid spheres of different sizes, protruding from a flat crack plane, and adopting a rigid-plastic stress-strain relation for the matrix between the particles.
4. All particle fractions contribute qualitatively in the same way to the transfer of stresses across the crack; only fractions containing merely particles with a diameter smaller than two times the crack width may be considered to be inactive.
5. For the friction between particles and the matrix, a friction coefficient, $\mu = 0.4$, independent of the concrete quality and the level of the stresses, gives the best results. The yielding strength of the matrix, which has to be used in order to get the best results, is a function of the concrete strength.

The values for both the friction coefficient and the matrix yielding strength are in good agreement with expectations, based on experiments described in the literature.

6. The resistance of the crack faces against shear displacements is most of all governed by the strength of the concrete. The size of the aggregate particles in the range tested, D_{max} = 16–32 mm (0.63–1.26 in.), plays a subordinate role.

7. The grading curve of the aggregate has some influence: A theoretical comparison between two mixes, one composed according to a Fuller curve (large particles) and the other containing a large sand fraction, displays an influence on the shear stiffness at larger crack widths. The development of the normal stresses is hardly influenced.

8. If the friction between the crack faces would be reduced e.g., by oil, this would result in a considerable reduction of the resistance against shear stresses and an increase of the overriding at the expense of the deformational mode of behavior.

9. The behavior of cracks, subject to cyclic loading, as known from the literature, can be well explained and described by the theoretical model, at least in a qualitative way.

Summary

A mathematical model has been developed describing the mechanism of aggregate interlock in cracks. The model is based on the behavior on particle level, taking into account the deformation of the hardened cement matrix and frictional forces between aggregate particles and matrix during sliding. The relations between the displacements of the crack faces and the stresses across the crack have been related to the structure of the crack faces, which has been established with a statistical analysis. The results of the theoretical model are in adequate agreement with the results of experiments, carried out separately. Thus, the model enables a further analysis of the mechanism of aggregate interlock. In this way insight could be obtained into the role of the aggregate distribution, the size of the aggregate, the contribution of aggregate fractions, and the role of deformation and friction on particle level. The model makes possible an explanation of the experimental tendencies, found in tests of other investigators, for instance, for cyclic loading.

Acknowledgment

The financial support and encouragement of the CUR, Research Committee of the Dutch Concrete Association, is gratefully acknowledged.

Appendix I.—References

1. Bazant, Z. P., and Gambarova, P., "Rough Cracks in Reinforced Concrete," *Journal of the Structural Division*, ASCE, Vol. 106, No. ST4, Proc. Paper 15330, Apr., 1980, pp. 819–842.
2. Bazant, Z. P., and Tsubaki, T., "Optimum Slip-Free Limit Design of Concrete Reinforcing Nets," *Journal of the Structural Division*, ASCE, Vol. 105, No. ST2, Proc. Paper 14344, Feb., 1979, pp. 327–346.

3. Birkeland, P. W., and Birkeland, H. W., "Connections in Precast Concrete Construction," *Journal of the American Concrete Institute*, Vol. 63, No. 3, Mar., 1966, pp. 345–368.
4. Bremer, F., and Steindorfer, F., "Bruchfestigkeit und Bruchverformung von Beton unter mehraxialer Belastung bei Raumtemperatur," *Deutscher Ausschuss für Stahlbeton*, Heft 263, Ernst und Sohn, Berlin, West Germany, 1976.
5. Cedolin, L., and Dei Poli, S., "Non-Linear Plane Stress Analysis of Reinforced Concrete by the Finite Element Method," *Construzioni in Cemento Armato, Studi e Rendiconti*, Politecnico di Milano, Vol. VIII, Milan, Italy, 1977, pp. 3–33.
6. Cedolin, L., and Dei Poli, S., "Finite Element Studies of Shear Critical R/C Beams," *Journal of the Engineering Mechanics Division*, ASCE, Vol. 103, No. EM3, Proc. Paper 12968, June, 1977, pp. 395–410.
7. Fattah-Shaikh, A., "Proposed Revisions to Shear-Friction Provisions," *Journal of the Prestressed Concrete Institute*, Vol. 23, No. 2, Mar./Apr., 1978, pp. 12–21.
8. Fenwick, R. C., and Paulay, T., "Mechanisms of Shear Resistance of Concrete Beams," *Journal of the Structural Division*, ASCE, Vol. 94, No. ST10, Proc. Paper 2325, Oct., 1968, pp. 2325–2350.
9. Geistefeld, H., "Stahlbetonscheiben in gerissenem Zustand-Berechnung mit Berücksichtigung der rissabhängigen Schubsteifigkeit im Materialgesetz," thesis presented to Technische Universität Braunschweig, at Braunschweig, Germany, in 1976, in partial fulfillment of the requirements for the degree of Doctor of Philosophy.
10. Goto, Y., "Cracks Formed in Concrete around Deformed Tension Bars," *Journal of the American Concrete Institute*, Proceedings, Vol. 68, No. 4, Apr., 1971, pp. 244–251.
11. Hand, F. R., Pecknold, D. A., and Schnobrich, W. C., "Non-Linear Layered Analysis of RC Plates and Shells," *Journal of the Structural Division*, ASCE, Vol. 99, No. ST7, Proc. Paper 9860, July, 1973, pp. 1491–1505.
12. Laible, F., White, R. N., and Gergely, P., "An Experimental Investigation of Seismic Shear Transfer across Cracks in Concrete Nuclear Containment Vessels," *ACI Special Publication SP-53*, Detroit, Mich., 1977.
13. Locher, F. W., and Wischers, G., "Aufbau und Eigenschaften des Zementsteins," *Zement Taschenbuch 1976/1977*, NCH Nederlandse Cement Handelsmaatschappij B.V., The Hague, The Netherlands, 1977, pp. 43–59.
14. Lin, C. S., and Scordelis, A. C., "Non-Linear Analysis of RC Shells of General Form," *Journal of the Structural Division*, ASCE, Vol. 101, No. ST3, Proc. Paper 11164, Mar., 1975, pp. 523–537.
15. MacGregor, J. G., and Hawkins, N. M., "Suggested Revisions to ACI Building Code Clauses Dealing, with Shear Friction and Shear in Deep Beams and Corbels," *Journal of the American Concrete Institute, Proceedings*, Vol. 74, No. 11, Nov., 1977, pp. 537–545.
16. Mast, R. F., "Auxiliary Reinforcement in Concrete Connections," *Journal of the Structural Division*, ASCE, Vol. 94, No. ST6, Proc. Paper 6002, June, 1968, pp. 1485–1504.
17. Mattock, A. H., "Shear Transfer in Concrete Having Reinforcement at an Angle to the Shear Plane," *ACI Special Publication SP-42, Shear in Reinforced Concrete*, Vol. I, 1974, pp. 17–42.
18. Reinhardt, H. W., and Walraven, J. C., "Shear Transfer in Reinforced Concrete with Small Crack Widths," presented at the April 14–18, 1980, ASCE Convention, Portland, Oreg. (Preprint 80-012).
19. Reinhardt, H. W., "Ansprüche des Konstrukteurs an den Beton," *Beton*, Vol. 27, No. 5, May, 1977, pp. 195–199.
20. Schäfer, H., "Zur Berechnung von Stahlbetonplatten," thesis presented to the Technische Universität Darmstadt, at Darmstadt, W. Germany, in 1976, in partial fulfillment of the requirements for the degree of Doctor of Philosophy.
21. Schimmelpfennig, K., "Bruchsicherheitsberechnung von Stahlbetondruckbehältern," *Deutscher Ausschuss für Stahlbeton*, Heft 257, Ernst and Sohn, Berlin, West Germany, 1976.
22. Swamy, R. N., and Andriopoulos, A. D., "Contribution of Aggregate Interlock and Dowel Forces to the Shear Resistance of Reinforced Beams without Web Rein-

forcement," *ACI Special Publication SP-42, Shear in Reinforced Concrete*, Vol. I, 1974, pp. 129–166.
23. Taylor, H. P. J., "The Fundamental Behavior of Reinforced Concrete Beams in Bending and Shear," *ACI Special Publication SP-42, Shear in Reinforced Concrete*, Vol. I, 1974, pp. 43–78.
24. Walraven, J. C., Vos, E., and Reinhardt, H. W., "Experiments on Shear Transfer in Cracks in Concrete, Part I: Description of Results," *Report 5-79-3*, Stevin Laboratory, Delft University of Technology, The Netherlands, Dec., 1978.
25. Walraven, J. C., "Experiments on Shear Transfer in Cracks in Concrete, Part II: Analysis of Results," *Report 5-79-10*, Stevin Laboratory, Delft University of Technology, The Netherlands, Nov., 1979.
26. Walraven, J. C., "Aggregate Interlock: A Theoretical and Experimental Investigation," thesis presented to the Delft University of Technology, at Delft, The Netherlands, in Oct., 1980, in partial fulfillment of the requirements for the degree of Doctor of Philosophy.
27. Weiss, R., "Ein Haufwerkstheoretisches Model der Restfestigkeit geschädigter Betone," thesis presented to the Technische Universität Braunschweig, at Braunschweig, West Germany, in 1978, in partial fulfillment of the requirement for the degree of Doctor of Philosophy.

Appendix II.—Notation

The following symbols are used in this paper:

$\bar{A}_x$ = expected average value of projection on y-plane of total contact area, obtained over unit crack area, for certain combination of w, Δ;
$\bar{A}_y$ = expected average value of projection on the x-plane of total contact area, obtained over unit crack area, for certain combination of w, Δ;
a_x = projected contact length in z-plane on x-axis;
a_{xR} = projected contact length in z-plane on x-axis for circle with radius R;
$\bar{a}_{xR}$ = expected average value of a_{xR};
a_y = projected contact length in z-plane on y-axis;
a_{yR} = projected contact length in z-plane on x-axis for circle with radius R;
$\bar{a}_{yR}$ = expected average value of a_{yR};
B_{nn}, ... = crack stiffness coefficients;
D = diameter of intersection circle;
D_{max} = diameter of maximum intersection circle (maximum particle);
D_x = arbitrary particle diameter;
D_0 = arbitrary particle diameter;
F_x = force in X direction per unit width in z direction;
F_y = force in Y direction per unit width in z direction;
G = shear stiffness modulus of uncracked concrete;
p_k = relative aggregate volume fraction;
R = radius of intersection circle or particle;
R_{max} = maximum value of R;
R_1 = minimum radius of an intersection circle for which contact can occur at a certain w, Δ combination;
R_2 = maximum radius of an intersection circle for which maximum

contact mode can occur at a certain w, Δ combination;

u = embedment depth, defined as distance from center point of intersection circle to central crack face (see, e.g., Fig. 10);

u_{max} = maximum value of u for which, at certain w, Δ, R combination contact is possible;

w = crack width;

α_s = shear stiffness reduction factor;

Δ = shear displacement;

Δ_0 = shear displacement below which no contact is possible at certain combination of u, w and R;

Δ_b = shear displacement above which the maximum contact mode occurs at certain combination of w and R;

μ = coefficient of friction between particles and matrix;

σ = normal stress;

σ = normal stress at plastic deformation of matrix;

τ = shear stress; and

τ_{pu} = shear stress at plastic deformation of matrix.

PACKAGE FOR OPTIMIZATION-BASED INTERACTIVE CAD[a]

By M. A. Bhatti,[1] K. S. Pister,[2] M. ASCE, and E. Polak[3]

INTRODUCTION

Common practice in the design of civil engineering structures is to use a trial and error design procedure. First, an initial design is chosen, which is then analyzed using a computer program simulating the behavior of the physical system. By looking at the results of the computer simulation, the designer adjusts the initial design in an attempt to satisfy a set of given specifications that are not met by the initial design or to obtain a better design in terms of its performance, or for both reasons. After the adjustment, a new simulation is performed, and the process is repeated until a satisfactory design is obtained. The success of this procedure depends critically on the experience of the designer and, even then, typically involves a considerable number of man hours.

Since the early 1950's, research in computer simulation of structural systems has made considerable progress, resulting in a number of excellent general purpose structural analysis programs (1,7). At the same time, several attempts have been made to automate the above design process using optimization techniques. A summary of this development is contained in the survey papers (8,11–13). Despite this considerable research activity, optimization techniques are not as widely used as might be expected. In the authors' opinion, the main reasons for this lack of interest are

1. Lack of a proper definition of design problems in terms of an optimization problem.
2. Lack of robust optimization algorithms applicable to general design problems involving dynamic constraints.
3. Lack of familiarity with optimization techniques.

[a]Presented at the October 27–31, 1980, ASCE Annual Convention, held at Hollywood, Fla. (Preprint 80–635).

[1]Asst. Prof., Div. of Materials Engrg., Univ. of Iowa, Iowa City, Iowa 52240.
[2]Prof. of Engrg. Sci., Univ. of California, Berkeley, Calif. 94720.
[3]Prof. of Electrical Engrg. and Computer Sci., Univ. of California, Berkeley, Calif. 94720.

Note.—Discussion open until April 1, 1982. To extend the closing date one month, a written request must be filed with the Manager of Technical and Professional Publications, ASCE. Manuscript was submitted for review for possible publication on September 16, 1980. This paper is part of the Journal of the Structural Division, Proceedings of the American Society of Civil Engineers, ©ASCE, Vol. 107, No. ST11, November, 1981. ISSN 0044-8001/81/0011-2271/$01.00.

The definition of a design problem in terms of an optimization problem involves identifying an objective function and suitable constraint functions. Historically, since optimization techniques were first used in the aerospace industry, structural weight has often been considered an objective function. For design of structures subjected to dynamic loads, such as earthquake excitation, some other objective functions such as life time cost and story shear forces have been considered (9). For special types of structures, such as braced frames, maximizing energy absorption by the bracing system could be a suitable objective. Thus, depending upon a particular application, any function of design parameters or structural response functions, or both, could be considered an objective. Obviously, along with different objective functions, one must define appropriate constraint functions in order that the problem be well-posed. The computer programs developed for optimal structural design, so far, have been specialized either for a particular objective functions, such as minimum weight, (6) or for particular structures, such as trusses or shear frames. Therefore, their application was limited. Thus, in order to look at different problem formulations, a more flexible programming structure is needed in which the users can define their own objective and constraint functions to solve a wide range of practical problems.

The most obvious, and also most primitive, method of coping with dynamical constraints in an optimization problem, is to discretize the time interval of interest to reduce the problem to an ordinary nonlinear programming problem with a large number of inequality constraints and then to apply a penalty function method. This approach has a number of drawbacks: (1) It requires a very large number of gradient evaluations; (2) it is prone to severe numerical ill-conditioning (with respect to conjugate gradient or quasi-Newton methods) as the penalty increases; and (3) it virtually never produces a design that satisfies specifications exactly. Even the more sophisticated methods, such as those of feasible directions, behave poorly when the direct discretization approach is used, because of the very large number of gradients that must be included in the search direction computation. Consequently, most of the early attempts to solve dynamically constrained design problems with complex excitations, such as those produced by earthquakes, have tended to result in failure. (A notable exception is found in problems involving "simply" excited systems whose dynamic response has a unique and prominent maximum because, in this case, the maximum response turns out to be a well-behaved, differentiable function. Because of this, it is not necessary to discretize the time interval of interest, as mentioned above, and the entire computation becomes much simpler.) There were, and still are, other reasons, optimization fails to produce results; for example, lack of skill in transcribing the design problem into an optimization problem produces an ill-conditioned optimization problem. Similarly, a poor selection of algorithm parameters or a badly chosen initial design can contribute to computational failure. The net result is that when difficulties are encountered the computations either converge slowly or jam up at a nonstationary point. Since optimization algorithms may require several structural analyses per iteration, it is clear that very slow convergence, or worse still, no convergence at all, must be considered to be an expensive accident.

Recently, new algorithms have been developed for general nonconvex problems involving dynamic constraints (4,10), which have better convergence properties. At the same time, methods for early detection of ill-conditioning in mathematical

programming problems are emerging. Since, in general, the transcription of a design problem into a mathematical programming problem is not unique, heuristics are currently being developed that suggest ways of changing the transcription to eliminate the ill-conditioning. However, these algorithms are still sensitive to the choice of internal parameters, as well as initial values of design parameters.

In order to deal with these difficulties, an interactive software system for optimal design is indispensable. Interactive computing permits one to stop, restart or modify any of the parameters as the computation progresses. This results in substantial savings, not only in computing time, but also in overall time needed to carry out a design.

An additional advantage of an interactive system using computer graphics is that it can be used as a tool to familiarize practicing engineers with optimization techniques. They can change parameters of the algorithm and perform a few iterations while monitoring the computation closely through graphical information displayed. This will give them a "feel" for these parameters and the algorithm itself reducing the "black box" quality of the process.

In the following sections, an interactive software system for optimal design of structures is described which is based upon the above considerations. The system is operating on a DEC VAX 11/780 computer obtained through a grant from the National Science Foundation. The operating system is a virtual memory version of UNIX (a Bell Labs System).

The next section describes briefly the algorithm, while interactive implementation and application to the design of a nonlinear impact isolator is examined later.

Design Algorithm

A class of design problems for dynamically loaded structures can be expressed as (2,9)

$$\min_{\mathbf{z}} f(\mathbf{z})$$

$$\text{subject to} \quad \max_{\omega} \phi^j(\mathbf{z}, \omega) \le 0; \quad j = 1, \ldots, m$$

$$\omega \in (\omega_o, \omega_c)$$

$$g^j(\mathbf{z}) \le 0; \qquad j = 1, \ldots, l \qquad \ldots\ldots\ldots\ldots\ldots\ldots (1)$$

in which $\mathbf{z} \in R^p$ = vector of design variables; $f: R^p \to R$ = objective or cost function; $\phi^j: R^p \times \Omega \to R \times \Omega$ = functional or dynamic constraints, in which Ω is a compact interval; and $g^j: R^p \to R$ = conventional inequality constraints which depend on design variables only. The problem is solved by using a Phase I–Phase II feasible directions algorithm. A short description of the algorithm is given below to facilitate the later discussion. Details of the convergence proof are given in (4) and implementation details are given in (3).

The feasible domain, F, is defined by:

$$F = \left\{ \begin{array}{l} \mathbf{z} \in R^p \,|\, \max\limits_{\omega} \phi^j(\mathbf{z}, \omega) \le 0; \quad j = 1, \ldots, m; \\ \qquad\qquad g^j(\mathbf{z}) \le 0; \qquad j = 1, \ldots, l \end{array} \right\} \ldots\ldots\ldots\ldots\ldots (2)$$

Define a function ψ as follows:

$$\psi(\mathbf{z}) = \max \{0; \max_{\omega} \phi^j(\mathbf{z},\omega); j = 1, \ldots, m; g^j(\mathbf{z}); j = 1, \ldots, l\} \quad \ldots\ldots\ldots (3)$$

Note that if $\mathbf{z} \in F$, then $\psi(\mathbf{z}) = 0$. Define the "ϵ-active constraint index" set for functional and conventional constraints as follows:

$$J_\phi = [(j,\omega) | \phi^j(\mathbf{z},\omega) - \psi(\mathbf{z}) \geq -\epsilon; j = 1, \ldots, m] \quad \ldots\ldots\ldots\ldots\ldots (4)$$

and ω is a left local maximizer

$$J_g = [j \,|\, g^j(\mathbf{z}) - \psi(\mathbf{z}) \geq -\epsilon; j = 1, \ldots, l] \quad \ldots\ldots\ldots\ldots\ldots\ldots (5)$$

Algorithm

Data

$\mathbf{z}_o \in R^p$ = initial design; $\epsilon_o > o$ = initial value of ϵ for ϵ-active constraints; α, β, $\delta \in (0,1)$ = Armijo parameters for step length computation; $S_{\max} > 0$ = parameter controlling maximum step length; $\gamma \geq 1$ = parameter influencing search direction when feasible; q_o, $q_{\max} \geq q_o$ = number of points into which the interval (ω_o, ω_c) is discretized; μ_1, $\mu_2 > 0$ = convergence parameters.

STEP 0: set $i = 0$, $q = q_o$

STEP 1: set $\epsilon = \epsilon_o$

STEP 2: compute functions $f(\mathbf{z}_i)$, $g^j(\mathbf{z}_i)$ and $\phi^j(\mathbf{z}_i,\omega)$ for all j.

STEP 3: Direction Finding: (1) Find ϵ-active constraints; (2) evaluate gradients of cost function and ϵ-active constraints; (3) compute the optimality function $\theta(\mathbf{z}_i)$; in which

$$\theta(\mathbf{z}_i) = \max_{\mu \geq c} \left\{ -\frac{1}{2} \left\| \mu_f \nabla_{\mathbf{z}} f(\mathbf{z}_i) + \sum_{j \in J_g} \mu_g^j \nabla_{\mathbf{z}} g^j(\mathbf{z}_i) + \sum_{(j,\omega) \in J_\phi} \mu_\phi^{j,\omega} \nabla_{\mathbf{z}} \phi^j(\mathbf{z}_i,\omega) \right\|_2^2 - \gamma \mu_f \psi(\mathbf{z}_i) \left| \mu_f + \sum_{j \in J_g} \mu_g^j + \sum_{(j,\omega) \in J_\phi} \mu_\phi^{j,\omega} = 1 \right\} \quad \ldots\ldots\ldots\ldots (6)$$

Using the values of μ's obtained by solving (6), compute the search direction $\mathbf{h}(\mathbf{z})$ in which

$$\mathbf{h}(\mathbf{z}_i) = \mu_f \nabla_{\mathbf{z}} f(\mathbf{z}_i) + \sum_{j \in J_g} \mu_g^j \nabla_{\mathbf{z}} g^j(\mathbf{z}_i) + \sum_{(j,\omega) \in J_\phi} \mu_\phi^{j,\omega} \nabla_{\mathbf{z}} \phi^j(\mathbf{z}_i,\omega) \quad \ldots\ldots\ldots (7)$$

STEP 4: ϵ-Reduction: If $\theta(\mathbf{z}_i) \leq -z\,\epsilon\,\delta$ go to Step 6. Else set $\epsilon = \epsilon/2$ and proceed.

STEP 5: Mesh Refinement and Termination Criteria: If $\epsilon > \epsilon_o\,\mu_1/g$ and $\psi(\mathbf{z}_i) > \mu_2/q$, go to Step 2. Otherwise, set $q = 2q$ and, if $q > q_{\max}$, STOP. Else go to Step 1.

STEP 6: Step Length Computation by Armijo Rule: Compute the largest step size $S = \beta^k \in (o, M]$ in which $M = \max\{1, S_{\max}/\|\mathbf{h}(\mathbf{z}_i)\|_\infty\}$ and k is an integer, such that if $\mathbf{z}_i \notin F$, then

$$\psi[\mathbf{z}_i + S\,\mathbf{h}(\mathbf{z}_i)] - \psi(\mathbf{z}_i) \leq -\alpha\,S\,\delta\,\epsilon \quad \ldots\ldots\ldots\ldots\ldots\ldots\ldots (8)$$

if $\mathbf{z}_i \in F$, then

$$f[\mathbf{z}_i + S\,\mathbf{h}(\mathbf{z}_i)] - f(\mathbf{z}_i) \leq -\alpha S \delta \epsilon$$

$$g^j[\mathbf{z}_i + S\,\mathbf{h}(\mathbf{z}_i)] \leq 0; \quad j = 1, \ldots, l$$

$$\phi^j[\mathbf{z}_i + S\,\mathbf{h}(\mathbf{z}_i), \omega] \leq 0; \quad j = 1, \ldots, m$$

$$\omega \in [\omega_o, \omega_c] \text{ discretized into } q \text{ points} \quad \ldots\ldots\ldots\ldots\ldots\ldots (9)$$

STEP 7: Set $\mathbf{z}_{i+1} = \mathbf{z}_i + S\,\mathbf{h}(\mathbf{z}_i)$. Set $i = i + 1$ and go to Step 2.

Remarks.—The algorithm as presented above does not require an initial design that is feasible. If $\mathbf{z}_o \notin F$, then $\psi(\mathbf{z}_o) \neq 0$ and the algorithm constructs a sequence of designs with monotonically decreasing $\psi(\mathbf{z})$ until it becomes zero. This aspect of the algorithm is very advantageous in case of complicated problems where choice of an initial feasible design is not obvious.

According to Step 3, the search direction calculation problem turns out to be the negative of the nearest vector to the origin in the convex hull of the

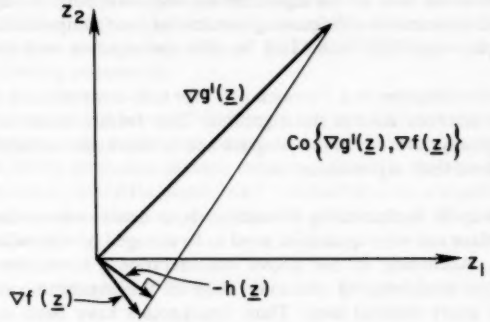

FIG. 1.—Geometry of Direction Finding Process

gradients of the cost and of the ϵ-active constraints. Fig. 1 shows the geometry of the problem when only one g constraint is active. From the figure, it is clear that if the norms of the ϵ-active constraint gradients are much larger than that of the cost gradient, then the direction obtained is not very good because it will be almost perpendicular to the constraint gradient. The best way to safeguard against such a problem is to formulate the mathematical problem in such a way as to insure that the constraints and their gradients have similar magnitudes. In most cases, a simple scaling of the problem works. In order to deal with cases where this is not possible, "push factors" are introduced in the direction finding problem, which effectively scale the gradients. For a more detailed discussion on these push factors, see Ref. 3.

Interactive Implementation of Algorithm

The design algorithm has been implemented on a computer with the batch

program, OPTDYN (3). Computational experience with this program revealed the following difficulties:

1. The choice of parameters best suited for the problem at hand was not obvious and required several adjustments before reaching a set of parameters that gave good computational behavior; and
2. Sometimes the problem was badly scaled with respect to the algorithm, which again required several adjustments before a tractable problem was obtained.

In order to cope with these difficulties, the program OPTDYN was made interactive by combining it with an interpreter of interactive language INTRAC-C, evolved from INTRAC, originally developed at the Department of Automatic Control, Lund Institute of Technology, Lund, Sweden (14). The interaction allows the designer:

1. To interrupt the computing process, change parameter values, and restart the process.
2. To control the flow of the algorithm by single-stepping through its loops. This feature is most useful in diagnosing reasons for poor computational behavior.
3. To display quantities computed by the optimization and simulation algorithms.
4. To use the computer as a "scratch pad" for side computations on variables, vectors, and matrices used in the algorithm. This feature is useful to perform tests not originally foreseen in the program and to check, for example, condition of key matrices, their eigenvalues, etc.

The first step in implementing interaction is to decide where the interaction should take place and what quantities need to be changed or otherwise manipulated, or both. According to the above considerations, interaction should be implemented at each step of the main loop of the algorithm, as well as at each step of every internal loop. Thus, breakpoints have been inserted after the corresponding statement of OPTDYN. At each breakpoint, a subroutine, INTCAL, is called which checks the condition associated with the breakpoint. The condition may be NEVER, ALWAYS, or an IF-clause. If it is NEVER, no action is taken and the control is returned to the OPTDYN. If it is ALWAYS, then INTRAC-C is called an interaction phase takes place. The quantities which need to be changed or displayed are declared into a symbol table (data base). During the interaction phase (marked by a prompt '>'), the user has access to all these quantities and can modify them using the SET command of INTRAC-C.

Some of the more commonly used commands will be described below. A command has the generic form

< command identifier > < argument list >

The arguments must not contain spaces, but they may be separated by an arbitrary number of spaces. If no doubts can arise, the arguments need not be separated by any space (for example, when one of the arguments is a delimiter). The following notation is used when describing the structure of the commands: | = or (separates terms in a list from which one and only one must be chosen); { } = groups terms together; [ ] = groups terms together and denotes that

the group is optional; and < > denotes that the enclosed tem is not used literally but is replaced by its appropriate value. The commands are divided into the following categories: (1) Commands for control flow; (2) commands to handle the symbol table; (3) commands for graphics; (4) commands for scratch pad; (5) miscellaneous commands; and (6) original INTRAC commands. In addition to these commands, there are a number of "macros" written to make the interaction easier. A macro is a text file stored on mass storage containing a sequence of commands. The macro can be used as a new command and the sequence of the commands will be executed. Some of the more useful macros are also described.

The HALT command has the following structure: HALT <breakpoint> <condition>, in which <breakpoint> is the name of the breakpoint where the condition is to be set, and <condition> can be ALWAYS, NEVER, or an IF-clause followed by ALWAYS or NEVER. The IF-clause is used to change the condition dynamically. For example, the command HALT ARMIJO IF ITER> 3 ALWAYS, sets the condition of the breakpoint ARMIJO to ALWAYS if the number of iterations in the Armijo step is larger than 3.

A number of other commands are available for the control of flow of INTEROPTDYN. For the sake of brevity, we shall not describe them here.

The variables in the symbol table of INTEROPTDYN can be changed by using the following commands:

1. The SET command has the following structure: SET<variable> = <argument>, in which <argument> can be either <variable> or <number>.
2. The SETDIM command changes the dimension of a variable in the symbol table. Its syntax is SETDIM{ncol|nrow} (<variable>) = <argument>, where <ncol> and <nrow> are, respectively, the column and the row dimension of the variable.

The graphics commands of INTRAC-C can be grouped in two parts:

1. Low level primitives for vector generation, initialization, terminal control, text output, positioning, and windowing.
2. High level display functions.

These commands can be executed on the following graphics interactive terminals: Tektronix 4027, Ramtek Micrographics, and HP 2648. The first two terminals are color graphics terminals. About 15 low level primitives are available. For the sake of brevity, we are going to examine only one of these; the VECTOR command. It is used to draw a vector between two points. Its syntax is:

VECTOR <$x1$><$y1$><$x2$><$y2$>

in which <$x1$> and <$x2$> are the x-coordinates of the two points and <$y1$> and <$y2$> are the y-coordinates of the two points.

Two high level display commands are available; a CURVE and a BAR command. Both commands have the same syntax. The syntax of the commands is

<command><array><$y$min><$y$max>[<topcolor>] [<botcolor><threshold>]

in which <array> contains the name of the array carrying the information

to be displayed, <*y*min> and <*y*max> are used for the *y*-axis scaling, the optional <topcolor> specifies the color to be used in the output if the second option is not used. If the optional <botcolor> is given, then a numeric <threshold> must follow. All entires in the <array> above the <threshold> will appear in the <topcolor> while all entries below the <threshold> will appear in the <botcolor>. The CURVE command plots all the entires in the <array>, while the BAR command produces a barchart.

In addition to the main symbol table, there is a second, or scratchpad symbol table, which is separate from the main symbol table. This is used for the results of the side computations. In order to protect the main symbol table, the scratch-pad commands can access both symbol tables, but can only alter values in the scratch-pad symbol table. The most interesting commands of the scratch pad are

1. PDIM: This command creates arrays in the symbol table. Its syntax is PDIM <array> [(<nrow>[:<ncol>])]<type> in which <array> is the name of the variable which is being created, <nrow> and <ncol> are the row dimension and the column dimension of the array which can be given optionally. If <nrow> and <ncol> are not given, then the variable being created is a scalar. If <ncol> is not given, then the variable being created is a column vector and so on. <type> indicates which type is to be attached to the variable. The scratch-pad set of commands accepts four types, namely, integer, real, double precision real, and complex.
2. PMAT: This command is used to perform mathematical operations on arrays. It takes two forms: (1) PMAT <array> = {<array><number>}<op><array>, in which the first <array> is the name of the array in which the result of the operation is stored; the second is the first operand; the third is the second operand; and <op> is one of the following matrix operations: * for multiplication; + for addition, and − for subtraction; (2) PMAT <array> = <func> <array>, in which <func> can be INV for inversion; TRANS for transposition; TRACE for trace; DET for determinant; or COND for condition number; and (3) PSCAL: This command is used to perform mathematical operations on the scalars. Its syntax is similar to PMAT except for the <array>, which now is replaced by <scalar>. The operations available are the functions allowed in FORTRAN.

Finally, the last component of the system is a set of macros written in the INTRAC-C language and have been found to be sufficiently useful to warrant depositing them in our library. These macros can be divided into three groups:

1. Macros that manage the execution of the optimization algorithm.
2. Macros that implement high level display functions.
3. Macros that make the use of the scratch-pad feature easier.

The main macro of the first set is called RUN. This macro enables the execution of a specified number of overall iterations of the optimization algorithm. Its syntax is RUN <nitn> [<display>], in which nitn is an integer indicating the number of iterations one wants to perform and <display> is the name of the macro which can be coupled to RUN. This macro will be executed at each iteration of the overall algorithm. The program will stop after the number

of iterations specified has been reached (of course, the program may stop before if the optimal design is reached). When the program stops, the macro displays on the screen a set of questions indicating to the user possible changes of algorithm parameters before running more iterations. It is very useful to combine RUN with a display macro which prints or displays graphically the values of the cost and of the constraints while the computation is progressing. In fact, on the basis of the information displayed on the screen, the designer may decide to suspend the execution of the macro RUN and to perform side computations or change the values of a few parameters via the SET command.

Several macros are available which implement high level display functions. For example, the macro GRAPH is used to plot the values of an array. Its syntax is GRAPH<array><color><mark> [<index1><index2>] in which <array> is the name of the column vector whose entries have to be plotted, <color> is the name of the color to be used when plotting the array and <mark> can assume either the value yes or no. In the first case, the points of the graph corresponding to the entries of the array are marked with a small asterisk. The optional <index1> and <index2> are used to plot only a subset of entries

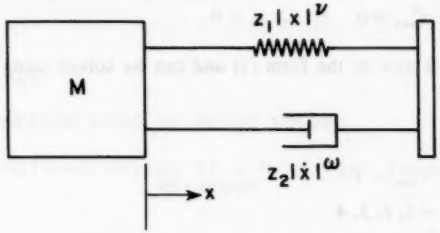

FIG. 2.—Nonlinear Impact Absorber

of the array, namely the ones between the elements with index equal to index1 and with index equal to index2. The macro computes the scale factors to fit the curve in a given window on the screen and it clips out the subarray defined by the indices. Thus, the option can be used to zoom in on a part of the graph which looks particularly interesting to the designer.

Example Problem.—As an example, optimal design of a nonlinear single degree of freedom impact absorber is presented. The problem has been used in the literature for comparing different algorithms (5). The system, shown in Fig. 2, has a fixed mass, M, and two design variables, z_1 and z_2, that represent spring and damper coefficients, respectively. The exponents ν and ω are held fixed for each design.

The system impacts a fixed barrier at time $t = o$, so the equations of motion are

$$M\ddot{x}(z,t) + z_2|\dot{x}(z,t)|^{\omega}\, sgn(\dot{x}(z,t)) + z_1|x(z,t)|^{\nu}\, sgn(x(z,t)) = 0$$

$$x(z,o) = 0; \quad \dot{x}(z,o) = V \qquad (10)$$

The objective is to minimize the maximum acceleration of the mass, i.e.,

$$\min_{z} \max_{t \in T} \left[\frac{1}{M^2} \{ z_2 |\dot{x}(\mathbf{z}, t)|^{\omega} sgn(\dot{x}(\mathbf{z}, t)) + z_1 |x(\mathbf{z}, t)|^{\nu} sgn(x(\mathbf{z}, t)) \}^2 \right] \quad . \quad . \quad . \quad (11)$$

A constraint on extreme displacement is imposed as:

$$\max_{t \in T} [x(\mathbf{z}, t)]^2 \leq [x_{\max}]^2 \quad . \quad . \quad .

APPENDIX I

```
% structure

          Optimization Based Computer-Aided Design Group
                University of California
                  Berkeley, California
                      U. S. A.

                    INTRAC-OPTDYN
          An Interactive Optimization Program for
          Design Problems Which can be Expressed as

                        Minimize  f (z)
                           z
          subject to
                         max  phi(z,t) <= 0
                          t
                              g(z)     <= 0
 Select problem: (1 to  4):
  1: pid
  2: pile1
  3: pile2
  4: svd.gust
 >
          DESIGN PROBLEM BEING SOLVED:

          Optimal Design of a Nonlinear Impact
                        Absorber



          DESCRIPTION:
              A mass "m" travelling at a velocity V
          hits the impact absorber which consists
          of a nonlinear spring and a dashpot. The
          design problem consists of choosing
          parameters of the spring and the dashpot
          so as to minimize the maximum acceleration
          of the mass.

          Design Variables:
             z(1) = spring coefficient
             z(2) = dashpot coefficient
             z(3) = dummy cost variable

          Cost Function:
               f  = z(3)
          Functional Constraints:
             phi(1,t)  = mass acceleration - z(3)
             phi(2,t)  = mass displacement - 1.0
          Conventional Constraints:
             g(1),g(2),g(3) = positivity constraints
                              on design variables
             g(4)           = constraint on acceleration
                              of mass at impact.
```

```
>
>INFPSIZG
type the number of iterations you intend to carry out
  #30
enter terminal type (2=4027 3=RAMTEK 4=HP):
4
>INITSTR
do you wish to use the default values e = .2, oldstp = 1. ?
  #YES
do you wish to use the default values z(1) = z(2) = .001 ?
  #NO
type in z(1)
  #.1
type in z(2)
  #.1
do you wish to use the default values:

    mass sm = 1.
    nonlinearity coefficient nu = 2.
    nonlinearity coefficient iomega = 1.
    initial velocity V0 = 1.
    bound on initial acceleration accmax = 1.
    bound on total displacement y1max = 1.

  #YES
>RUN 20 STORE
RESTART STEP2
The results of the entire computation will be stored
in the arrays FG PSIG and ZG(N:K).
Please state the total number of iterations you intend to
carry out: type in K = ?
    #30
I = 1  F = 0.469954  PSI = 3.64429  THETA = 0.  E = 0.2
I = 2  F = 0.469954  PSI = 0.678503  THETA = -0.208241  E = 0.2
I = 3  F = 2.13662  PSI = 0.  THETA = -0.12874  E = 0.2
I = 4  F = 1.54119  PSI = 0.  THETA = -0.297716  E = 0.2
I = 5  F = 1.24119  PSI = 0.  THETA = -0.5  E = 0.2
I = 6  F = 0.704518  PSI = 0.  THETA = -0.268336  E = 0.2
I = 7  F = 0.677518  PSI = 0.  THETA = -0.5  E = 0.2
I = 8  F = 0.666542  PSI = 0.  THETA = -0.00548789  E = 0.2
I = 9  F = 0.636424  PSI = 0.  THETA = -0.0501963  E = 0.2
I = 10  F = 0.627868  PSI = 0.  THETA = -0.00427787  E = 0.1
I = 11  F = 0.613105  PSI = 0.  THETA = -0.273402  E = 0.1
I = 12  F = 0.602385  PSI = 0.  THETA = -0.00535964  E = 0.1
I = 13  F = 0.592637  PSI = 0.  THETA = -0.0541579  E = 0.1
I = 14  F = 0.58223  PSI = 0.  THETA = -0.0578179  E = 0.1
I = 15  F = 0.577522  PSI = 0.  THETA = -0.00784567  E = 0.05
I = 16  F = 0.569422  PSI = 0.  THETA = -0.5  E = 0.05
I = 17  F = 0.565502  PSI = 0.  THETA = -0.241992  E = 0.05
I = 18  F = 0.562441  PSI = 0.  THETA = -0.00510146  E = 0.05
I = 19  F = 0.549251  PSI = 0.  THETA = -0.244256  E = 0.05
I = 20  F = 0.547923  PSI = 0.  THETA = -0.00738024  E = 0.025
Execution suspended at the end of STEP2
You may want to modify
 1. the current design vector Z
 2. the smear parameter E
>
>GRAPHF N
```

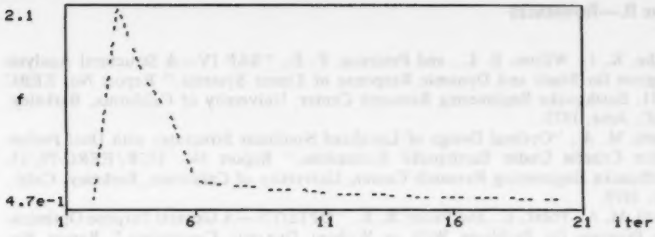


```
>GRAPHPSI N
```

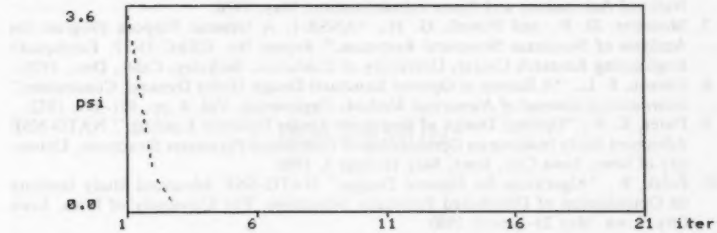


```
>ERASE
>GRAPHF N

 >LNFG 3
>RATE LNFG
rate = 0.659111
>PLT LNFG GREEN N

 >LBL LNFG GREEN 2
  #LNF
```

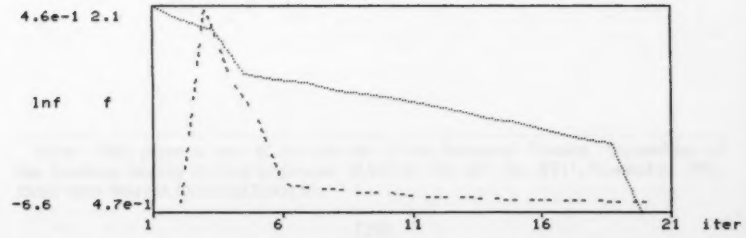

Appendix II.—References

1. Bathe, K. J., Wilson, E. L., and Peterson, F. E., "SAP IV—A Structural Analysis Program for Static and Dynamic Response of Linear Systems," Report No. EERC 73-11, Earthquake Engineering Research Center, University of California, Berkeley, Calif., June, 1973.
2. Bhatti, M. A., "Optimal Design of Localized Nonlinear Structures with Dual Performance Criteria Under Earthquake Excitations," Report No. UCB/EERC-79/15, Earthquake Engineering Research Center, University of California, Berkeley, Calif., July, 1979.
3. Bhatti, M. A., Polak, E., and Pister, K. S., "OPTDYN—A General Purpose Optimization Program for Problems With or Without Dynamic Constraints," Report No. UCB/EERC-79/16, Earthquake Engineering Research Center, University of California, Berkeley, Calif., July, 1979.
4. Gonzaga, G., Polak, E., and Trahan, R., "An Improved Algorithm for a Class of Optimization Problems with Functional Inequality Constraints," Electronics Research Laboratory, Memo No. UCB/ERL-M78/56, University of California, Berkeley, Calif., 1978.
5. Haug, E. J., and Arora, J. S., *Applied Optimal Design: Mechanical and Structural Systems*, John Wiley and Sons, Inc., New York, N.Y., 1979.
6. Miura, H., and Schmit, L. A., Jr., "ACCESS-1, Approximation Concepts for Efficient Structural Synthesis—Program Documentation and User's Guide," NASA CR-144905, National Aeronautics and Space Administration, May, 1976.
7. Mondkar, D. P., and Powell, G. H., "ANSR-1, A General Purpose Program for Analysis of Nonlinear Structural Response," Report No. EERC 75-37, Earthquake Engineering Research Center, University of California, Berkeley, Calif., Dec., 1975.
8. Pierson, B. L., "A Survey of Optimal Structural Design Under Dynamic Constraints," *International Journal of Numerical Methods Engineering*, Vol. 4, pp. 491–499, 1972.
9. Pister, K. S., "Optimal Design of Structures Under Dyanmic Loading," NATO-NSF Advanced Study Institute on Optimization of Distributed Parameter Structures, University of Iowa, Iowa City, Iowa, May 21–June 4, 1980.
10. Polak, E., "Algorithms for Optimal Design," NATO-NSF Advanced Study Institute on Optimization of Distributed Parameter Structures, The University of Iowa, Iowa City, Iowa, May 21–June 4, 1980.
11. Prager, W., and Sheu, C., "Recent Developments in Optimal Structural Design," *Applied Mechanics Reviews*, Oct., 1968.
12. Rangacharyulu, M. A. V., and Donc, G. T. S., "A Survey of Structural Optimization Under Dynamic Constraints," *Shock and Vibration Digest*, Vol. 11, No. 12, Dec., 1979.
13. Venkayya, V. B., "Structural Optimization: A Review and Some Recommendations," *International Journal of Numerical Methods Engineering*, Vol. 13, pp. 203–228, 1978.
14. Wieslander, J., and Elmquist, H., "INTRAC—A Communication Module for Interactive Programs," Department of Automatic Control, Memo LUTFD2/(TFRT-3149)/1-060/(1978), Lund Institute of Technology, Lund, Sweden, Aug., 1978.

DISCUSSION

Note.—This paper is part of the Journal of the Structural Division, Proceedings of the American Society of Civil Engineers, ©ASCE, Vol. 107, No. ST11, November, 1981. ISSN 0044-8001/81/0011-2287/$01.00.

Discussions

Discussions may be submitted on any Proceedings paper or technical note published in any *Journal* or on any paper presented at any Specialty Conference or other meeting, the *Proceedings* of which have been published by ASCE. Discussion of a paper/technical note is open to anyone who has significant comments or questions regarding the content of the paper/technical note. Discussions are accepted for a period of 4 months following the date of publication of a paper/technical note and they should be sent to the Manager of Technical and Professional Publications, ASCE, 345 East 47th Street, New York, N.Y. 10017. The discussion period may be extended by a written request from a discusser.

The original and three copies of the Discussion should be submitted on 8-1/2-in. (220-mm) by 11-in. (280-mm) white bond paper, typed double-spaced with wide margins. The length of a Discussion is restricted to two *Journal* pages (about four typewritten double-spaced pages of manuscript including figures and tables); the editors will delete matter extraneous to the subject under discussion. If a Discussion is over two pages long it will be returned for shortening. All Discussions will be reviewed by the editors and the Division's or Council's Publications Committees. In some cases, Discussions will be returned to discussers for rewriting, or they may be encouraged to submit a paper or technical note rather than a Discussion.

Standards for Discussions are the same as those for Proceedings Papers. A Discussion is subject to rejection if it contains matter readily found elsewhere, advocates special interests, is carelessly prepared, controverts established fact, is purely speculative, introduces personalities, or is foreign to the purposes of the Society. All Discussions should be written in the third person, and the discusser should use the term "the writer" when referring to himself. The author of the original paper/technical note is referred to as "the author."

Discussions have a specific format. The title of the original paper/technical note appears at the top of the first page with a superscript that corresponds to a footnote indicating the month, year, author(s), and number of the original paper/technical note. The discusser's full name should be indicated below the title (see Discussions herein as an example) together with his ASCE membership grade (if applicable).

The discusser's title, company affiliation, and business address should appear on the first page of the manuscript, along with the *Proceedings* paper number of the original paper/technical note, the date and name of the *Journal* in which it appeared, and the original author's name.

Note that the discusser's identification footnote should follow consecutively from the original paper/technical note. If the paper/technical note under discussion contained footnote numbers 1 and 2, the first Discussion would begin with footnote 3, and subsequent Discussions would continue in sequence.

Figures supplied by the discusser should be designated by letters, starting with A. This also applies separately to tables and references. In referring to a figure, table, or reference that appeared in the original paper/technical note use the same number used in the original.

It is suggested that potential discussers request a copy of the *ASCE Authors' Guide to the Publications of ASCE* for more detailed information on preparation and submission of manuscripts.

Parametric Investigation of Vibrating Cable Networks[a]

Closure by Louis F. Geschwindner,[4] and Harry H. West,[5] Members, ASCE

The writers think that the single discusser has missed the thrust of the paper. He suggests that the paper involved a model study of a real structure; however, it was a parameter study of a real structure. Thus, most of the discusser's points are not in the context of the writers' presentation. Because of this misinterpretation, it is understandable that he would conclude that the writers were "confused." The writers, however, are certain that there is no confusion for those who understand the intent of their study.

Suspension Bridge Vibrations: Computed and Measured[b]

Discussion by Robert H. Scanlan,[7] M. ASCE

The paper mentions the problems its authors encountered getting calculated bridge frequencies to agree with those observed in the field. This may reflect failure of the theoretical models to represent the bridge correctly, particularly since simple bending, torsion and sway may not clearly decouple for a deck that arches. On the other hand, many existing computer codes can handle this problem routinely. As an example, the first 10 or 11 modes and frequencies of a model of the highly unusual Ruck-a-Chucky design (curved in plan), were correctly predicted using a version of the SAP program (8). In such cases general three-dimensional modes are exhibited, being defined, typically, by the two components of displacement of the local deck c.g. and the rotation about it.

Three-dimensional modes are thus well enough defined but might alternately be defined in terms of deck section rotations about "effective rotation centers." This does not imply, however, that there need be any analytical concern whatever for the "effective moment of inertia" of the deck sections about such centers, since the motional energy in each mode is already correctly accounted for by the local translations and rotations of the deck about local c.g.'s.

---

[a]March, 1979, by Louis F. Geschwindner and Harry H. West (Proc. Paper 14436).

[4]Asst. Prof. of Architectural Engrg., Pennsylvania State Univ., University Park, Pa.

[5]Assoc. Prof. of Civ. Engrg., Pennsylvania State Univ., University Park, Pa.

[b]May, 1979, by Peter G. Buckland, Roy Hooley, Brian D. Morgenstern, Johann H. Rainer, and Aegide M. van Selst (Proc. Paper 14557).

[7]Prof., Dept. of Civ. Engrg., Princeton Univ., Princeton, N.J. 08544.

Neither are such concerns in any way associated with what should be inferred from a section aerodynamic model. Such a model cannot truly represent the full bridge, even with an adjusted "effective moment of inertia." The model can only be indicative of gross instability tendencies and act as an analog computer of static and motional aerodynamic derivatives. But proper analytical exploitation of such section model results implies that a full-span aeroelastic model may not have to be resorted to at all (19,20,21,22).

Finally, as to damping: the motion-dependent aerodynamic coefficients show that vertical damping usually increases with wind velocity V, as suggested in the paper, although for certain bridges (such as the original Tacoma Narrows), it may act otherwise. However, torsional damping for many bridges does not continue to increase with increasing wind velocity, but instead exhibits a reversal in sign. Trends for certain bridges (of which number 6 is the original Lions' Gate) are shown in the accompanying figure, extracted from Ref. 19, where H_1^* is the vertical and A_2^* the torsional aerodynamic damping, plotted versus reduced velocity V/NB, N being a reference (torsional) frequency and B the deck width. The slowly-reversing character of the torsional aerodynamic damping of the Lions' Gate probably underlies much of the concern with the marginal aerodynamic performance of that bridge.

To sum up: The writer believes that analytical devices exist that can produce good agreement with full scale results, both for modal calculations and for overall bridge performance in wind. Section models offer the necessary link of aerodynamic data. On the other hand, full-bridge aeroelastic models, while expensive to build and to test, offer analog solutions to the entire problem as one unit.

In these considerations, we follow some illustrious predecessors. Writing in 1954 on the Tacoma Narrows care, Farquharson (23, Part IV, p. 11) stated:

> The full model used in the design of the new Tacoma Narrows Bridge was in continuous use from the beginning of 1943 through 1945 and was used for intermittent experimentation until 1950 . . . However, because the cost of even simple revisions on the 100 ft. long suspended structure was exceedingly high, it proved expedient to perform the bulk of the experimentation on section models.

Later (23, Part V., p. 11) he also stated:

> In the course of these tests, the outlines of a general method for predicting prototype behavior entirely from section model tests began to appear . . .

A quarter-century later, while we have made a number of forward steps, we are still working on the general problem.

The authors are to be commended for their particular helpful contributions, especially the all-too-rare field measurements.

APPENDIX.—REFERENCES

18. Godden, W. G., and Aslam, M., "Dynamic Model Studies of Ruck-a-Chucky Bridge," *Journal of the Structural Division*, ASCE, Vol. 104, No. ST12, Proc. Paper 14206, Dec., 1978, pp. 1827–1844.

19. Scanlan, R. H., and Tomko, J. J. "Airfoil and Bridge Deck Flutter Derivatives," *Journal of Engineering Mechanics*, ASCE, Vol. 97, No. EM6, Dec., 1971, Proc. Paper 8609, pp. 1717–1737.
20. Scanlan, R. H., "Recent Methods in the Application of Test Results to the Wind Design of Long, Suspended-Span Bridges," *Report No. FHWA-RD-75-115*, Federal Highway Administration Office, of Research and Development, U.S. Department of Transportation, Washington, D.C., 1975.
21. Scanlan, R. H., "The Action of Flexible Bridges Under Wind, I: Flutter Theory, 'II: Buffeting Theory," *Journal Sound and Vibration*, Vol. 60 (2), 1978.
22. Scanlan, R. H., "State-of-the-Art Methods for Calculating Flutter, Vortex-Induced, and Buffeting Response of Bridge Structures," *Report 80-SM-27*, Dept. of Civil Engineering, Princeton University, for FHWA, U.S. Department of Transportation, May, 1980 (To appear as FHWA Report).
23. Farquharson, F. B., ed., *Aerodynamic Stability of Suspension Bridges*, Univ. of Washington Experiment Station, *Bulletin No. 116*, Parts I–V, Univ. of Washington Experiment Station, June 1949–1954.

Aerodynamic Response of Long H-Sections[a]

Errata

The following correction should be made to the discussion by Gronquist (June 1981):

Page 1143, second paragraph, last line: Should read "span of 1,644 ft (501.2 m)" instead of "1,664 ft. (501.2 m)."

Dome Effect in RC Slabs: Elastic-Plastic Analysis[b]

Closure by Mikael W. Braestrup,[4] and C. T. Morley[5]

The writers would like to express their appreciation of Chattopadhyay's interest in the paper.

[a]January, 1980, by Francis J. Maher and Larry E. Wittig (Proc. Paper 15105).
[4]Consultant, Steinman Boynton Gronguist & Birdsall, 50 Broad Street, New York, N.Y. 10004.
[b]June, 1980, by Mikael W. Braestrup and C. T. Morley (Proc. Paper 15502).
[4]Civ. Engr., Dept. of Struct. Engrg., Tech Univ. of Denmark, Copenhagen, Denmark.
[5]Lect., Engrg. Dept., Cambridge Univ., Cambridge, England.

The anomalous 'zero deflection at maximum load' disappears as soon as one modifies a rigid-plastic approach (by deformation or flow theory) by introducing elasticity of any sort. Both the deformation and flow theories of plasticity imply a rectangular stress block, the main difference lying in the treatment of unloading, thus affecting the size of the block at a given deflection. Of course it is correct that, because of the different behavior of concrete in tension and compression, which affects the levels of the neutral axes in pure flexure, dome action starts as soon as the concrete cracks, when the compression concrete will still be in the elastic range. Thus a better description of the rising part of the load-deflection curve would be obtained by a more complex analysis using a stress distribution which is initially triangular. This was done for the slab strip by McDowell, McKee and Sevin (11, Ref. 30 of the companion paper), but is outside the scope of the paper, which was primarily concerned with the peak load: this seems to be adequately predicted by the modified flow theory described.

The deflection at the Johansen load might indeed be expected to depend on the stiffness of the edge beam—though Fig. 1 shows little significant effect in the experiments except in the test without an edge beam ($\phi \rightarrow \infty$). A more sophisticated analysis of this effect would be useful, though the authors suspect that this might best be done using elastic bending theory for a cracked concrete section (with dome action) rather than by the simultaneous use of Eqs. 24 and 25 which were intended as alternatives. There is little we can usefully add in a short closure to the description of the test rig given halfway down p. 1260. The ring beam was 100 sq mm in section, and was cast integrally with the slab: it was reinforced by up to five circular reinforcing bars of varying size to produce different values of ϕ. The center of the ring beam was level with the middle of the compression zone in the plastic hinge over the support. The test specimens did not include one with no reinforcement, but we would expect the theory to be reasonably adequate in this case, for which Eq. 25 gives $\alpha = 0.5 + \phi/4$.

Appendix.—Reference

11. McDowell, E. L., McKee, K. E., and Sevin, E., "Arching Action Theory of Masonry Walls," *Journal of the Structural Division*, ASCE, Vol. 82, No. ST2, Proc. Paper 913, Mar., 1956, pp. 915-1–915-18.

Concrete Reinforcing Net: Safe Design[a]

Closure by Zdeněk P. Bažant,[5] F. ASCE, Tatsuya Tsubaki,[6] and Ted B. Belytschko,[7] M. ASCE

Marti's perspicacious analysis provides valuable deeper insight and is deeply appreciated by the writers. They basically agree with Marti and would question only a few minor points.

Although under some restrictions the plasticity theory based on Coulomb yield criterion leads to equivalent results, as Marti observes, there are certain important differences in concept (as well as deformation kinematics). Marti's arguments about isotropy ignore the fact that a different premise can lead to the same result. It is not correct to say that requiring equilibrium for *any* crack direction implies material isotropy. This is a property which characterizes the material before any stresses are produced. In plastic analysis, the crack is produced by the collapse and is absent before collapse begins, hence isotropy. By contrast, the slip-free (frictional) limit design is based on the assumption of preexisting parallel cracking, i.e., cracks that exist *before* any stresses are produced; therefore anisotropy. The fact that the results of plasticity analysis happen to be equivalent (under certain restrictions) is due to the fact that only equilibrium conditions are used in both solutions (as stated on page 1905), and that (under proper assumptions) the yield surface of net-reinforced concrete is obtained by a rigid-body translation of the yield surface for plain concrete, as pointed out by Marti. However, significant differences arise when kinematics of the deformation at collapse and deformations prior to collapse are considered.

Marti's observation on the similarity of the results of Lampert and Thürlimann is quite interesting. This is however, only a similarity in the overall shape of the limit design envelope. As the numerical values, the optimum slip-free (frictional) design requires 17% heavier reinforcement than the solution of Lampert and Thürlimann shown by Marti in Fig. 5(*c*), provided that the tails of the limit design envelope are matched. Moreover, their limit design envelope has, contrary to ours, a discontinuous slope at points *E* and *F* [Fig. 5(*c*)].

In conclusion, a general philosophical comment is in order. The assumption of plasticity of concrete, albeit often useful, is in the writer's opinion basically unjustified, in fact preposterous if one considers strictly the experimentally determined stress-strain diagrams. Concrete is *not* plastic, except under very high confining pressures which do not exist in ordinary structures. Plasticity theory requires ductility. It does not allow decrease of stress immediately after

[a]September, 1980, by Zdeněk P. Bažant, Tatsuya Tsubaki, and Ted B. Belytschko (Proc. Paper 15705).

[5]Prof. of Civ. Engrg., Northwestern Univ., Evanston, Ill. 60201.

[6]Assistant Prof., Dept. of Civ. Engrg., Yokohama National University, 156 Tokiwadai, Hodogaya-Ku, Yokohama, Japan 240.

[7]Prof. of Civ. Engrg., Northwestern Univ., Evanston, Ill. 60201.

reaching the peak stress (strain-softening and brittle failure). The limit theorems of plasticity are invalid when internal friction is present (due to lack of normality). The fact that plasticity-based solutions often work is chance and luck, arising from various aspects that are extraneous to the line of argument in plasticity. In many cases, plasticity works because the model of concrete is unimportant, the plastic yield of steel being the cause of collapse. In our case, plasticity works because the equations resulting from it happen to coincide, as this discussion demonstrates, with those obtained from direct analysis of the actual behavior at collapse.

End Restraint and Column Stability[a]

Discussion by Tibor Tarnai[3]

The author has offered a survey of the current (and proposed) research on the stability of end restrained columns and has made mention (among other things), of a research project at Washington University on end restrained in-plane columns with out-of-straightness.

Although Ref. 4 is not available for the writer's review it seems very remarkable to him that, without assumptions with regard to the shape of the initial crookedness, using an effective length factor gives a lower bound for the maximum strength. This result of the preliminary studies (4) is very important since it is known that assuming the initial crookedness in a fixed form (e.g., in a sine half-wave on the effective length), the effective length concept based on the theory of elastic bifurcation can result in a value greater than the true maximum strength. It depends on whether the amplitude of the initial crookedness on the effective length is supposed to be a linear or quadratic function of the effective slenderness ratio, $\lambda = (KL)/r$, or the effective slenderness parameter, $\bar{\lambda} = (1/\pi)(\sqrt{\sigma_y/E})(KL/r)$. The error caused by the effective length concept may be nonconservative in the linear case for $K > 1$ and in the quadratic case for $K < 1$.

A research project similar to the one at Washington University, was started last year at the Hungarian Institute for Building Science (22). The aim of the research is to ascertain the effect of end restraint upon the maximum strength of initially imperfect columns and to discover what modifications are needed in order that the pinned-end column curves may be utilized for the design of end restrained columns.

In the preliminary investigation, the magnitude of the error caused by the effective length concept is studied. It is supposed that, in agreement with some specifications [e.g., with the Czechoslovakian, and indirectly, the Hungarian

[a]November, 1980, by Wai F. Chen (Proc. Paper 15796).

[3]Sr. Research Fellow, Hungarian Inst. for Building Science, Budapest, Dávid F.u.6., H-1113.

design codes (21)], the aforementioned amplitude is given in the form

$$a_0 = cj\bar{\lambda}^2 \quad \ldots \ldots \ldots

Nonlinear Creep Buckling of Reinforced Concrete Columns[a]

Discussion by Jostein Hellesland,[3] and James G. MacGregor,[4] F. ASCE

Introduction

The authors are to be complemented on their study of sustained loading effects on reinforced concrete columns. Some comments on some aspects of their paper might be in order.

The study presented by the authors incorporates one of the most complete creep laws yet used in analyses of this type. Such analyses may, apart from being used to establish information on the mechanics of behavior of columns subjected to sustained loading, be used to provide data to determine when simplifications in material laws may be warranted. This is of interest with regard to analyses of more complex structures, with regard to code regulations as well as with regard to interpretation of existing data obtained using simpler models. In this context it is of interest to know if the authors have carried out comparative studies to determine the degree to which the load carrying capacities of columns are affected by: (1) Creep adaptation (low stress creep nonlinearity); (2) strength and stiffness adaption (accelerated hardening only); and (3) accurate representation of strength degradation a high stress levels.

Decrease in Strength due to Sustained Loads

Following a literature review showing the beneficial effects of low and intermediate stress levels on strength, the authors state that:

> "based on these test data, Hellesland and Green (17) proposed empirical formulas for the decrease of strength due to sustained loads that are constant up to failure."

This interpretation is somewhat inaccurate and a clarification might be of value. First, the model in Ref. 17 is based on test data by Rüsch (31) that deals with detrimental effects of high sustained stress on strength rather than the data referred to by the authors. The beneficial effects at lower stress levels are discussed in Ref. 17 but not included in the formulation, as pointed out by the authors. The rather elegant and simple accelerated aging concept proposed by the authors could readily be incorporaed into the hydration part of the Hellesland and Green model, however.

---

[a]November, 1980, by Zdeněk P. Bažant and Tatsuya Tsubaki (Proc. Paper 15811).

[3]Visiting Research Assoc., Dept. of Civ. Engrg., Univ. of Alberta, Edmonton, Canada; on leave from Dr. Ing. A. Aas-Jakobsen, Structural Consulting Engineers, Oslo, Norway.

[4]Prof., Dept. of Civ. Engrg., Univ. of Alberta, Edmonton, Canada.

Second, and this is a minor point and probably only a question of terminology, the strength prediction model proposed in Ref. 17 can be used to predict strength changes under any arbitrary stress history, and not only for "sustained stresses that are constant up to failure." The model, which is based on empirical formula for the "constant stress failure envelope" and a hypothesis for the rate of change of strength with time at a given stress, appears to be one of the first attempts to model the gradual strength degradation at high stress levels, and can easily be incorporated into the type of analyses presented by the authors. Indeed, it has previously been used in a similar study (39,40).

Degrading Strength

In the authors' analysis the degrading effect of high stresses on the strength is taken into account by reducing the short time strength $f'_c(t)$, Eq. 17, to $0.8f'_c(t)$ for long time loading. However, if a column is subjected to a short time loading following a sustained load period, the nondegraded strength $f'_c(t)$ is again assigned to all compression layers constituting the various cross sections. Presumably this also applies to layers that reach the plastic range, defined by a stress equal to $0.8f'_c(t)$ (Fig. 3(*c*) of the original paper), during the sustained loading. If it is accepted that the reduction in sustained load strength is due to microcracking, it would seem that a more rational procedure would be to retain the degraded strength for these "plastic" layers in the subsequent short time loading analysis. For layers stressed below $0.8f'_c(t)$ during the sustained loading, the strength is not affected and therefore should not be reduced.

Creep Nonlinearity

The high-stress creep nonlinearity in the creep formulation is given basically as a function of the nominal stress level σ/f'_c, in which f'_c = the strength at initial loading. Would it not have been more correct to replace f'_c by the current strength, i.e., by $f'_c(t)$ and $0.8f'_c(t)$ in the elastic and plastic range, respectively?

Design Implications

The writers would also like to comment on the authors' comparison with the ACI Code (11) predictions. The column considered is hinged at both ends and has a slenderness of $L/D = 20$ and an initial imperfection (eccentricity) at midheight of $v_o/D = 0.01$. A square cross section with side $D = 5$ in. is, in order to simplify integration over the cross section, replaced by an idealized two-layer section, with half the concrete and steel area centered a distance $H = 1.443$ in. from the centroid (the value of $H = 2.887$ in. given by the authors appears to be wrong). Comparisons of ultimate loads according to the authors' analysis (P^*) and the ACI Code (P'_u) are given in Table 1, and indicate a difference of 100% for the short time loading case (live load only). This is not at all surprising for the small initial eccentricity ($v_o/D = 0.01$) used in the comparison, and also confirms findings by others that the ACI Code significantly underestimates ultimate load capacities for small eccentricities and large slenderness values (38). This is due, in part to the fact that the stiffness

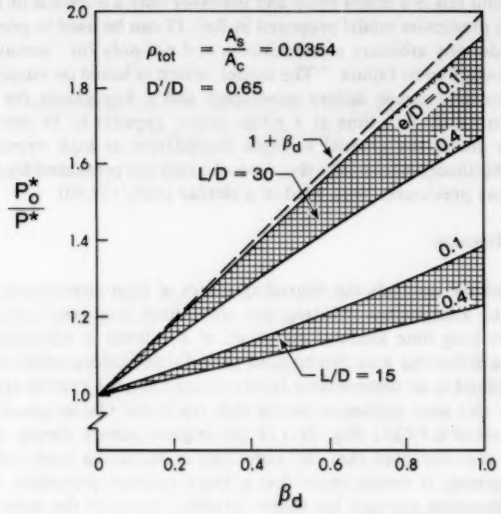

FIG. 11.—Effect of Combined Dead and Live Load on Load Capacity According to ACI 318-77

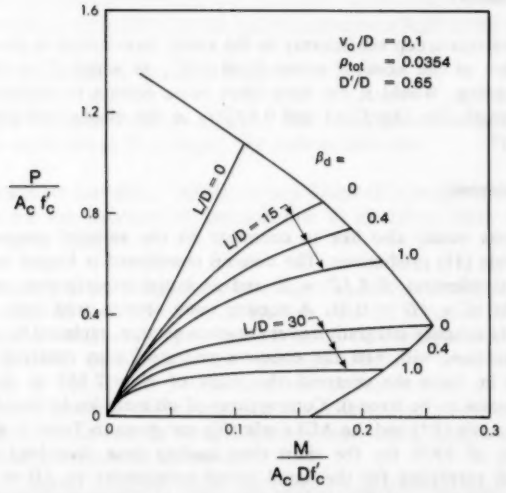

FIG. 12.—P-M Interaction on Diagram and Moment-Magnifier Results According to ACI 318-77

equations in the ACI Code (Eq. 10.9 and 10.10) were derived for columns with v_o/D ratios primarily in the range 0.1–0.4. It should be noted that the ACI Code specifies a minimum eccentricity, which for columns of practical size would be 0.05 D–0.08 D. At this range of eccentricities the effects of bending are significant.

The authors have also compared test results, showing the effect of sustained loading, with ACI Code predictions [Fig. 10(b)]. In this comparison it has been assumed that the ratio of ultimate load, P_0^*, under live load alone, to the ultimate load, P^*, under combined dead load and live load can be written $P_0^*/P^* = 1 + \beta_d$ according to the ACI Code. While this simplification would be warranted for small initial eccentricities and intermediate and large slenderness values, it becomes increasingly inaccurate with increasing eccentricity and decreasing slenderness as can be seen in Fig. 11. The load capacities used to plot Fig. 11 were obtained in the standard manner, from results such as those in Fig. 12, at the intersection between the P-M curve obtained using the ACI Moment Magnifier Equation 10-8, and the cross section P-M interaction diagram for a column similar to those tested by Drysdale and Huggins (13). The cross section considered was rectangular and symmetrically reinforced ($D'/D = 0.65$). Strengths and modulae were $f'_c = 4{,}600$ psi (31.7 MPa), $f_y = 59$ ksi (407 MPa), $E_c = 60{,}000\sqrt{f'_c}$ psi ($5{,}000\sqrt{f'_c}$ MPa), and $E_s = 29.10^6$ psi (200,000 MPa). For the test columns ($v_0/D = 0.2$ and $L/D \sim 30$), a similar study would show that the ratios P_0^*/P^* corresponding to the ACI Code would be up to 20% less than indicated in Fig. 10(b). As a result the dashed curve proposed by the authors would similarly need to be shifted downwards. Consequently, the authors' proposal would be unsafe for some β_d values for the hinged columns considered. This might be further augmented by the fact that the test results are obtained for relatively short load durations. Longer sustained load periods might, depending on the counteracting effects of continued concrete hardening and further creep deflections, cause larger reductions in load capacities.

It should be emphasized that the aforementioned discussion is based on the assumption made by the authors that the sustained loads in the test series are equal to the factored design dead load (1.4 D) as implied by the ACI Code. If instead, the sustained test load was considered equal to the unfactored dead load (1.0 D), as has been done in other studies (41,42), all test points in Fig. 10(b) would be shifted horizontally $0.4\beta_d$ to the right. Thus, the interpretation of the meaning of β_d when considering the sustained loads in tests or computer experiments has a significant effect on comparisons with code predictions.

APPENDIX.—REFERENCES

38. Drysdale, R. G., Sallam, S., and Tan, K. B., "Effects of Slenderness and Sustained Load on the Capacity of Reinforced Concrete Columns: An Analysis of Parameters," *IABSE Symposium on Design and Safety of Reinforced Concrete Compression Members*, Quebec, Canada, 1974, pp. 117–125.
39. Hellesland, J., and Green, R., "Strength Characteristics of Reinforced Concrete Columns under Sustained Loading," *IABSE Symposium on Design of Concrete Structures for Creep, Shrinkage and Temperature Changes*, Final Report, Madrid, Spain, 1970, pp. 209–217.
40. Hellesland, J., "A Study into the Sustained and Cyclic Load Behaviour of Reinforced Concrete Columns," thesis presented to the University of Waterloo, at Waterloo,

Ontario, Canada, in 1970, in partial fulfillment of the requirements for the degree of Doctor of Philosophy.
41. MacGregor, J. G., Oelhafen, U. H., and Hage, S. E., "A Re-Examination of the EI Value for Slender Columns," *Publication SP-50*, American Concrete Institute, 1975.
42. Oelhafen, U. H., "Accuracy of Simple Design Procedures for Concrete Columns," *IABSE Symposium on Design and Safety of Reinforced Concrete Compression Members*, Quebec, Canada, 1974, pp. 93–115.

Errata.—The following corrections should be made to the original paper:

Page 2237, Eq. 6: Should read "$\beta_\sigma = 1 + a_0 I_1(t)$" instead of "$\beta_\sigma = 1 - a_0 I_1(t)$"
Page 2243, line 2 from the bottom: Should read "$H = 1.443$ in. (36.66 mm)" instead of "$H = 2.887$ in. (73.33 mm)"
Page 2245, Paragraph 2, line 5: Should read "$H = e_s = 1.443$ in. (36.66 mm)" instead of "$H = e = 2.887$ in. (73.33 mm)"
Page 2245, Paragraph 2, line 16: Should read "$f_y = 40{,}000$ psi" instead of "$f_y = i40{,}000$ psi"
Page 2251, line 8: Should read "we then get" instead of "we than get"
Page 2257, Ref. 24: Should read "MacGregor" instead of "McGregor"

Closure by Zdeněk P. Bažant,[5] F. ASCE, and Tatsuya Tsubaki[6]

The comments of Hellesland and MacGregor are valuable and point out some useful further aspects of the problem. Various comparative studies of the effect of various parameters have been carried out, as reported in the paper. Simplified preliminary calculations indicated that the effects of creep adaptation at low stress, of strength and stiffness adaptation, and of strength degradation at high stress level are all important. No further comparative calculations beyond those reported in the paper could be run with the full model within the scope of this sponsored project.

The discussers are certainly right in pointing out that Hellesland's model (17) can be applied at variable stress, not just at constant stress, and that it accounts for the strength increase due to hydration. This model is based on the simplifying assumption that the rate of strength loss and the limiting long-time strength (for infinite load duration) are independent of the accumulated damage at previous stress levels, so that a simple superposition of the constant load effect can be used. It would actually be reasonable to consider the strength loss to be affected by the stress history, as mentioned also in Ref. 17.

The discussers are right that if the sustained stress is equal to $0.8 f'_c$, the degraded strength must be used for the subsequent short-time loading to failure. However, this case is not of much practical interest, since at sustained stress near $0.8 f'_c$ the lifetime of the column is rather short, generally about one week

[5]Prof. of Civ. Engrg., Northwestern Univ., Evanston, Ill. 60201.
[6]Asst. Prof. of Civ. Engrg., Yokohama National Univ., 156 Tokiwadai, Hodogaya-Ku, Yokohama, Japan 240; formerly, Postdoctoral Research Assoc., Dept. of Civ. Engrg., Northwestern Univ., Evanston, Ill. 60201.

(31), which is nearly the same as a short-time loading. The sustained stresses which were considered in the calculations were all well below $0.8f'_c$ and less than the stresses which cause microcracking, and for these the use of the nondegraded strength for the subsequent loading was proper. The cases of short-time loading subsequent to a sustained stress near $0.8f'_c$ give results rather close to those for pure sustained loading, and so there was no need to consider them in calculations.

The discussers suggest characterizing the high-stress nonlinearity as a function of $\sigma/f'_c(t)$. This, however, does not seem to be realistic, since concrete does not gain strength under high constant sustained stress [close to $f'_c(t)$]. It gains strength only at low sustained stresses at which there is no high-stress nonlinearity.

The writers were well aware that the ACI Code implies an excessively high safety factor if the eccentricity is small. No conclusions were, however, based on the actual values of the safety factor. The objective of the analysis was the relative difference in the safety factor between the cases of short-time loading and long-time loading. It was found that the safety margin of the ACI Code is not uniform; for some β_d it is higher than for the short-time loading while for the other β_d it is lower. These results may, however, also depend on the eccentricity and slenderness (v_0/D and L/D). Their values in the numerical examples were chosen in the range of available test results.

The meaning of β_d is not a matter of logical deductions but a matter of definition. For calculations as well as laboratory tests, the primary objective is to determine the failure load, which is set equal to the sum of design loads times their load factors. From the failure load β_d may then be evaluated according to its definition as stated on p. 2250. The definition implied in ACI Code was used in the paper. For other definitions the curve of β_d would obviously look different, although it would be equivalent in the practical sense. Discussers' considerations based on their Figs. 11 and 12 are interesting but rather crude, neglecting various effects considered in the paper. More realistic calculations would be desirable. The writers agree that it is possible, and certainly most likely, that the proposed β_d curve still does not provide a very uniform safety margin particularly when other cases are considered. According to the calculations and experimental comparisons in the paper, this curve does, however, provide a more uniform safety margin than the existing formula.

Research Needs in Stability of Metal Structures[a]

Discussion by S. Unnikrishna Pillai,[5] M. ASCE

The SSRC Committee on Research Priorities is to be commended for presenting a comprehensive survey of the immediate research needs in the area of Stability

[a] December, 1980, by Reidar Bjorhovde (Proc. Paper 15926).

[5] Prof. of Civ. Engrg., The Royal Military College of Canada, Kingston, Ontario, Canada.

of Metal Structures. This paper was one of the items of consideration of the SSRC Task Group 3—Columns with Biaxial Bending, at its annual meeting held in Chicago, April 6, 1981. The present discussion is concerned with biaxially loaded beam-columns and the intent is to present some recent research findings which provides at least partial answers to some of the problems raised in the paper.

For biaxially loaded columns, three areas were identified in the paper for further research. These are: (1) Validity of equivalent moment factor, c_m, for biaxially loadings; (2) assessment of the conservatism in using the weak axis column strength in the axial load term of interaction equations together with allowance for lateral-torsional buckling effect in the major axis bending strength; and (3) statistical evaluation of performance data in order to develop appropriate resistance factors for use in LRFD.

Results of 81 full scale tests on columns under biaxially eccentric loads causing unsymmetrical and reversed curvature bending in both planes were recently reported by Anslijn and Massonet (53). In these tests, the eccentricities about both axes ranged between 0 and 3 times the respective kern distance. The moment distribution along the length of the member was nonuniform in one or both planes of bending, with end moment ratios of -1, 0, 0.5, and 1. Slenderness ratios ranged between 40 and 100. In a recent report (54) to SSRC Task Group 3, the writer has compared these test results with both the linear interaction Eqs. 40 and 41 and the more precise exponential interaction equations (25). Using the C_m factors (sway prevented), the exponential equations resulted in an average ratio test capacity/predicted capacity of 1.001 with a coefficient of variation of 8.63%. This level of accuracy suggests that the equivalent moment factor, C_m, although developed for uniaxial bending, does lead to satisfactory prediction of capacity of biaxially loaded beam columns as well, for the sway-prevented case. Further, in these comparisons, the weak axis column strength was used in the axial load term in the interaction equation and a reduced moment capacity (allowing for lateral-torsional buckling effect) was used in the bending term, as is the present practice. Again the accuracy of predictions tends to dispel the suspicion that such a procedure is unduly conservative.

The results of the comparison, however, indicated that the linear interaction equation is conservative, with an average ratio test capacity/predicted capacity of 1.114 and a coefficient of variation of 9.8%. These differing accuracies of the two approaches (linear versus exponential interaction equations) emphasize the need to relate the resistance factors to the performance statistics in order to obtain consistent margins of safety.

Appendix.—References

53. Anslijn, R., and Massonet, C. E., "New Tests on Steel I Beam-Columns in Mild Steel, Subjected to Thrust and Biaxial Bending," Festschrift Otto Jungbluth—60 Jahre, Published by Dr. Keller, Lehrstuhl für Stahlbau, Technische Hochschule Darmstadt, Germany, 1978, pp. 103–123.
54. Pillai, S. U., "Comparison of Test Results with Design Equations for Biaxially Loaded Steel Beam Columns, *Civil Engineering Research Report No. CE80-2*, Report to SSRC Task Group 3, Royal Military College of Canada, Kingston, Ont., Canada, Aug., 1980, 57 p.

Discussion by Jacques Rondal[6]

The author is to be congratulated for his efforts to summarize all the points which need further research in the field of stability of metal structures.

The purpose of present discussion is restricted to the interaction between local and overall buckling in tubular columns. Since 1977 till 1979, the writer has conducted a theoretical and experimental research on this subject, with the financial aid of the ECSC (European Community of Steel and Coal) and the CIDECT (Comité International pour le Développement et l'Etude de la Construction Tubulaire) (55,56).

With 320 tested columns, this research is likely the most important one carried out at present time. The influence of manufacturing procedure of hollow sections and of the residual stresses has been taken into account for the choice of tubes which have been tested.

A theoretical method for predicting the limit load of the columns with thin walled hollow sections has been developed. The agreement between theoretical and experimental results is very good, in view of the level of difficulties encountered in this problem.

The suggested theoretical method is based on a modification of the European buckling curves; it leads to a complete analytical formulation of the design problem of columns with thin walled hollow sections.

Appendix.—References

55. Braham, M., Grimault, J. P., and Rondal, J., "Flambement des profils creux à parois minces. Cas des profils rectangulaires chargès axialement," Commission des Communautés Européennes, *Research 6210.SA/3/301*, Final Report, Nov., 1979.
56. Braham, M., Grimault, J. P., Massonnet, C., Mouty, J., and Rondal, J., "Buckling of Thin-Walled Hollow Sections. Cases of Axially Loaded Rectangular Sections," Acier-Stahl-Steel, Bruxelles, Belgium, Nov. 1, 1980.

Discussion by Donald R. Sherman,[7] F. ASCE

The paper identifies five topics of research needs related to tubular columns. These were identified by Task Group 18 of the SSRC in 1978 as topics encountered by practitioners but with little or conflicting guidance available. In compiling a list of current worldwide research, the TG was gratified to note that some work is underway in several of these areas. Hopefully, some guidance for design may be forthcoming even though certain questions may remain unanswered for several years.

In view of the current research, the TG has recently identified several other priority topics that should be considered in future research concerning the stability of tubular members.

---

[6]Asst. Prof., Univ. of Liège, Inst. du Genie Civil, Quai Banning 6, 4000 Liège, Belgium.
[7]Prof. of Civ. Engrg., Univ. of Wisconsin, Milwaukee, Wisc. 53201. (Chmn. SSRC Task Group 18.)

Inelastic Shear Buckling.—Most information on shear buckling of circular cylinders concerns the elastic buckling of very thin tubes in torsion. Test data and related theory on buckling of manufactured or fabricated tubes especially in thicknesses where shear buckling may be inelastic is lacking. It has also not been established if the same criteria can be applied for torsional loadings and flexural shear. Shear buckling of rectangular tubes is currently treated as a web buckling problem similar to a wide flange web. This approach has not been verified for torsional loadings which will be encountered with the increasing use of shaped tubes in complex structures.

Test Data on Fabricated Cylinders.—Much of the test data for cylinders under axial loads, flexure, pressure, and combinations thereof has used manufactured tubing and pipe with diameter/thickness ratios less than 100. These members have different stress-strain properties and residual stresses than cylinders fabricated by forming and welding plates of structural steels. The limited data currently available indicate that local buckling characteristics in particular may be different for fabricated and manufactured cylinders.

Alternatives to Stub Column Tests.—A significant difference in the column strengths of rectangular tubes is known to exist between hot formed and cold formed sections. Since the difference is related to residual stresses, it is possible to increase the strength of cold formed columns by providing a degree of stress relief to reduce the residual stresses closer to the levels in hot formed tubes. It is difficult, however, to determine if the desired reduction in residual stresses has been achieved. The most efficient method currently in use is to determine proportional limit in a stub column test. Unfortunately, the stub column is relatively expensive, time consuming and requires large capacity equipment. A simpler alternative procedure based on a bending test is theoretically possible but requires verification that it will provide a good correlation with the stub column.

Fabricate Cylinders with D/t up to 500.—In recent years, a large data base has been generated for cylinders with D/t less than 150 used in structural and pressure applications. Thin cylinders with D/t greater than 1,000 have also been studied for aerospace and tankage applications. Until recently, there has been little motivation to investigate the stability of cylinders in the intermediate range. However, the offshore industry is now interested in the D/t from 250–500 as they venture into deepwater concepts. It is essential to know the stability characteristics of members with the residual stress and tolerances of fabricated cylinders having the stress-strain properties of 36 ksi and 50 ksi (245 NPa and 341 NPa) yield strength steels.

Errors in Utilization of Cold-Formed Steel Members[a]

Discussion by Duane S. Ellifritt,[2] M. ASCE

It is unfortunate that the author quoted the failure statistics gathered by the Connecticut Engineers in Private Practice with no further breakdown of the categories. He reported that, of the failures of buildings built since 1960, "84% were either steel joist construction or manufactured metal buildings." It makes no sense at all to lump these two categories into one. Such statements tend to leave the reader with the impression that both steel joint construction and manufactured metal buildings are similar kinds of construction that represented equally serious problems in the winter of 1977–78 in Connecticut.

Furthermore, it is important to understad the difference between a "manufactured metal building" as used by the author and a "metal building system" as designed and sold by many reputable manufacturers.

Any building made of components manufactured from metal can be described as a "manufactured metal building." In fact, all of the examples shown in the author's paper were just such structures. From what information is available in the paper, however, it would appear that *none* of them are metal building systems. The fact that a designer makes use of Z purlins and metal deck does not make his building a metal building system. There is a vast difference in the design of a complete system as opposed to the design of individual parts.

After the publication of this paper, I contacted the Connecticut Engineers in Private Practice who supplied me with the information necessary to further breakdown the "84%" mentioned by the author. Here are th post-1960 failures as reported by structural type:

11	Steel Joist Construction
4	Metal Building Systems
3	Timber Construction
18	

It should be noted that several of the steel joist failures were reported as "noticeable deflections." Whether or not these should be considered failures is a debatable point. Also, one of the four metal building systems listed as a failure had its roof punctured by ice falling from a 910 ft tower nearby.

The behavior of the carport described in the paper would have surprised no one familiar with metal building system design. A flat roof not anchored at the ends with Z purlins all facing the same direction is a recipe for disaster that any engineer who understands the behavior of Z purlins and their interaction

[a]December, 1980, by Frank J. Zamecnik (Proc. Paper 15941).

[2]Dir. of Engrg. and Research, Metal Building Manufacturers Association, 1230 Keith Building, Cleveland, Ohio 44115.

with roofing material would immediately recognize. A shear diaphragm is worthless unless the in-plane force is taken out at the boundaries. Even a concrete slab would not have helped the carport in question if the edges were not anchored. This is not so much a failure to follow the AISI Specifications, as the author suggests, as it is a misunderstanding of the basic behavior of unsymmetrical cold-formed sections.

The AISI Cold-Formed Specification *does* have some catching up to do regarding this subject and the Specification Advisory Committee is hard at work trying to insure that the latest research will be incorporated in the future addenda to the Specifications as quickly as possible.

Discussion by Gilliam S. Harris,[3] F. ASCE

The author makes some good points regarding the misuse of cold-formed steel members. In his final example (warehouse facility) the author cites a building with "Z" shaped cold-formed steel purlins supporting a steel deck with built-up roof and tar and gravel surface. This is not the typical application of "Z" purlins in metal building systems. In such cases where relatively heavy dead loads are imposed on "Z" shaped purlins during construction, there is a tendency for the "Z" beams to progressively twist in response to the application of these building materials. Where adequate resistance to twist is not provided, the purlin is distorted to an unfavorable attitude for carrying its assigned load. For low sloped roofs the direction of twist is clockwise as indicated in the author's Fig. 18. Where proper provisions have been made to prevent this initial twist, purlins have been found to perform quite satisfactorily.

Referring to the comment section of the subject article it should be pointed out that considerable research has been devoted to studying the behavior of "Z" beams whose twist is inhibited by the attachment of metal panels by means of self-tapping screws. For many metal building configurations this system has been found to be quite effective in inhibiting torsional flexural buckling.

Much research on this subject has been done under the direction of Teoman Pekoz at Cornell University under the sponsorship of Metal Building Manufacturers Association and American Iron and Steel Institute. Pekoz has written a program which will evaluate the effect of panel attachment on torsional stresses in "Z" beams. Related to this is the "F" test which quantifies the torsional stiffness of "Z" beams due to its attachment to panels.

The author jumps to a rather conservative conclusion in his final paragraph of the comments by recommending the quarter point bridging in addition to restraint against rotation at supports. This requirement was never intended to apply to members attached to sheathing and this has been clarified in the 1980 Edition of the Specifications. This revision, along with the removal of the torsional restraint footnote, was not actually published until the issuance of the September, 1980 edition of the AISI Specification which was after the original data of the author's article (October 22, 1979).

Good results have been achieved by observing three basic requirements:

[3]Dir. of Engrg. and Research, American Buildings Co., Eufaula, Ala. 36027.

1. Adequate restraint against excessive twisting at the supports.
2. Sufficient torsional restraint provided by the panels and their attachment.
3. Proper inplane stiffness of the roof panels acting as a diaphragm properly supported at its boundaries.

Literally billions of square feet of buildings are in successful service in this country using metal panels mechanically fastened to cold-formed "Z" and channel members.

Proposed Specifications for Steel Box Girder Bridges[a]

Discussion by F. Tupula Yamba[2] and M. S. Troitsky[3]

It is encouraging that effort is being made to provide appropriate design rules for this type of bridges which is regarded as of great interest by bridge engineers. The authors are to be congratulated as the topic afforded is quite complex.

The writers would like to make comments on some points that seem to be not clear, but as the paper looks to be a short summary, the questions could have explanation in the original work.

1. The authors have insisted on the weakening effect of the initial geometrical imperfections of both plate and stiffeners, of the residual welding stresses and of some uncertainties. This weakening effect was discussed in Refs. 5 and 6 and by numerous papers dealing with the design of the compression flange of steel box girder bridges. However, in the proposed specifications, Fig. 4, it is not clear how those factors are accounted for. Are the factor λ_{col} and λ_{pl} based on the properties of the full cross sections, or on that of the effective sections accounting for the weakening factors as proposed in the secant stiffness method by Horne, et al. (11) and in the method by Chatterjee, et al. (8).

Although curves are the easiest means for design, it is interesting for design engineer to understand how the main factors are being considered, specially for such complex topic. Such understanding permit good estimation of the degree of conservatism. The strut method by Little (1) is theoretically complex, but in his paper one may understand how the weakening factors are accounted for, e.g., Little's Figs. 3–9.

2. The authors also recognize the effect of web and flange interaction on their respective strength. As this interaction is function of the rigidity of the connecting element at flange/web edge, it may be helpful if the design specifications may provide means of evaluating the required minimum rigidity, specially

[a]December, 1980, by Roman Wolchuk (Proc. Paper 15942).
[2]Ph.D. Student, Concordia Univ., Montreal, Quebec, Canada.
[3]Prof. and Chmn., Dept. Civ. Engrg., Concordia Univ., Montreal, Quebec, Canada.

for the tension field action (post-buckling behavior) to be considered effective in the web panels. it is true that mathematical formulation of the problem is too complex, but attempt could be made with test results.

As in the proposed criteria, the strength of the web is obtained independently of the flange properties, and also it is recognized that the tension field action is questionable in the case of steel box girder, it is clear that the doubt still exists in the proposed specifications and it is difficult to evaluate the level of conservatism.

3. It is interesting to note that the proposed specifications treat the problem of the required minimum rigidity for the web stiffeners to remain rigid and straight up to and after the buckling of web subpanels. Is the same treatment done for the compression flange stiffeners? As this was pointed out by Dubas (9,10) and Massonnet, et al. (12). Recent experimental tests conducted at Concordia University (15) on steel box girder bridge models have led to the conclusion that for the range of b/t ratios (45–56) and of stiffeners slenderness L/r ratios (5.9–8.3) tested, to remain rigid and straight up to and after the buckling of plate elements, the required optimum rigidity for longitudinal stiffeners is almost 3.5 times the minimum rigidity determined on the basis of classical elastic plate buckling theory (14), which theory is the basis of the present design critiera for the compression flange (13).

4. It is now well established, that for the design of the compression flange of steel box girder bridges, account should be made of the failure mode, plate or stiffener failure mode, as the ultimate strength may change completely depending on which mode initiate failure. This point was pointed out by several researchers including Little (1). Is this difference made in the proposed specifications? Tests conducted at Concordia University (14) have confirmed that the stiffener failure mode, initiated by the compression in the stiffener outstand is the most critical, the failure is abrupt and lower load is associated with it.

Appendix.—References

8. Chatterjee, S., Dowling, P. J., "The Design of Box Girder Compression Flanges," *Steel Plated Structures, An International Symposium*, Crosby Lockwood Staples, London, England, 1976.
9. Dubas, P., "Essais sur le comportement post-critique de poutres en caisson raidies," *Seminar of International Association for Bridges and Structural Engineers*, London, England, 1971, pp. 367–379.
10. Dubas, P., "Plated Structures with Closed-Section Stiffeners," *Steel Plated Structures, An International Symposium*, Crosby Lockwood Staples, London, England, 1976.
11. Horne, M. R., Narajanan, R., "Design of Axially Loaded Stiffened Plates," *Journal of the Structural Division*, ASCE, Vol. 103, No. ST11, Proc. Paper 13344, Nov., 1977, pp. 2243–2257.
12. Massonnet C., Maquoi, R., "Discussion of the Report by P. Dubas," *Seminar of IABSE*, London, England, 1971, pp. 381–389.
13. "Standard Specifications for Highway Bridges," The American Association of State Highway Officials, 11th ed., 1973.
14. Timoshenko, S. P., Gere, J. M., "Theory of Elastic Stability," 2nd ed., McGraw-Hill Publishing Co., Inc., New York, N.Y., 1961.
15. Tupula Yamba, F., "Buckling Behaviour of Steel Box Girder Bridges," *Reports No. 5, No. 6 and No. 7, Experimental Investigation*, Department of Civil Engineering, Concordia University, Montreal, Canada, June, 1980.

Impact of Solid Missiles on Concrete Barriers[a]

Discussion by Achintya Haldar,[2] M. ASCE

The author is to be congratulated for his work in addressing the difficult problem of missle impact on concrete barriers. The subject is very complicated and a complete theoretical treatment of the problem is not yet available. The author attempted to develop the theory in a crude and sometimes unjustified way, then tried to fit the relationship thus produced with the experimental results presently available using the Bayesian approach. Even in this type of semianalytical formulation, some basic and important areas need to be addressed properly.

In developing the model, the author assumed that the strain energy can be estimated by considering a circle of radius r_u (Eq. 11). This is not a valid assumption. It has been observed in many experiments that cracks will be developed in the vicinity of the impact area in all directions (11). The strain energy needs to be calculated by considering an area, definitely not along the periphery of a circle. The ultimate result (Eqs. 15 and 16) may not be influenced by this assumption, but the aforementioned formulation is not correct.

The scabbing and perforation thicknesses (Eqs. 17 and 25) are developed while completely ignoring the effect of missile penetration in the target. Impact formulation for concrete structures without considering the penetration depth may not be adequate. To emphasize this statement, the penetration depths according to the NDRC equations and the impact areas for a given impact energy are plotted in Fig. 7. The penetration depth decreases as the impact area increases. This is expected. However, even when the impact area is large, i.e., 140 sq in. (9,030 sq mm), the penetration depth for the given example is about 6.99 in. (177.5 mm), which is not negligible.

In the Bayesian analysis section, a normal variable Y is introduced. The author assumed Y to be normal because "The chance that all worst conditions or all favorable conditions for the impact take place at the same time is small." This reasoning is not adequate according to this writer. The normal variable Y is a function of the product and division of three other random variables C_1, C_2, and C_3. When C_1, C_2, and C_3 are independent lognormal variables, Y can be assumed as lognormal but not normal. The question of whether Y can take any value less than zero needs to be addressed. It appears that a lognormal distribution of Y may be a better choice. However, this will create problems for the Bayesian approach.

The author estimated the prior mean and variance for Y, i.e., $E(\mu) = 1.8$ and $E(\sigma^2) = 0.04$ without mentioning how many sample points he used in these estimations. However, the author updated the information by considering 8 additional sample points. The updated statistics of Y are found to be $E(\mu)$

[a]February, 1981, by Wen S. Chang (Proc. Paper 16031).
[2]Asst. Prof., School of Civ. Engrg., Georgia Inst. of Tech., Atlanta, Ga. 30332.

= 1.84 and $E(\sigma^2) = 0.0348$. These improvements are not significant in light of the uncertainty associated with them. The author failed to mention why he updated information using old and nonrepresentative information (e.g., small diameter missiles). The basic purpose of the Bayesian updating approach is updating old information using more recent and appropriate information available on the subject.

In Fig. 6, the author compared the proposed equations for scabbing and perforation thicknesses with the NDRC equations and commented that the author's proposed SAF relationships are considerably better than the NDRC equations. The comparison is not adequate. The penetration depth x and the scabbing thickness s according to the NDRC equations along with mean; mean $+\sigma$, mean $+2\sigma$, and mean $+3\sigma$ values of the proposed relationship (Eq. 17) are plotted in Fig. 7. As mentioned earlier, the penetration depth according

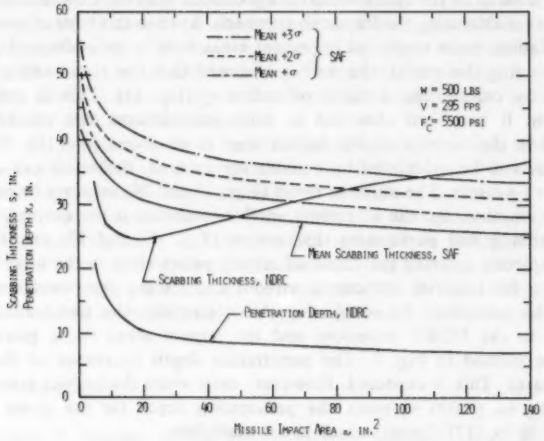

FIG. 7.—Comparison Between NDRC and SAF Equations

to the NDRC equations decreases as the diameter of the missile increases, as expected. It is also clear from Eqs. 43 and 45 that the scabbing thickness increases as the penetration depth increases. However, the diameter of the missile plays a very important role in those equations. This is completely overlooked by the author. The writer (14) observed that the NDRC equations indicate the upper bound estimate of the penetration depth. However, in Fig. 6, the mean SAF relationship is compared to the NDRC equations. By doing this, does the author imply that the NDRC equations also give the mean scabbing thickness? To the best of this writer's knowledge, the NDRC equations have never been shown to predict the mean spallation thickness. In this sense, the comparison made in Fig. 6 is meaningless. The point is amplified in Fig. 7.

It would also be very helpful if the units of parameters in Eqs. 17 and 25 were given properly. They are not similar to the NDRC equations.

APPENDIX.—REFERENCE

14. Haldar, A., "Turbine Missile—A Critical Review," *Journal of Nuclear Engineering and Design*, Vol. 55, No. 3, Nov., 1979, pp. 293–304.

RESPONSE OF REINFORCED CONCRETE SHEAR WALL UNDER GROUND MOTIONS[a]

Discussion by Catherine E. Wolfgram[5]

The authors have utilized a plane stress finite element approach to determine the nonlinear response of a RC shear wall subject to ground motions.

They indicate that this procedure should be used in lieu of the "modified EI" approach (11,12,14,16,26) in cases where backbend is induced in the walls. (The "modified EI" approach is not defined in the paper.) The writer thinks that the authors do not present sufficient justification for the use of their finite

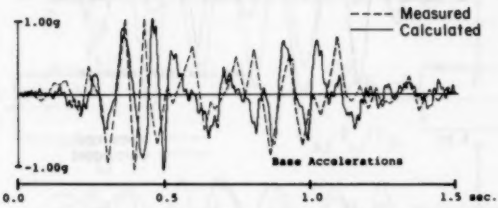

FIG. 11.—Base Acceleration used in Analytical Model vs. Base Acceleration Measured Experimentally

element method in place of the modified stiffness procedures. More complicated analyses do not always lead to better results.

The writer also wishes to address a problem with the numerical example in the paper. The authors intended to justify their procedure by comparing it with experimental results and calculations employing a modified stiffness approach.

A comparison of the response histories in the paper with those determined experimentally (14) appears to indicate that there is no correlation whatsoever. (See Figs. 11 and 12.) The root of this problem lies in the fact that the authors used different input base motions than the experimental model; although the maximum values they used were the same.

[a]February, 1981, by A. B. Agrawal, L. G. Jaeger, and A. A. Mufti (Proc. Paper 16061).

[5]Grad. Research Asst., Civ. Engrg. Dept., Univ. of Illinois, Urbana, Ill. 61801.

If the authors were interested only in the maximum responsae, there is no need for the detailed response histories.

An apparent inconsistency in the report is found in the conclusion. The authors suggest that their model could be enhanced by refining the value of the shear factor. However, no more than three paragraphs before this statement, they concluded that the actual value of the shear factor did not have much effect on the solution.

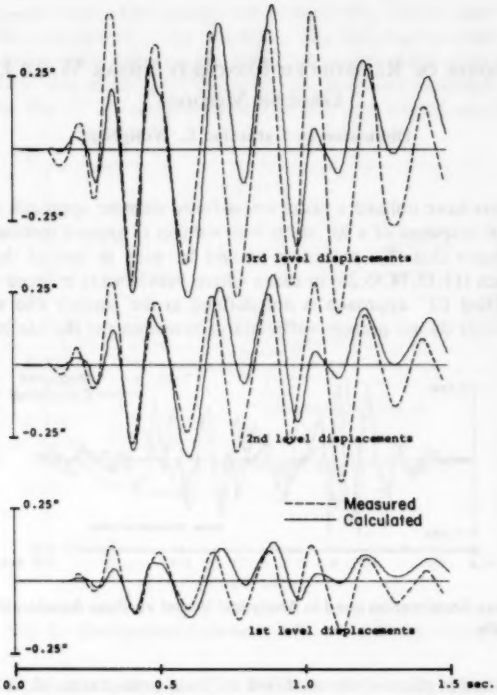

FIG. 12.—Calculated vs. Measured Relative Displacements for Shear Wall D-4 (1 in. = 25.4 mm)

The writer suggests running the finite element model with the same input motions as the experimental models and comparing the resulting response histories. This will give a better indication of the validity of their model. It may also provide some insight in defining the cases which require the additional complexity of the finite element model in place of simpler "modified EI" procedures.

EXPERIMENTAL EVALUATION OF COMPOSITE ACTION[a]

Discussion by R. Hussein[4]

The authors presented experimental results to verify their mathematical model for diaphragm systems.

It was stated in the paper that the theoretical and experimental results are in reasonable agreement. This statement is not clear from Table 2. The discrepancy

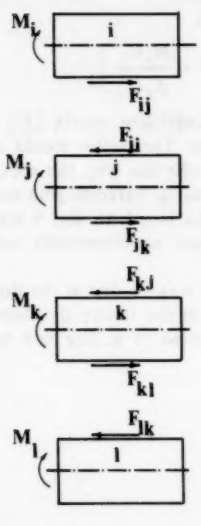

FIG. 9.—Analysis Model for Multilayer Diaphragm System

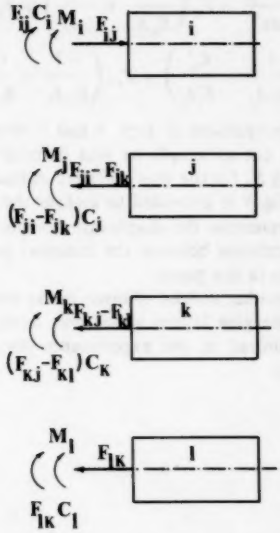

FIG. 10.—Modified Model for Multilayer Diaphragm System

is about 10% only at the location of gage no. 2. The error is about 94%, e.g., at gage no. 5 in the same table.

The authors do not present satisfactory explanations for the discrepancy between the theoretical and experimental results. The high percentage of error seems to be due to the incorrect evaluation of the diaphragm stiffness. The

[a]March, 1981, by Rafik Y. Itani, Houssain M. Morshed, and Robert J. Hoyle (Proc. Paper 16140).

[4]Research Assoc., Centre for Building Studies, Concordia Univ., Montreal, Quebec, Canada.

interlayer shear forces are acting at the interfaces between the different layers (Fig. 9). To consider these shear forces at the neutral plane of each layer, an additional bending moment should be taken into consideration (Fig. 10). At any layer, the additional moment is equal to the interlayer shears times half the thickness of that layer. As a consequence, Eqs. 2 and 3 become

$$\epsilon_{jb} = \frac{F_{ji} - F_{jk}}{E_j A_j} + \frac{M_j C_j}{E_j I_j} - \frac{(F_{ji} - F_{jk}) C_j^2}{E_j I_j} \quad \ldots\ldots\ldots\ldots\ldots\ldots\ldots (7)$$

$$\epsilon_{kt} = \frac{F_{kj} - F_{kr}}{E_k A_k} + \frac{M_k C_k}{E_k I_k} + \frac{(F_{kj} - F_{kr}) C_k^2}{E_k I_k} \quad \ldots\ldots\ldots\ldots\ldots\ldots\ldots (8)$$

Substituting Eqs. 7 and 8 in Eq. 4 yields

$$\frac{1}{S}\frac{d^2 F_{jk}}{dx^2} = F_{ij}\left(\frac{-1}{E_j A_j} + \frac{C_j^2}{E_j I_j}\right) + F_{jk}\left(\frac{1}{E_k A_k} + \frac{C_k^2}{E_k I_k}\right.$$

$$\left. + \frac{1}{E_j A_j} - \frac{C_j^2}{E_j I_j}\right) + F_{kr}\left(\frac{-1}{E_k A_k} - \frac{C_k^2}{E_k I_k}\right) - \left(\frac{M_j C_j}{E_j I_j} + \frac{M_k C_k}{E_k I_k}\right) \quad \ldots\ldots\ldots (9)$$

Comparison of Eqs. 5 and 9 reveals that the coefficient matrix $[K]$ in Eq. 6 is not as simple as was derived by the authors. The writer would suggest using S_{jk} for the glue stiffness instead of S in Eq. 9. By this way, the application of Eq. 9 is extended to include the possibility of using different glue materials to assemble the diaphragm. Numerical evaluations based on Eq. 9 were not undertaken because the material properties obtained experimentally were not given in the paper.

Another source of error in the results presented may be due to the thickness of the glue layers which was neither considered in the theory developed nor minimized in the experiments (the average thickness of a glue line was 2.3 mm).